

Electronic Theses and Dissertations, 2004-2019

2010

Environmental Degradation Of Oxidation Resistant And Thermal Barrier Coatings For Fuel-flexible Gas Turbine Applications

Prabhakar Mohan
University of Central Florida

 Part of the [Materials Science and Engineering Commons](#)
Find similar works at: <https://stars.library.ucf.edu/etd>
University of Central Florida Libraries <http://library.ucf.edu>

This Doctoral Dissertation (Open Access) is brought to you for free and open access by STARS. It has been accepted for inclusion in Electronic Theses and Dissertations, 2004-2019 by an authorized administrator of STARS. For more information, please contact STARS@ucf.edu.

STARS Citation

Mohan, Prabhakar, "Environmental Degradation Of Oxidation Resistant And Thermal Barrier Coatings For Fuel-flexible Gas Turbine Applications" (2010). *Electronic Theses and Dissertations, 2004-2019*. 4203.
<https://stars.library.ucf.edu/etd/4203>

ENVIRONMENTAL DEGRADATION OF OXIDATION RESISTANT AND
THERMAL BARRIER COATINGS FOR FUEL-FLEXIBLE GAS TURBINE
APPLICATIONS

by

PRABHAKAR MOHAN

M.S. University of Central Florida, 2007

B.Tech. Central Electrochemical Research Institute, Madurai Kamaraj University, 2003

A dissertation submitted in partial fulfillment of the requirements
for the degree of Doctor of Philosophy
in the Department of Mechanical, Materials and Aerospace Engineering
in the College of Engineering and Computer Science
at the University of Central Florida
Orlando, Florida

Spring Term
2010

Major Professor: Yong-Ho Sohn

© 2010 Prabhakar Mohan

ABSTRACT

The development of thermal barrier coatings (TBCs) has been undoubtedly the most critical advancement in materials technology for modern gas turbine engines. TBCs are widely used in gas turbine engines for both power-generation and propulsion applications. Metallic oxidation-resistant coatings (ORCs) are also widely employed as a stand-alone protective coating or bond coat for TBCs in many high-temperature applications. Among the widely studied durability issues in these high-temperature protective coatings, one critical challenge that received greater attention in recent years is their resistance to high-temperature degradation due to corrosive deposits arising from fuel impurities and CMAS (calcium-magnesium-alumino-silicate) sand deposits from air ingestion. The presence of vanadium, sulfur, phosphorus, sodium and calcium impurities in alternative fuels warrants a clear understanding of high-temperature materials degradation for the development of fuel-flexible gas turbine engines. Degradation due to CMAS is a critical problem for gas turbine components operating in a dust-laden environment. In this study, high-temperature degradation due to aggressive deposits such as V_2O_5 , P_2O_5 , Na_2SO_4 , $NaVO_3$, $CaSO_4$ and a laboratory-synthesized CMAS sand for free-standing air plasma sprayed (APS) yttria stabilized zirconia (YSZ), the topcoat of the TBC system, and APS CoNiCrAlY, the bond coat of the TBC system or a stand-alone ORC, is examined. Phase transformations and microstructural development were examined by using x-ray diffraction, scanning electron microscopy, and transmission electron microscopy.

This study demonstrated that the V_2O_5 melt degrades the APS YSZ through the formation of ZrV_2O_7 and YVO_4 at temperatures below 747°C and above 747°C , respectively. Formation of YVO_4 leads to the depletion of the Y_2O_3 stabilizer and the deleterious transformation of the YSZ

to the monoclinic ZrO_2 phase. The investigation on the YSZ degradation by Na_2SO_4 and a $Na_2SO_4 + V_2O_5$ mixture (50-50 mol. %) demonstrated that Na_2SO_4 itself did not degrade the YSZ, however, in the presence of V_2O_5 , Na_2SO_4 formed vanadates such as $NaVO_3$ that degraded the YSZ through YVO_4 formation at temperature as low as $700^\circ C$. The APS YSZ was found to react with the P_2O_5 melt by forming ZrP_2O_7 at all temperatures. This interaction led to the depletion of ZrO_2 in the YSZ (i.e., enrichment of Y_2O_3 in t'-YSZ) and promoted the formation of the fluorite-cubic ZrO_2 phase. Above $1250^\circ C$, CMAS deposits were observed to readily infiltrate and significantly dissolve the YSZ coating via thermochemical interactions. Upon cooling, zirconia reprecipitated with a spherical morphology and a composition that depended on the local melt chemistry. The molten CMAS attack destabilized the YSZ through the detrimental phase transformation ($t' \rightarrow t \rightarrow f + m$).

Free standing APS CoNiCrAlY was also prone to degradation by corrosive molten deposits. The V_2O_5 melt degraded the APS CoNiCrAlY through various reactions involving acidic dissolution of the protective oxide scale, which yielded substitutional-solid solution vanadates such as $(Co,Ni)_3(VO_4)_2$ and $(Cr,Al)VO_4$. The molten P_2O_5 , on the other hand, was found to consume the bond coat constituents significantly via reactions that formed both Ni/Co rich phosphates and Cr/Al rich phosphates. Sulfate deposits such as Na_2SO_4 , when tested in encapsulation, damaged the CoNiCrAlY by Type I acidic fluxing hot corrosion mechanisms at $1000^\circ C$ that resulted in accelerated oxidation and sulfidation. The formation of a protective continuous Al_2O_3 oxide scale by preoxidation treatment significantly delayed the hot corrosion of CoNiCrAlY by sulfates. However, CoNiCrAlY in both as-sprayed and preoxidized condition suffered a significant damage by $CaSO_4$ deposits via a basic fluxing mechanism that yielded

CaCrO_4 and CaAl_2O_4 . The CMAS melt also dissolved the protective Al_2O_3 oxide scale developed on CoNiCrAlY by forming anorthite platelets and spinel oxides.

Based on the detailed investigation on degradation of the APS YSZ and CoNiCrAlY by various corrosive deposits, an experimental attempt was carried out to mitigate the melt-induced deposit attack. Experimental results from this study demonstrate, for the first time, that an oxide overlay produced by electrophoretic deposition (EPD) can effectively perform as an environmental barrier overlay for APS TBCs. The EPD protective overlay has a uniform and easily-controllable thickness, uniformly distributed closed pores and tailored chemistry. The EPD Al_2O_3 and MgO overlays were successful in protecting the APS YSZ TBCs against CMAS attack and hot corrosion attack (e.g., sulfate and vanadate), respectively. Furnace thermal cyclic oxidation testing of overlay-modified TBCs on bond-coated superalloy also demonstrated the good adhesive durability of the EPD Al_2O_3 overlay.

This dissertation is dedicated as an appreciation to my real-life heroes: humanitarians who constantly strive to change the lives of unfortunate people for better.

ACKNOWLEDGMENTS

I would like to take this opportunity to express my sincere gratitude to those people, whose support and special concern got me this far with my doctoral degree at UCF. First, I would like to express my gratitude to Dr. Yongho Sohn, my advisor at UCF, for his sincere guidance, continuous support and encouragement throughout the course of my doctoral degree. Without his honest appreciation and encouraging comments, completion of this dissertation would not have been possible. I am certainly thankful to Dr. Sohn for all his belief in me and for letting me participate in a variety of research activities at UCF, which helped me decide my career choice. I would also like to extend my sincere gratitude to Dr. Vimal Desai, who supported me with technical guidance and financial assistance during the initial two years of my Ph.D. program at UCF. I would like to extend my gratitude to my dissertation committee members: Dr. Vimal Desai, Dr. Helge Heinrich, Dr. Linan An, Dr. Kevin Coffey and Dr. Anand Kulkarni for their valuable suggestions and thoughtful discussions.

I would like to express my special thanks to all my fellow colleagues (current and past) at the Laboratory of Materials and Coatings for Extreme Environment (MCEE): Travis, Rashmi (Mo), Hyunju, Bo, Manny, Jing, Narayana, Balaji, Srimi, Carmen, Ashley, Nathan, Biao, Sriparna, Catalina, William, Sara, Clara, Joshua, Zhengtao, Andrew and Ananda. It was certainly a great learning experience working with all of them. I would like to thank Srimi and Balaji, especially for those encouraging words years ago, to this stranger, which helped me choose UCF to pursue with a Ph.D.

I would like to extend my appreciation to the engineers and staff members of AMPAC and MCF: Karen, Kirk, Mikhail, Qi, Zia, Kari, Cindy, Angie and Waheeda. I would also like to

extend my appreciation to the faculty and staff members of the MMAE department as well as the International Services Center (ISC), the Career and Experiential Learning, the UCF libraries and the whole UCF community for helping me in one way throughout the course of my graduate studies. I am also grateful to the UCF Graduate Studies and the Student Government Association (SGA) at UCF, for various travel grants to attend conferences.

I would like to acknowledge the financial support that funded my Ph.D. research from Department of Energy (DOE) through University Turbine Systems Research (UTSR) program, NASA through State University System Florida Turbine Initiative (SFTI), Florida Center for Advanced Aero-propulsion (FCAAP) and turbine OEMs.

I am thankful to all my friends and roommates in Orlando for their care and timely assistance that helped me in many ways. I would like to express my unending gratitude to my good friends: Anna, Harish, Batty, Kaushik, Prakash, Karen, Hyunju, Mo, Balaji, Giridhar and Tao, for being the ones I could count on during many occasions.

Finally, I would like to thank my parents and my sister, who always tried their best to make my wish come true. I have no words to express my appreciation for their love, understanding and belief in me.

TABLE OF CONTENTS

LIST OF FIGURES	xiv
LIST OF TABLES	xxvi
LIST OF ABBREVIATIONS.....	xxvii
CHAPTER 1: INTRODUCTION	1
1.1. High-Temperature Protective Coatings for Gas Turbine Applications	1
1.2. Molten Deposit-Induced Environmental Degradation of TBCs	5
1.3. Objectives of this Doctoral Research.....	7
CHAPTER 2: LITERATURE REVIEW	10
2.1. TBCs and ORCs: Materials and Processing	10
2.1.1. Ceramic Topcoat of TBCs	10
Processing Techniques of YSZ topcoat	15
(i) Air Plasma Spraying:	15
(ii) Electron Beam Physical Vapor Deposition (EB-PVD):	19
(iii) Dense Vertically Cracked (DVC) TBCs:.....	21
2.1.2. Overlay ORCs and Bond Coat of TBCs	24
2.1.3. TGO formation in TBCs	28
2.2. Failure Mechanisms of TBCs	30
2.2.1. Failure Mechanisms in APS TBCs	32
2.2.2. Failure Mechanisms in EB-PVD TBCs	35
2.2.3. TBCs with Improved TGO Adhesion	37
2.3. High Temperature Degradation of TBCs by Molten Deposits	38

2.3.1. Degradation of TBCs and ORCs by Molten Deposits from Fuel Impurities.....	40
2.3.2. Degradation of TBCs by CMAS Sand Deposits.....	47
2.4. Mitigation Approaches to Protect TBCs from Molten Deposit Attack	49
2.4.1. Surface Sealing Treatments for YSZ-based TBCs	50
2.4.2. Corrosion-Resistant Stabilizers for ZrO ₂ TBCs	51
2.4.3. Novel Topcoat Materials.....	53
2.4.4. Impermeable and/or Sacrificial Oxide Overlay for the YSZ TBCs.....	57
2.5. Electrophoretic Deposition of Ceramic Coatings	58
CHAPTER 3: EXPERIMENTAL DETAILS.....	63
3.1. Air Plasma Sprayed Free Standing YSZ and CoNiCrAlY Coatings	63
3.2. High Temperature Isothermal Exposure to Molten Deposits	65
3.2.1. Hot Corrosion Testing of Free Standing YSZ and CoNiCrAlY	65
3.2.2. High Temperature CMAS Deposit Testing of Free Standing YSZ and CoNiCrAlY.	69
3.3. Microstructural Investigation of YSZ and CoNiCrAlY Specimens	70
3.4. Environmental Barrier Overlay for TBCs by Electrophoretic Deposition (EPD)	74
3.4.1. Al ₂ O ₃ Overlay for APS TBCs.....	74
3.4.2. MgO Overlay for APS TBCs.....	76
3.4.3. Al ₂ O ₃ -MgO composite Overlay for APS TBCs.....	77
3.4.4. YSZ Overlay for APS TBCs.....	78
3.5. Exposure of the free-standing APS YSZ with EPD Overlay to Molten Deposits	78
3.6. Durability Study of Commercial TBCs modified with EPD Overlay	79
CHAPTER 4: RESULTS.....	82

4.1. As-sprayed Free-Standing APS YSZ and CoNiCrAlY Coatings	82
4.2. Thermochemical Degradation of APS YSZ by Corrosive Molten Deposits	85
4.2.1. Vanadium Pentoxide (V_2O_5).....	85
4.2.2. Phosphorus Pentoxide (P_2O_5)	91
4.2.3. Sodium Sulfate (Na_2SO_4).....	95
4.2.4. $Na_2SO_4+V_2O_5$ Mixture	97
4.3. Thermochemical Degradation of APS YSZ by Molten CMAS Deposit	100
4.4. Thermochemical Degradation of APS CoNiCrAlY by Corrosive Molten Deposits	107
4.4.1. Vanadium Pentoxide (V_2O_5).....	107
4.4.2. Phosphorus Pentoxide (P_2O_5)	113
4.4.3. Sodium Sulfate (Na_2SO_4).....	115
4.4.4. Calcium Sulfate ($CaSO_4$)	119
4.4.5. Sodium Metavanadate ($NaVO_3$).....	120
4.5. Thermochemical Degradation of APS CoNiCrAlY by Molten CMAS Deposit	123
4.6. Ceramic Overlay for APS YSZ by EPD	126
4.6.1. YSZ Overlay	126
4.6.2. Alumina Overlay.....	134
4.6.3. Magnesia Overlay	144
4.6.4. Alumina-Magnesia Composite Overlay	147
4.7. Commercial TBCs modified with EPD Overlay	152
CHAPTER 5: DISCUSSION.....	156
5.1. Degradation of APS YSZ by Molten Deposits due to Fuel Impurities.....	156

5.1.1. Degradation of APS YSZ by V ₂ O ₅ Deposit.....	156
5.1.2. Degradation of APS YSZ by P ₂ O ₅ Deposit	164
5.1.3. Degradation of YSZ by molten Na ₂ SO ₄	165
5.1.4. Degradation of YSZ by Molten Na ₂ SO ₄ + V ₂ O ₅ mixture (50 – 50 mol. %)	166
5.2. Degradation of APS YSZ by Molten CMAS Deposits.....	167
5.3. Degradation of APS CoNiCrAlY by Molten Deposits from Fuel Impurities.....	169
5.3.1. Degradation of APS CoNiCrAlY by V ₂ O ₅ Deposit.....	169
5.3.2. Degradation of APS CoNiCrAlY by P ₂ O ₅ Deposit	171
5.3.3. Degradation of APS CoNiCrAlY by Na ₂ SO ₄ Deposit.....	172
5.3.4. Degradation of APS CoNiCrAlY by CaSO ₄ Deposit	175
5.3.5. Degradation of APS CoNiCrAlY by NaVO ₃ Deposit	176
5.4. Degradation of APS CoNiCrAlY by Molten CMAS Deposits.....	177
5.5. Protection of YSZ TBCs against Molten Deposit Attack by Electrophoretically Deposited Overlay.....	178
5.5.1. Rationale behind Selecting EPD as an Overlay Deposition Process for APS TBCs	178
5.5.2. Rationale behind Selecting the EPD Process Parameters for Overlay Deposition...	180
5.5.3. YSZ Overlay for APS YSZ TBCs by EPD.....	182
5.5.4. Alumina Overlay for APS YSZ TBCs by EPD	183
Mitigation of the CMAS Attack by EPD Alumina Overlay	183
Kinetics of Electrophoretic Deposition of Alumina	185
5.5.5. MgO Overlay for APS YSZ TBCs by EPD.....	191

5.5.6. Al ₂ O ₃ -MgO composite Overlay by Electrophoretic Codepositon for APS YSZ TBCs	191
5.6. Promising Durability of EPD Overlay-Modified Commercial TBCs.....	193
CHAPTER 6: CONCLUSION	194
APPENDIX A: FUTURE DIRECTIONS	200
APPENDIX B: LIST OF PUBLICATIONS AND PRESENTATIONS FROM THIS DISSERTATION.....	203
LIST OF REFERENCES.....	207

LIST OF FIGURES

- Figure 1.1: A schematic plot illustrating the temperature capability of high-temperature protective coatings for gas turbine applications. ORC stands for oxidation resistant coatings..... 3
- Figure 1.2: Typical cross-sectional micrograph of an EB-PVD TBC superimposed with a temperature gradient. 4
- Figure 2.1: Equilibrium phase-diagram of ZrO_2 - $YO_{1.5}$ system highlighting the regions of transformable (t) and non-transformable (t') metastable tetragonal zirconia polymorphs [63-65]. 12
- Figure 2.2: Crystal structures of ZrO_2 polymorphs: (a) tetragonal, (b) monoclinic and (c) fluorite-cubic ZrO_2 13
- Figure 2.3: Cross-sectional backscattered electron micrographs showing typical microstructures of (a) APS TBC (APS YSZ/LPPS MCrAlY/Superalloy) and (b) EB-PVD TBC (EB-PVD YSZ/(Ni,Pt)Al/Superalloy). 14
- Figure 2.4: A schematic representation of a typical plasma spray torch employed in APS technique. 15
- Figure 2.5: Effect of the YSZ topcoat density on the thermal cyclic lifetime of YSZ TBCs [68]. 18
- Figure 2.6: A schematic illustration of the EB-PVD process that takes place inside an evaporation chamber. The parts are typically rotated and revolved while being heated by a laser heat source and the ceramic ingots are heated by an electron beam to form a vapor rich environment, which deposits on the turbine blades [72]. 20
- Figure 2.7: Cross-sectional backscattered electron micrograph of a DVC TBC with segmented vertical macrocracks [75]. 23
- Figure 2.8: Equilibrium binary phase diagram of Ni-Al system [86]. 26

Figure 2.9: A schematic map illustrating the effectiveness of various coating materials system against high-temperature oxidation and corrosion.....	27
Figure 2.10: Cross-sectional microstructures of nearly failed APS TBCs showing different failure mechanisms.....	34
Figure 2.11: A cross-sectional micrograph of an EB-PVD TBC hypothetically illustrating the two common failure mechanisms.	35
Figure 2.12: A schematic illustration of dominant degradation mechanisms (Type I and II hot corrosion mechanisms and oxidation) at various temperatures.	45
Figure 2.13: Measured solubilities of various oxides in pure Na ₂ SO ₄ at 1200 K [1].	46
Figure 2.14: EBPVD TBC failure on a turbine airfoil due to air-ingested CMAS deposit: (a) Macrograph showing significant TBC spallation, (b) SEM micrograph showing surface morphology of spalled surface revealing amorphous CMAS deposit [103].....	47
Figure 2.15: Secondary electron micrographs revealing the modification of YSZ surface morphology due to laser glazing sealing treatment; (a) as-sprayed, (b) laser-glazed with CO ₂ laser and (c) laser-glazed with Nd-YAG laser [43].	50
Figure 2.16: Simulated contour map of thermal conductivity as a function of ionic radii of A and B for pyrochlore (A ₂ B ₂ O ₇) structured compounds [108].....	54
Figure 2.17: A schematic illustration of a proposed mechanism for mitigation of CMAS-attack by novel SPPS processed TBCs [50].	56
Figure 2.18: Secondary electron micrographs of the YSZ coating on a LSM substrate obtained by EPD followed by sintering at 1300°C for 3 h: (a) surface morphology and (b) cross-sectional microstructure [117].....	61
Figure 3.1: Macrographs of free standing APS YSZ and CoNiCrAlY coatings.	64
Figure 3.2: Experimental tools used for high temperature molten deposit testing of the free-standing YSZ and CoNiCrAlY.	66

Figure 3.3: A simple schematic representation of hot corrosion testing of APS coatings.....	68
Figure 3.4: Equilibrium phase diagram of the $V_2O_5 - Na_2SO_4$ system and the selected composition of mixture for this study (shaded) [127].	68
Figure 3.5: Materials characterization tools employed in this study.	72
Figure 3.6: Sequential ion beam images from TEM specimen preparation by focused ion beam (FIB) in-situ lift out (INLO) technique: : (a) Pt layer deposited at a site of specific interest; (b) focused ion milling carried out to create a wedge-shaped specimen, (c) specimen welded to a W omniprobe, and (d) lifted out, (e) Cu grid, (f) specimen welded to TEM grid, (g), (h) and (i) thinned further for TEM analysis [84].	73
Figure 3.7: A schematic representation showing the assembly of electrophoretic deposition (EPD) cell along with the mechanism of particle coagulation during cathodic deposition.....	76
Figure 3.8: Macrographs showing the as-processed commercial APS TBCs (APS YSZ/LPPS CoNiCrAlY on IN738LC superalloy) and APS TBCs modified with EPD overlay.	80
Figure 3.9: CM 1710 Rapid High Temperature Furnace used for thermal cyclic tests and a schematic illustration of cyclic oxidation testing.....	81
Figure 4.1: XRD pattern obtained from the as-sprayed free standing YSZ topcoat surface confirming the phase constituent of YSZ as the t' - ZrO_2	82
Figure 4.2: Cross-sectional (a) backscattered electron micrograph showing the typical microstructure of as-sprayed free standing YSZ topcoat with uniformly thick YSZ topcoat that consists of (b) splat-quenched microstructure observed by secondary electron micrograph.	83
Figure 4.3: (a) and (b) Secondary electron micrographs of free standing APS CoNiCrAlY coating showing the uniform cross-section and the typical surface splat microstructure; (c) cross-sectional backscattered electron micrograph presenting the microstructure of heat-treated free standing CoNiCrAlY after 20 h isothermal treatment at 1100°C and (d) secondary electron micrograph revealing the respective surface morphology of TGO scale evolved from isothermal heat-treatment.	84

Figure 4.4: XRD patterns illustrating the degradation of free-standing APS YSZ during YSZ–V₂O₅ reaction at 720°C: (a) as-sprayed; (b) 720°C for 30 minutes; (c) 720°C for 2 h and (d) ZrV₂O₇ standard. 85

Figure 4.5: (a) Cross-sectional backscattered electron micrograph of free-standing APS YSZ after reaction with V₂O₅ at 720°C for 30 minutes and the characteristic XEDS spectra showing (b) the unreacted YSZ (region 1), (c) reaction product ZrV₂O₇ (region 2) and (d) the solidified residue from molten V₂O₅ (region 3). 86

Figure 4.6: (a) Bright-field TEM micrograph showing the phase constituents of the APS YSZ after reaction with V₂O₅ at 720°C for 30 minutes. Electron diffraction patterns from the two phases present are indexed as (b) cubic ZrV₂O₇ and (c) tetragonal ZrO₂ with zone axes of [2 3 1] and [2 1 1] respectively. 87

Figure 4.7: XRD patterns illustrating the degradation of free-standing APS YSZ during YSZ–V₂O₅ reaction at 800°C: (a) as-sprayed; (b) 800°C for 30 minutes; (c) monoclinic ZrO₂ standard. 88

Figure 4.8: (a) Cross-sectional backscattered electron micrograph of free-standing APS YSZ after reaction with V₂O₅ at 800°C for 30 minutes and (b) and (c) characteristic XEDS spectra, showing the regions 1, 2 and 3 as unreacted YSZ, reaction product YVO₄, and the solidified residue from molten V₂O₅ respectively. 89

Figure 4.9: (a) Bright-field TEM micrograph from the APS YSZ after reaction with V₂O₅ at 800°C for 30 minutes. Electron diffraction patterns from the two phases present are indexed as (b) monoclinic ZrO₂ with a zone axis of [1 1 4] and (c) tetragonal YVO₄ with a zone axis of [001]. 90

Figure 4.10: XRD patterns obtained from the APS YSZ specimens after interaction with V₂O₅ melt at 750°C for various test durations. 91

Figure 4.11: XRD patterns illustrating the degradation of the APS YSZ during YSZ–P₂O₅ reaction: (a) as-sprayed; (b) 350°C for 1 h; (c) 450°C for 1 h; (d) cubic ZrP₂O₇ standard. 92

Figure 4.12: A magnified view of the XRD patterns in the 2θ range, 56<2θ<62, illustrating the degradation of free-standing APS YSZ during YSZ–P₂O₅ reaction: (a) as-sprayed; (b) 350°C for 1 h; and (c) 450°C for 1 h. 92

Figure 4.13: Cross-sectional backscattered electron micrograph of APS YSZ after reaction with molten P_2O_5 at $350^\circ C$ for 1 hour showing the reaction product ZrP_2O_7	94
Figure 4.14: XRD patterns illustrating the degradation of APS YSZ during YSZ– P_2O_5 reaction at elevated temperatures up to $1200^\circ C$	94
Figure 4.15: XRD patterns obtained from YSZ after testing with Na_2SO_4 deposit for various durations at $950^\circ C$ and $1000^\circ C$	95
Figure 4.16: Cross-sectional backscattered electron micrographs showing the inert nature of YSZ after hot-corrosion testing with Na_2SO_4 deposit and the corresponding XEDS spectra from regions of interest.....	96
Figure 4.17: XRD pattern obtained from quenched $Na_2SO_4+V_2O_5$ (50-50 mol.%) mixture confirming the presence of vanadates of sodium.....	97
Figure 4.18: XRD patterns illustrating the degradation of free-standing APS YSZ during YSZ– $Na_2SO_4+V_2O_5$ mixture reaction at $700^\circ C$ for 1 hour due to the formation of YVO_4	98
Figure 4.19: Backscattered electron micrograph showing the development of surface morphology of free-standing APS YSZ due to interaction with $Na_2SO_4+V_2O_5$ mixture at $720^\circ C$ for 1 hour. Region 1: YVO_4 (reaction product), Region 2: YSZ and Region 3: Applied sodium vanadate mixture.	99
Figure 4.20: Cross-sectional backscattered electron micrographs near the (a) top and (b) bottom surfaces of the APS YSZ coating subjected to molten CMAS infiltration at $1250^\circ C$ for 4 h. Regions 1 and 2 correspond to solidified CMAS and bulk YSZ.....	101
Figure 4.21: Backscattered electron micrographs obtained from the YSZ coating infiltrated by molten CMAS at $1300^\circ C$ for 4 h. (a) and (b) Cross-sections at low and high magnifications respectively. (c) Micrograph of surface morphology showing the CMAS infiltrated coating with coarse and fine reprecipitated ZrO_2 grains from CMAS melt. (d) Characteristic XEDS spectra from solidified CMAS and bulk YSZ. Regions 1, 2 and 3 correspond to solidified CMAS, bulk YSZ and reprecipitated ZrO_2 respectively.....	102

Figure 4.22: X-ray diffraction patterns illustrating the phase transformation of YSZ due to CMAS infiltration: (a) Collected patterns from (i) as sprayed YSZ coating – top surface, (ii) Top surface and (iii) bottom surface of the YSZ infiltrated by molten CMAS at 1300°C for 4 h. 103

Figure 4.23: Magnified representation of the XRD pattern at a narrow 2θ range of 57° to 62° collected from (i) as sprayed YSZ coating – top surface, (ii) Top surface and (iii) bottom surface of the YSZ after infiltration by molten CMAS at 1300°C for 4 h. 104

Figure 4.24: (a) Bright-field TEM micrograph obtained from the APS YSZ coating subjected to molten CMAS attack at 1350°C for 2 h. The corresponding electron diffraction patterns obtained from the phases present, which are indexed as (b) monoclinic ZrO_2 and (c) amorphous CMAS glass..... 105

Figure 4.25: (a) and (b) Bright-field TEM micrographs obtained from the APS YSZ after exposure to molten CMAS at 1350°C for 2 h showing significant presence of remaining t' - ZrO_2 in unaffected YSZ. (c) and (d) Corresponding electron diffraction patterns from t' - ZrO_2 and amorphous CMAS glass. 106

Figure 4.26: XRD pattern from V_2O_5 degraded CoNiCrAlY surface revealing monoclinic $(Cr,Al)VO_4$ as the primary phase constituent evolved during thermochemical interaction between APS CoNiCrAlY and molten V_2O_5 after 2 h at 700°C..... 107

Figure 4.27: (a) and (b) Secondary electron micrographs showing the surface morphologies of microstructural evolution during APS CoNiCrAlY – V_2O_5 melt interaction at 700°C for 2 h; (c) and (d) Characteristic XEDS spectra obtained from regions of interest..... 108

Figure 4.28: Cross-sectional backscattered electron micrographs demonstrating the accumulation of V_2O_5 melt at bottom of the coating in (a) and the melt infiltration throughout free-standing APS CoNiCrAlY in (b). Regions 1, 2 and 3 correspond to V_2O_5 melt, bulk CoNiCrAlY coating and internal alumina resulted from pre-oxidation treatment, respectively. 110

Figure 4.29: XRD pattern from the V_2O_5 degraded CoNiCrAlY surface confirming orthorhombic $(Co,Ni)_3(VO_4)_2$ and cubic $(Ni,Co)(Cr,Al)_2O_4$ as the primary phase constituents evolved during thermochemical interaction between APS CoNiCrAlY and molten V_2O_5 after 2 h at 900°C.... 111

Figure 4.30: (a) and (b) Secondary electron micrographs showing the surface morphologies of microstructural evolution during APS CoNiCrAlY – V_2O_5 melt interaction at 900°C for 2 h; (c) and (d) Characteristic XEDS spectra obtained from regions of interest..... 111

Figure 4.31: (a) Cross-sectional backscattered electron micrograph demonstrating the extent of degradation by V_2O_5 melt, where region 1 is the 100 nm-thick scale developed by consumption of free-standing APS CoNiCrAlY; (b) and (c) Characteristic XEDS spectra obtained from regions of interest – region 1: V-rich corroded scale and region 2: unaffected CoNiCrAlY bulk. 112

Figure 4.32: XRD pattern from P_2O_5 degraded CoNiCrAlY surface revealing the presence of monoclinic $(Ni,Co)(PO_3)_2$ and monoclinic $(Cr,Al)(PO_3)_3$ as the primary phase constituents of interaction between APS CoNiCrAlY and molten P_2O_5 at 350°C for 2 h. 113

Figure 4.33: (a) Backscattered electron micrograph showing the morphological difference of reaction compounds, region 1 – $(Ni,Co)(PO_3)_2$, and region 2 – $(Cr,Al)(PO_3)_3$ after free-standing APS CoNiCrAlY was exposed to P_2O_5 at 350°C for 2 h. (b) and (c) Characteristic XEDS spectra obtained from different reaction products. 114

Figure 4.34: (a) and (b) Secondary electron micrographs illustrating the surface morphology and phase evolution due to significant degradation by Na_2SO_4 melt of as-sprayed APS CoNiCrAlY at 1000°C for 50 h; (c) XEDS spectra identifying the reaction products as Cr_2S_3 116

Figure 4.35: Cross-sectional backscattered electron micrographs of Na_2SO_4 degraded as-sprayed APS CoNiCrAlY at 1000°C for 50 h: (a) degradation through significant internal oxidation is evident, (b) localized sulfidation resulted in formation of Cr_2S_3 within the bulk of CoNiCrAlY is observed. 117

Figure 4.36: Cross-sectional backscattered electron micrographs of Na_2SO_4 degraded pre-oxidized APS CoNiCrAlY at 1000°C for 50 h: (a) Presence of Na_2SO_4 deposit (region 1) and mixed oxide scale $(Al,Cr)_2O_3$ (region 2) are seen; (b) Presence of Na_2SO_4 deposit (region 1), spinel oxide $(Ni,Co)(Al,Cr)_2O_4$ (region 3) and TGO alumina (region 4) are observed as the surface scale constituents. 118

Figure 4.37: (a) Cross-sectional backscattered electron micrograph of $CaSO_4$ degraded CoNiCrAlY (pre-oxidized) at 1000°C for 50 h. (b) and (c) XEDS spectra collected from different reaction products. 119

Figure 4.38: (a) and (b) Cross-sectional backscattered electron micrographs of CoNiCrAlY (in as-sprayed state) after exposure to $NaVO_3$ at 900°C for 5 h showing the dissolution of coating constituents by V rich melt, (c) Corresponding XEDS spectrum from region 1. 121

Figure 4.39: (a) and (b) Cross-sectional backscattered electron micrographs of CoNiCrAlY (in pre-oxidized state) after exposure to NaVO₃ at 900°C for 5 h showing the modified surface scale (TGO) constituents; region 1: (Ni,Co)(Al,Cr)₂O₄ spinel and region 2: TGO alumina (α Al₂O₃). 122

Figure 4.40: (a) and (b) Secondary electron micrographs of CoNiCrAlY (pre-oxidized) surface after degraded by CMAS deposit at 1250°C for 5 h showing microstructural evolution due to thermochemical interaction; (c) Respective XEDS spectra from regions of interest. 124

Figure 4.41: (a) and (b) Cross-sectional backscattered electron micrographs of CoNiCrAlY (pre-oxidized) after degraded by CMAS deposit at 1250°C for 5 h showing microstructural evolution due to thermochemical interaction; (c) Corresponding XEDS spectra from regions of interest; region 1: crystallized CMAS, region 2: applied CMAS. 125

Figure 4.42: XRD patterns obtained from (a) Air plasma sprayed (APS) YSZ coating that is primarily composed of metastable tetragonal ZrO₂ phase (t' – ZrO₂), (b) YSZ green compact obtained from EPD consisting of a mixture of ZrO₂ equilibrium phases and (c) YSZ overlay coating after sintering at 1300°C for 4 h primarily composed of t' – ZrO₂. 127

Figure 4.43: Secondary electron micrographs illustrating the surface morphology of (a) YSZ green compact after EPD and (b) YSZ overlay coating after sintering at 1300°C for 4 h. 128

Figure 4.44: Secondary electron micrographs demonstrating the crack-free EPD YSZ surface morphology on a APS YSZ specimen with the right half uncoated during EPD. 129

Figure 4.45: Cross-sectional secondary electron micrographs showing the typical EPD overlay microstructure: (a) a continuous YSZ overlay coating fabricated by EPD followed by sintering at 1300°C for 4 h and (b) the EPD YSZ / APS YSZ coating interface. 130

Figure 4.46: Secondary electron micrographs revealing the surface morphology of (a) YSZ overlay coating after sintering at 1300 °C for 4 h and (b) YSZ overlay coating after sintering at 1350 °C for 4 h..... 131

Figure 4.47: Cross-sectional secondary electron micrographs of EPD YSZ overlay coatings with varying porosity by different sintering conditions: (a) sintered at 1300°C for 4 h and (b) sintered at 1350°C for 4 h..... 132

Figure 4.48: Cross-sectional backscattered electron micrographs showing the ingress of CMAS through EPD YSZ during high-temperature CMAS exposure at 1300°C for 1 h: (a) CMAS infiltrated APS YSZ with EPD YSZ overlay, (b) a magnified view of EPD YSZ overlay after S attack; Region 1: YSZ, Region 2: solidified CMAS..... 133

Figure 4.49: XRD pattern collected from the surface of EPD alumina overlay on free-standing APS YSZ coating showing rhombohedral α -Al₂O₃ as the primary phase constituent. 134

Figure 4.50: Secondary electron micrographs of EPD alumina overlay achieved by sintering at 1200°C for 10 h reveal the typical sintered microstructure. 135

Figure 4.51: Cross-sectional micrographs: (a) backscattered electron micrograph showing free-standing YSZ coatings with 60µm thick alumina overlay achieved by EPD followed by sintering at 1200°C for 10h; (b) secondary electron micrograph showing a magnified view of cross-sectional microstructure of EPD overlay. 136

Figure 4.52: Plot of sintered alumina overlay thickness vs. deposition time during EPD processing of alumina overlay for APS YSZ..... 138

Figure 4.53: Cross-sectional secondary electron micrographs showing (a) a 100 µm thick alumina overlay achieved by EPD for 15 minutes followed by sintering at 1200°C for 10 h and (b) APS YSZ/EPD Alumina interface. 138

Figure 4.54: Secondary electron micrographs showing the surface microstructural evolution due to thermochemical interaction between APS YSZ with alumina overlay and CMAS melt at 1300°C for 1 h: (a) CMAS crystallized as platelets; (b) Alumina overlay arresting the CMAS melt ingress through crystallization. 139

Figure 4.55: Cross-sectional backscattered electron micrograph demonstrating the complete arrest of CMAS melt ingress by the crack-free alumina overlay; (b) secondary electron micrograph also reveals the suppression of CMAS melt ingress and (c) Corresponding XEDS spectra revealing the increase of Al content in crystallized CMAS. 140

Figure 4.56: XRD patterns obtained from as-processed EPD alumina overlay and CMAS interacted EPD alumina after isothermal testing at 1300°C for 1 h. Primary phase constituents corresponding to the complete crystallization of CMAS due to the interaction are hexagonal anorthite (CaAl₂Si₂O₈) and orthorhombic MgAl₂O₄ spinel..... 141

Figure 4.57: (a) and (b) Bright field TEM micrographs obtained from crystallized CMAS region resulted from thermochemical interaction with alumina at 1300°C for 1 h highlighting and the presence of anorthite ($\text{CaAl}_2\text{Si}_2\text{O}_8$) platelets and (c) the corresponding selected area electron diffraction pattern obtained from platelet (region 1) indexed to $\text{CaAl}_2\text{Si}_2\text{O}_8$ 142

Figure 4.58: (a) and (b) Bright field TEM micrographs obtained from crystallized CMAS region resulted from thermochemical interaction with alumina at 1300°C for 1 h highlighting the presence of equiaxed spinel MgAl_2O_4 and (c) the corresponding selected area electron diffraction pattern indexed to orthorhombic MgAl_2O_4 143

Figure 4.59: (a) Secondary electron micrograph of MgO surface achieved by EPD on the APS YSZ followed by sintering at 1100°C for 10 h. (b) Secondary electron micrograph of a fractured MgO cross-section showing the microstructural homogeneity. 144

Figure 4.60: Cross-sectional backscattered electron micrograph shows the 25 μm thick EPD MgO overlay on a free-standing APS YSZ specimen. 145

Figure 4.61: (a) Secondary electron micrograph shows the surface morphological changes of MgO overlay due to microstructural evolution during interaction with V_2O_5 deposit at 900°C for 1 h, (b) Cross-sectional backscattered electron micrograph highlighting the suppression of V_2O_5 melt ingress and MgO- V_2O_5 interaction layer..... 146

Figure 4.62: XRD pattern obtained from V_2O_5 -interacted EPD MgO after isothermal testing at 900°C for 1 h. Primary phase constituents corresponding to the complete arrest of V_2O_5 melt ingress are triclinic $\text{Mg}_2\text{V}_2\text{O}_7$ and orthorhombic $\text{Mg}_3\text{V}_2\text{O}_8$ 147

Figure 4.63: Cross-sectional backscattered electron micrographs (a and b) illustrate the continuous crack-free characteristics of Al_2O_3 -MgO composite overlay on APS YSZ achieved by electrophoretic codeposition followed by sintering at 1100°C for 5 h; (c) Characteristic XEDS spectra from regions 1 and 2 confirm the phase constituents of overlay as Al_2O_3 -MgO composite and MgAl_2O_4 spinel respectively..... 148

Figure 4.64: Microstructural evolution due to thermochemical interaction of CMAS and Al_2O_3 -MgO composite overlay (on APS YSZ) at 1250°C for 1 h: (a) and (b) surface secondary electron micrographs illustrating the crystallization of CMAS due to thermochemical interaction with the composite barrier overlay; (c) and (d) cross-sectional backscattered electron micrographs demonstrating the complete suppression of CMAS ingress through crystallization; (e) characteristic XEDS spectrum of region 1 confirm Diopside [$\text{Ca}(\text{Mg},\text{Al})(\text{Si},\text{Al})_2\text{O}_6$] as one of the products of crystallized CMAS..... 150

Figure 4.65: Microstructural evolution due to thermochemical interaction of V_2O_5 melt and Al_2O_3 -MgO composite overlay (on APS YSZ) at $900^\circ C$ for 1 h: (a) surface secondary electron micrograph showing the evolution of V-rich reaction products due to thermochemical interaction with the composite barrier overlay; (b) characteristic XEDS spectrum of V-rich reaction products [$Mg_2V_2O_7$ and $Mg_3V_2O_8$]; (c) cross-sectional backscattered electron micrograph demonstrating the complete suppression of V_2O_5 ingress through formation of reaction products that have melting temperature. 151

Figure 4.66: Plot of average lifetime of TBCs with and without EPD Al_2O_3 overlay assessed through 1-hour thermal cyclic exposure testing at $1100^\circ C$ under the absence of any corrosive deposit. 152

Figure 4.67: Macrographs of commercial TBCs with and without EPD Al_2O_3 overlay before and after failure during 1-hour thermal cyclic exposure at $1100^\circ C$ under the absence of any corrosive deposit. 153

Figure 4.68: Cross-sectional backscattered electron micrographs of commercial TBC without EPD Al_2O_3 overlay failed after an average lifetime of 191 “1-hour” cycles at $1100^\circ C$ 154

Figure 4.69: Cross-sectional backscattered electron micrographs of commercial TBC modified with a $75\ \mu m$ thick EPD Al_2O_3 overlay failed after a lifetime of 196 “1-hour” cycles at $1100^\circ C$ 155

Figure 5.1: Plot of volume fraction of monoclinic zirconia phase (f_m) vs. exposure duration (t) associated with V_2O_5 attack of YSZ at three different temperatures and the corresponding AJMK expression-fit. 161

Figure 5.2: Plot of $\ln(k)$ vs $1/T$ shows the Arrhenius type temperature dependence of the rate constant (k). 163

Figure 5.3: Plot of temperature-dependent k vs. temperature (T) and the derived Arrhenius relation. 163

Figure 5.4: Equilibrium CaO-SiO₂-Al₂O₃ ternary isotherm at $1200^\circ C$ [50]. 185

Figure 5.5: Plot of alumina overlay thickness as a function of deposition duration during EPD. 186

Figure 5.6: Plot used to derive the phenomenological expression that explains the film growth kinetics. 189

Figure 5.7: A schematic plot showing the overlay thickness variation as a function of deposition duration during EPD with various controlling parameters (voltage, suspension concentration).
..... 190

LIST OF TABLES

Table 2.1: Various solvents used in EPD processing of different materials.....	62
Table 3.1: List of APS process parameters employed to fabricate free standing coatings.	64
Table 3.2: Details of the high temperature molten deposit tests carried out in this study.	67
Table 5.1: The constants and the incubation period for the degradation mechanism associated with V_2O_5 attack of YSZ at three different temperatures.	161

LIST OF ABBREVIATIONS

APS	Air Plasma Spraying
CMAS	Calcium Magnesium Alumino Silicate
DVC	Dense Vertically Cracked
EB-PVD	Electron Beam Physical Vapor Deposition
EPD	Electrophoretic Deposition
HVOF	High Velocity Oxy Fuel
LPPS	Low Pressure Plasma Spraying
ORC	Oxidation Resistant Coating
SAED	Selected Area Electron Diffraction
SEM	Scanning Electron Microscope
SPPS	Solution Precursor Plasma Spraying
STEM	Scanning Transmission Electron Microscope
TBC	Thermal Barrier Coating
TEM	Transmission Electron Microscope
TIT	Turbine Inlet Temperature
VPS	Vacuum Plasma Spraying
XEDS	X-ray Energy Dispersive Spectroscopy
XRD	X-ray Diffraction
YSZ	Yttria Stabilized Zirconia

CHAPTER 1: INTRODUCTION

Advancements in materials technology led to success in many engineering challenges, for example; space vehicles re-entering the earth's atmosphere are able to withstand an inevitable exposure to extreme environment, i.e., high temperature and pressure. In the meantime, continuing efforts in pushing current-generation materials to their limits for improved performance come with many challenges in terms of environmental degradation [1-3]. With increasing service temperature, the severity of the environmental degradation of materials, which is a thermally-activated process in most cases, is expected to increase. The high temperature behavior and the environmental degradation of engineering materials have been widely studied for various industrial applications [4-7]. However, due to the development of novel materials and concurrent increase in severity of environmental attack, high-temperature degradation of structural materials is still an area of intense research [8].

1.1. High-Temperature Protective Coatings for Gas Turbine Applications

In power generation and aero-propulsion sectors, development of advanced gas turbines for a superior performance with improved efficiency has been a wide subject of research for many decades. The ever increasing demand for energy led to various ground-breaking materials developments for advanced gas turbines, in specific. Superalloys, a class of structural alloys for high temperature applications with excellent mechanical properties and superior resistance to environmental degradation, have been extensively employed in load-bearing hot section components of gas turbines [9]. However, because of the ever increasing demand to increase the turbine inlet temperature (TIT) for improved engine efficiency, a materials system to effectively

protect the hot section turbine components has been a critical requirement for current-generation combustion turbines. Rotating and stationary turbine components such as airfoils and vanes made of superalloys with complicated internal cooling schemes have not been sufficient to withstand the demanding aggressive combustion environment [10]. Extensive research efforts over decades led to advanced protective coatings for turbine components, primarily for thermal insulation as well as to enhance the oxidation/hot corrosion resistance of turbine components [11-17].

Development of thermal barrier coatings (TBCs) has undoubtedly been the most critical advancement in materials technology for gas turbine applications. TBCs are widely used in both industrial gas turbine (IGT) and aircraft engines [15]. TBCs facilitate a quantum leap in TIT (up to 150°C) by providing thermal insulation to hot section metallic components [10]. TBCs, besides facilitating such a tremendous increase in TIT, also protect the load bearing structural alloys of combustion turbines from extreme environment (high temperature, high pressure, corrosion) and have become the materials system of choice for improved efficiency and performance of gas turbine engines. Continuing efforts in the development of TBCs represent one of the most challenging tasks for scientists and engineers. In addition, given that TBC technologies have the most significant impact on the sales and the repair business of the gas turbine industry, they continue to be a prime focus of R&D for turbine OEMs. A schematic plot illustrating the temperature capability of gas turbine components with advanced protective coatings is shown in Fig. 1.1.

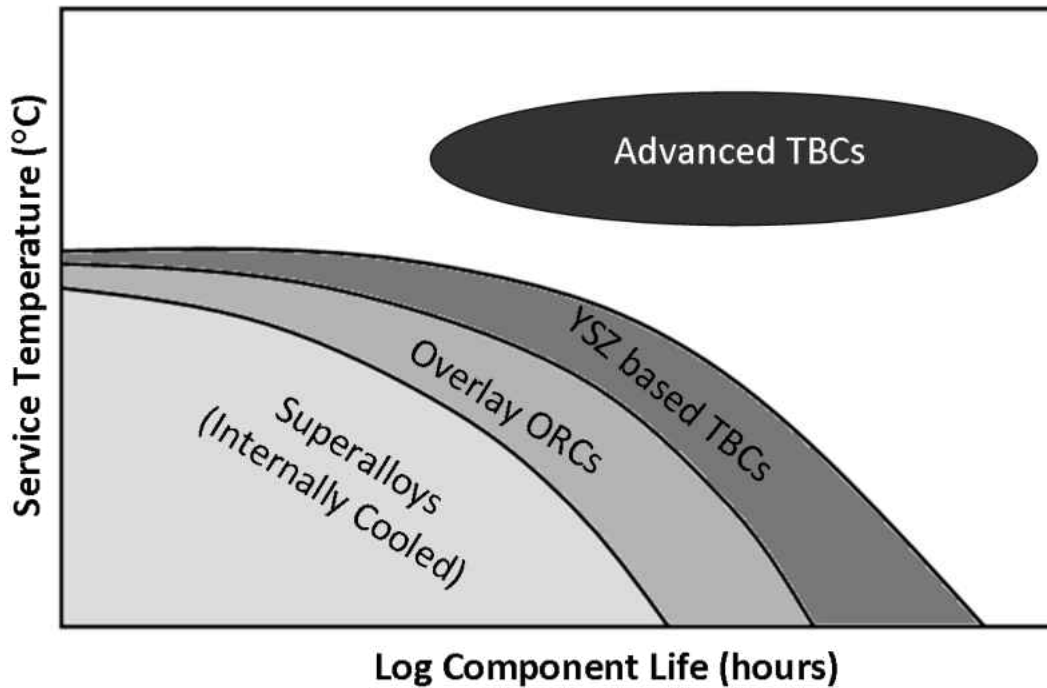


Figure 1.: A schematic plot illustrating the temperature capability of high-temperature protective coatings for gas turbine applications. ORC stands for oxidation resistant coatings.

Because of the demanding extreme operating conditions, TBCs possess the most complex structure among the widely available coatings that are used to protect structural materials from various environments. TBCs are multilayered systems consisting of a ceramic topcoat for thermal insulation, a thermally grown oxide (TGO) scale, predominantly Al_2O_3 , a metallic bond coat that provides oxidation/hot corrosion resistance, and a superalloy substrate, which is the load-bearing component [12, 15]. The ceramic topcoat of TBCs, typically made of zirconia stabilized with yttria (YSZ – yttria stabilized zirconia), is often deposited either by air plasma spray (APS) or electron beam physical vapor deposition (EB-PVD); the choice of the respective deposition process depends on factors such as coating thickness, aerodynamic requirement, reparability and production costs [10]. A typical cross-sectional microstructure of EB-PVD

TBCs, as presented in Fig. 1.2, clearly illustrates the temperature gradient across the multi-layered TBC system.

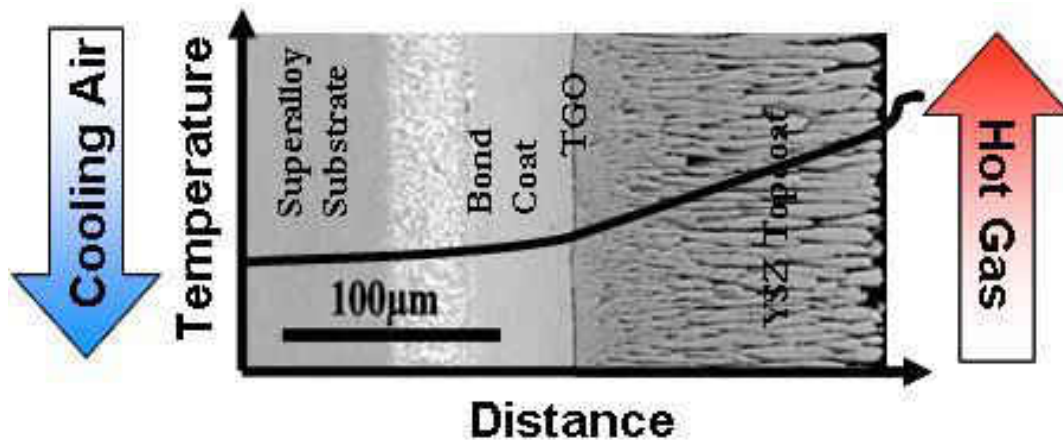


Figure 1.: Typical cross-sectional micrograph of an EB-PVD TBC superimposed with a temperature gradient.

The bond coat is primarily designed as a local Al reservoir for facilitating the formation of α -Al₂O₃ as the TGO scale in preference to other oxides [17-21]. This bond coat material system has also been widely employed as overlay oxidation resistant coatings (ORCs). Because of its major influence on TBC durability through the morphology and structure of the TGO formed, the bond coat has been considered as the most crucial component of TBCs [17, 18]. Two different types of widely used bond coats are: MCrAlY (M = Ni and/or Co) and Pt-modified nickel aluminide, (Ni,Pt)Al. Development in thermal spray processing techniques of MCrAlY type bond coats identified Low Pressure Plasma Spraying (LPPS) or Vacuum Plasma Spraying (VPS) technique as an effective method to fabricate denser and less oxidized bond coats [22]. Other techniques include the conventional Air Plasma Spraying (APS) [23, 24], High Frequency

Pulse Detonation (HFPD) [25], and High Velocity OxyFuel (HVOF), which has gained attention as another cost effective alternative technique for fabricating bond coats of desired quality [26, 27].

1.2. Molten Deposit-Induced Environmental Degradation of TBCs

Among the various life-limiting factors, one key durability issue of TBCs is their resistance to environmental degradation due to molten deposits arising from the aggressive combustion environment as well as from air-ingested foreign particles. Effective use of environmentally acceptable and economically viable large coal reserves and various other petroleum products as alternative fuels for power generation, especially in Integrated Gasification Combined Cycle (IGCC) power plants, has been believed to improve the economy of power generation. IGCC power plants, compared to the conventional coal-burning steam turbine plants, operate at higher TIT and provide a more efficient energy source with reduced CO₂, SO_x and NO_x emissions. However, these IGCC plants need advanced combustion turbines that operate at higher firing temperature, while requiring significantly improved tolerance to the contaminants that erode, corrode and deposit onto hot section turbine components. Thus the development of technology to improve the fuel-flexibility of gas turbine engines in order to use alternative fuels that contain appreciable elemental impurities, e.g., syngas, petroleum coke (petcoke), coal/petcoke blends and biomass-derived fuels for power generation, requires a clear understanding of high temperature materials degradation due to the aggressive combustion byproducts arising from alternative fuels. In addition, land-based military and marine engines can be operated with low quality fuels containing elemental impurities such as vanadium, phosphorus, sodium, calcium and sulfur. In such cases, molten corrosive compounds of V, S, Ca,

Na, and P may be deposited on the surface of the turbine components during long term operation at elevated temperature [12, 28]. Thus hot corrosion resistance over extended exposures to low quality fuel is another key durability issue for the expanding applications of TBCs and ORCs.

Another rising and critical durability issue for TBCs is their resistance to degradation due to air ingested CMAS (calcium-magnesium aluminosilicate) sand deposits. TBCs are increasingly susceptible to CMAS attack, especially in aircraft engines that operate in a dust-laden environment wherein ingestion of siliceous debris into engines has been commonly reported [29]. Similar to the contaminants due to fuel impurities, at elevated temperature these airborne deposits adhere, melt and degrade the TBC system via a repeated freeze-thaw action and, to a certain extent, direct chemical reaction with TBC constituents. The interactions that can accelerate the failure of TBCs and underlying components include destabilization of the ceramic YSZ topcoat, accelerated oxidation and hot corrosion of the underlying metallic bond coat and superalloys [29, 30].

The high temperature degradation of TBCs by CMAS attack and hot corrosion through molten deposits from fuel impurities has been widely studied [28-48]. In addition to the critical threat due to thermo-mechanical damage via infiltration, degradation due to thermochemical interactions can be significantly accelerated based on the contaminant content of alternative fuels. Thus in order to protect TBCs from both thermo-mechanical and thermochemical degradation of molten deposits, melt ingress into the porous YSZ topcoat should be completely suppressed. Various studies have attempted to mitigate the melt ingress by surface sealing of the YSZ topcoat through employing surface processing techniques such as laser glazing [43], or by employing inert environmental barrier layers as impermeable overlay

protection [44, 45]. Modifying the YSZ topcoat chemistry was also studied [46-50]. Zirconia stabilized with novel stabilizers were thoroughly studied as an alternate to YSZ-based TBCs towards development of novel TBCs with superior resistance against environmental degradation. Recently, rare-earth zirconates (REZ pyrochlores) such as $A_2Zr_2O_7$ (A: La→Gd) received greater attention due to their promising resistance against CMAS attack [49-52].

1.3. Objectives of this Doctoral Research

In this investigation, attempts were made to thoroughly understand the thermochemical degradation mechanisms of YSZ based APS TBCs by various possible corrosive molten deposits [53-55]. APS YSZ and MCrAlY coatings as free-standing coatings without the substrate were thoroughly tested by various corrosive species in isolation, and degradation reactions were identified as a function of temperature. Hot corrosion studies of MCrAlY coatings by sulfate and vanadate melts were also performed. A clear understanding of hot corrosion reactions by which YSZ and MCrAlY coatings degrade by molten deposits would serve as a baseline for development of protective coatings for fuel-flexible gas turbine applications as well as for expanding the applications of current-generation TBCs and ORCs. With a motivation to identify a promising engineering solution that requires only a slight modification to existing materials and coating technology, various mitigation approaches were reviewed. Employing an environmental barrier overlay composed of a desired material through a cost-effective scale-up-ready coating processing technique, electrophoretic deposition (EPD) has been extensively explored for the first time for such applications to protect thermally sprayed YSZ TBCs against molten deposit attack [56-58]. The promising capability of EPD barrier overlay coatings in

protecting APS TBCs from environmental degradation and the mitigation mechanisms were thoroughly examined.

Thus, the objectives of this study were: (i) to achieve a thorough understanding of the thermochemical aspects of degradation of the APS YSZ and APS CoNiCrAlY coatings by molten deposits and (ii) to develop a promising engineering solution to improve the resistance of these protective coatings to such deposit-induced high temperature degradation. To achieve the overall objective, the following goals were identified, and the corresponding work was carried out.

1. To understand the degradation mechanisms of the APS YSZ coatings by corrosive compounds that could arise from fuel impurities such as V_2O_5 , P_2O_5 , Na_2SO_4 and a Na_2SO_4 - V_2O_5 mixture.
2. To understand the degradation mechanisms of the APS YSZ by air-ingested CMAS sand deposits at elevated temperatures.
3. To obtain a thorough understanding on degradation through hot corrosion of the APS CoNiCrAlY coatings (e.g., TBC bond coats and overlay ORCs) by corrosive compounds that could arise from fuel impurities such as V_2O_5 , P_2O_5 , Na_2SO_4 , $NaVO_3$ and $CaSO_4$.
4. To understand the degradation mechanisms of the APS CoNiCrAlY coatings by air-ingested CMAS sand deposits at elevated temperatures.
5. To identify a promising engineering solution (materials/process modification) in order to protect the current-generation APS TBCs from such molten deposit-induced environmental attack.

6. To demonstrate the potential of a cost-effective scale-up ready coating processing technique, EPD, for fabricating an oxide overlay with the desired microstructure for protecting TBCs.
7. To identify the mitigation mechanisms for the improved resistance against hot corrosion/CMAS attack in TBCs with the EPD overlay.
8. To demonstrate the durability of the EPD overlay in terms of TBC lifetime during high temperature exposure.

CHAPTER 2: LITERATURE REVIEW

2.1. TBCs and ORCs: Materials and Processing

TBCs and overlay ORCs have become design-integrated parts of the high-temperature materials system in gas turbine components. In the 1970s, plasma sprayed TBCs, primarily composed of MgO stabilized zirconia found applications as protective coatings in commercial gas turbine engines [12]. Continuous efforts in finding ideal materials for highly durable TBCs for an improved component life led to various materials and process developments.

2.1.1. Ceramic Topcoat of TBCs

The selection of materials for TBCs, ceramic topcoat in specific, is restricted by critical requirements including:

- (1) High melting point,
- (2) Phase stability between room temperature and operating temperature,
- (3) Low thermal conductivity,
- (4) Chemical inertness,
- (5) Thermal expansion match with the metallic substrate,
- (6) Good adherence to the metallic substrate and
- (7) Low sintering rate to maintain the strain-tolerant microstructure.

Hence, there are only very few materials that can be considered. Zirconia in its stabilized form can satisfy most of the requirements stated above as a material for the topcoat. Also partially stabilized zirconia has excellent thermal shock resistance because of microcracking and transformation toughening [59-61]. Stabilization of zirconia has been achieved with various

stabilizers such as CaO, MgO, Y₂O₃, Sc₂O₃, InO₂, CeO₂ and other rare earth oxides when alloyed as a solid solution in ZrO₂ [12, 62]. Extensive studies on various ZrO₂ stabilizers for TBC applications demonstrated yttria as the preferred choice of stabilizer, with a specific composition of 7-8 wt.% as a solid solution in ZrO₂ that yields partially stabilized zirconia (7-8YSZ: zirconia stabilized with 7-8 wt.% yttria). The advantages of 7-8 YSZ are: high thermal expansion coefficient; low thermal conductivity and high thermal shock resistance [15-17]. The YSZ TBCs possess their long-term durability at high temperatures with a high strain compliance and the long term stability of metastable, tetragonal prime ZrO₂ phase (t'-ZrO₂) [60].

As seen from the phase diagram of the ZrO₂-YO_{1.5} system, presented in Fig. 2.1, the equilibrium phases for the YSZ topcoat at typical gas turbine temperatures are a mixture of tetragonal (t) and fluorite-cubic (f) phases [63-64]. However, during deposition processing of the YSZ, a rapid quench promotes the formation of the metastable tetragonal-prime phase (t'-ZrO₂). This t' phase helps prevent the phase transformation to room temperature equilibrium phases such as monoclinic (m) and fluorite-cubic (f) phases during thermal cycling. It is well known that the phase transformation to the m-ZrO₂ phase is accompanied by a large destructive volume change (3 to 5%) that could lead to delamination and spallation of the ceramic topcoat [66]. Phase constituents of the YSZ also depend on the concentration of the oxide stabilizer. Different compositions of the yttria stabilizer give rise to different phases. A mixture of 2-3 mol.% of Y₂O₃ with ZrO₂, when annealed at 1400°C to 1600°C and cooled at appropriate rates, yields a metastable tetragonal (t) ZrO₂ phase instead of a mixture of equilibrium monoclinic and cubic phases. This in turn may contain cubic phases that depend on the processing conditions. This phase is also known as Tetragonal Zirconia Polycrystalline (TZP) phase [60]. For proper

distinction from other phases, it is also termed as Ytria-Tetragonal Zirconia Polycrystalline (Y-TZP) phase. On the other hand, 4-5 mol.% Y_2O_3 content as ZrO_2 stabilizer, under appropriate annealing ($2200^\circ C$ - $2400^\circ C$) and rapid quenching yields, a metastable non-transformable tetragonal (t') phase.

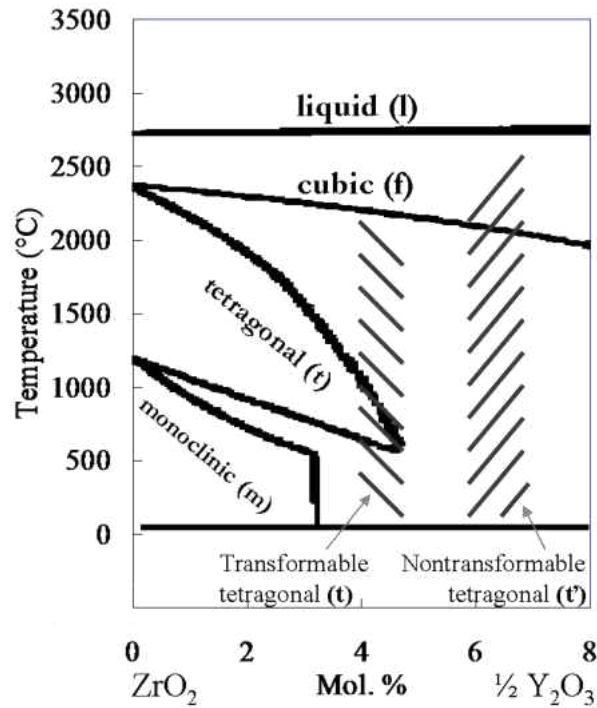


Figure 2.: Equilibrium phase-diagram of ZrO_2 - $YO_{1.5}$ system highlighting the regions of transformable (t) and non-transformable (t') metastable tetragonal zirconia polymorphs [63-65].

Formation of the t' -phase is very critical and is often described as Y-PSZ or PSZ, to differentiate from fully stabilized zirconia (Y-FSZ or FSZ). The t -phase, in general, is considered as the strongest ceramic because of its high strength and fracture toughness, greater than $15 \text{ MPa}\sqrt{m}$ [59]. The fracture toughness of the TZP is a result of transformation toughening mechanism where a transformation to the monoclinic phase under high stress (e.g. crack tip) occurs [60]. When energy is dissipated at the crack tip and results in volume expansion further

crack propagation will be arrested, whereas the t' -phase is completely stable even under high mechanical stress and hence is called a non-transformable tetragonal phase. Extensive investigations by various researchers concluded the following: (1) the transformation of the cubic to the tetragonal t -phase is diffusion controlled; (2) the rapidly quenched tetragonal t' -phase is formed by a diffusionless transformation and (3) the tetragonal-to-monoclinic transformation toughening process is martensitic with the grain size and Y_2O_3 content being the primary factors determining the martensitic start (M_s) temperature [60]. The equilibrium crystal structures of the three polymorphs (fluorite-cubic, monoclinic and tetragonal) of zirconia are illustrated in Fig. 2.2.

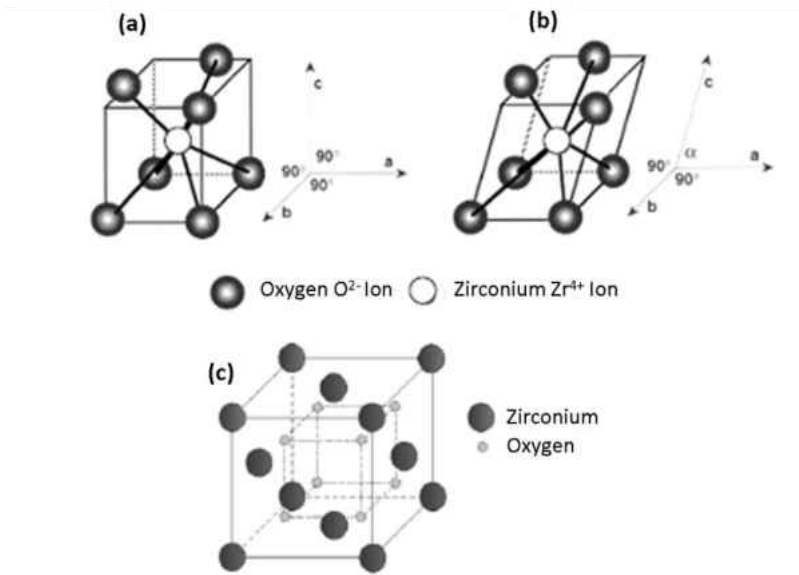


Figure 2.: Crystal structures of ZrO_2 polymorphs: (a) tetragonal, (b) monoclinic and (c) fluorite-cubic ZrO_2 .

The YSZ coatings are often deposited either by air plasma spray (APS) or electron beam physical vapor deposition (EB-PVD); the choice of the respective deposition process depends on

factors such as coating thickness, aerodynamic requirement, repairability and production costs [13-15]. These are the preferred techniques that provide high cooling rates necessary to achieve the desirable γ' ZrO₂ phase. Besides the non-transformable characteristic of the γ' -phase, it is also regarded to have excellent strength and toughness. Typical microstructures of APS and EB-PVD TBCs are presented with cross-sectional backscattered electron micrographs in Fig. 2.3.

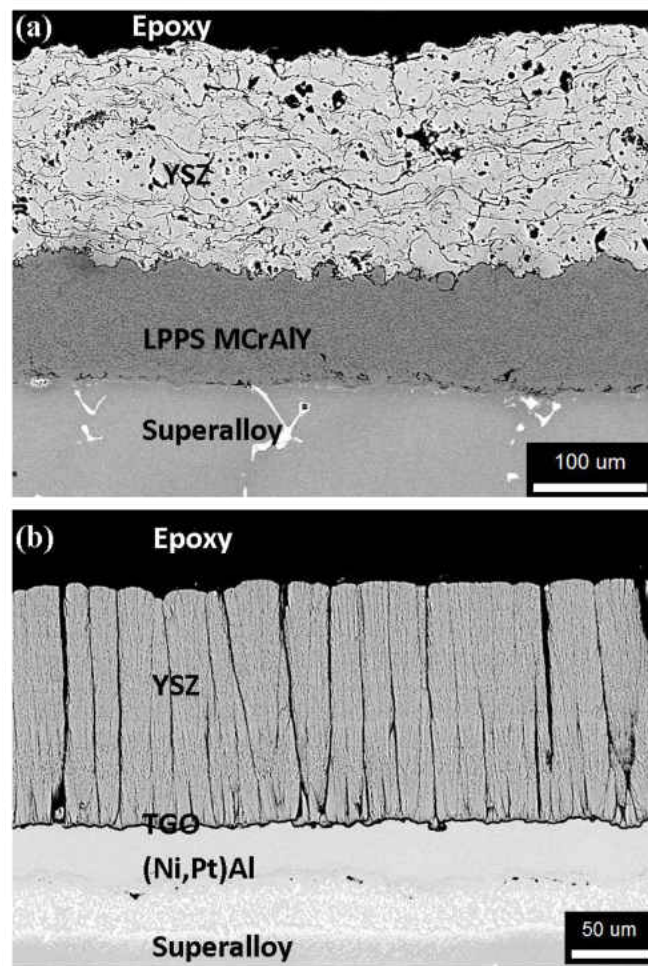


Figure 2.: Cross-sectional backscattered electron micrographs showing typical microstructures of (a) APS TBC (APS YSZ/LPPS MCrAlY/Superalloy) and (b) EB-PVD TBC (EB-PVD YSZ/(Ni,Pt)Al/Superalloy).

Processing Techniques of YSZ topcoat

(i) Air Plasma Spraying:

Atmospheric (or Air) plasma spray (APS) technique has been widely developed and employed for TBC applications. Ceramic topcoats with controlled porosity have been readily achieved by the APS technique [67]. Figure 2.4 shows a schematic representation of the APS technique. The plasma gun typically consists of a thoriated tungsten cathode and tungsten anode surrounded by a cooling jacket (water-cooled) and passages for the carrier gas. A high temperature, high velocity plasma is generated by striking a DC potential between the cathode and anode in the carrier gas (mixture of argon and hydrogen or hydrogen and nitrogen) in a confined space. The temperature of the plasma at the nozzle tip is around 6000-12000°C and travels with a velocity in the range of 200-600 m/s. The standoff distance or gun to work distance (GTW) can typically range from 75 mm to 150 mm to form the desired coating. A plasma torch can be operated in a power range up to 200 KW depending upon the torch model.

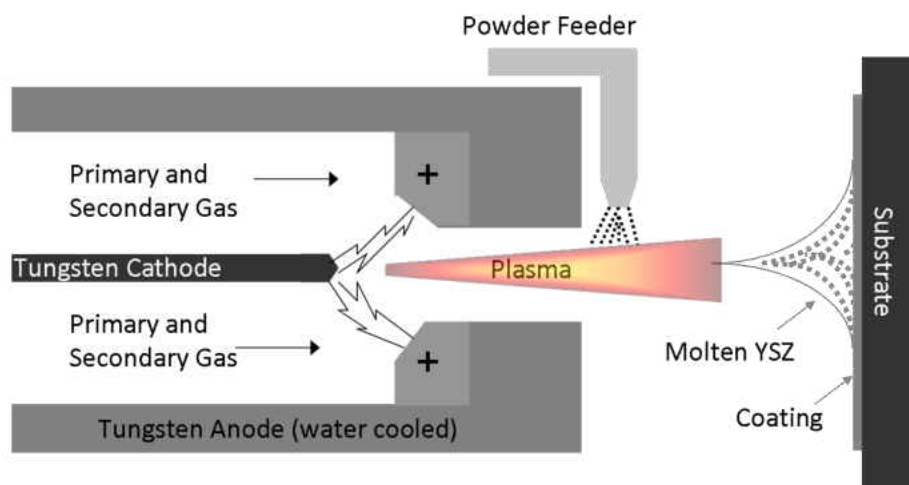


Figure 2.: A schematic representation of a typical plasma spray torch employed in APS technique.

In general, the APS process utilizes a high DC arc current of 100 A to 1000 A to strike an arc between the electrodes in the presence of an electrically excitable primary gas to generate a high temperature, high velocity plasma. Argon or nitrogen are commonly used as the primary gas. To enhance the plasma performance, a high enthalpy secondary gas, typically N₂, H₂ or He is injected into the established plasma plume. The APS torch components are typically water cooled during operation to prevent degradation and melting of the cathode and anode by the high temperature plasma. To deposit a coating, powders of the coating material are injected into the plasma plume (externally or internally depending on the gun design), where they are heated to their molten state and accelerated onto the work piece (substrate). Spraying of molten particles (splats) through multiple passes yields a splat-quenched coating microstructure of desired thickness.

Even though the APS technique is simple, many different factors can be controlled for process optimization [69]. Typical parameters of APS processing include:

- Torch design: nozzle diameter and electrode configuration (multiple cathodes).
- Powder feed configuration: powder injection location and injection angle.
- Spraying operation: arc power, gas composition, plasma temperature, stand-off distance, and surface preparation of the work piece.
- Starting powder: size, shape, chemical homogeneity, and the distribution of phase constituents.

Primary and secondary gas flow rates control the amount of electrically excitable gas available for plasma generation, which subsequently affects the temperature and velocity of the particle plume. An increase in the amount of plasma gas, both primary and secondary, will

increase the temperature and velocity of the spray particle. It is obvious that arc current decides the total amount of energy available to generate and sustain the plasma plume. By increasing the arc current, increases in particle temperature and velocity can be achieved due to the higher energy transfer to the particles from the plasma plume. Powder feed rates, controlled by powder mass flow and carrier gas flow rates, is another critical process variable that yields optimum deposition rates for a given plasma state. Increasing the powder mass flow tends to decrease the available energy per particle for heating and acceleration, which in turn reduces the particle temperature and velocity. On the other hand, an increase in the carrier gas flow that result in better transfer of momentum to the powders, enables more particles to enter into the hottest central zone of the plasma plume. This generally increases particle temperatures. Additionally, the stand-off distance greatly affects the coating characteristics by controlling the amount of dwell time the molten particles experience in ambient state, especially during APS of metallic particles. It has been reported that a decrease in stand-off distance tends to yield higher particle temperature and velocities that give rise to better adhesion and deposition efficiencies [69]. It should be noted that an optimum stand-off distance is required based on the plasma plume length, since a smaller stand-off distance can over-heat the substrate. Substrate preparation is equally important for the coating adhesion strength. In general, the substrate surface needs to be roughened to allow improved mechanical bonding of the molten spray particles. Roughening of substrates is usually done by a grit blasting step before APS processing. Upon impact with the grit-blasted substrate, molten particles flatten to form splats. These splats mechanically interlock onto the roughened substrate surface to form a coating with superior adhesion.

Porosity is inherent in the plasma sprayed coatings. It is introduced during the process of splat formation from molten droplets during rapid quenching. Porosity has an important role to play in the performance and durability of TBCs, since it significantly influences the thermal conductivity, thermal shock resistance and erosion resistance. An increase in the amount of porosity would result in better thermal insulation and spallation resistance, however, a porous coating would possess inferior erosion and hot corrosion resistance due to the increased channels for molten deposits to infiltrate the coating. In addition, the thermal cycle life has been reported to be sensitive to the density of the ceramic topcoat as shown in Fig. 2.5.

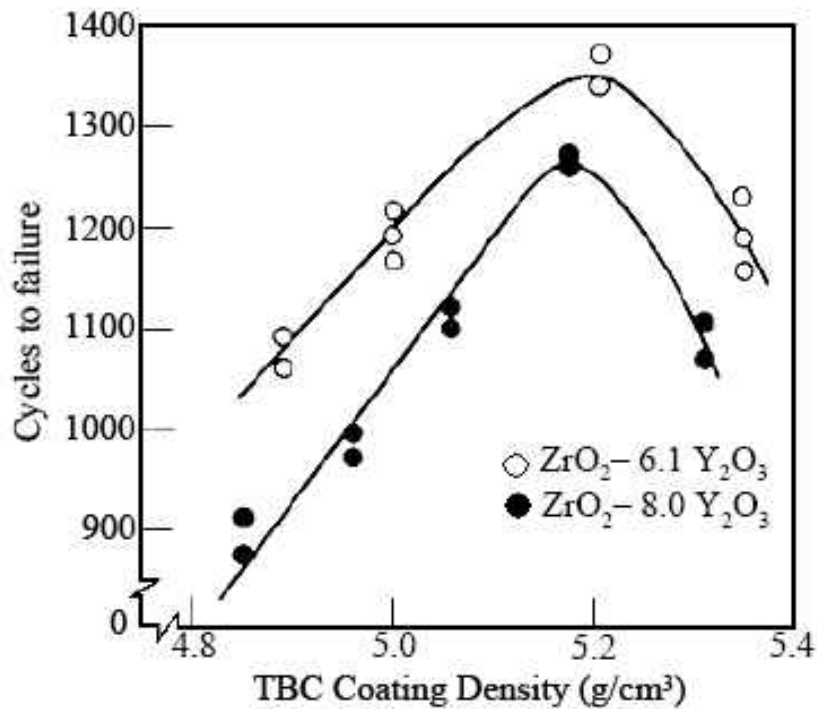


Figure 2.: Effect of the YSZ topcoat density on the thermal cyclic lifetime of YSZ TBCs [68].

The APS technique, being a cost-effective versatile manufacturing technique, has also been widely employed to spray different kinds of coatings for various high temperature

applications. Metallic coatings (ORCs and TBC bond coat) have also been processed by the APS technique with controlled processing conditions that can minimize their inevitable internal oxide content [69].

(ii) Electron Beam Physical Vapor Deposition (EB-PVD):

EB-PVD is a widely used technique in the gas turbine industry for applying coatings to turbine blades and vanes for protection against oxidation and hot corrosion. EB-PVD coatings that are typically used in aero-engine turbine applications have excellent spallation resistance [70, 71]. Their superior properties in comparison to plasma sprayed counterparts are (1) longer thermal cyclic lifetime, (2) smoother surface finish, (3) better surface finish retention, and (4) superior erosion resistance. A schematic of an EB-PVD production facility is shown in Fig. 2.6. In order to deposit 7-8YZ, it is essential to provide certain oxygen partial pressure within the chamber to maintain oxygen stoichiometry of the ZrO_2 -based coatings.

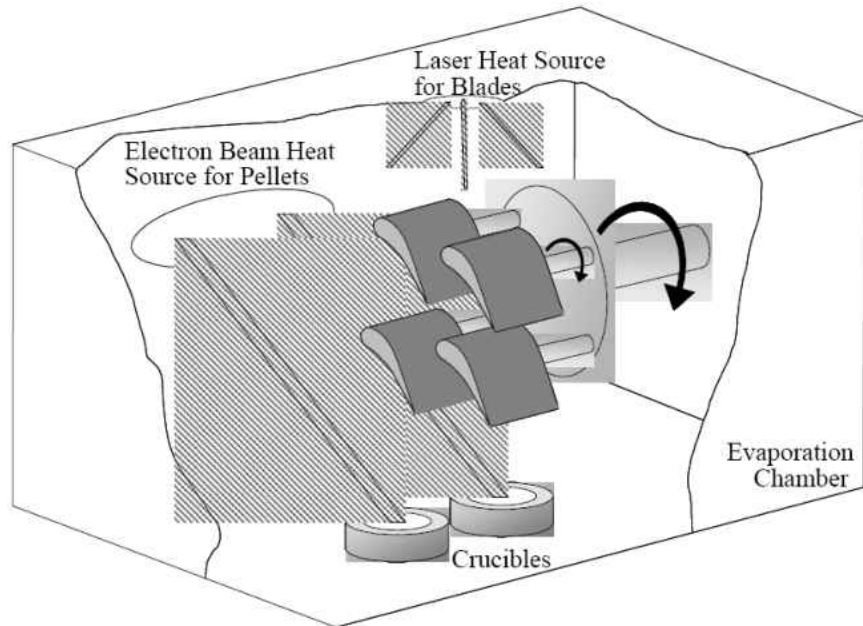


Figure 2.: A schematic illustration of the EB-PVD process that takes place inside an evaporation chamber. The parts are typically rotated and revolved while being heated by a laser heat source and the ceramic ingots are heated by an electron beam to form a vapor rich environment, which deposits on the turbine blades [72].

The EB-PVD process involves [70]:

- High power electron beam focused onto the YSZ ingot that melts locally and creates a YSZ vapor rich environment.
- The vapor deposits on parts that are held in rotatable and retractable fixtures above the vapor source.
- For best adhesion, the bond coat surface must be smooth. Adhesion in the EB-PVD TBCs involves a chemical bonding between the YSZ and the substrate.

EB-PVD TBCs possess a columnar microstructure, which can be clearly seen in the typical cross-sectional micrograph presented in Fig. 2.3 (b). This is the beneficial characteristic

of EB-PVD coatings since the columnar microstructure is believed to alleviate the stress generated within the YSZ coating due to the thermal expansion mismatch. The advantage lies in the fact that strain within the YSZ topcoat is accommodated by free expansion or contraction of the columns into the intercolumnar gaps that results in negligible stress buildup [73, 74]. However, such an improved durability in comparison to APS processed coatings comes with a trade-off. There is an increase in the thermal conductivity of the coatings by a factor of 2 as compared to the plasma sprayed coatings [70]. It should be noted that a thin layer of dense YSZ forms during the onset of the coating deposition on the bond coat surface until columnar YSZ structure eventually develops. This is because of the initial deficiency of oxygen in the chamber just before zirconia deposition. Thus, the thickness of such dense YSZ layer is dependent on the time with which oxygen is introduced once the YSZ deposition has started.

(iii) Dense Vertically Cracked (DVC) TBCs:

Air plasma sprayed coatings are typically prone to large scale spallation as the cracks induced due to thermal stresses propagate easily. In order to relieve the thermal stresses in TBCs that arise from the thermal expansion mismatch, vertically segmented cracks have been deliberately introduced into the ceramic topcoat in order to improve the lifetime of TBCs. Dense vertically cracked (DVC) TBCs are typical ceramic coatings, and by definition, are dense, hard and difficult to abrade. DVC TBCs are often employed in combustor components so as to produce a segmented ceramic structure having numerous macrocracks (20 to 200 cracks/inch), which are oriented substantially perpendicular to the surface [75-77].

DVC TBCs have greater resistance to particle erosion than those previously employed in gas turbine engine combustors, which is particularly advantageous in the wet (or water injection)

environment. These quasi-columnar structured dense vertically cracked TBCs typically possess a porosity of less than approximately 12% and a tensile strength in the range of approximately 4-7 ksi. The YSZ based DVC TBCs are processed in the following way [77]:

Thermal deposition of YSZ powders onto a substrate by APS technique with modified processing parameters such as substrate temperature in order to achieve “hot spraying”. Formation of a monolayer having at least two superimposed splats of the deposited YSZ powders in which the temperature of a subsequent deposited splat is higher than the temperature of previously deposited splat is typically achieved.

During hot spraying, with increased substrate temperature, the typical shrinkage of splat during cooling is hindered, which generates in-plane tensile stress within the sprayed monolayer. Subsequent initiation of vertical cracks in order to relieve the generated tensile stress occurs.

Repeating these steps so that at least 70% of the generated vertical cracks in a monolayer are aligned with vertical cracks in an adjacent monolayer to form a vertical macrocrack. Increased substrate temperature also tends to facilitate the remelting of quenched splats by subsequently depositing splats resulting in microwelding of monolayers. This would avoid the detrimental horizontal branching cracks that typically form during poor DVC processing. An increase in torch current and a decrease in stand-off distance were found to greatly promote the vertical crack formation. Moreover, plasma gun speed and powder feed rate also seem to affect the formation of vertical cracks and their density in DVC TBCs.

Segmented TBCs by DVC processing could also be achieved by spraying a plurality of layers of a ceramic topcoat onto the turbine component by typically utilizing a plasma-spray torch at a first distance followed by plasma-spraying a sacrificial layer of the ceramic coating,

with the plasma-spray torch at a second, greater distance from the turbine component, and thereby make the sacrificial layer less dense than the plurality of layers. Subsequent cooling and solidification during this process often results in vertical macrocracks. Abrading the sacrificial layer to remove some or the entire sacrificial layer to achieve a desired final coating thickness and surface roughness is usually performed. A typical DVC TBC microstructure is represented in backscattered electron micrograph shown in Fig. 2.7.

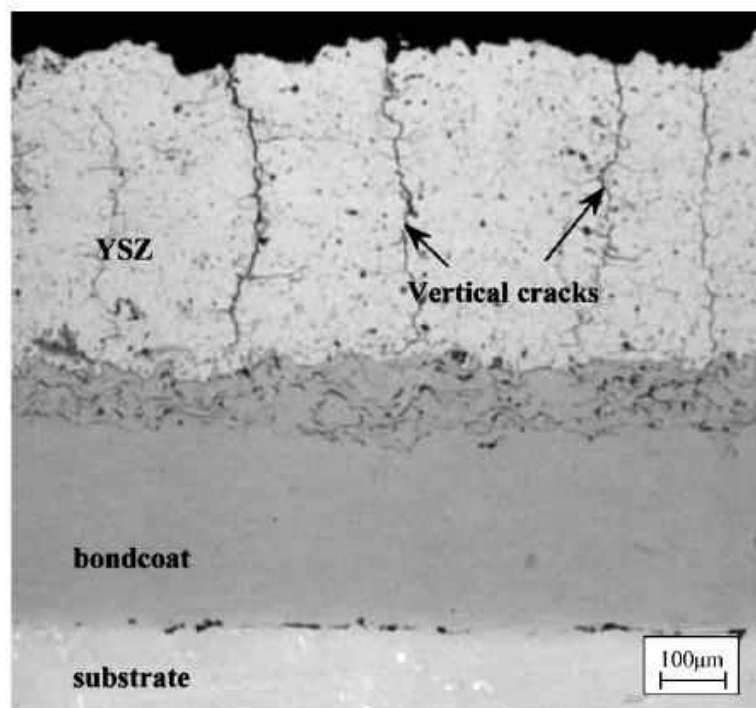


Figure 2.: Cross-sectional backscattered electron micrograph of a DVC TBC with segmented vertical macrocracks [75].

2.1.2. Overlay ORCs and Bond Coat of TBCs

Based on research efforts during the 1960s that demonstrated the exceptional oxide adherence (alumina) during thermal cyclic exposure of novel Fe-base alloys (Fe-25%Cr-4%Al-1.0%Y), MCrAlY type overlay oxidation resistant coatings emerged [69]. CoCrAlY coatings having excellent hot corrosion resistance were not suitable for applications in airfoils, since they failed to satisfy the ductility requirement. NiCoCrAlY was ultimately found to have exceptional ductility with adequate oxidation and hot corrosion resistance. The superior hot corrosion and oxidation resistance of these coatings is attributed to the formation of highly adherent alumina scales, for which the growth rate is slow as a result of the widely studied reactive element effect that is attributable to yttrium. In addition, their high Cr contents make them useful protective coatings against hot corrosion. These overlay coatings are typically deposited using low pressure plasma spray (LPPS), a modified thermal spray process performed completely in a low-pressure chamber [22]. The EB-PVD technique has also been employed for metallic coating processing. The EB-PVD process is preferred for high quality coatings in order to completely avoid the oxidation of the MCrAlY coating that occurs during thermal spray processing. However, the thermal spray processes are favored for their cost-effectiveness. Overlay coatings also show interdiffusion effects with alloy substrates and Itoh et al., demonstrated that the rate of interdiffusion decreases in the order NiCrAlY > CoCrAlY > NiCoCrAlY > CoNiAlY, where NiCo represents higher Ni content compared to Co and vice-versa [69]. Research efforts to minimize coating/substrate interdiffusion by employing a diffusion barrier with an optimum composition have also been made.

In general, turbine components protected with TBCs operate in an oxygen rich combustion environment at elevated temperatures. In order to protect the superalloy substrate from oxidation, an oxidation resistant bond coat is applied in-between the topcoat and the substrate. This bond coat is 75 - 300 μm in thickness, and has been believed to dictate the ultimate failure of TBCs [23]. At peak operating conditions, the temperature at the bond coat surface exceeds 900°C, which results in bond coat oxidation and the formation of the thermally grown oxide (TGO). Although the formation of the TGO is inevitable, an ideal bond coat is engineered to ensure that the TGO forms $\alpha\text{-Al}_2\text{O}_3$ and its growth is slow, uniform and defect free. The growth of the TGO during engine operation is the most important phenomena responsible for the spallation failure of TBCs [78-84]. Thus, the TGO scale that forms between the YSZ topcoat and the metallic bond coat significantly influences the durability of TBCs.

The bond coat is primarily designed as a local Al reservoir for facilitating the formation of $\alpha\text{-Al}_2\text{O}_3$ as the TGO scale in preference to other oxides [16, 17]. Because of its major influence on the TBC durability through the morphology and phase constituents of the TGO, the bond coat has been considered as the most crucial component in TBCs. Two different types of widely used bond coats are: MCrAlY (M = Ni and/or Co) and Pt-modified nickel aluminide (Ni,Pt)Al. MCrAlY bond coats, as discussed earlier, are typically deposited by LPPS, and consist of two phases: $\beta\text{-NiAl}$ and either $\gamma\text{-Ni}$ solid solution or $\gamma'\text{-Ni}_3\text{Al}$. Yttrium acts as a solid state getter for elemental S impurities that diffuse from the superalloy substrate and thus the Y addition at a lower concentration improves the adhesion of the TGO [85]. An equilibrium phase diagram of the Ni-Al binary system is shown in Fig. 2.8. Pt-modified nickel aluminide coatings, which are primarily a single phase $\beta\text{-NiAl}$ with Pt in solid solution, are usually fabricated by

electroplating a thin layer of platinum onto the superalloy substrate and then aluminizing by either chemical vapor deposition or pack cementation [10]. In general, (Ni,Pt)Al coatings that are completely composed of β -NiAl are widely employed in aero-engine applications. In EBPVD ceramic TBC systems, a superior oxidation resistance with the desired TGO characteristics has been the promising characteristic attributed to the (Ni,Pt)Al bond coat [81]. Thus, a superior performance in thermal cycling conditions in typical aero-propulsion applications has been achieved by EB-PVD TBCs with (Ni,Pt)Al bond coat.

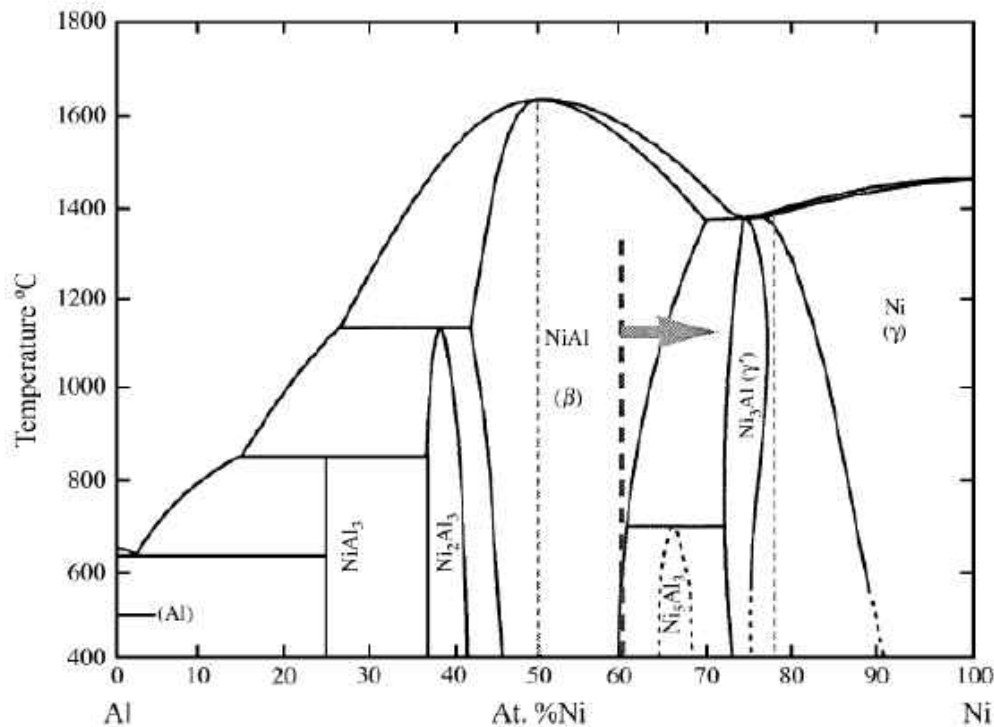


Figure 2.: Equilibrium binary phase diagram of Ni-Al system [86].

A schematic map showing the effectiveness of these widely classified bond coat material systems (or ORCs) for protection against high temperature oxidation and corrosion is shown in Fig 2.9. This map shows, for example, CoCrAlY coatings are not effective for oxidation

resistance compared to NiCoCrAlY or CoNiCrAlY. In order to exploit the complete potential of MCrAlY-type coatings for an appropriate oxidation and hot corrosion resistant applications, coatings having a composition gradient have also been envisaged by Nicholls et al [87]. The so-called smart coatings consist of a commercial base coating (Co-32Ni-21Cr-8Al-0.5Y) adjacent to the substrate, a Cr enriched layer of variable composition from Ni-60Cr-20Al to Ni-35Cr-40Al sandwiched between the base coating and a surface layer of composition Ni-15Cr-32Al. Even though such coatings impose challenges in terms of coating ductility, these overlay coatings were found to outperform their Pt-modified nickel aluminide counterparts.

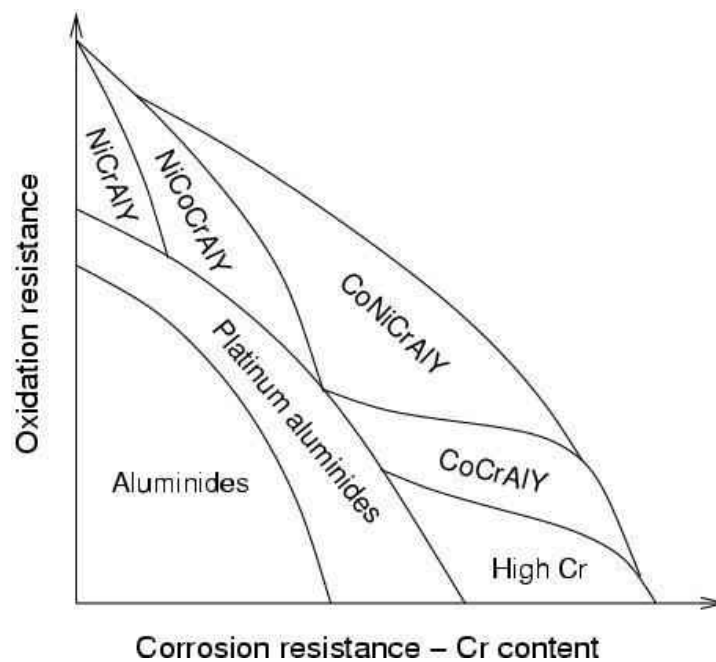


Figure 2.: A schematic map illustrating the effectiveness of various coating materials system against high-temperature oxidation and corrosion.

Development in thermal spray processing techniques of MCrAlY-type bond coats identified Low Pressure Plasma Spraying (LPPS), also known as the Vacuum Plasma Spraying (VPS) technique as an effective method to fabricate denser and less oxidized bond coats [22].

Other techniques include the conventional Air Plasma Spraying (APS) [23, 24], High Frequency Pulse Detonation (HFPD) [25], and High Velocity OxyFuel (HVOF), which has gained attention as another cost effective alternative technique for fabricating bond coats of the desired quality [26, 27].

2.1.3. TGO formation in TBCs

In TBCs, the TGO scale grown at the interface between the bond coat and the YSZ topcoat is very critical and typically dictates the durability of TBCs. The pre-heat treatment before the YSZ deposition for a better coating adhesion, and the O₂ introduction during the EB-PVD process to maintain required oxygen stoichiometry in the YSZ also oxidizes the bond coat. The formation and growth of the TGO scale (α -Al₂O₃) depletes Al content from the bond coat via selective oxidation. If Al depletion is severe, it is possible to form other oxides, such as Ni-, Cr- and Co-rich oxide, including NiO, Cr₂O₃, CoO, and spinels such as (Ni,Co)(Al,Cr)₂O₄ that possess low fracture toughness. In addition, excessive alloying with reactive elements can also result in the formation of oxide pegs and brittleness of the coatings [84]. For example, formation of Y₃Al₅O₁₂ (yttrium aluminum garnet - YAG) and/or Y₂O₃ within the TGO scale, and the corresponding loss of adhesion between the TGO and bond coat has been reported [88, 89]. Also, the primary constituent of the TGO scale, Al₂O₃ has various polymorphs such as the equilibrium α -Al₂O₃, metastable θ -Al₂O₃ and metastable γ -Al₂O₃. Other oxides such as NiO, Cr₂O₃, (Al,Cr)₂O₃, CoO, and spinels such as (Ni,Co)(Al,Cr)₂O₄ may also form in the TGO scale due to transient oxidation and severe degradation of the bond coat [27, 88]. Transient oxides are usually observed to form in the TGO scale for TBCs at a very early stage of oxidation in air as a result of the compositional inhomogeneity in the APS YSZ [27]. Localized volume changes due to the

formation of these oxides can cause crack nucleation and growth into the YSZ. Reduced formation of transient oxides can be achieved by improved composition homogeneity. Premature failure of TBCs can be prevented by reducing crack formation from the transient oxides. During the oxidation of bond coats, the diffusion-controlled TGO growth, stress state, polymorphic transformation of Al_2O_3 and other oxidation products (e.g., oxides Ni, Cr, Co, Hf and Y) can vary as a function of processing, composition, microstructure, and operating conditions [16, 17]. Thus, the TGO plays a very critical role in determining the lifetime of TBCs. The failure of TBC systems is typically associated with cracking at the TGO/bond coat interface, and/or within the TGO, and/or at the YSZ/TGO interface, and/or within the YSZ [16, 17, 79-81]. Accordingly, the adhesion of the TGO layer and residual stress within the TGO scale was found to have a profound influence on the damage mechanisms and spallation failure of TBCs. The α - Al_2O_3 is the preferred constituent of the TGO scale, because of its low oxygen diffusivity and superior adhesion to the metallic bond coat surface. The TGO consisting of α - Al_2O_3 also develops extremely large residual compressive stress upon cooling because of its thermal expansion misfit (2~6 GPa) [91-93], and its growth due to constrained volume expansion (1GPa) [94]. Transformations of the metastable phases and the bond coat surface roughness can also influence the residual stress in the TGO scale. Clarke et al. elaborated on the stresses that develop during the growth of alumina and also the rumpling effect of alumina [95-97]. The stress development and oxide rumpling cause the alumina layer to detach from the bond coat. Because the crack is typically initiated near the YSZ-bond coat interface, YSZ delamination occurs.

2.2. Failure Mechanisms of TBCs

Durability of TBCs has always been a major issue due to the inevitable introduction of thermal stresses into the ceramic coating during gas turbine operation in extreme environments. Extensive efforts have been made to identify the failure mechanisms of the TBCs. An extensive review by Evans et al., presents the common failure mechanisms of APS and EB-PVD TBCs [16-17].

The various possible factors/phenomena influencing the TBC failure are listed below:

- Sintering in the ceramic topcoat increases the thermal conductivity and modulus of elasticity resulting in high metal surface temperature and subsequent enhancement of bond coat oxidation and creep. This subsequently results in stress-induced spallation at the interface between the topcoat and TGO. This mode of failure has been reported in APS TBCs [16].
- Thermal expansion mismatch stresses between the TBC/TGO/bond coat layers.
- Growth of the TGO scale at the interface between the bond coat and YSZ because of the bond coat oxidation, which results in stresses at the interface of the TGO/bond coat.
- Depletion of Al from the bond coat leading to the formation of the brittle oxides other than α -Al₂O₃, such as spinel [(Ni,Co)(Al,Cr)₂O₄].
- Cyclic creep of the bond coat.
- Degradation of the metal ceramic interface toughness.
- Delamination, cracking and crack coalescence.
- Foreign object damage.

- Environmental degradation due to corrosive molten deposits arising from alternative low-quality fuel and air-ingested CMAS sand deposits.

Durability of TBCs is typically governed by a sequence of crack nucleation, propagation, and coalescence events. These failure characteristics are analogous to that of low cycle fatigue failure in structural alloys. Sequential crack propagation that leads to ultimate TBC failure occurs through following steps [81]:

- (1) Small cracks and separations nucleate at defects in (or near) the TGO.
- (2) Once nucleated, the small cracks extend and coalesce, but the TBC remains attached.
- (3) Failure occurs through localized but complete delamination at YSZ/bond coat interface, causing a separation large enough to create either a large-scale buckle or an edge delamination that results in spallation.

It should be noted that TBCs processed by APS and EB-PVD are completely different in their microstructure, morphology, and thermophysical properties and thus fail through different failure mechanisms. In APS TBCs, failure occurs by crack evolution in the YSZ topcoat itself, occurring in planes parallel to the substrate. In contrast, EB-PVD coatings are often deposited on a smooth bond coat and fail typically by loss of adherence of the TGO to the bond coat. Also, the dominant failure mechanisms are different for the two areas of application, propulsion and power generation, due to the different thermal histories. Systems used for propulsion and peak-load purposes experience multiple thermal cycles and can fail when the TGO thickness ranges from 1-5 μ m. TBCs in turbines for base-load power generation are typically operated with fewer thermal cycles and fail when the TGO thickness ranges between 5-15 μ m. Thermal cycling diminishes the durability of the TBCs.

2.2.1. Failure Mechanisms in APS TBCs

Failure due to various cracking mechanisms (I-IV) in APS TBCs are clearly presented through a series of cross-sectional backscattered electron micrographs of a near-failure APS TBC as shown in Fig. 2.10. The common failure mechanisms observed in APS TBCs [80] can be explained as follows:

- Mechanism I: Cracking at the YSZ Topcoat/TGO Interface:

The thermal expansion mismatch between the ceramic topcoat and the metallic bond coat typically results in introduction of compressive stresses during cooling. In addition, the sintering of the YSZ topcoat also contributes to the stress generation. It should be noted that the stresses within the YSZ are generally lower than the residual stresses within the TGO. The rough topcoat/bond coat interface inherent in APS TBCs is responsible for the out-of-plane stresses at the vicinity of topcoat/TGO interface. A tensile stress in the crests and compressive stress in troughs could ultimately lead to cracking at the YSZ/TGO interface.

- Mechanism II and III: Cracking at the TGO/Bond coat Interface and within TGO

Two types of out-of-plane stresses act at the TGO/bond coat interface, tensile and compressive stresses at the crests and troughs, respectively. During thermal exposure, a continuous growth of the TGO ultimately results in an increase in the out-of-plane tensile stress leading to cracking at the TGO/BC interface, which typically gets initiated at crests as shown in Fig. 2.10. With the TGO thickening at the expense of oxidation of the bond coat, thermal stresses are locally dominated by thermal expansion mismatch between the

bond coat and TGO, which is rather higher than just the bond coat and topcoat. There is a certain critical thickness beyond which the coefficient of thermal expansion of the bond coat and TGO becomes lower than that of both bond coat and topcoat. This reverses the nature of the stresses in the troughs associated with the topcoat undulation from compressive to tension. The reversal from compression to tension in the troughs would eventually cause cracking within the TGO, which in most cases extends into the YSZ that consists of pre-existing microcracks and intersplat boundaries.

- Mechanism IV: Cracking within the YSZ

Similar to the mechanism I, the development of out-of-plane stresses at the vicinity of the topcoat/TGO interface could also result in cracking within the YSZ due to the fact that the porous, yet brittle YSZ is more susceptible to cracking to relieve the generated stress. Cracks form through the pre-existing intersplat boundaries within the YSZ.

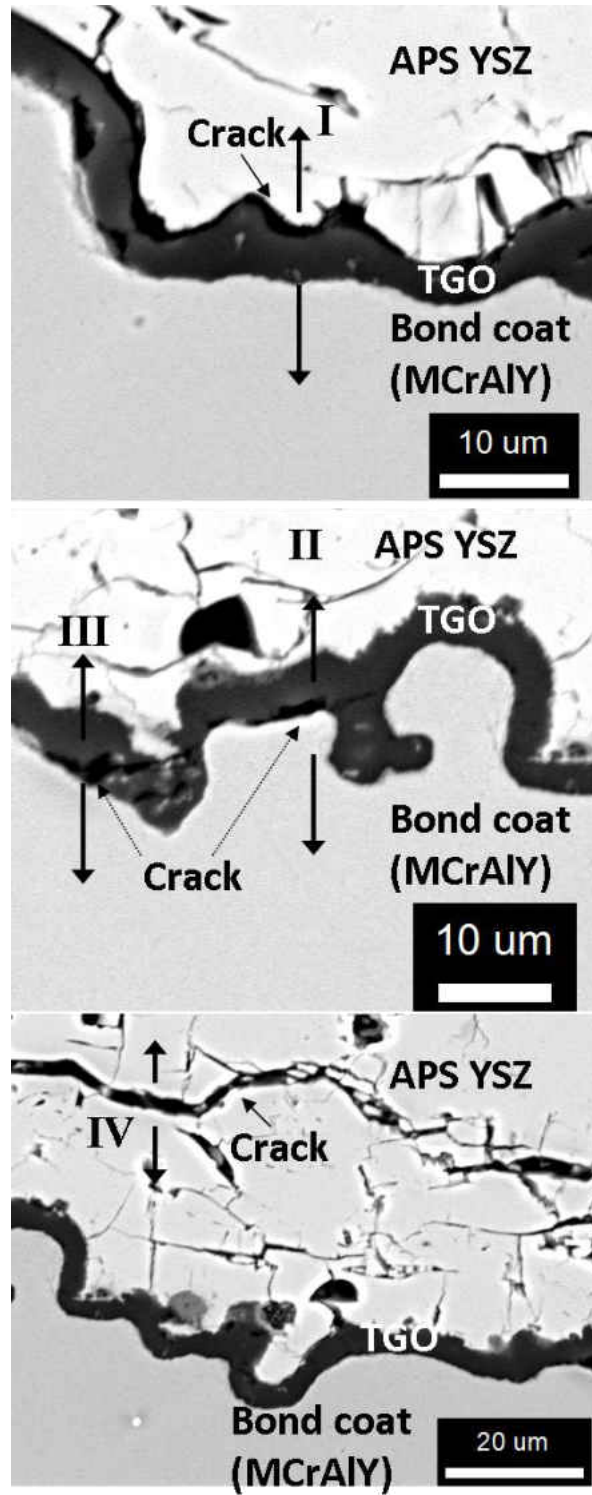


Figure 2.: Cross-sectional microstructures of nearly failed APS TBCs showing different failure mechanisms.

2.2.2. Failure Mechanisms in EB-PVD TBCs

The EB-PVD TBCs with columnar microstructure are more strain tolerant than APS TBCs. Inelastic deformation of the YSZ layer occurs in the plasma sprayed TBCs during thermal cycling, whereas in the case of EB-PVD TBCs, it would remain elastic, with the life-limiting factor being the strain that develops within the TGO [16]. Failure in EB-PVD TBCs occurs at the bond coat/TGO or the TGO/topcoat interfaces. Fig. 2.11 is a schematic representation of failure mechanisms in EB-PVD TBCs.

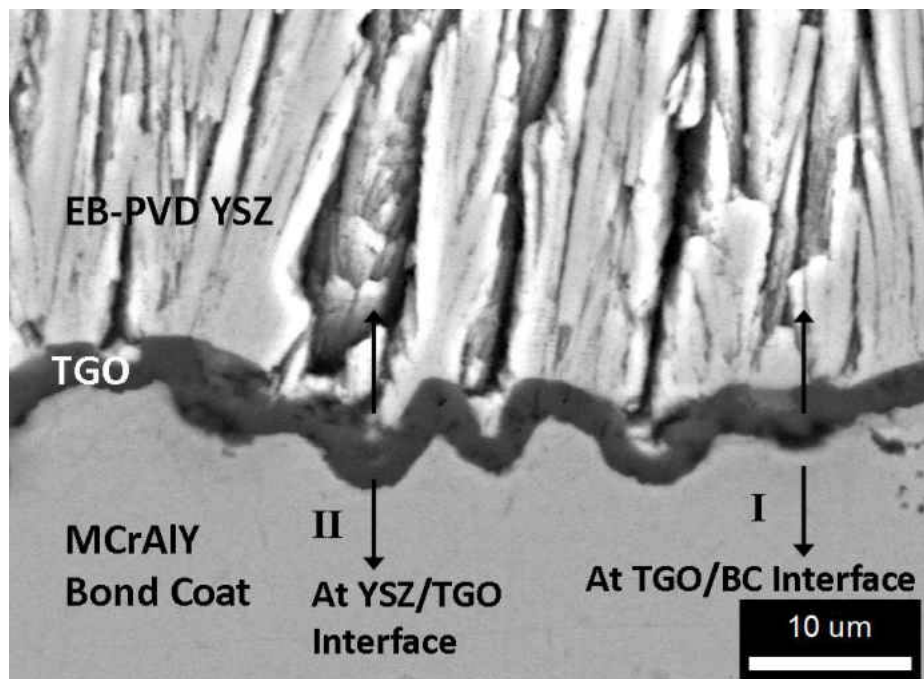


Figure 2.: A cross-sectional micrograph of an EB-PVD TBC hypothetically illustrating the two common failure mechanisms.

- Mechanism I: At bond coat/TGO interface

This is similar to that of the APS TBCs. The crests in case of EB-PVD TBCs are surface irregularities or undulations. Formation of voids and Ni/Co-rich TGO are the primary reasons for the degradation of the TGO/Bond coat interface. The development of voids and internal oxidation is observed to begin after the depletion of Al rich β -phase (NiAl).

- Mechanism II: At TGO/Topcoat interface

Separation of the TGO from the topcoat with penetration may be due to the following mechanisms.

- ✓ Roughening of the TGO because of the bond coat creep during cooling.
- ✓ Phase transformations within the YSZ and TGO, and sintering of the YSZ.
- ✓ Cavity formation in the bond coat is inherent in the CVD aluminizing process. Such cavities could also lead to decohesion at the TGO/YSZ interface.
- ✓ Occasional presence of embedded oxides due to the surface smoothening treatment of the bond coat before EB-PVD deposition also affects the TGO/topcoat interface strength. These oxides grow at an accelerated rate and promote cracking within the TGO.
- ✓ The other possible mechanism is the formation of the Ni/Co rich oxides (spinels) at the TGO/YSZ interface. These spinels being extremely brittle in nature can result in delamination of TBC through decohesion at the YSZ/TGO interface.

2.2.3. TBCs with Improved TGO Adhesion

In order to improve the durability of TBCs, numerous attempts to improve the stability of TGO interfaces and the properties of alumina scale have been undertaken [98-101]. Some of the approaches are:

Improvement in alumina scale properties:

- Assuring that the TGO is predominantly composed of α -Al₂O₃.
- Reducing the growth rate of the TGO – assuring high purity of α -Al₂O₃.
- Minimizing the growth stress in alumina.
- Employing additional steps (pre and post heat treatments during processing of TBC) at desired treatment conditions to assure the formation of continuous α -Al₂O₃ as the TGO before service.

Superior TGO interface stability:

- Inhibiting the bond coat rumpling – minimizing the thermal expansion mismatch between the bond coat and the superalloy.
- Avoiding the martensitic β phase transformation ($\beta \rightarrow$ L10) near the interface.
- Improving the TGO adhesion to the topcoat by minimizing the formation of impurity oxides.
- Improving the TGO adhesion at the bond coat interface – modifying the substrate alloy chemistry by adding reactive elements (up to 2% Hf and/or Y) that facilitates pegging of the TGO scale at the interface.
- Minimizing the interfacial sulfur activity.

Modifications to TBCs, such as controlling the processing parameters, additional processing steps (surface smoothing, additional heat-treatment in a desired environment), alloying additions to superalloy and employing various processing techniques have been shown to significantly affect/improve the lifetime of TBCs through various mechanisms [10].

2.3. High Temperature Degradation of TBCs by Molten Deposits

In gas turbine engines, due to the increasing severity of the combustion environment that results from attempts to improve the power generation efficiency and economy, molten-deposit induced high-temperature degradation of TBCs has become another critical durability issue. The use of cost-effective alternative fuels that could have high levels of impurities can promote the formation of corrosive compounds rich in S, V, Na, Ca, K, and P, which get deposited on hot-section turbine components [12, 28]. CMAS ($\text{CaO-MgO-Al}_2\text{O}_3\text{-SiO}_2$), typical air-ingested sand, having a melting temperature of 1240°C can be another source of such life-limiting corrosive deposits on TBCs [29, 30]. At elevated temperature, these deposits adhere, melt and degrade the TBC system via repeated freeze-thaw action and, to a certain extent, direct chemical interaction with TBC constituents. The interactions that can accelerate the failure of TBCs and underlying components include destabilization of the YSZ topcoat, dissolution of the TGO ($\alpha\text{-Al}_2\text{O}_3$), accelerated oxidation and the hot corrosion of underlying metallic bond coat and superalloys [30-58].

The superior performance of the YSZ-based TBCs is primarily attributed to the metastable t' ZrO_2 phase, which is thermally stable up to 1200°C for any long term exposure. Preferential chemical reaction of corrosive deposits with the yttria stabilizer of YSZ would intuitively result in destabilization of the YSZ. The YSZ depleted in yttria content would

eventually go through the disruptive phase transformation to monoclinic ZrO_2 ($t' \rightarrow t \rightarrow m+f$). It has been proven that TBC durability is greatly affected by this $t' \rightarrow m$ ZrO_2 phase transformation due to the accompanying volume change [66]. Thus, any degradation mechanism resulting in the YSZ destabilization and formation of the m - ZrO_2 phase is of critical importance that needs to be inhibited.

The thermomechanical degradation by a repeated freeze-thaw action due to the ingress of a corrosive melt through the porous YSZ topcoat is of equal importance. A review by Strangman et al., postulated that the thermomechanical damage through infiltration was more important than the reactions that destabilize the YSZ. However, the extent of chemical damage can vary significantly as a function of contaminant-content in fuel blends. Further, in most studies a complete infiltration of the YSZ topcoat by molten deposits at elevated temperatures has been observed [28]. This clearly warrants an understanding of the interaction of the corrosive molten deposits with the underlying metallic bond coat. Even though MCrAlY type overlay coatings are widely used for oxidation/hot corrosion resistance in high temperature applications, the presence of molten deposits that can readily dissolve the protective oxide (Al_2O_3 or Cr_2O_3) could result in accelerated oxidation and consumption of coating constituents. Thus, hot corrosion of TBCs and ORCs over extended exposure has been a critical issue that warrants a clear understanding for expanded applications of TBCs.

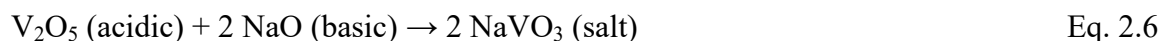
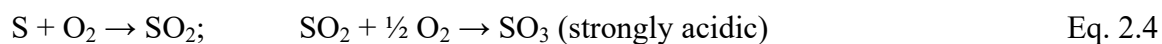
The hot corrosion of TBCs due to molten deposits can be categorized into four different degradation modes [28]:

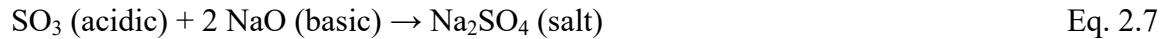
1. Thermochemical interaction resulting in dissolution and reprecipitation of the YSZ and destabilization due to the depletion of yttria stabilizer through chemical reactions.

2. Mineralization – a type of phase reaction involving a non reactive melt that tends to stabilize a nonequilibrium phase to an equilibrium phase. This mode of degradation has not been observed in YSZ TBCs.
3. Hot corrosion of the MCrAlY bond coat that significantly consumes the bond coat constituents and thus affects the TGO growth mechanism.
4. Thermomechanical degradation due to a repeated freeze-thaw action during melt ingress followed by solidification.

2.3.1. Degradation of TBCs and ORCs by Molten Deposits from Fuel Impurities

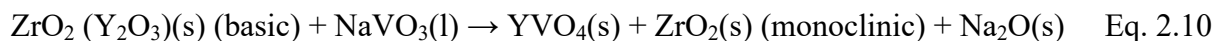
The principal fuel impurities that can cause hot corrosion in TBCs are sodium, calcium, sulfur, vanadium and possibly phosphorus. During combustion these fuel impurities tend to form corrosive oxides that are strongly acidic or basic. Hot corrosion is typically controlled by Lewis acid-base oxide reactions, where oxides of acidic and basic nature interact readily. Also, these strong acidic and basic corrosive oxides tend to readily form salts (sulfates and vanadates) that can melt at a relatively lower temperature compared to the individual oxides. Chemical reactions resulting in such corrosive compounds in a combustion environment can be written as follows:



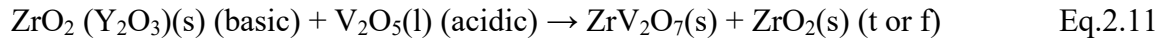


In addition to these typical corrosive compounds, sulfates of potassium (K_2SO_4) and iron (FeSO_4) have also been reported to be critical threats. These sulfates are expected to degrade TBCs through similar interactions as that of Na_2SO_4 and CaSO_4 . An extensive review on hot corrosion of TBCs by Jones [12, 28] presents the various possible degradation reactions that could result in TBC failure.

Vanadium pentoxide (V_2O_5), a strong acidic oxide with a melting point (T_m) of 690°C and sodium metavanadate (NaVO_3), a corrosive salt (T_m : 610°C) that could form in the presence of both Na and V in fuel, have been considered as major threats for TBCs. Extensive studies on degradation by V rich compounds, revealed their aggressive acidic nature on TBC constituents [35-40]. YSZ has been reported to be readily affected through chemical reactions that result in destabilization. As explained in the following reactions, Eq. 2.9 and 2.10, the yttria stabilizer readily reacts with V_2O_5 and NaVO_3 to form yttrium vanadate (YVO_4), which is thermally stable with a high melting point (T_m : 1810°C). This resulted in the depletion of the Y_2O_3 stabilizer from the YSZ that consequently led to the disruptive YSZ phase transformation to monoclinic ZrO_2 ($t' \rightarrow t \rightarrow m+f$) [35-40].



Even though, ZrO_2 itself has resistance against V_2O_5 attack, some recent research efforts including this doctoral study, found direct interaction of ZrO_2 with V_2O_5 with a temperature dependence on the preferential attack of V_2O_5 [53]. Formation of zirconium pyrovanadate ($Zr_2V_2O_7$) as described in Eq. 2.11, has been identified through a thorough investigation in this study.

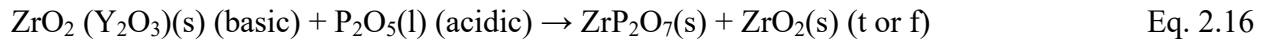


Hot corrosion studies on MCrAlY type bond coats (ORCs) by V rich compounds have been seldom documented [31]. A corrosive melt rich in V had been reported to consume MCrAlY (M = Ni or Ni+Co) coating constituents by dissolution of protective oxides such as Al_2O_3 and Cr_2O_3 to form $AlVO_4$ and $CrVO_4$, respectively. Due to the depletion of the Al and Cr content through hot corrosion mechanisms, the oxidation of Ni to NiO and subsequent formation of nickel vanadate ($Ni_3V_2O_8$) has also been reported [102]. Reactions resulting in such acidic dissolution of protective oxides of MCrAlY are presented by Equations 2.12 to 2.14.

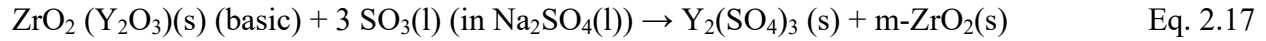


The presence of phosphorus as a fuel impurity can also degrade TBCs through similar mechanisms. Even though researchers speculated that P-rich corrosive compounds such as P_2O_5 ,

which is strongly acidic in nature, could degrade TBCs in a manner similar to that of a acidic V_2O_5 melt, there is no existing report of such degradation reactions. P_2O_5 can react with Y_2O_3 and ZrO_2 of YSZ to form yttrium phosphate (YPO_4) and zirconium pyrophosphate (ZrP_2O_7), respectively, at elevated temperatures [28]. The reactions resulting in YSZ degradation by P_2O_5 can be represented as shown in Equations 2.15 and 2.16. The YSZ degradation through destabilization by P_2O_5 due to the consumption of the yttria stabilizer is a speculation only and clearly warrants experimental evidence. On the other hand, P_2O_5 could also consume the MCrAlY coatings by the acidic dissolution of the protective oxides (Al_2O_3 and Cr_2O_3) and the consumption of the coating constituents through the accelerated oxidation of Ni and Co. This also results in subsequent acidic dissolution of NiO and CoO.



As mentioned earlier, S can possibly form corrosive deposits such as Na_2SO_4 , K_2SO_4 and $CaSO_4$ on turbine components. Hot corrosion of superalloys and MCrAlY overlay coatings due to sulfate deposits and S-rich oxidizing environment (SO_2 , SO_3 gases) have been extensively studied. However, studies on the YSZ degradation due to Na_2SO_4 showed only a minimal interaction despite the long-term exposure [42]. YSZ destabilization could occur through formation of $Y_2(SO_4)_3$ as represented in Eq. 2.17. Besides, in order to maintain a molten sulfate salt on the TBC surface, a minimum SO_3 partial pressure (p_{SO_3}) of 10^{-4} atm is required at temperatures above $700^\circ C$.



MCrAlY (M = Ni and Co) coatings can suffer accelerated oxidation and sulfation of transient oxides such as NiO and CoO when exposed to a Na₂SO₄ salt film in the presence of SO₂/SO₃ gases. In superalloys, hot corrosion mechanisms affecting the protective oxide growth kinetics as well as oxide scale constituents due to the significant formation of NiSO₄ and CoSO₄ and their subsequent dissolution in the Na₂SO₄ melt has been widely accepted. Hot corrosion is often classified into two forms of degradation, “Type I” (high temperature hot corrosion – HTHC) and “Type II” (low temperature hot corrosion – LTHC). Type I hot corrosion typically occurs in the temperature range of 850°C – 950°C, where the molten sulfate salt (Na₂SO₄ in most cases) dissolves the protective oxide and results in accelerated oxidation. Type II hot corrosion, which has been mainly observed to occur in the temperature range of 650°C - 800°C and that results in localized pitting of superalloys is due to formation of NiSO₄-Na₂SO₄ or CoSO₄-Na₂SO₄ eutectic. For type II hot corrosion, a relatively higher p_{SO_3} is required in comparison to Type I hot corrosion. A schematic representation illustrating the dominant degradation mechanisms at various temperatures is shown in Fig. 2.12.

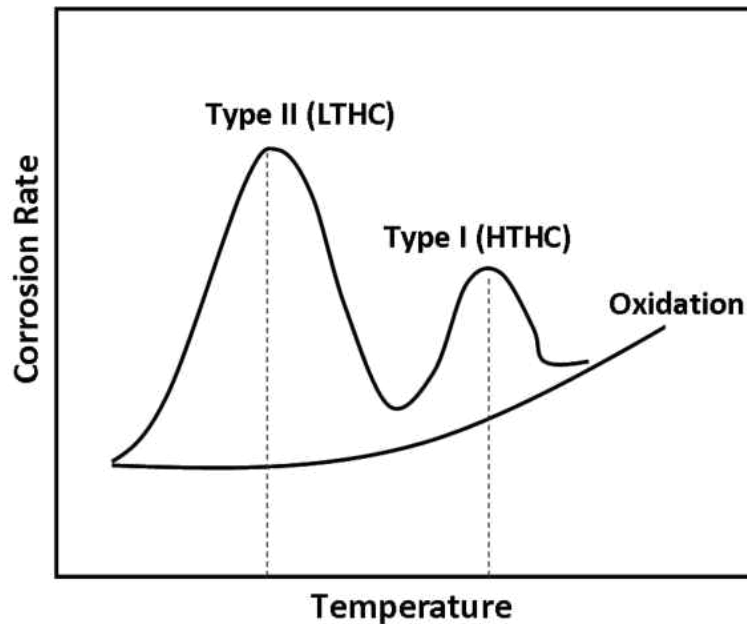


Figure 2.: A schematic illustration of dominant degradation mechanisms (Type I and II hot corrosion mechanisms and oxidation) at various temperatures.

An extensive review on hot corrosion mechanisms by Rapp presents the compiled data for solubilities of critical oxides (Cr_2O_3 , Al_2O_3 , SiO_2 , NiO , CoO) in a Na_2SO_4 melt as a function of melt basicity ($a_{\text{Na}_2\text{O}}$) [1, 8]. As shown in Fig. 2.13, a very high melt acidity (a_{SO_3}) is required to dissolve protective oxides such as Al_2O_3 or Cr_2O_3 . Fortunately, these protective oxides exhibit only minima in their solubilities at a typical p_{SO_3} that is achieved in a real engine operation. This has been reported as the protection mechanism by which, MCrAlY coatings that readily form Al_2O_3 and/or Cr_2O_3 are resistant to hot corrosion during high temperature applications.

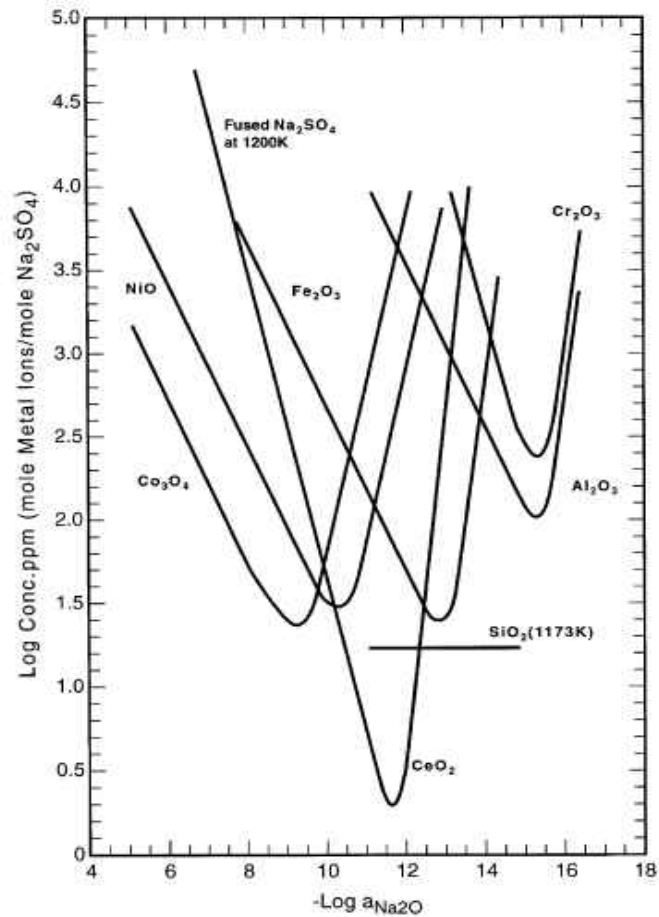


Figure 2.: Measured solubilities of various oxides in pure Na_2SO_4 at 1200 K [1].

In order to trap the common fuel impurities such as S and V, it has been a common practice to employ MgO inhibitors. MgO readily traps S and V, and forms MgSO_4 and $\text{Mg}_3\text{V}_2\text{O}_8$. However, presence of Na and Ca in the fuel would tend to disturb the trapping mechanisms resulting in deposition of vanadates and sulfates of sodium as well as calcium on turbine components.

2.3.2. Degradation of TBCs by CMAS Sand Deposits

Because of the ever increasing demand to raise the TIT for improved power generation efficiency, issues that were envisioned as potential threats for TBCs have become real challenges in current-generation combustion turbines. Ingestion of CMAS (calcium-magnesium aluminosilicate) sand deposits into gas turbine engines is one such issue. TBCs are increasingly susceptible to degradation by molten CMAS in gas turbine engines, especially in aircraft engines, which operate in a dust-laden environment wherein ingestion of siliceous debris into engines has been commonly reported [29]. Such airborne deposits like CMAS were reported to melt, adhere and ingress into TBCs above 1150°C, and subsequently degrade the TBCs via ingress and repeated freeze-thaw action as well as direct chemical reaction with the TBC constituents [30]. TBC failure due to CMAS attack on a turbine airfoil of an aero-engine is presented in Fig. 2.14.

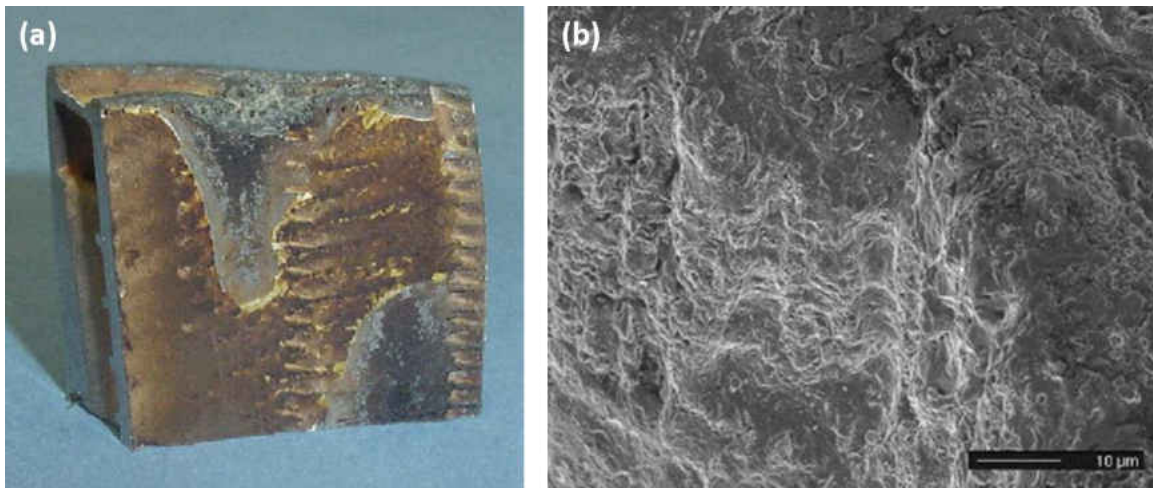


Figure 2.: EBPVD TBC failure on a turbine airfoil due to air-ingested CMAS deposit: (a) Macrograph showing significant TBC spallation, (b) SEM micrograph showing surface morphology of spalled surface revealing amorphous CMAS deposit [103].

The thermomechanical damage mechanism has been investigated as a dominant degradation mechanism, since a sufficient stress is generated in the coating due to infiltration of molten CMAS that solidifies upon cooling during thermal cycling. A cold shock delamination mechanism with a critical CMAS penetration depth of 30 μm in columnar EBPVD YSZ is required for TBC spallation to occur [103]. Repeated shock of infiltrated regions could cause large area spalls due to sequential material removal.

Additional damage mechanisms associated with the thermochemical interaction between molten CMAS and TBCs have been reported recently [30]. In general, the degradation mechanisms involve dissolution of the YSZ by CMAS melt, followed by reprecipitation of ZrO_2 with a composition and microstructure based on the local melt chemistry [30]. Reprecipitated ZrO_2 was found to be predominantly yttria depleted monoclinic ZrO_2 . Thus the thermomechanical and thermochemical interactions can accelerate the failure of TBCs and underlying components by various deleterious mechanisms such as destabilization of YSZ topcoat ($t \rightarrow t \rightarrow m+f$), accelerated oxidation and hot corrosion of the underlying metallic bond coat and superalloy substrate. Even though the dissolution of the TGO by CMAS is expected to occur, a thorough understanding of degradation of the bond coat by the CMAS deposit is mandatory.

2.4. Mitigation Approaches to Protect TBCs from Molten Deposit Attack

In order to protect TBCs from both thermomechanical and thermochemical degradation of molten deposits, melt ingress into the porous TBC topcoat must be suppressed. Various studies have attempted to mitigate the melt ingress by surface sealing of the YSZ topcoat [43], or by employing inert (e.g., mullite, alumina and calcium silicate) environmental barrier layers fabricated by APS and EB-PVD [44, 45]. Modifying the YSZ topcoat chemistry was also studied to a great extent. Zirconia stabilized with novel stabilizers such as YTaO_4 , Ta_2O_5 , CeO_2 , Sc_2O_3 and In_2O_3 were thoroughly studied as an alternate to YSZ-based TBCs towards development of novel TBCs with superior resistance against environmental degradation [46-50]. Recently, zirconate pyrochlores such as $\text{La}_2\text{Zr}_2\text{O}_7$ and $\text{Gd}_2\text{Zr}_2\text{O}_7$ received greater attention due to their promising resistance against CMAS attack [49-52].

Promising approaches to mitigate molten deposit attack of TBCs can be categorized as:

- employing an impermeable surface coating for TBCs that can act as an inert barrier between molten deposit and TBC [104];
- utilizing a sacrificial overlay that can trap deposit melt through chemical interactions, which could potentially result in increased melting temperature and viscosity of deposit melt [105] – a method examined in this study [56-58];
- surface sealing of the YSZ topcoat [43]; and
- modifying the YSZ topcoat chemistry [45-50].

2.4.1. Surface Sealing Treatments for YSZ-based TBCs

Efforts are carried out to seal the surface of plasma sprayed TBCs by various sealing treatments such as laser glazing or employing various “seal-coats” in order to prevent penetration of a corrosive melt through the interconnected pores and cracks of the YSZ TBCs [43]. Laser glazing typically results in remelting and subsequent solidification of the YSZ surface yielding a denser top layer with a new microstructure with reduced surface roughness. However, formation of extensive cracks perpendicular to the surface near the pore-free top layer could not be avoided. Surface morphology showing the modified surface microstructure due to laser glazing of the YSZ TBCs are presented in Fig. 2.15.

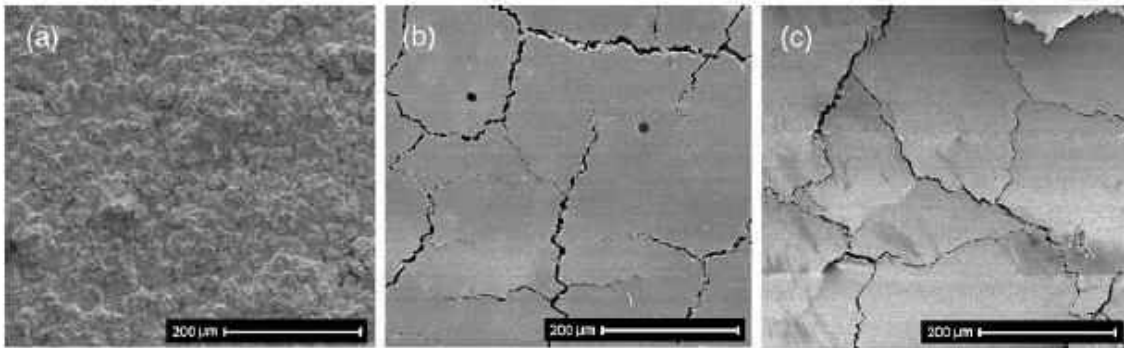


Figure 2.: Secondary electron micrographs revealing the modification of YSZ surface morphology due to laser glazing sealing treatment; (a) as-sprayed, (b) laser-glazed with CO₂ laser and (c) laser-glazed with Nd-YAG laser [43].

Zaplatynsky et al. had studied the effect of laser glazing in lifetime improvement of 8YSZ TBCs [106]. A four fold increase in lifetime was observed when TBCs were tested for hot corrosion in a burner rig testing. On the other hand, another study reported the lifetime to be worse than as-sprayed TBCs, which was attributed to the rapid ingress of molten sulfate during hot corrosion testing through the perpendicular crack network in the laser-glazed TBCs.

Batista et al. reported that laser-glazed TBCs were not efficient to provide resistance against molten salt attack, but helped reduce the degradation rate due to the denser microstructure of the TBC [43]. From another work by Ahmaniemi et al., a superior strain tolerance and erosion resistance of laser-glazed TBCs was observed even though their hot corrosion resistance was not significantly improved in comparison to as-sprayed TBCs [107]. In addition to such surface processing techniques, sealing the TBC surface by phosphate based sealants has also been attempted. Strengthening of the coating structure with improved erosion resistance was achieved but such “seal-coat” based modification also limits the use of modified TBCs at elevated temperatures because of the challenges with phase stability.

2.4.2. Corrosion-Resistant Stabilizers for ZrO₂ TBCs

Zirconia itself has an excellent resistance to hot corrosion attack by S or V rich corrosive compounds. However, during hot corrosion by sulfates and vanadates, the degradation reactions of stabilized ZrO₂-based TBCs typical involve a direct reaction of the stabilizers such as Y₂O₃, MgO and CaO to form respective sulfates and vanadates, e.g., YVO₄, Mg₃V₂O₈, Y₂(SO₄)₃, MgSO₄, CaSO₄. Hence, zirconia stabilized with a more corrosion-resistant stabilizer has been believed to be a promising solution. CeO₂ [40, 47], Sc₂O₃ [48], In₂O₃, Yb₂O₃, Ta₂O₅ and YTaO₄ [46] are examples of such stabilizers that were investigated extensively [28].

Sc₂O₃ and In₂O₃ are less basic than Y₂O₃ and thus could be more corrosion-resistant against acidic corrosive species. Chemical studies confirmed that as pure oxides, Sc₂O₃ and In₂O₃ are more resistant to molten vanadates or SO₃-Na₂SO₄ in comparison to Y₂O₃, with the order of resistance identified as In₂O₃ > Sc₂O₃ > Y₂O₃, MgO [28]. However, in addition to corrosion resistance, the critical characteristic of these stabilizers is their stabilizing ability. A

thorough understanding of the stabilizing ability for these stabilizers on ZrO_2 -based ceramics does not exist. Sasaki et al. have ranked Sc_2O_3 and In_2O_3 as less effective in stabilizing ZrO_2 in comparison to Y_2O_3 . On the other hand, Jones demonstrated a better stabilizing ability of Sc_2O_3 in addition to the superior hot corrosion resistance of Sc_2O_3 - ZrO_2 APS TBCs. Ceria stabilized zirconia (CSZ) on the other hand was found to be more tolerant in terms of thermochemical interaction by molten vanadates and sulfates of sodium [47]. However, destabilization of CSZ ($t \rightarrow m+f$) without the formation of CeVO_4 by vanadate melt was also identified by other researchers. This was reported to be a result of mineralization effect on CSZ ceramics, where even with the absence of a direct chemical interaction, the vanadate melt destabilized the metastable ZrO_2 phase to room-temperature equilibrium phases ($m+f$). In contrast, CSZ was also found to completely suffer destabilization through formation of CeVO_4 in the presence of high activity V-rich melts such as V_2O_5 . Another study on YTaO_4 and Ta_2O_5 stabilized ZrO_2 demonstrated that YTaO_4 based TBCs are more resistant to acidic attack (V_2O_5 -rich) compared to the YSZ TBCs [46]. However, both YTaO_4 and Ta_2O_5 are more prone to reaction by basic oxides such as Na_2O to form NaTaO_3 and thus are not suitable in preventing m - ZrO_2 formation when used as stabilizers for versatile corrosion-resistant applications.

2.4.3. Novel Topcoat Materials

Progress in finding an alternate material for TBC topcoat applications has been steady. The primary motivation for an alternate topcoat has been the desire to employ a low- κ TBC that can facilitate a higher TIT for a better engine efficiency. Obviously other numerous refractory materials of various crystal structures have been explored. By using insights from crystal chemistry and atomistic simulation, the search has been made more efficient. Many different oxides with various crystal structures such as fluorite and pyrochlore structures have been studied. Pyrochlores with a stoichiometry, $A_2B_2O_7$ (A=Y, Nd, Gd, La, Sm and B=Zr, Ti, Mo) possess low thermal conductivity compared to the YSZ [49]. The pyrochlore unit cell can be viewed as eight fluorite unit cells, each of which contains on average a single oxygen vacancy. The close relationship between fluorite and pyrochlore structures can be understood by considering $Y_2Zr_2O_7$ pyrochlore and $(ZrO_2)_2\text{-}Y_2O_3$ fluorite structures. $Y_2Zr_2O_7$ is unstable to the disordered fluorite $(ZrO_2)_2\text{-}Y_2O_3$ [108]. On the other hand, replacing Y^{3+} ions with larger cations such as La^{3+} and Ga^{3+} results in a stable pyrochlore structure up to 1500°C. Similarly, replacing Zr^{4+} by smaller cations such as Ti^{4+} or Mo^{4+} can also stabilize the pyrochlore structure [108]. These pyrochlore structured refractory compounds have lower thermal conductivity than YSZ. A contour map, simulated at 1200°C, illustrating the reduced thermal conductivity (κ) as a function of cationic radii (A and B) of $A_2B_2O_7$ structured compounds, is shown in Fig. 2.16.

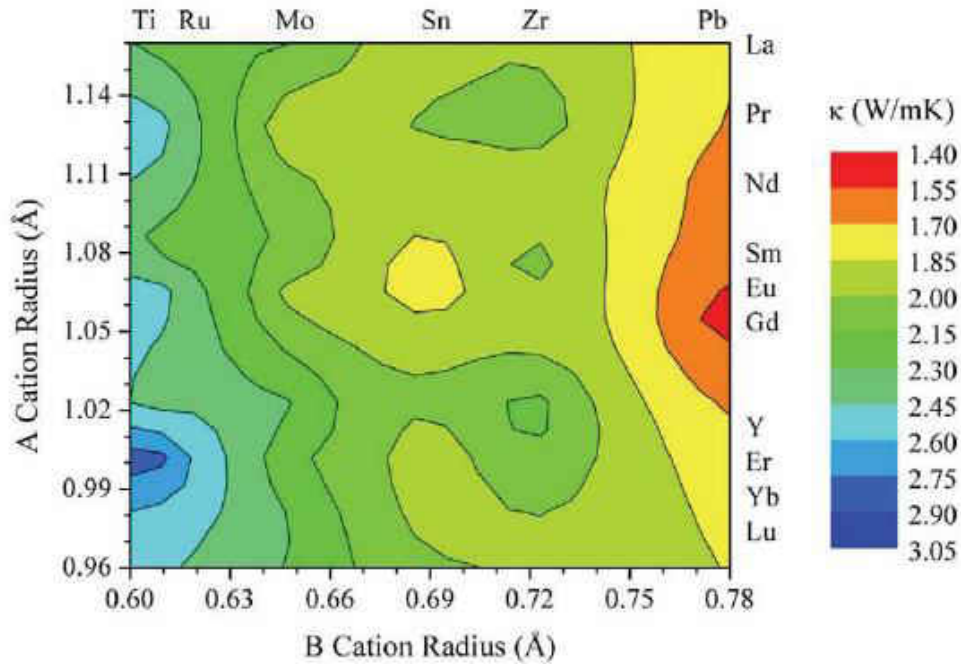


Figure 2.: Simulated contour map of thermal conductivity as a function of ionic radii of A and B for pyrochlore ($A_2B_2O_7$) structured compounds [108].

Besides the beneficial low thermal conductivity, rare-earth zirconates (REZs), $A_2Zr_2O_7$, where $A = La \rightarrow Gd$, have gained substantial interest because of their excellent thermal stability up to 1550°C for $Gd_2Zr_2O_7$ and up to 2300°C for $La_2Zr_2O_7$. Challenges with high temperature thermal stability of YSZ due to the phase transformation of $t' ZrO_2$ to $t ZrO_2$ and subsequently to m and $f ZrO_2$ phases during long term aging has been limiting the temperature capability of TBCs. Such issues would be resolved with advanced TBCs employing these alternate low k topcoats having superior thermal stability. Interestingly, REZs were also identified to be more resistant to CMAS attack. For example, Kramer et al., reported that $Gd_2Zr_2O_7$ TBCs produced by EBPVD technique to be more tolerant to CMAS attack [51]. The improved tolerance to CMAS attack was attributed to the spontaneous formation of crystalline apatite phase $Gd_8Ca_2(SiO_4)_6O_2$ and fluorite ZrO_2 with Ca and Gd in solid solution during dissolution of $Gd_2Zr_2O_7$ by the CMAS

melt. The crystalline apatite phase formation was found to increase the viscosity of the CMAS melt and seal the open channels that are available for CMAS melt to ingress. Similar thermochemical interactions could be expected for other REZs when exposed to CMAS melt. On the other hand, a comparison study of the YSZ and $\text{La}_2\text{Zr}_2\text{O}_7$ (LZ) for the hot corrosion resistance against V and S containing compounds revealed $\text{La}_2\text{Zr}_2\text{O}_7$ to be worse in a S-rich environment [109]. Even though vanadate attack was minimal with the evident formation of LaVO_4 , sulfates were found to degrade the LZ coatings by a significant consumption of coating constituents. Thus, REZs as alternate to the YSZ in a corrosive combustion environment need more careful investigation. Moreover, REZs were found to possess a significant thermal expansion mismatch with the bond coat and TGO ($\alpha\text{-Al}_2\text{O}_3$) and this poses a durability issue. Continuous efforts to employ such low κ , CMAS resistant pyrochlores as a TBC topcoat led to the evolution of a double-ceramic layer (DCL) TBCs, where the REZ of desired thickness acts as topcoat with a YSZ layer sandwiched between the topcoat and metallic bond coat [110, 111]. Novel TBCs based on DCL LZ/YSZ showed an improved thermal cyclic lifetime compared to the individual YSZ or LZ based TBCs. DCL coatings with a composition gradient that facilitates the lowering of the stress due to thermal expansion mismatch would be a more promising alternate for TBC applications.

Another study towards finding a promising materials solution for CMAS attack by Aygun et al. led to the development of novel TBCs with improved solid solubility processed by solution precursor plasma spraying (SPPS) [50]. Alumina has been reported to be a potential inhibitor for CMAS attack, where CMAS melt in contact with alumina becomes enriched with Al content due to the spontaneous dissolution of alumina. With an increased Al content, the CMAS has been

reported to crystallize out as anorthite crystals ($\text{CaAl}_2\text{Si}_2\text{O}_8$) [50]. Thus, the YSZ based TBCs with alumina in solid solution was considered to be a potential materials solution. In order to obtain the YSZ with extended alumina solid solubility, a modified plasma spraying process that employs solution precursor (SPPS), instead of powder particle, was employed. YSZ with 20 mol.% Al_2O_3 and 5 mol.% TiO_2 were achieved as a TBC topcoat. This novel TBC was found to possess excellent resistance to molten CMAS attack because the crystallization of the CMAS melt to anorthite phase readily occurred due to the increased Al content in the CMAS. A schematic illustration showing the arrest of CMAS melt by these novel TBCs is shown in Fig. 2.17. Thus, various attempts to find an ideal materials solution for resistance against the molten deposit attack of TBCs are still in progress.

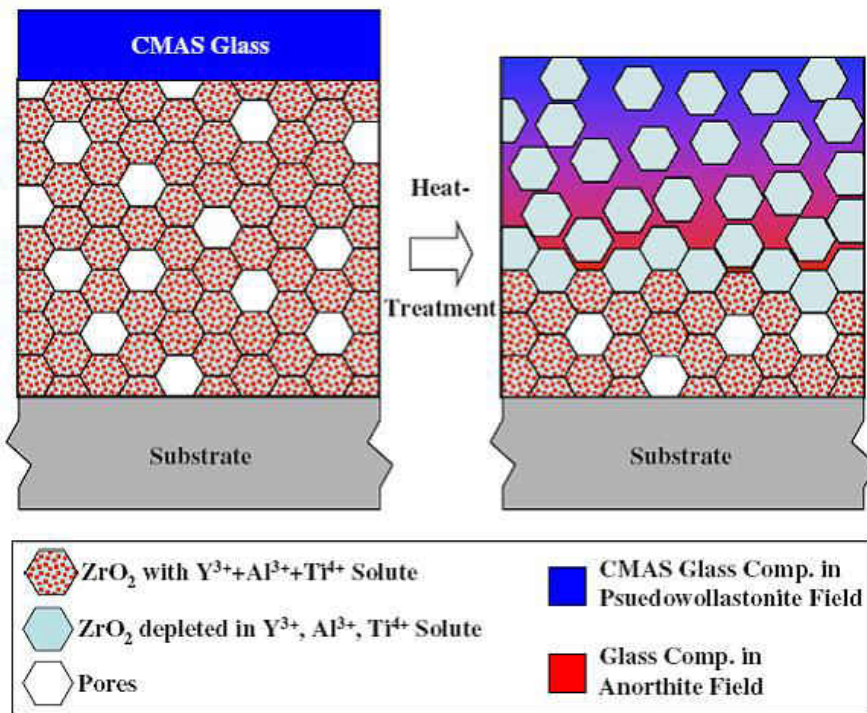


Figure 2.: A schematic illustration of a proposed mechanism for mitigation of CMAS-attack by novel SPPS processed TBCs [50].

2.4.4. Impermeable and/or Sacrificial Oxide Overlay for the YSZ TBCs

Various novel ideas to protect the YSZ TBCs from molten deposit attack have been patented numerously. Protecting TBCs by applying either an impermeable non-wetting ceramic/metallic (Pt) barrier on TBCs or a sacrificial oxide that can react with molten deposit and further crystallize the melt into compounds having higher melting temperature, have been patented by Hasz et al [104, 105]. The patent by Nagaraj et al. [112] demonstrated the ability of a multilayer overlay composed of Al_2O_3 as sacrificial oxide and Pt group metal as impermeable layer to protect TBCs from CMAS attack. In another study, various APS environmental barrier layers composed of mullite ($3\text{Al}_2\text{O}_3 \cdot 2\text{SiO}_2$), BAS ($\text{BaO} \cdot \text{Al}_2\text{O}_3 \cdot 2\text{SiO}_2$) and calcium silicate ($1.8\text{CaO} \cdot \text{SiO}_2$) have also been evaluated for hot corrosion resistant for APS TBC applications [45]. Mullite and BAS showed a potential to limit the ingress of sulfate salt. TBCs with mullite or BAS environmental barrier demonstrated similar thermal cyclic durability as that of the standard YSZ TBCs. Alumina as an environmental barrier was also investigated for APS TBCs by Chen et al. A 25 μm thick dense alumina overlay processed by EB-PVD on APS YSZ TBCs was found to suppress molten salt (Na_2SO_4 , V_2O_5) infiltration by acting as a dense barrier. Even though a complete protection was not provided, degradation rate was reduced and Al_2O_3 was also found to degrade by the formation of a low-melting liquid phase during exposure to the molten mixture of sulfate and vanadate.

As discussed above, various novel approaches have been examined in order to provide a promising materials solution for protection of TBCs against molten deposit attack. One obvious cost-effective solution would be to employ a barrier overlay that can act as impermeable and/or sacrificial oxide. Patents by Hasz et al., identified no processing method as an effective, scale-

up-ready technique to fabricate an environmental barrier of the desired density and thickness. In this doctoral study, electrophoretic deposition (EPD), which has the potential to fabricate ceramic coatings of controlled thickness and density, is explored. EPD is a versatile, scale-up-ready processing technique that can fabricate overlay ceramic layers of thickness ranging from 10 μm to 100 μm within minutes. EPD requires a thermal densification step that is typically performed to sinter the deposited power compact without any pressure. A thorough review of the EPD process, influencing process parameters and capability of EPD to fabricate ceramic coatings of any chemistry is presented in the following section.

2.5. Electrophoretic Deposition of Ceramic Coatings

EPD is primarily a two-step process: electrophoresis, where charged particles (neutral particles adsorbed by charged species) move under the influence of an electric field; and deposition, which is the coagulation of particles to a dense compact mass. Two set of parameters that determine the characteristics of the EPD process are (i) those related to the suspension and (ii) those related to the deposition process [113]. In order to obtain a crack-free homogeneous deposit, a stable colloidal suspension is required. Desired characteristics for a stable suspension are low viscosity, high dielectric constant, and low conductivity [113]. For the EPD of ceramics, organic solvent based suspensions are typically used rather than aqueous suspensions, because of the low conductivity, higher density and good chemical stability. Even though the lower dielectric constant of organic solvents limits the charge density on particles due to the lower dissociation ability, a higher field strength can be applied [114]. An aqueous suspension with applied high field strength imposes difficulties due to electrolytic gas evolution, joule heating and electrochemical attack. The Zeta potential of particles is a critical EPD parameter that

determines the suspension stability. The Zeta potential is the measure of potential difference between the particle surface and the shear plane formed by the adsorbed ions. Since the Zeta potential is closely related to the double layer thickness of the particle, agglomeration of particles in the suspension can be explained by the Zeta potential. [114]. In general, the higher the absolute value of the measured Zeta potential, the better is the dispersion of particles in the suspension. Particle size also has a profound influence on the stability of the EPD suspension. It is difficult to obtain a uniform deposit from a sedimenting suspension containing large particles. In an ideal colloidal suspension, sub-micron sized particles would tend to remain suspended for a long duration due to Brownian motion. In general, particles larger than 1 μm in size require a continuous hydrodynamic agitation to remain in suspension. The solid loading is another critical parameter, which also affects the viscosity of the suspension.

In order to fabricate a crack-free dense protective ceramic layer, controlling the as-deposited green compact thickness is mandatory. Deposition time is one of the process parameters that needs to be optimized in order to obtain a green compact of controlled thickness. Deposition rate is typically constant during the early stage of EPD. However, the formation of an insulating ceramic compact on the electrode surface during EPD, which affects the electric field generated from the constant voltage applied between electrodes, would eventually reduce the deposition rate. Applied voltage is another process parameter that needs to be controlled. In general, deposition rate tends to increase with an increase in applied voltage. However, at a higher applied voltage that might cause turbulence in the suspension, particles might not find enough time for lateral movement after depositing on the electrode surface to form a close-packed structure. It was found that more uniform films are deposited at a moderate applied

voltage (25 to 100 V/cm). It is quite evident that the quality of deposit and kinetics of EPD is highly dependant on numerous parameters. In general, a well-dispersed stable suspension will yield a better deposition. Process parameters such as applied voltage, deposition time and particle concentration in the suspension are few of the most influencing parameters of the EPD process. To obtain a dense ceramic layer by EPD, the drying and subsequent sintering steps should also be carefully performed. Extensive reviews of the EPD process by Besra et al. and Vander Biest et al., clearly explain the EPD process and also list the critical process variables in order to obtain a ceramic coating of desired quality [113, 114].

The EPD process requires a post densification step in order to obtain the ceramic coating of desired porosity. A completely dense coating is achievable by carefully controlling the thickness and sintering conditions. The EPD process was studied to process YSZ TBCs by Van der Biest et al., where a stable YSZ nanopowder suspension was used to obtain a 300 μm thick TBC by EPD accompanied by a hybrid microwave sintering densification step [116]. Even though a low thermal conductivity of 0.8 W/mK was reported for EPD TBCs, the thermal stability of the YSZ coating and its durability was not explored in detail. EPD of YSZ coatings was extensively studied primarily for solid oxide fuel cell (SOFC) applications [117]. A dense YSZ coating was obtained by EPD of YSZ powders (51 – 65 nm) followed by sintering at 1300°C for 3 h on a porous strontium doped lanthanum manganite (LSM) substrate as shown in Fig. 2.18.

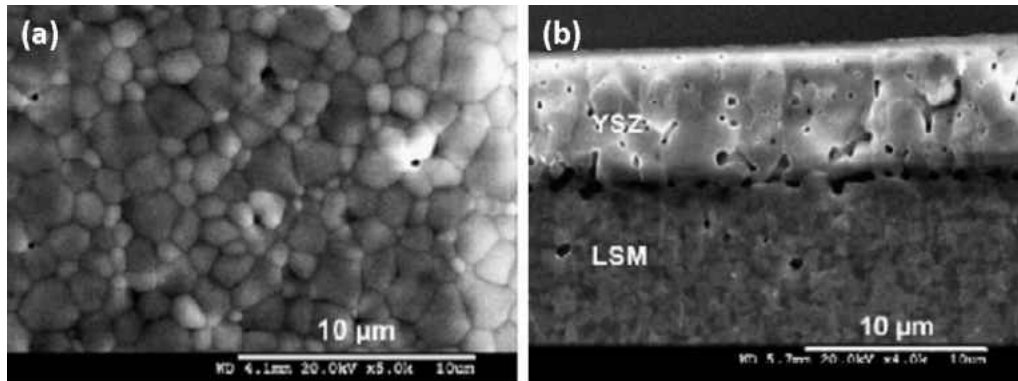


Figure 2.: Secondary electron micrographs of the YSZ coating on a LSM substrate obtained by EPD followed by sintering at 1300°C for 3 h: (a) surface morphology and (b) cross-sectional microstructure [117].

The EPD process, being a versatile technique, has been greatly explored for fabricating coatings and structures of various materials [118, 119]. Some of the commonly used aqueous and organic solvents as colloidal suspension medium are listed in Table 2.1. EPD has also been studied for codeposition of two or more oxides by controlling the solid content of each oxide powders in the colloidal suspension [120]. Deposition kinetics of the individual oxides depend on various characteristics, such as particle size and Zeta potential [121]. Further, by modifying the concentration of individual oxides during the EPD process, functionally graded coatings can also be obtained.

Table 2.: Various solvents used in EPD processing of different materials.

Deposited Material	Solvent Medium
Al_2O_3 , $\text{Al}_2\text{O}_3/\text{ZrO}_2$	Water [122]
YSZ	Acetone [119]
YSZ	Acetone-Ethanol [119]
YSZ	Acetylacetone [118]
YSZ	Cyclohexane [123]
Hydroxyapatite (HAP)	Isopropanol [124]
Al_2O_3 , ZrO_2	Ethanol [57]
Al_2O_3 , MgO	Acetone-Ethanol [56]
CeO_2 , SnO_2 , CaSiO_3	Ethanol-Water [125]
MgO, Al_2O_3	Ethanol-Acetylacetone [126]

CHAPTER 3: EXPERIMENTAL DETAILS

3.1. Air Plasma Sprayed Free Standing YSZ and CoNiCrAlY Coatings

In order to investigate the individual thermochemical degradation of TBC coating constituents by various molten deposits, free standing air plasma sprayed YSZ and CoNiCrAlY coatings were prepared in this study. An in-house thermal spray facility at UCF was employed to produce the free standing coatings. For APS YSZ coating, 8 YSZ powders (ZRO-182, agglomerated and sintered, Praxair Inc., Danbury, CT, USA); zirconia stabilized with 8 wt.% yttria, with average particle size of 106 μm were thermally sprayed on grit blasted graphite substrates. A Sulzer Metco F4 MB plasma gun (Sulzer Metco (US) Inc., Westbury, NY, USA) was used. A spraying current of 675 A at a stand-off distance of 100 mm, with a primary gas Ar flow of 100 SCFH (standard cubic feet per hour), a secondary gas H₂ flow of 20 SCFH and a carrier gas Ar flow of 8 SCFH were employed as the processing conditions. The graphite substrate was subsequently burnt off by heat-treating the APS specimen (YSZ on graphite) at 900°C for 1 h, which yielded the free standing YSZ coatings.

Using a similar APS processing technique, free standing metallic CoNiCrAlY coatings were produced. These coatings are commonly used as a bond coat material in TBCs and overlay oxidation/hot corrosion resistant coatings in high temperature applications. CoNiCrAlY coatings were thermally sprayed with the same plasma gun on graphite substrates using CoNiCrAlY powders (CO-159, Praxair Inc, Danbury, CT, USA) with composition of 38.5 wt.% Co, 32 wt.% Ni, 21 wt.% Cr, 8 wt.% Al, and 0.5 wt.% Y and average particle size of 75 μm . A spraying current of 675 A with a primary gas Ar flow of 120 SCFH, a secondary gas H₂ flow of 18 SCFH and a carrier gas Ar flow of 8 SCFH at a stand-off distance of 100 mm were employed.

Subsequent heat-treating yielded the free standing CoNiCrAlY coatings. Figure 3.1 shows the macrographs of as-sprayed free standing coatings. APS process parameters employed in this study are also reported in Table 3.1. The YSZ and CoNiCrAlY coatings were used extensively throughout this study for a thorough investigation of thermochemical degradation due to aggressive molten deposits. The CoNiCrAlY coatings were also initially pre-oxidized at 1100°C for 50 h to have a coating microstructure with internal oxidation and appreciably thick TGO scale on the surface that is likely to be exposed to such molten deposits in a real engine operation.

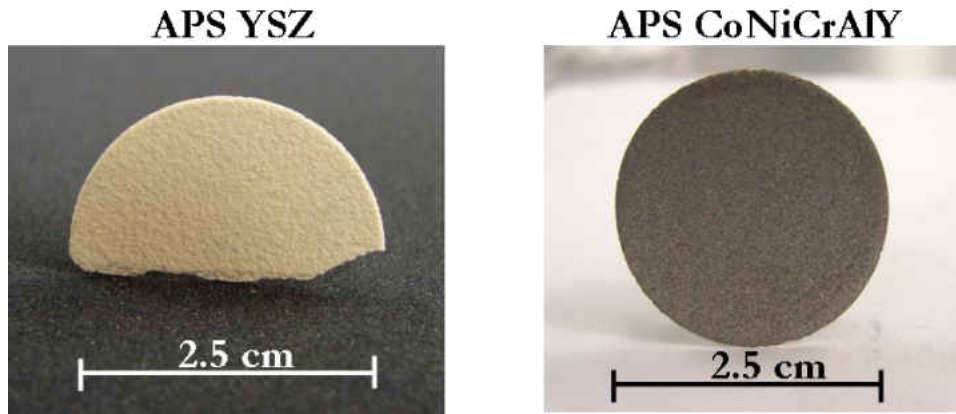


Figure 3.: Macrographs of free standing APS YSZ and CoNiCrAlY coatings.

Table 3.: List of APS process parameters employed to fabricate free standing coatings.

Coating Type	Plasma Gun	Spraying Current (A)	Primary Gas (Ar) Flowrate (SCFH)	Secondary Gas (H ₂) Flowrate (SCFH)	Carrier Gas (Ar) Flowrate (SCFH)	Stand-off Distance (mm)
YSZ (ZRO-182)	Sulzer Metco F4 MB	675	100	20	8	100
CoNiCrAlY (CO-159)	Sulzer Metco F4 MB	675	120	18	8	100

3.2. High Temperature Isothermal Exposure to Molten Deposits

High temperature isothermal testing in dry air was performed to study the individual degradation reaction mechanisms of the YSZ and CoNiCrAlY coatings when exposed to corrosive compounds containing vanadium, phosphorus, sodium, calcium and sulfur at elevated temperatures. The reactions with each compound were isolated, thereby eliminating mixed interactions and combined effects. Although in practice such mixed interactions may enhance or inhibit the hot corrosion attack, the objective in this work was to study the degradation mechanisms of the YSZ and CoNiCrAlY by different types of species in isolation. One major part of this study focused on investigating the thermochemical interactions between APS coatings and CMAS sand deposit. Experimental details of such molten deposit exposure testing (hot corrosion and CMAS testing) are described below.

3.2.1. Hot Corrosion Testing of Free Standing YSZ and CoNiCrAlY

Low-quality alternate fuel containing significant levels of elemental impurities such as vanadium, sodium, calcium, phosphorus and sulfur can form highly corrosive compounds that deposit on hot-section components of gas turbine engines. For hot corrosion testing, coating specimens (1 cm x 1 cm) were sectioned from the as-sprayed free-standing YSZ and CoNiCrAlY. These specimens, in contact with different corrosive impurities of high purity, namely V_2O_5 , P_2O_5 , Na_2SO_4 , $Na_2SO_4 + V_2O_5$ mixture (50 – 50 mol.%), $NaVO_3$ and $CaSO_4$ were subjected to isothermal heat-treatment. The testing temperature ranged between 200°C and 1200°C for up to 5 hours. During each test, samples with the corrosive deposit of interest at a specific concentration were loaded into the furnace that was preheated to the test temperature. At the end of each test, samples were removed and subjected to air-quench. All tests were performed in air

using a Thermolyne 46100 muffle furnace (1700°C max) shown in Fig. 3.2. Details of molten deposit testing and the potential source of corrosive compounds are listed in Table 3.2. Emphasis was given to test temperatures close to the melting point of the contaminant in order to thoroughly investigate the thermochemical interactions with YSZ and CoNiCrAlY without vaporizing the corrosive species.

Thermolyne 46100 Muffle Furnace



Lindberg/Blue 3-zone Tube Furnace



High Vacuum System

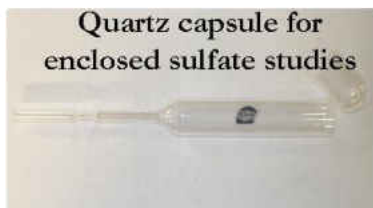


Figure 3.: Experimental tools used for high temperature molten deposit testing of the free-standing YSZ and CoNiCrAlY.

During each run of the hot corrosion testing, the contaminant of interest in the form of powder was spread uniformly over the as-sprayed free standing YSZ specimen surface at a concentration of 20 mg/cm². In addition, Na₂SO₄ was applied at even higher concentrations such as 30 mg/cm² and 50 mg/cm² because of its inert nature during testing with the YSZ.

Table 3.: Details of the high temperature molten deposit tests carried out in this study.

Material	Contaminant and Testing Environment			Temperature Range	Contaminant Source
	Corrosive Compounds	Air	Enclosed in quartz capsule		
APS YSZ	V ₂ O ₅	✓		700°C to 1000°C	V ₂ O ₅ - Vanadium from fuel.
	P ₂ O ₅	✓		200°C to 1000°C	P ₂ O ₅ - Phosphorus from fuel.
	Na ₂ SO ₄	✓	✓	900°C to 1100°C	Na ₂ SO ₄ - Sodium and sulfur from fuel.
	Na ₂ SO ₄ + V ₂ O ₅	✓		600°C to 1000°C	Na ₂ SO ₄ - Sodium and sulfur from fuel.
	CMAS	✓		1200° to 1350°C	CMAS - Air ingested sand.
APS CoNiCrAlY (As-Sprayed and Pre-Oxidized)	V ₂ O ₅	✓		700°C to 1000°C	V ₂ O ₅ - Vanadium from fuel.
	P ₂ O ₅	✓		200°C to 1000°C	P ₂ O ₅ - Phosphorus from fuel.
	Na ₂ SO ₄	✓	✓	700°C to 1000°C	Na ₂ SO ₄ +V ₂ O ₅ (or NaVO ₃) - Eutectic mixture having lower melting point.
	CaSO ₄	✓		700°C to 1100°C	CaSO ₄ - Sulfur from fuel and Ca from ash.
	NaVO ₃	✓		700°C to 1000°C	CaSO ₄ - Sulfur from fuel and Ca from ash.
	CMAS	✓		1250°C	CMAS - Air ingested sand.

A simple schematic showing the molten deposit testing of APS coatings is shown in Fig. 3.3. It is worth mentioning that Na₂SO₄ + V₂O₅ mixture was made for this study to examine the effects of the vanadates of sodium on the YSZ. This was performed by selecting a specific composition of 50 – 50 mol.% of Na₂SO₄ and V₂O₅, and melting the mixture at 1000°C. This molten mixture was then quenched to obtain vanadates of sodium predominantly consisting of sodium metavanadate (NaVO₃). This vanadate salt was used to study the effect of Na₂SO₄ +

V_2O_5 mixture. An equilibrium phase diagram of V_2O_5 - Na_2SO_4 system [127] along with the selected composition (shaded) is presented in Fig. 3.4.

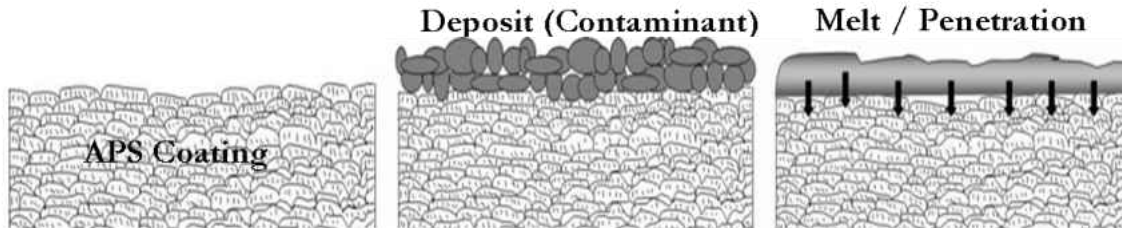


Figure 3.: A simple schematic representation of hot corrosion testing of APS coatings.

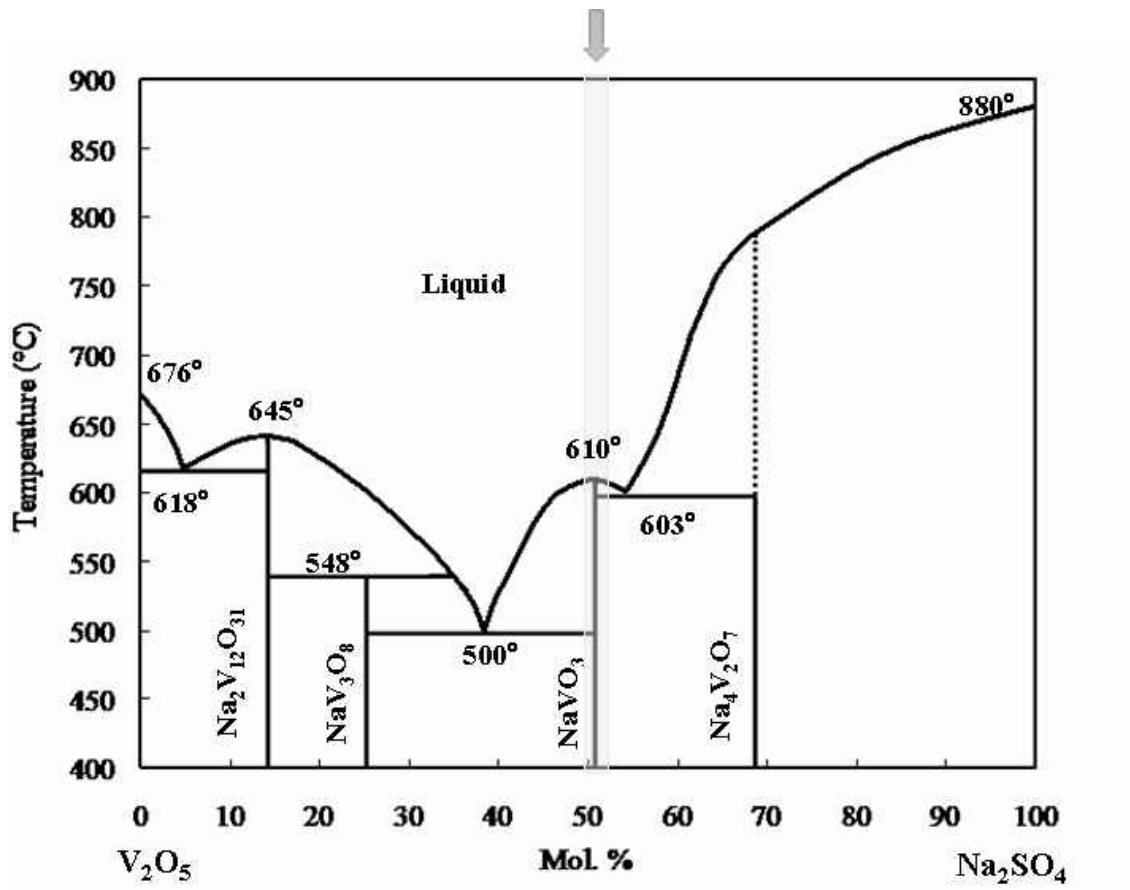


Figure 3.: Equilibrium phase diagram of the V_2O_5 - Na_2SO_4 system and the selected composition of mixture for this study (shaded) [127].

In the case of CoNiCrAlY studies, both as-sprayed and pre-oxidized specimens were subjected to the corrosive deposits listed in Table 3.2 through a similar testing procedure. Tests involving sulfate deposits (Na_2SO_4) were performed in an enclosed quartz capsule in order to trap the SO_2/SO_3 gas during dissociation of Na_2SO_4 , and maintain a molten salt film on the specimen throughout the test duration. Sulfate salt coated specimens were inserted in quartz capsules, which were subsequently evacuated using a high vacuum system shown in Fig. 3.2. Based on the partial pressure of SO_x (SO_2 , SO_3) resulting from the high-temperature dissociation of applied Na_2SO_4 salt, quartz capsules were refilled with the desired amount of oxygen in order to achieve 1 atm pressure at test temperature and loaded into a tube furnace (Lindberg Blue 3-zone tube furnace). It should be noted that the excess concentrations of contaminants were chosen primarily to examine the mechanisms of degradation at an accelerated rate, and not to simulate the actual condition that turbine blades with TBCs may be exposed to.

3.2.2. High Temperature CMAS Deposit Testing of Free Standing YSZ and CoNiCrAlY

Air ingested CMAS sand deposits have been identified as a critical threat to the durability of TBCs. A detailed investigation on the degradation of YSZ and CoNiCrAlY by a laboratory-synthesized CMAS deposit was carried out. Based on the average composition reported for deposits on aircraft turboshaft shrouds operated in a desert environment [29, 30], the laboratory-synthesized CMAS used in this study had a chemical composition of 35 CaO – 10 MgO – 7 Al_2O_3 – 48 SiO_2 that can be referred as $\text{C}_{35}\text{M}_{10}\text{A}_7\text{S}_{48}$ (composition in mole percent). This CMAS was prepared by mechanically milling the individual oxides of high purity in a SPEX shaker mill (SPEX CretPrep, Metuchen, NJ) for 1 hour at room temperature, which yielded completely

amorphous CMAS deposits. The APS YSZ and CoNiCrAlY coating specimens of known dimensions were deposited with as-milled CMAS powders at a concentration of 20 mg/cm². The YSZ and CoNiCrAlY specimens in contact with CMAS were subjected to isothermal heat-treatment using a Thermolyne 46100 muffle furnace at temperatures ranging from 1200°C to 1350°C for up to 4 hours.

The molten deposit tests were carried out with the deposit of interest spread uniformly on the YSZ surface at the desired concentration in the form of a powder. In cases where these deposits could not be applied in the form of powder, e.g. tests in enclosed quartz capsule, water based suspension, in case of insoluble compounds, or an aqueous solution of soluble salts, such as sulfates, was used to apply the corrosive compound by spraying on heated specimens. After the testing, specimens were thoroughly analyzed for melt penetration, reaction product identification and degradation mechanisms.

3.3. Microstructural Investigation of YSZ and CoNiCrAlY Specimens

After a careful visual inspection, tested specimens were thoroughly examined by materials characterization tools (at Materials Characterization Facility (MCF), UCF) for microstructural analysis and phase identification. Characterization tools at UCF MCF that were extensively employed in this study are shown in Fig. 3.5. X-ray diffraction (XRD) studies were performed on the hot corrosion and CMAS tested samples to examine the development of constituent phases. This was performed by using a Rigaku D-Max B Diffractometer (Tokyo, Japan) with Cu K α radiation. XRD patterns after appropriate background correction were indexed based on the available JCPDS resources using MDI Jade software. Surface and cross-

sectional microstructural analysis were carried out to examine the deposit penetration, reaction products and degradation mechanisms by using JEOL 6400F field-emission scanning electron microscope (FE-SEM) (Tokyo, Japan) and Hitachi S3500N scanning electron microscope (SEM) (Tokyo, Japan), both equipped with an X-ray energy dispersive spectrometer (XEDS). For cross-sectional microstructural characterization, specimens were embedded in epoxy resin and metallographically prepared down to 0.25 μm using diamond paste. For microstructural analysis, specimens tested for hot corrosion using sulfate deposits were prepared with organic solvent to minimize the water exposure and preserve the soluble corrosion products for further analysis. For SEM characterization, epoxy mounted cross-sectional specimens and as-tested surfaces were coated with a thin Au-Pd (10 nm) film using an EMITECH K550 D.C. sputter coating system. Backscattered and secondary electron imaging modes were extensively employed for microstructural analysis by SEM. The FE-SEM utilized a cold cathode field emission electron gun and has a resolution of 1.5 nm. Images were collected with a voltage ranging from 15 to 30 kV at a constant emission current of 8 μA . EDS spectra were also collected at regions of interest for a qualitative/quantitative compositional analysis. Detailed microstructural investigation using a Philips/FEI Tecnai F30 300KeV transmission electron microscope (TEM) (Hillsboro, OR, USA), equipped with high angle annular dark field (HAADF) and XEDS was also performed to examine the detailed reaction mechanisms and the phase constituents (e.g. phase transformations and reactions) of the YSZ and CoNiCrAlY due to infiltration and degradation by molten deposits.



Figure 3.: Materials characterization tools employed in this study.

Sample preparation for TEM was performed by focused ion beam (FIB) in-situ lift-out (INLO) using a FEI 200 TEM FIB (Hillsboro, OR, USA) through a procedure shown in Fig. 3.6. Details of FIB-INLO can be found elsewhere. In the TEM study, selected area electron diffraction analysis was extensively carried out on individual grains of interest for a complete investigation to confirm the thermochemical interactions and phase evolution (phase

transformation, reaction product identification) due to molten deposit degradation of the free-standing YSZ and CoNiCrAlY coatings.

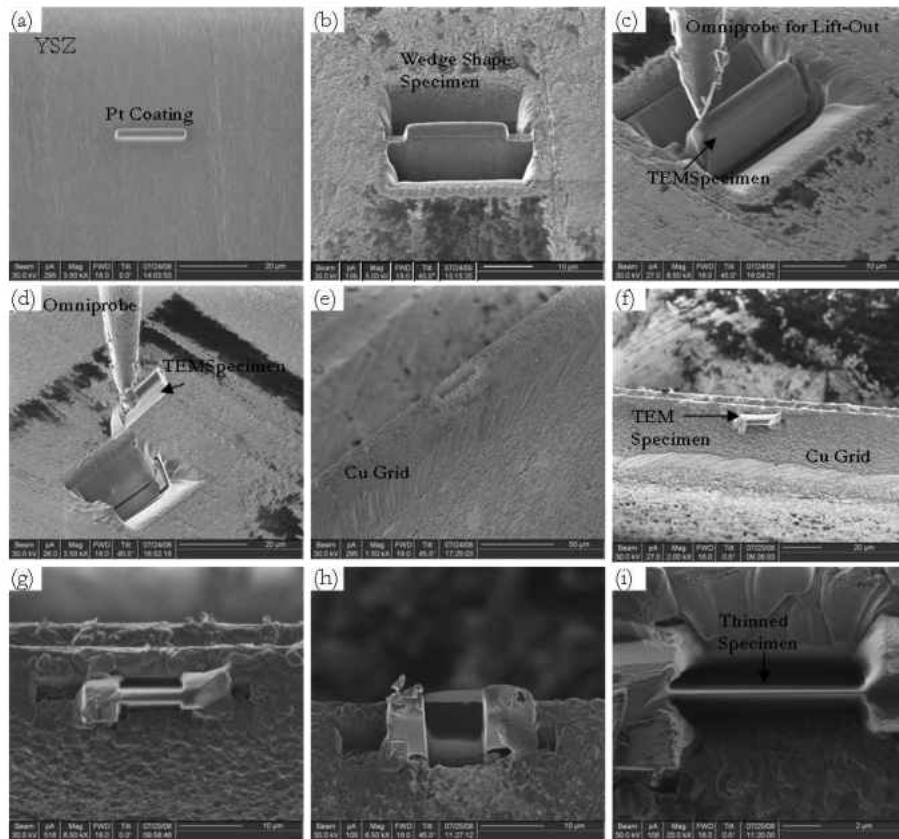


Figure 3.: Sequential ion beam images from TEM specimen preparation by focused ion beam (FIB) in-situ lift out (INLO) technique: : (a) Pt layer deposited at a site of specific interest; (b) focused ion milling carried out to create a wedge-shaped specimen, (c) specimen welded to a W omniprobe, and (d) lifted out, (e) Cu grid, (f) specimen welded to TEM grid, (g), (h) and (i) thinned further for TEM analysis [84].

3.4. Environmental Barrier Overlay for TBCs by Electrophoretic Deposition (EPD)

In order to deposit a ceramic overlay of desired chemistry on the APS YSZ, the EPD process was explored in this study. Various overlay coatings made of YSZ, Al₂O₃, MgO and an Al₂O₃-MgO composite of desired thickness and porosity were produced with EPD followed by a densification step, i.e., controlled sintering. APS YSZ coatings, thermally sprayed on graphite substrates (1" diameter disks) as described in section 3.1 were directly deposited with overlay ceramics by the EPD technique. During sintering, which is a critical densification step required for EPD, the graphite substrates were burnt-off yielding free standing YSZ coatings with a ceramic overlay.

3.4.1. Al₂O₃ Overlay for APS TBCs

In order to protect TBCs from CMAS attack, Al₂O₃ overlay coatings for APS YSZ were processed by EPD, since CMAS was reported [50] to readily react with Al₂O₃ and crystallize out as high melting phases that suppress further CMAS melt ingress. In order to deposit alumina powders by the EPD process, a stable colloidal suspension of α -Al₂O₃ powders in an organic solvent with additives was prepared. Al₂O₃ powders (α -Al₂O₃ powder, Metlab Corporation, Niagara Falls, NY, USA) with particle size of 0.3 μ m were dispersed in an acetone-ethanol (Fisher Scientific, Pittsburgh, PA, USA) organic solvent mixture (volume ratio, 1:1) at a solid loading of 10 g/l. Iodine (Fisher Scientific, Pittsburgh, PA, USA) at a concentration of 0.4 g/l was used as an additive. This colloidal suspension was mechanically stirred for 10 minutes and subsequently subjected to ultrasonication for 2 h to break down the particle agglomerates for a

stable colloidal suspension of individually dispersed alumina particles. The EPD process requires the working electrode (cathode) to have an electrically conducting surface, in order to apply a uniform electric field for cathodic deposition. APS YSZ coatings on graphite disks were used as the working electrodes, which were made electrically conductive by applying a thin Pt or Au-Pd layer (~ 10 nm) using EMITECH K550 D.C. sputter coating system. The YSZ coated with Pt/Au-Pd was used as a cathode and an inert graphite disk of the same surface area and geometry was used as anode. The EPD cell was simply assembled by completely immersing the electrodes in alumina colloidal suspension that had a constant hydrodynamic agitation using a magnetic stirrer. The distance between cathode and anode was kept constant at 1 cm throughout this study. A DC voltage of 30 V was applied between the cathode and anode for deposition durations up to 15 minutes using a Protek 3032B DC power supply. During EPD, positively charged α -Al₂O₃ powders in colloidal suspension drifted and deposited onto the electrically conductive APS YSZ cathode. A simple schematic of the EPD cell is shown in Fig. 3.7, which also demonstrates the particle deposition on cathode surface during cathodic deposition. The deposited powder compact by EPD was dried at ambient atmosphere for 2 hours, and subjected to densification by sintering. It should be noted that a controlled slow ramping rate during sintering is required in order to densify the EPD powder compact and fabricate a dense adherent coating. Sintering was performed at 1200°C for 10 h with a carefully controlled ramp-up and ramp-down rates of 2°C/min using a Thermolyne 46100 high temperature muffle furnace. A modified free-standing YSZ coating assembly consisting of a 300 μ m thick APS YSZ coating with a dense 25-50 μ m thick EPD alumina overlay coating was produced. The thickness of the EPD overlay was

controlled by deposition time during EPD, where a 100 μm thick alumina coating was produced with a deposition duration of 15 minutes.

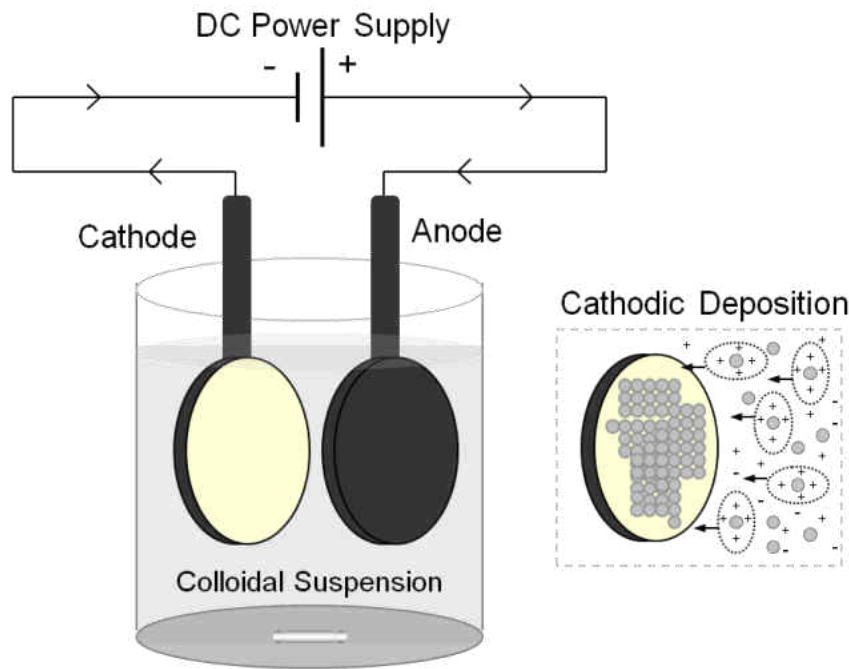


Figure 3.: A schematic representation showing the assembly of electrophoretic deposition (EPD) cell along with the mechanism of particle coagulation during cathodic deposition.

3.4.2. MgO Overlay for APS TBCs

MgO is a promising trap for corrosive compounds such as Na_2SO_4 and V_2O_5 . For deposition of MgO on APS YSZ coatings by EPD technique, a colloidal suspension of MgO powders with an average particle size of 1 μm (Mallinckrodt Baker, Inc., Phillipsburg, NJ, USA) was prepared with the same colloidal bath chemistry as used for alumina deposition. The chosen EPD processing parameters were a 25 V/cm applied voltage and a deposition time of 10 minutes. MgO powder compact prepared by EPD was subsequently sintered at 1100 $^\circ\text{C}$ for 10 h with a

carefully controlled ramp-up and ramp-down rates of 2°C/min. A free standing YSZ with MgO overlay coating of 25-30 µm in thickness was obtained.

3.4.3. Al₂O₃-MgO composite Overlay for APS TBCs

With a motivation to protect the APS YSZ from CMAS as well as highly corrosive sulfate and vanadate deposits, Al₂O₃-MgO composite overlay was also produced on APS YSZ. Besides, thermal expansion mismatch between the YSZ and overlay ceramic coating may be a critical characteristic, which would typically dictate the durability of such overlay coatings. Since the YSZ has a coefficient of thermal expansion (CTE), ~ 10.5x10⁻⁶ /°C, alumina with ~ 7x10⁻⁶ /°C and MgO with ~ 12.8x10⁻⁶ /°C, Al₂O₃-MgO composite would be a better candidate as an overlay.

EPD of Al₂O₃-MgO composite overlay was produced by similar EPD processing route as described for the case of Al₂O₃ or MgO overlays. A colloidal suspension of Al₂O₃ and MgO powder mixture at a solid loading concentration of 10g/l (weight ratio, 1:1) was prepared with the same colloidal bath chemistry as used for Al₂O₃ deposition. The chosen EPD processing parameters were 30 V/cm applied voltage and a deposition time of 3-5 minutes. Al₂O₃-MgO powder compact prepared by EPD was subsequently sintered at 1100°C for 5 h with a carefully controlled ramp-up and ramp-down rates of 2°C/min. Free-standing YSZ with Al₂O₃-MgO composite overlay coating of 25 to 50 µm in thickness was obtained.

3.4.4. YSZ Overlay for APS TBCs

In addition to the aforementioned overlay ceramic, it is obvious that a fully-dense YSZ overlay could seal the porous APS YSZ surface and be a potential solution without any challenges due to thermal expansion mismatch. In order to deposit YSZ powders by EPD process, a stable colloidal suspension of the YSZ was prepared with the same colloidal bath chemistry used for Al_2O_3 deposition. TZ-3Y powders (Tosoh Corporation, Tokyo, Japan), ZrO_2 stabilized with 5.4 wt.% Y_2O_3 with an average particle size of $0.6\ \mu\text{m}$ (crystallite size of 27 nm) were dispersed in an acetone-ethanol organic solvent mixture. A DC voltage of 25 V/cm was applied for deposition duration up to 10 minutes. Sintering was performed at two different temperatures of 1300°C and 1350°C for 4 h with carefully controlled ramp-up and ramp-down rates of $2^\circ\text{C}/\text{min}$ using a Thermolyne 46100 high temperature muffle furnace. After sintering at elevated temperatures, a free standing YSZ coating assembly consisting of $300\ \mu\text{m}$ thick APS YSZ coating with a dense $25\text{-}50\ \mu\text{m}$ thick EPD YSZ overlay was produced.

3.5. Exposure of the free-standing APS YSZ with EPD Overlay to Molten Deposits

APS YSZ modified with various ceramic overlays, Al_2O_3 , MgO, $\text{Al}_2\text{O}_3\text{-MgO}$ composite and YSZ were studied individually to demonstrate the beneficial effects of overlay ceramics in protecting TBCs against molten deposit attack. APS YSZ specimens with Al_2O_3 and $\text{Al}_2\text{O}_3\text{-MgO}$ composite overlay in contact with laboratory synthesized CMAS deposit were isothermally exposed to temperatures ranging from 1250°C to 1300°C for 1 h. Similarly, YSZ specimens with MgO and $\text{Al}_2\text{O}_3\text{-MgO}$ composite overlay in contact with V_2O_5 deposit were tested for hot corrosion resistance at 800°C to 900°C for 1 h. After the testing, specimens were thoroughly

characterized by XRD, SEM, EDS, FIB and TEM to document the beneficial effects and mitigation mechanisms of overlay coatings in protecting APS TBCs against molten deposit attack.

3.6. Durability Study of Commercial TBCs modified with EPD Overlay

In this study, Al_2O_3 and Al_2O_3 -MgO composite overlay coatings demonstrated a great potential in protecting APS TBCs from molten deposit attack. With due consideration for real engine applications, the durability of the EPD Al_2O_3 overlay on a commercial TBC specimen (8YSZ/CoNiCrAlY/IN738LC) was examined by furnace thermal cyclic testing using CM 1710 Rapid High Temperature Furnace. LPPS CoNiCrAlY coated IN738LC superalloy substrates were used to produce commercial TBCs by thermally spraying 8YSZ powders using APS YSZ process described in section 3.1. A 50 μm thick EPD Al_2O_3 overlay coating was deposited on commercial-TBCs that were composed of 300 μm thick APS YSZ topcoat, 100 μm thick LPPS CoNiCrAlY bond coat and IN738LC superalloy substrate. EPD processing of the ceramic overlay on commercial TBCs employed the processing routes described in section 3.4. Deposition durations were limited within 5 minutes in order to produce uniform overlay coatings of 50 μm thickness. APS TBCs before and after deposition of ceramic overlay by EPD are shown in Fig. 3.8.

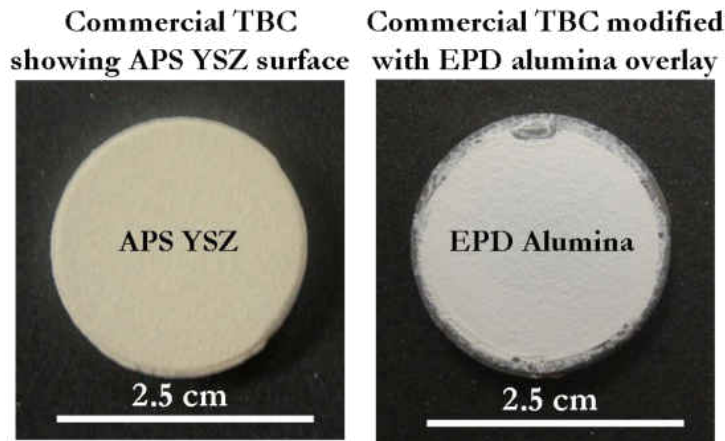


Figure 3.: Macrographs showing the as-processed commercial APS TBCs (APS YSZ/LPPS CoNiCrAlY on IN738LC superalloy) and APS TBCs modified with EPD overlay.

The durability of these TBCs modified with ceramic overlay coatings were examined by lifetime assessment through thermal cyclic testing at 1100°C. For furnace thermal cycling in air, a CM 1710 Rapid High Temperature Furnace with bottom loading capability was employed, where each thermal cycle consisted of 10 min heat-up to 1100°C, 60 min hold at 1100°C, followed by 10 min forced-air-quench. Figure 3.9 shows the cyclic high temperature furnace employed with a schematic illustrating the furnace operation during cyclic oxidation testing. Thermal cyclic tests were performed until failure of TBC, defined by a minimum of 50% (area) YSZ spallation. Adhesion and structural integrity of the EPD Al₂O₃ overlay was thoroughly examined after failure of TBC by cross-sectional microstructural analysis using SEM.

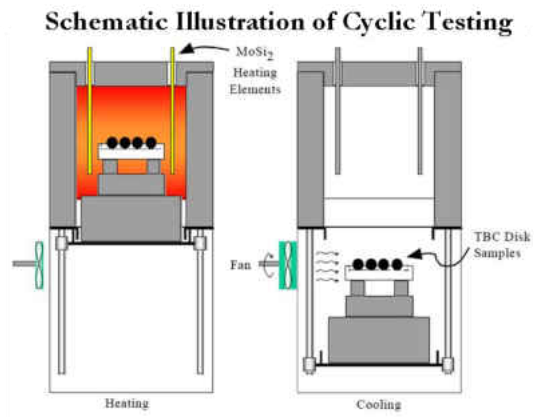


Figure 3.: CM 1710 Rapid High Temperature Furnace used for thermal cyclic tests and a schematic illustration of cyclic oxidation testing.

CHAPTER 4: RESULTS

4.1. As-sprayed Free-Standing APS YSZ and CoNiCrAlY Coatings

As-sprayed free-standing YSZ topcoat specimens were characterized for initial microstructure and phase constituents. The initial phase constituent of YSZ specimens before any hot corrosion treatment was examined by XRD as presented in Fig. 4.1. The as-sprayed YSZ was found to exist as metastable tetragonal zirconia phase (t' - ZrO_2), which is the desirable phase for TBC applications. Cross-section of free standing APS YSZ showing a uniform thickness of 300 μm is shown in Fig. 4.2. Backscattered electron micrograph of metallographically prepared YSZ cross-section in Fig. 4.2(a) illustrates the typical porous topcoat microstructure. Secondary electron micrograph of a fractured YSZ cross-section shown in Fig. 4.2 (b) reveals the typical splat-quenched microstructure of APS YSZ with the columnar grains within the splats.

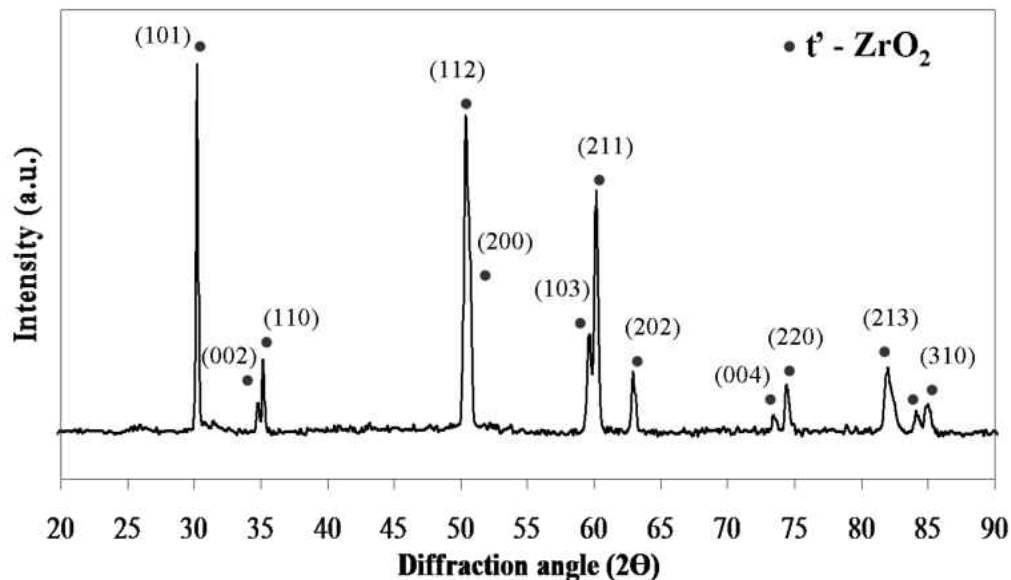


Figure 4.: XRD pattern obtained from the as-sprayed free standing YSZ topcoat surface confirming the phase constituent of YSZ as the t' - ZrO_2 .

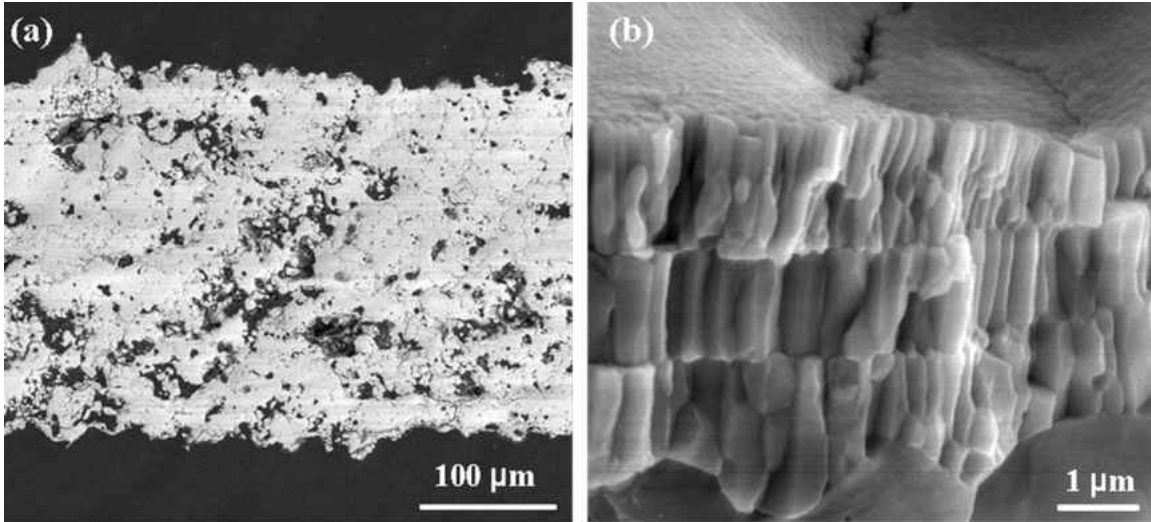


Figure 4.: Cross-sectional (a) backscattered electron micrograph showing the typical microstructure of as-sprayed free standing YSZ topcoat with uniformly thick YSZ topcoat that consists of (b) splat-quenched microstructure observed by secondary electron micrograph.

Free-standing APS CoNiCrAlY coatings were found to be uniformly thick with an average thickness of 300 μm as seen in cross-sectional secondary electron micrograph presented in Fig. 4.3(a). Surface morphology revealing the typical splat microstructure resulted from APS is shown in Fig. 4.3(b). As mentioned in Chapter 3, in order to examine the degradation of CoNiCrAlY by molten deposits, specimens were also preheated in air at 1100°C for 20 h to develop a TGO scale as the surface oxide scale with an internally oxidized CoNiCrAlY microstructure. Cross-sectional backscattered electron micrograph as presented in Fig. 4.3(c) illustrates the typical oxidized APS CoNiCrAlY microstructure with appreciably thick TGO scale and significant internal oxide at the inter-splat boundaries. A secondary electron micrograph illustrating the high magnification view of the morphology of surface TGO oxide (alumina) evolved during oxidation of CoNiCrAlY is also shown in Fig. 4.3(d).

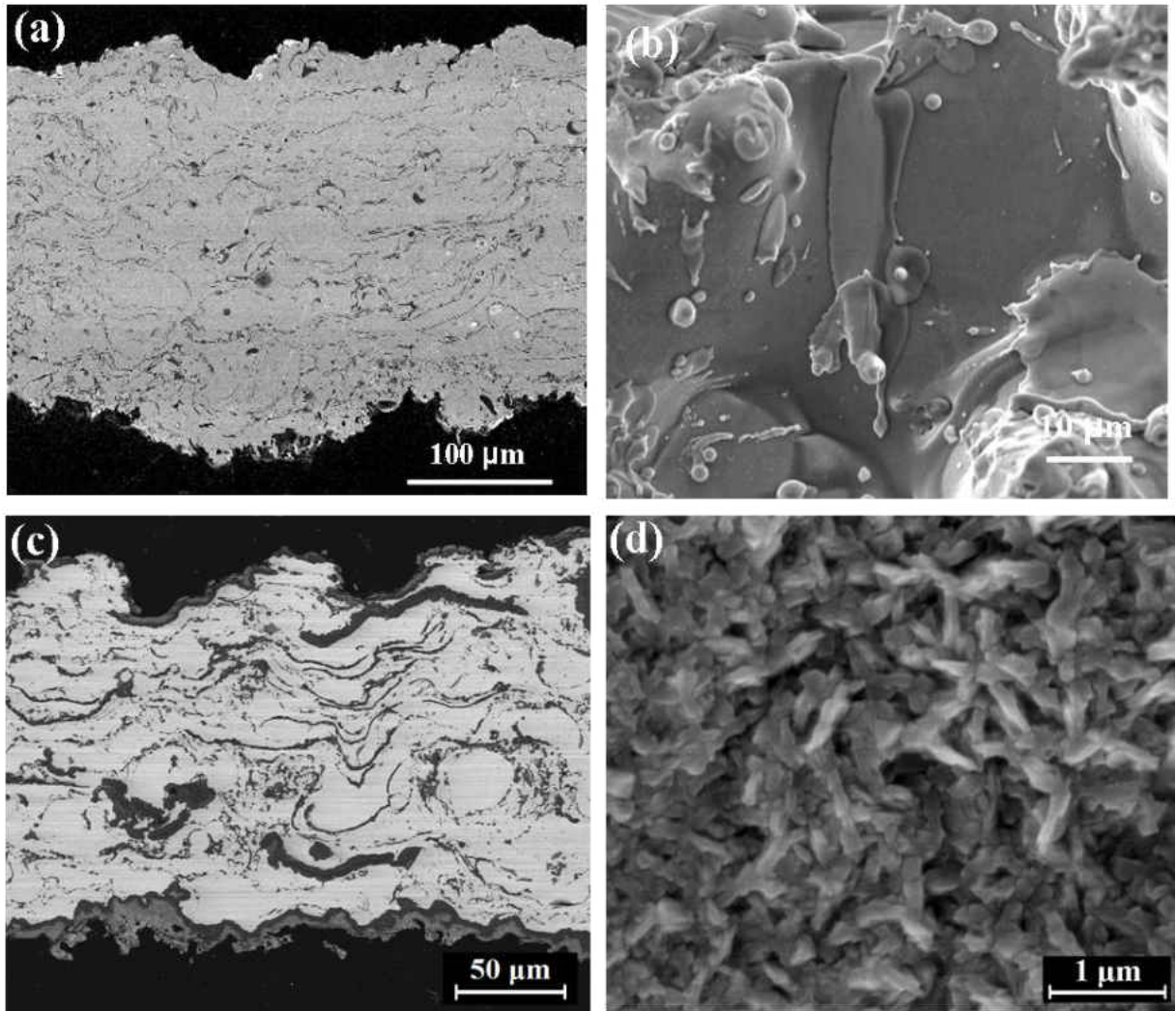


Figure 4.: (a) and (b) Secondary electron micrographs of free standing APS CoNiCrAlY coating showing the uniform cross-section and the typical surface splat microstructure; (c) cross-sectional backscattered electron micrograph presenting the microstructure of heat-treated free standing CoNiCrAlY after 20 h isothermal treatment at 1100°C and (d) secondary electron micrograph revealing the respective surface morphology of TGO scale evolved from isothermal heat-treatment.

4.2. Thermochemical Degradation of APS YSZ by Corrosive Molten Deposits

4.2.1. Vanadium Pentoxide (V_2O_5)

V_2O_5 melts at 690°C , which is a relatively low temperature compared to turbine engine operating conditions. In this investigation, degradation studies were performed at temperatures ranging from 700°C to 900°C . At 700°C , in spite of molten V_2O_5 penetration through the porous YSZ specimen, no reaction product or phase transformation was observed. However, studies at 720°C and exposures up to 2 hours revealed the YSZ reaction with molten V_2O_5 . Figure 4.4 shows the XRD patterns obtained from the YSZ specimens exposed to molten V_2O_5 at 720°C for durations of 30 minutes and 2 h. The newly evolved peaks are from the reaction product, zirconium pyrovanadate (cubic ZrV_2O_7). No significant phase transformation of the YSZ was observed from XRD analysis.

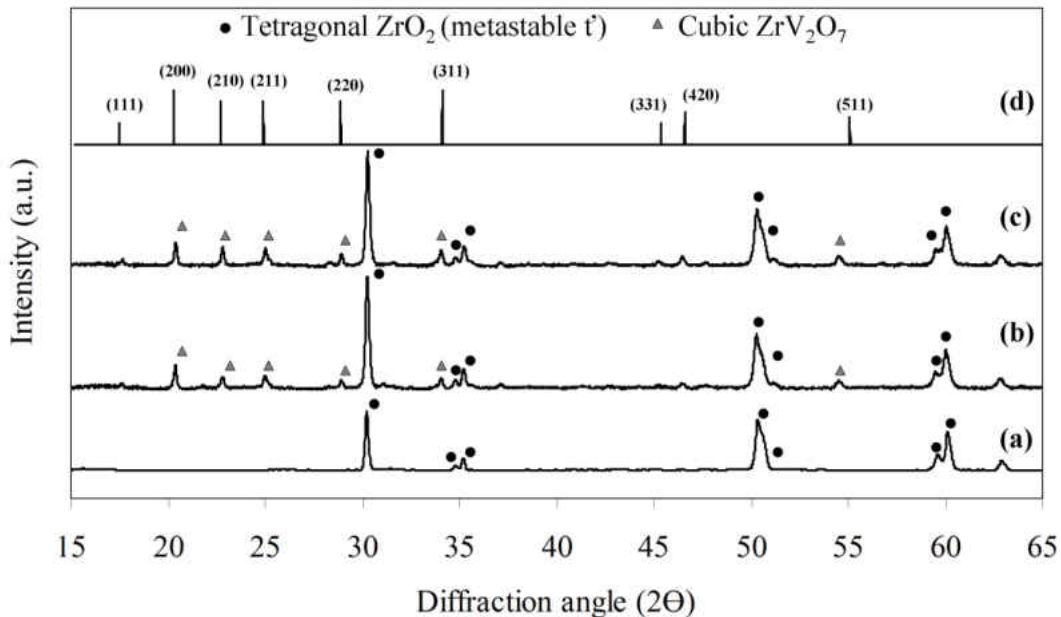


Figure 4.: XRD patterns illustrating the degradation of free-standing APS YSZ during YSZ– V_2O_5 reaction at 720°C : (a) as-sprayed; (b) 720°C for 30 minutes; (c) 720°C for 2 h and (d) ZrV_2O_7 standard.

Microstructural analysis revealed the formation of ZrV_2O_7 and infiltration by molten V_2O_5 as shown in Fig. 4.5. The respective XEDS obtained at different regions confirmed the reaction product ZrV_2O_7 (region 2) and the solidified residue of V_2O_5 (region 3) as shown in Fig. 4.5.

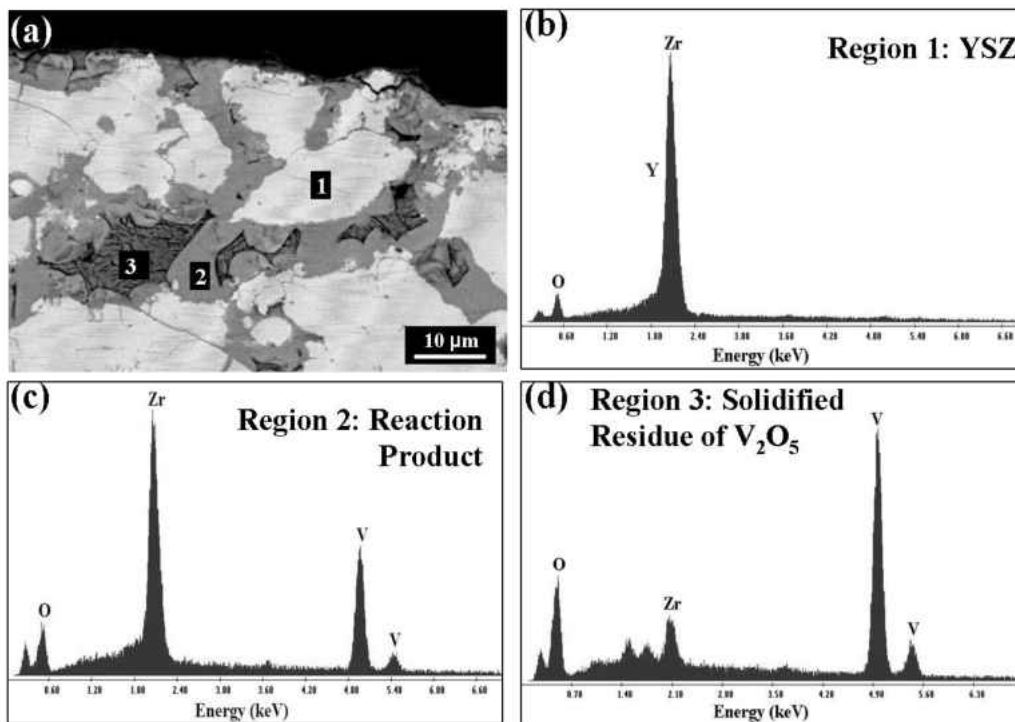


Figure 4.: (a) Cross-sectional backscattered electron micrograph of free-standing APS YSZ after reaction with V_2O_5 at 720°C for 30 minutes and the characteristic XEDS spectra showing (b) the unreacted YSZ (region 1), (c) reaction product ZrV_2O_7 (region 2) and (d) the solidified residue from molten V_2O_5 (region 3).

A thorough microstructural investigation by TEM along with selected area electron diffraction studies yielded more accurate evidence on YSZ degradation by V_2O_5 . Figure 4.6 highlights the results from the microstructural and electron diffraction studies performed by TEM on the YSZ specimen exposed to molten V_2O_5 at 720°C for 30 minutes. The bright-field TEM micrograph shown in Fig. 4.6(a) reveals the two different phases within the YSZ, which

were identified as cubic ZrV_2O_7 and tetragonal ZrO_2 based on selected area electron diffraction patterns presented in Figs. 4.6(b) & (c). It should be noted that the same thermochemical interactions and microstructural evolutions were observed in the YSZ degraded by V_2O_5 deposit at all test temperatures up to 750°C .

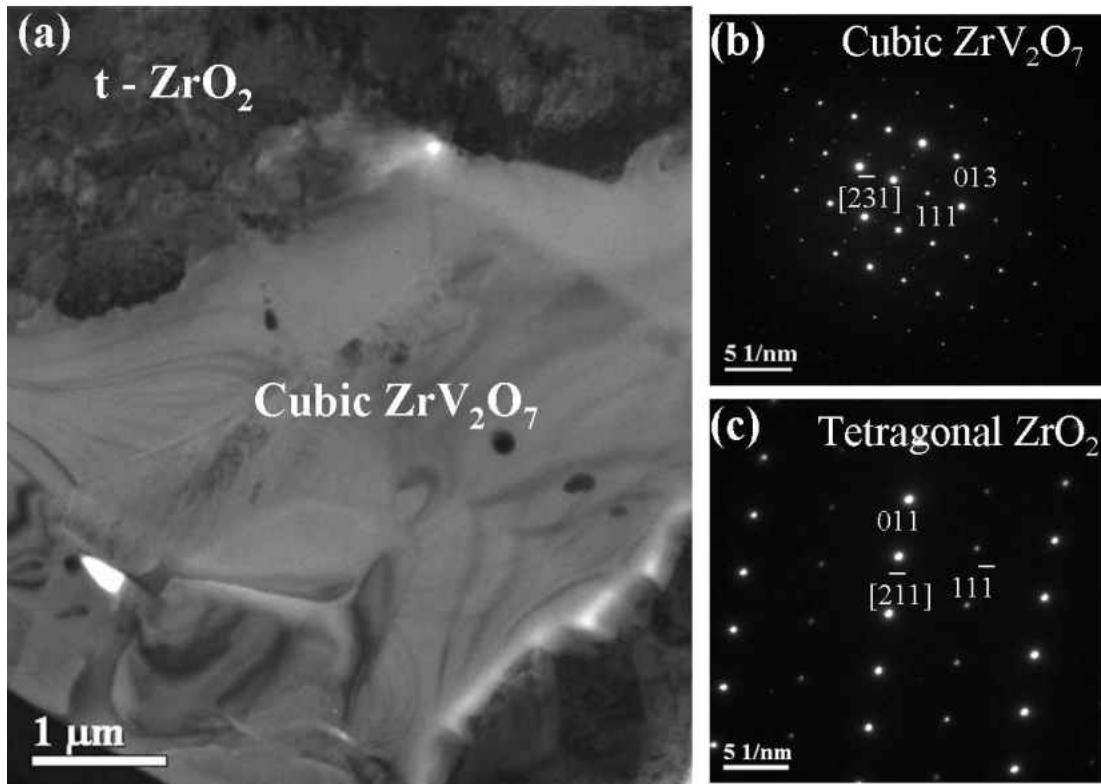


Figure 4.: (a) Bright-field TEM micrograph showing the phase constituents of the APS YSZ after reaction with V_2O_5 at 720°C for 30 minutes. Electron diffraction patterns from the two phases present are indexed as (b) cubic ZrV_2O_7 and (c) tetragonal ZrO_2 with zone axes of $[2\ 3\ 1]$ and $[2\ 1\ 1]$ respectively.

Figure 4.7 shows the XRD patterns obtained from the YSZ after hot corrosion testing with molten V_2O_5 at 800°C for 30 minutes. It is clearly visible that the reaction is completely different from the one observed at 720°C . Zirconia was predominantly found to exist as monoclinic phase after degradation by V_2O_5 at 800°C . The reaction of the V_2O_5 melt with the

yttria stabilizer of YSZ is also evident from the XRD results due to the presence of tetragonal YVO_4 . This reaction resulted in the disruptive zirconia phase transformation of tetragonal-to-monoclinic ($t \rightarrow t \rightarrow m+f$), which is in agreement with the degradation mechanism reported earlier [33-38].

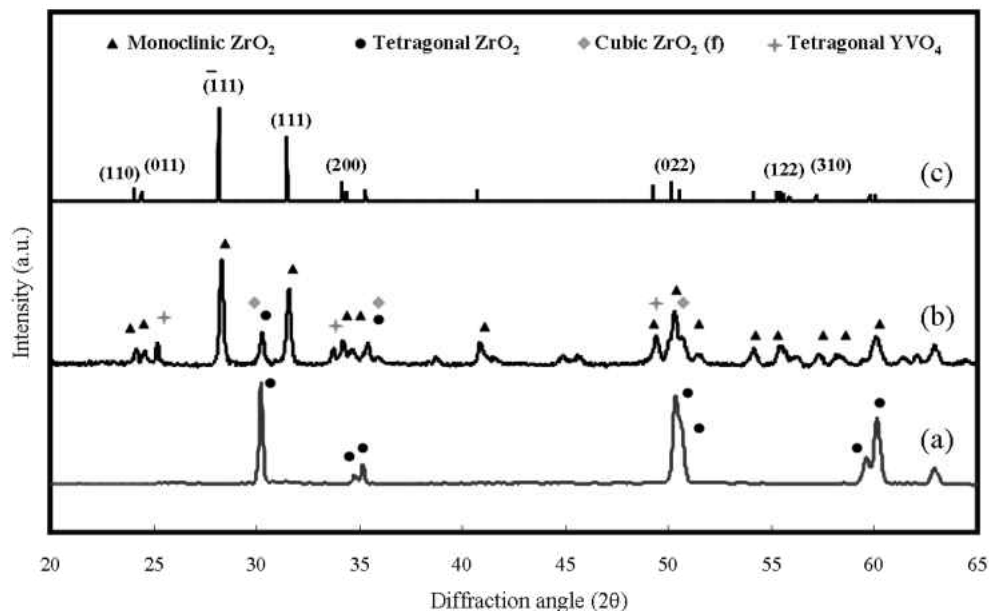


Figure 4.: XRD patterns illustrating the degradation of free-standing APS YSZ during YSZ– V_2O_5 reaction at 800°C : (a) as-sprayed; (b) 800°C for 30 minutes; (c) monoclinic ZrO_2 standard.

The cross-sectional microstructure of the YSZ specimen tested at 800°C for 30 minutes is presented in Fig. 4.8. Corresponding XEDS spectra confirmed the different regions as YSZ (region 1), the reaction product YVO_4 (region 2) and solidified V rich residue (region 3). Thermochemical degradation at 800°C was also confirmed by TEM analysis as presented in Fig. 4.9. The bright-field micrograph clearly shows the presence of the reaction compound YVO_4 . Figure 4.9 also shows the selected area electron diffraction patterns indexed for the reaction products, tetragonal YVO_4 and yttria-poor monoclinic ZrO_2 at 800°C that resulted from the

deleterious phase transformation ($t \rightarrow t \rightarrow m+f$). Above 750°C, formation of YVO_4 and the corresponding YSZ phase transformation to $m\text{-ZrO}_2$ was the only degradation mechanism observed. Figure 4.10 shows the XRD results obtained from samples infiltrated by molten V_2O_5 at 750°C for exposure periods of 5 min to 2 h. A progressive formation of $m\text{-ZrO}_2$ phase is clearly presented.

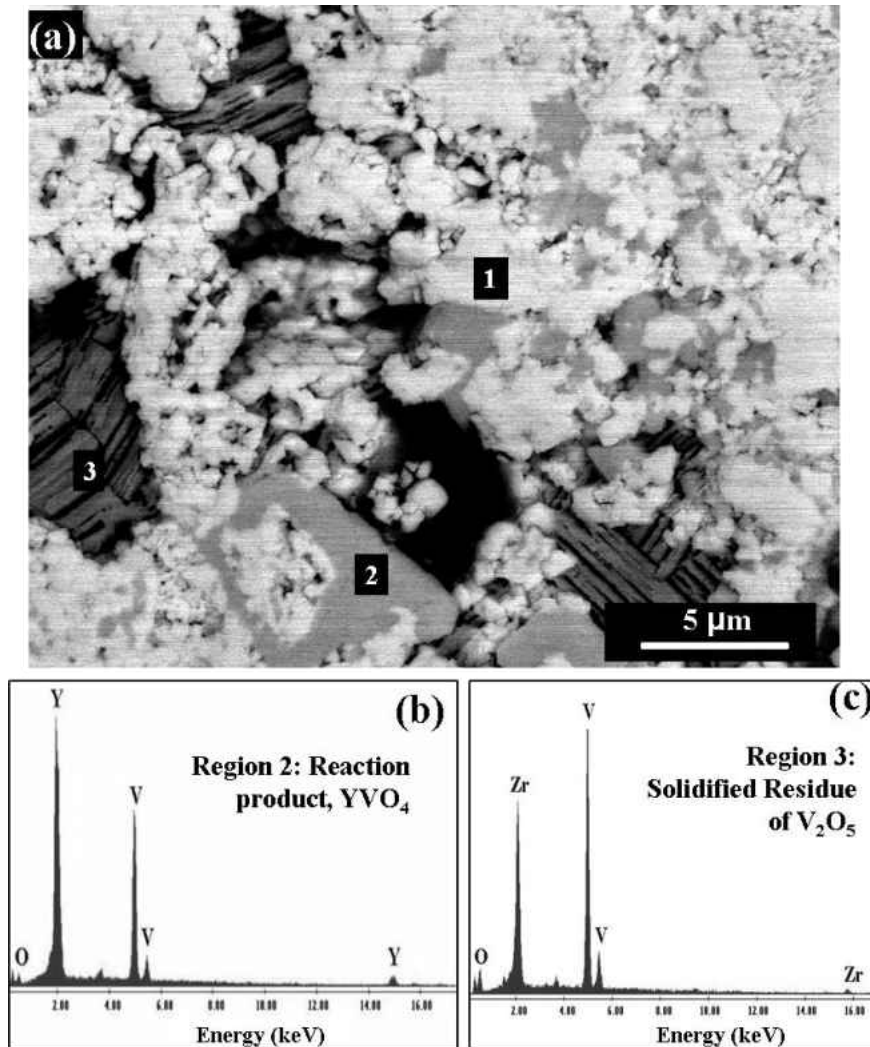


Figure 4.: (a) Cross-sectional backscattered electron micrograph of free-standing APS YSZ after reaction with V_2O_5 at 800°C for 30 minutes and (b) and (c) characteristic XEDS spectra, showing the regions 1, 2 and 3 as unreacted YSZ, reaction product YVO_4 , and the solidified residue from molten V_2O_5 respectively.

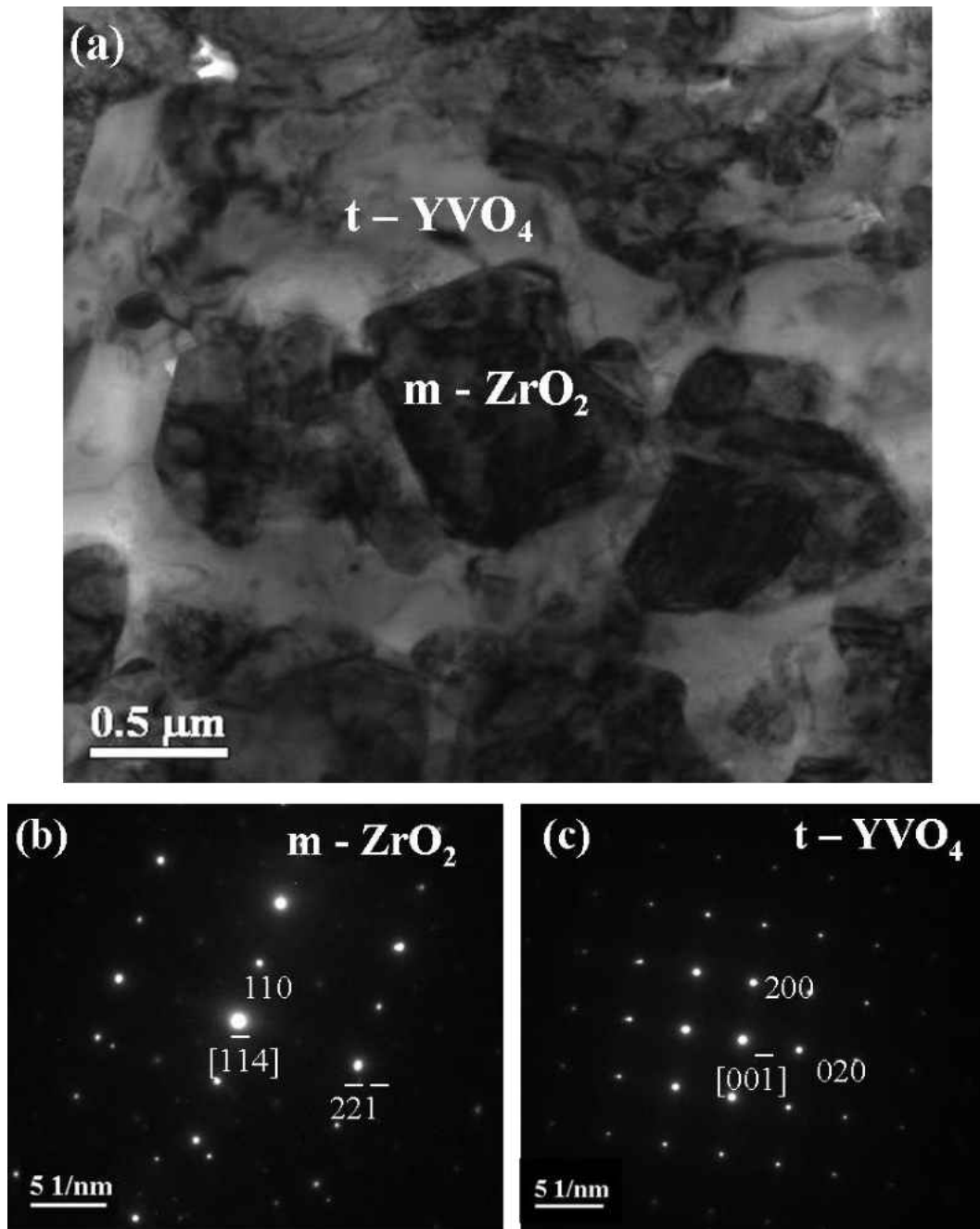


Figure 4.: (a) Bright-field TEM micrograph from the APS YSZ after reaction with V₂O₅ at 800°C for 30 minutes. Electron diffraction patterns from the two phases present are indexed as (b) monoclinic ZrO₂ with a zone axis of $[1\ 1\ 4]$ and (c) tetragonal YVO₄ with a zone axis of $[001]$.

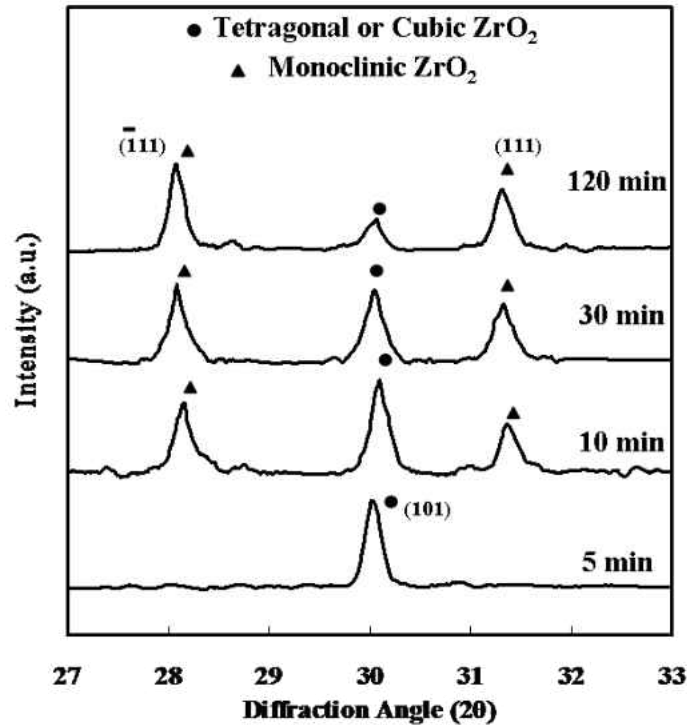


Figure 4.: XRD patterns obtained from the APS YSZ specimens after interaction with V_2O_5 melt at $750^\circ C$ for various test durations.

4.2.2. Phosphorus Pentoxide (P_2O_5)

Degradation of APS YSZ by P_2O_5 was examined with an emphasis at lower temperatures ranging from $200^\circ C$ to $500^\circ C$, because of the thermal instability of P_2O_5 at elevated temperature. XRD results after the reaction at $350^\circ C$ for 1 h and $450^\circ C$ for 1 h are presented in Fig. 4.11. The only reaction product found was zirconium pyrophosphate (cubic ZrP_2O_7). A magnified view of the shaded region in Fig. 4.11 is also presented as Fig. 4.12. Due to interaction of the YSZ with P_2O_5 melt, the two adjacent Bragg reflections from planes (103) and (211) of tetragonal zirconia transition to one single peak that corresponds to (311) of fluorite-cubic phase. Thus phase

transformation of t'-ZrO₂ to yttria-rich fluorite cubic zirconia (f-ZrO₂) is evident, which could be attributed to the formation of ZrP₂O₇ during YSZ-P₂O₅ interaction.

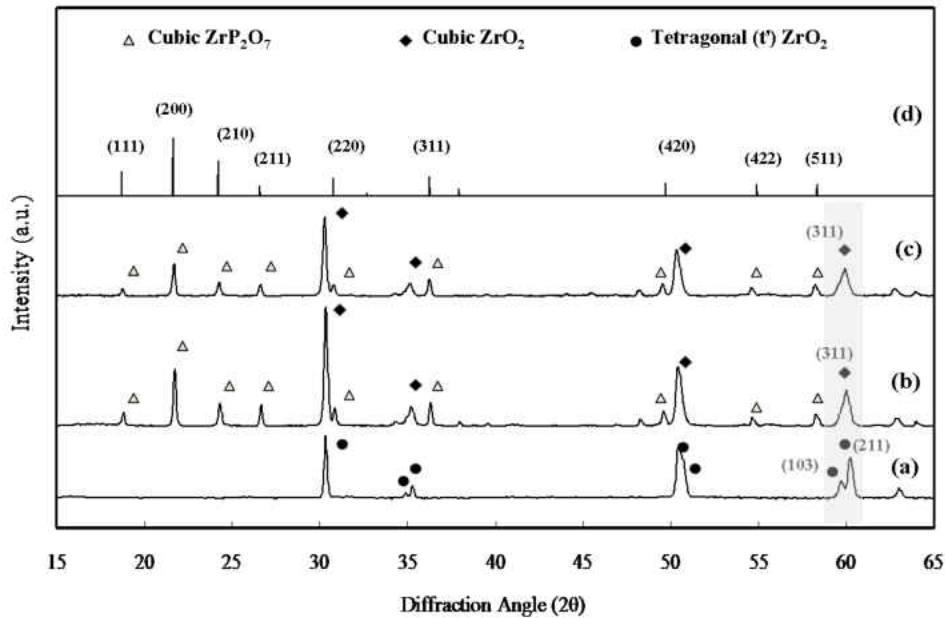


Figure 4.: XRD patterns illustrating the degradation of the APS YSZ during YSZ-P₂O₅ reaction: (a) as-sprayed; (b) 350°C for 1 h; (c) 450°C for 1 h; (d) cubic ZrP₂O₇ standard.

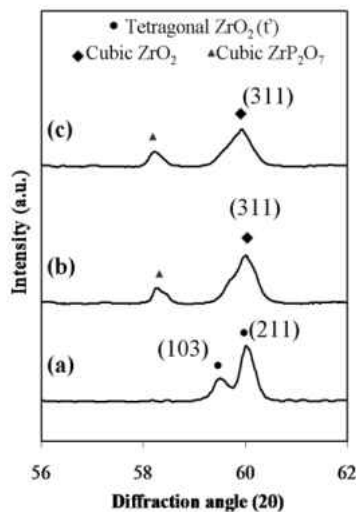


Figure 4.: A magnified view of the XRD patterns in the 2θ range, $56 < 2\theta < 62$, illustrating the degradation of free-standing APS YSZ during YSZ-P₂O₅ reaction: (a) as-sprayed; (b) 350°C for 1 h; and (c) 450°C for 1 h.

Figure 4.13 shows the cross-sectional backscattered electron micrograph of the APS YSZ specimen infiltrated by molten P_2O_5 at $350^\circ C$ for 1 h. ZrP_2O_7 is the only reaction product. Unlike the reaction product ZrV_2O_7 from the YSZ– V_2O_5 interaction, zirconium pyrophosphate (ZrP_2O_7) was found to be stable for all temperatures up to $1200^\circ C$. Thus molten P_2O_5 that readily reacted with the YSZ promoted the formation of yttria-rich cubic zirconia phases (f- ZrO_2) due to the enrichment in Y_2O_3 content in the YSZ. It should be noted that for all test temperatures in this study (up to $1200^\circ C$), formation of ZrP_2O_7 along with ZrO_2 phase transformation to f- ZrO_2 was the only degradation reaction observed. Due to the fact that P_2O_5 vaporized readily at elevated temperatures, clear microstructural evidence of degradation was difficult to document, even though at $T > 1000^\circ C$, spontaneous degradation of YSZ through similar reactions during rapid heating, while in contact with P_2O_5 , was observed. XRD patterns illustrating the ZrP_2O_7 formation at elevated temperatures (up to $1200^\circ C$) are also presented in Fig. 4.14. At such elevated temperatures, the P_2O_5 interaction was limited to the surface of the YSZ specimen due to the rapid vaporization of the contaminant. Thus, the microstructural evolution shown here for temperatures below $500^\circ C$ as presented by the XRD and SEM results demonstrates the most effective degradation of YSZ by P_2O_5 .

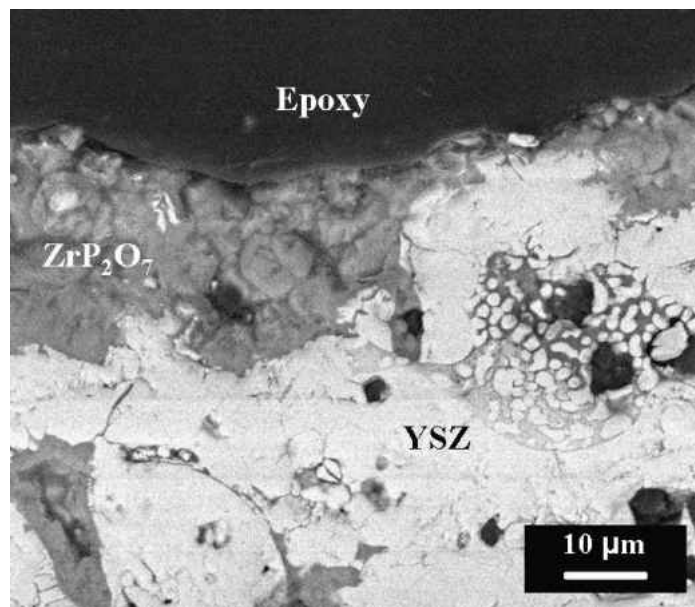


Figure 4.: Cross-sectional backscattered electron micrograph of APS YSZ after reaction with molten P_2O_5 at $350^\circ C$ for 1 hour showing the reaction product ZrP_2O_7 .

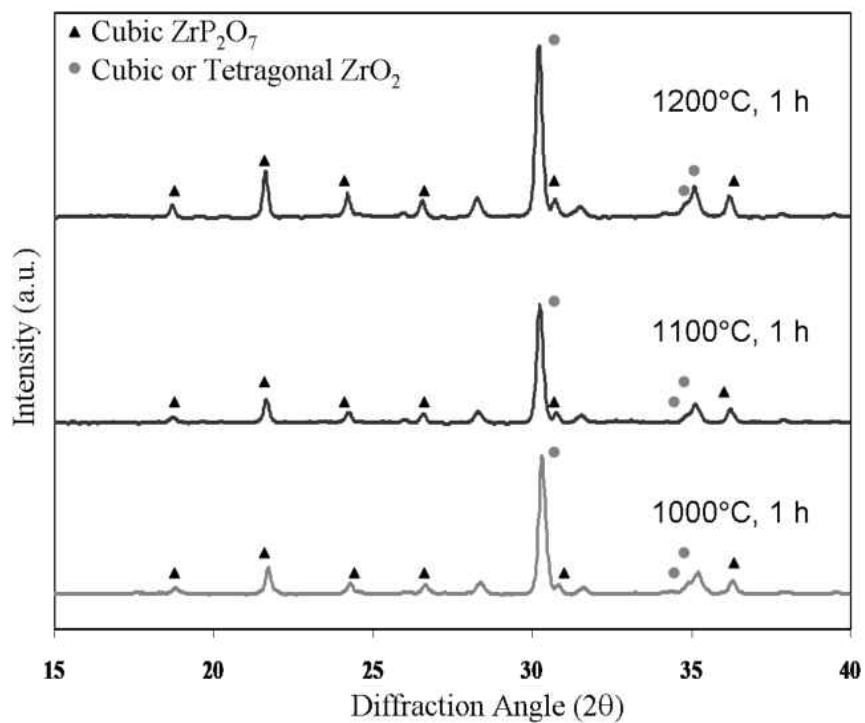


Figure 4.: XRD patterns illustrating the degradation of APS YSZ during $YSZ-P_2O_5$ reaction at elevated temperatures up to $1200^\circ C$.

4.2.3. Sodium Sulfate (Na_2SO_4)

YSZ specimens were tested for degradation by molten sodium sulfate at a temperature range of 900°C to 1200°C . Na_2SO_4 melts at 884°C . XRD results obtained from samples studied at 900°C for 1 h and 1000°C for 5 h revealed the presence of t' - ZrO_2 with no evidence of significant phase transformation or reaction between the YSZ and Na_2SO_4 . However, unlike other corrosive deposits, Na_2SO_4 was found to interact with the YSZ only after a long-term exposure, when tested in an enclosed quartz capsule in order to maintain a molten salt film throughout the testing. XRD results presented in Fig. 4.15 clearly show the presence of unreacted Na_2SO_4 at the YSZ surface even after 20 h of hot corrosion testing at 950°C . However, after exposure of 50 h at 1000°C , minimal evolution of monoclinic zirconia was observed as seen in Fig. 4.15.

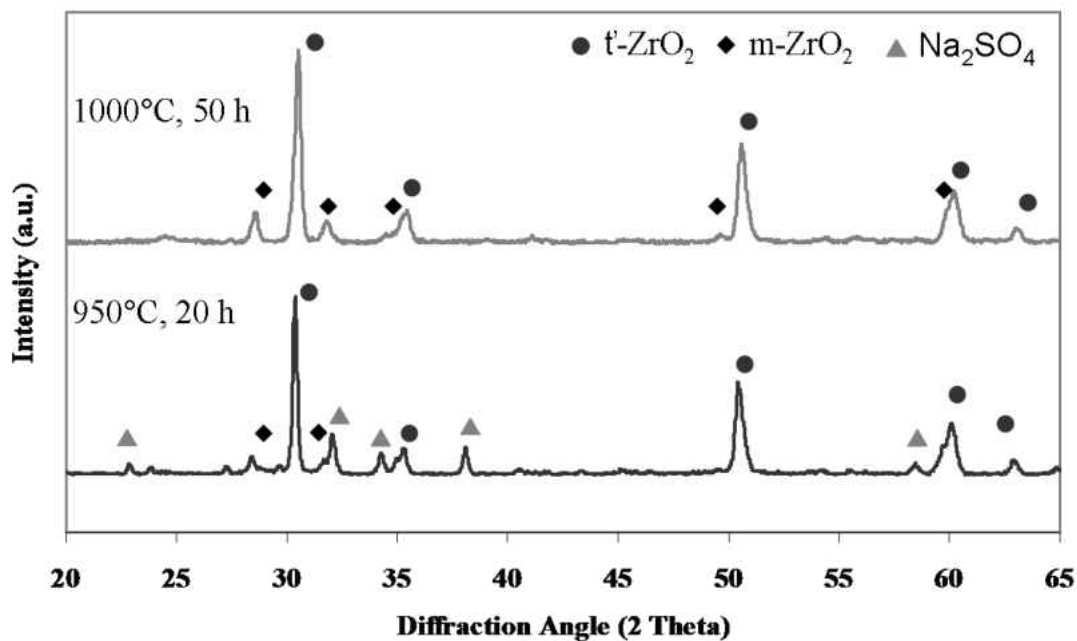


Figure 4.: XRD patterns obtained from YSZ after testing with Na_2SO_4 deposit for various durations at 950°C and 1000°C .

Due to the fact that YSZ- Na_2SO_4 interaction was only minimal and slow, documenting the evidence of any reaction product was not possible. Evolution of m- ZrO_2 after hot corrosion testing with Na_2SO_4 could be attributed to the expected interaction of yttria stabilizer with acidic SO_3 in Na_2SO_4 melt [12]. Minor presence of m- ZrO_2 phase after 50 h of testing demonstrates the minimal thermochemical degradation of YSZ by Na_2SO_4 melt. Microstructural evidence as seen in the cross-sectional backscattered electron micrographs in Fig. 4.16 also indicated that the molten Na_2SO_4 infiltrated through the open pores and interlamellar gaps of the APS YSZ with no obvious evidence of a reaction product. Molten salt was found to have crystallized out in the cracks and pores of the coating which may eventually lead to thermomechanical damage.

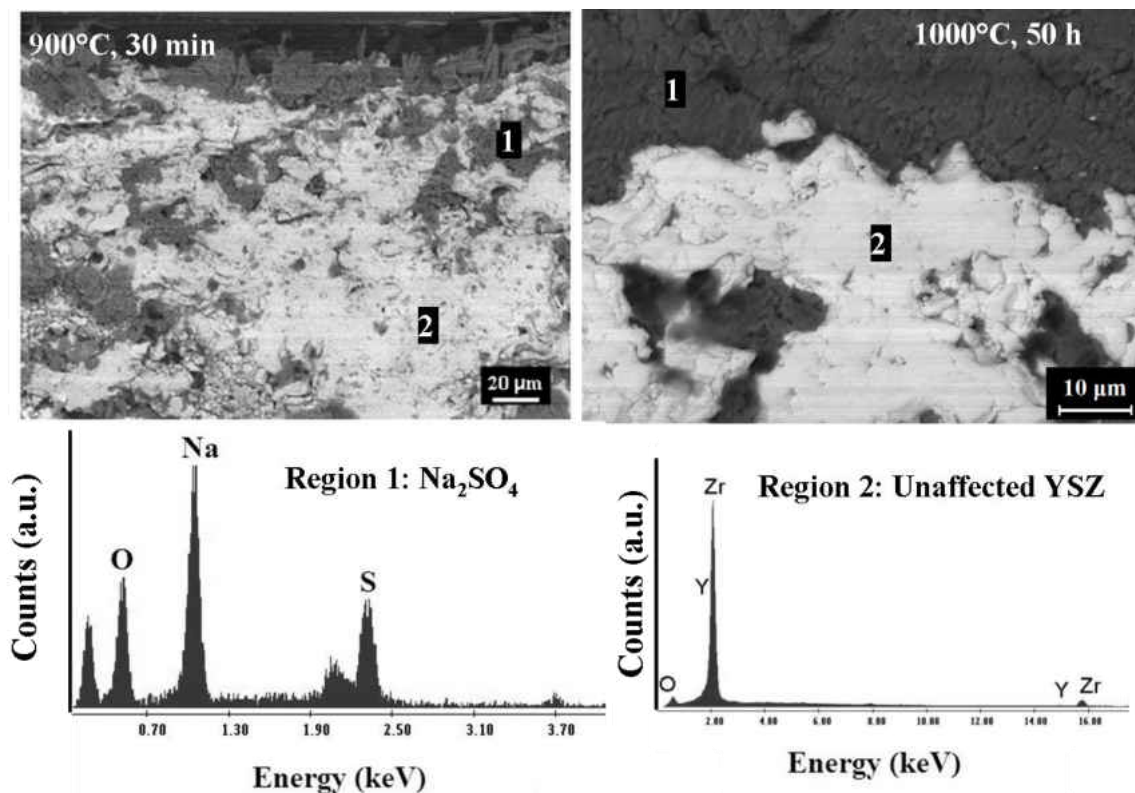


Figure 4.: Cross-sectional backscattered electron micrographs showing the inert nature of YSZ after hot-corrosion testing with Na_2SO_4 deposit and the corresponding XEDS spectra from regions of interest.

4.2.4. Na₂SO₄+V₂O₅ Mixture

Vanadates of sodium that are most likely to form during the presence of both V₂O₅ and Na₂SO₄ were also investigated in this study. An equilibrium phase diagram of Na₂SO₄-V₂O₅ system as presented in Chapter 3 (Fig. 3.4), shows the various vanadates of sodium in the binary system. One of the commonly forming vanadates of sodium, NaVO₃ (sodium metavanadate) with a low melting point of 610°C has been considered as a potential corrosive specie that could arise from low-quality fuel. A Na₂SO₄ + V₂O₅ mixture having a composition of 50 – 50 mol.% that was molten and air-quenched resulted in a mixture of the vanadates of sodium. The XRD pattern collected from the mixture shown in Fig. 4.17 reveals the major presence of NaVO₃ (T_m: 610°C) and NaV₃O₈ (T_m: 548°C).

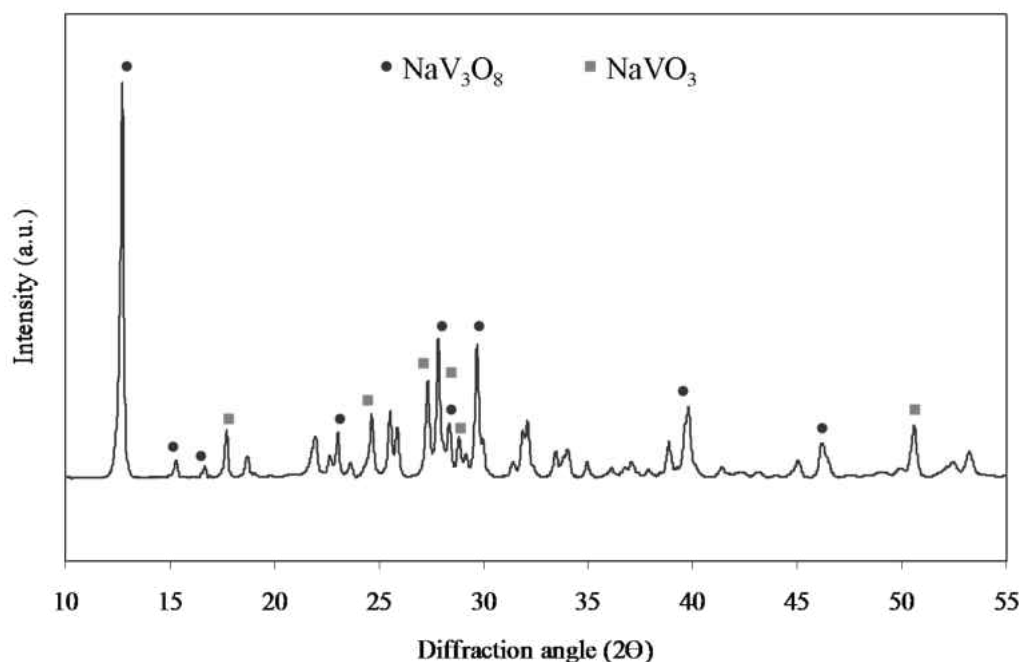


Figure 4.: XRD pattern obtained from quenched Na₂SO₄+V₂O₅ (50-50 mol.%) mixture confirming the presence of vanadates of sodium.

An eutectic mixture of these sodium vanadates can have a melting temperature as low as 500°C [127]. Thus, presence of Na₂SO₄ along with V₂O₅ has been considered as a critical threat. XRD results from the YSZ after interaction with molten Na₂SO₄+V₂O₅ mixture at 700°C for 1 h is shown in Fig. 4.18. The yttria depletion reaction with the formation of monoclinic ZrO₂ (similar to the degradation mechanism observed in YSZ–V₂O₅ interaction) was observed.

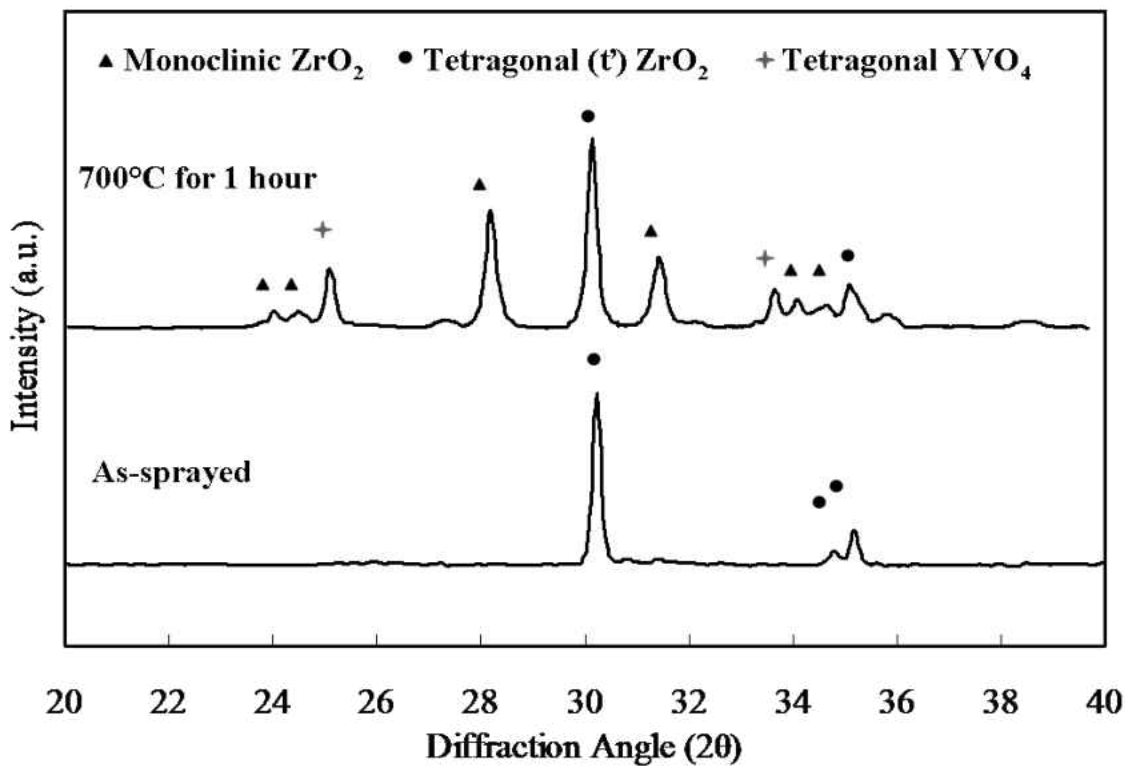


Figure 4.: XRD patterns illustrating the degradation of free-standing APS YSZ during YSZ–Na₂SO₄+V₂O₅ mixture reaction at 700°C for 1 hour due to the formation of YVO₄.

The surface morphology of the YSZ coating after degradation by molten sodium vanadate mixture at 720°C for 1 h is presented in Fig. 4.19. YVO₄ crystals (region 1) as thin plate-like structures varying in sizes up to 15 μm long are found to be embedded on the coating

surface. The various sizes of nucleated and grown YVO_4 crystals are also visible from surface morphology. The YSZ remnant and the applied corrosive mixture are marked as regions 2 and 3 respectively. A significant degradation through formation of YVO_4 that resulted in phase transformation of $t\text{-ZrO}_2$ to $m\text{-ZrO}_2$ was the only mechanism observed for all tested temperatures up to 900°C .

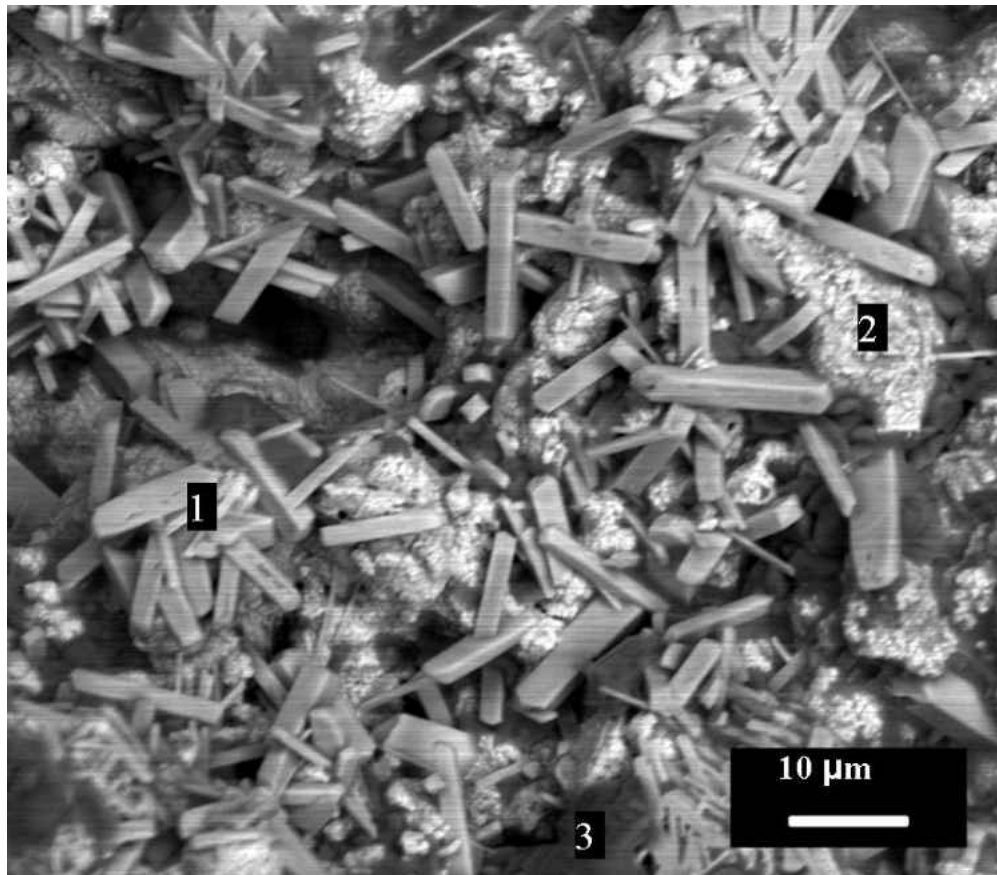


Figure 4.: Backscattered electron micrograph showing the development of surface morphology of free-standing APS YSZ due to interaction with $\text{Na}_2\text{SO}_4 + \text{V}_2\text{O}_5$ mixture at 720°C for 1 hour. Region 1: YVO_4 (reaction product), Region 2: YSZ and Region 3: Applied sodium vanadate mixture.

4.3. Thermochemical Degradation of APS YSZ by Molten CMAS Deposit

The interaction between the YSZ and the CMAS deposit was observed to occur only for elevated temperatures starting at 1250°C, where, CMAS was found to completely melt and infiltrate the YSZ coating specimen. Cross-sectional microstructural analysis of CMAS tested YSZ specimens revealed a microstructure similar for all samples that suffered CMAS attack at temperatures above 1250°C for all durations studied in this work (2 - 4 hours). Cross-sectional backscattered electron micrographs of the YSZ specimen subjected to molten CMAS infiltration at 1250°C for 4 h are presented in Fig. 4.20. The CMAS melt readily infiltrated the 300 µm thick free-standing YSZ. The solidified CMAS islands were observed near the top and bottom surfaces of the YSZ coating. It should be noted that the CMAS melt infiltration is complete in isothermal exposures; however it will vary in a real engine operation dictated by viscosity of the melt and thermal gradient across TBCs.

Morphological changes in the YSZ after infiltration by CMAS at 1300°C for 4 h are presented in the backscattered electron micrographs shown in Fig. 4.21. A typical microstructure consisting of solidified CMAS islands and the bulk YSZ is illustrated in Fig. 4.21(a). Due to the thermochemical interactions between the CMAS and YSZ, the evolution of spherical ZrO₂ grains reprecipitated from the CMAS melt, are evident from cross-section and surface micrographs presented in Figs. 4.21 (b) and (c). Backscattered electron micrograph from the YSZ surface in Fig. 4.21(c) also reveals the presence of spherical ZrO₂ grains varying in size. Qualitative information on the elemental concentration can be seen from the respective XEDS spectra collected from solidified CMAS and the unaffected bulk YSZ as shown in Fig. 4.21(d).

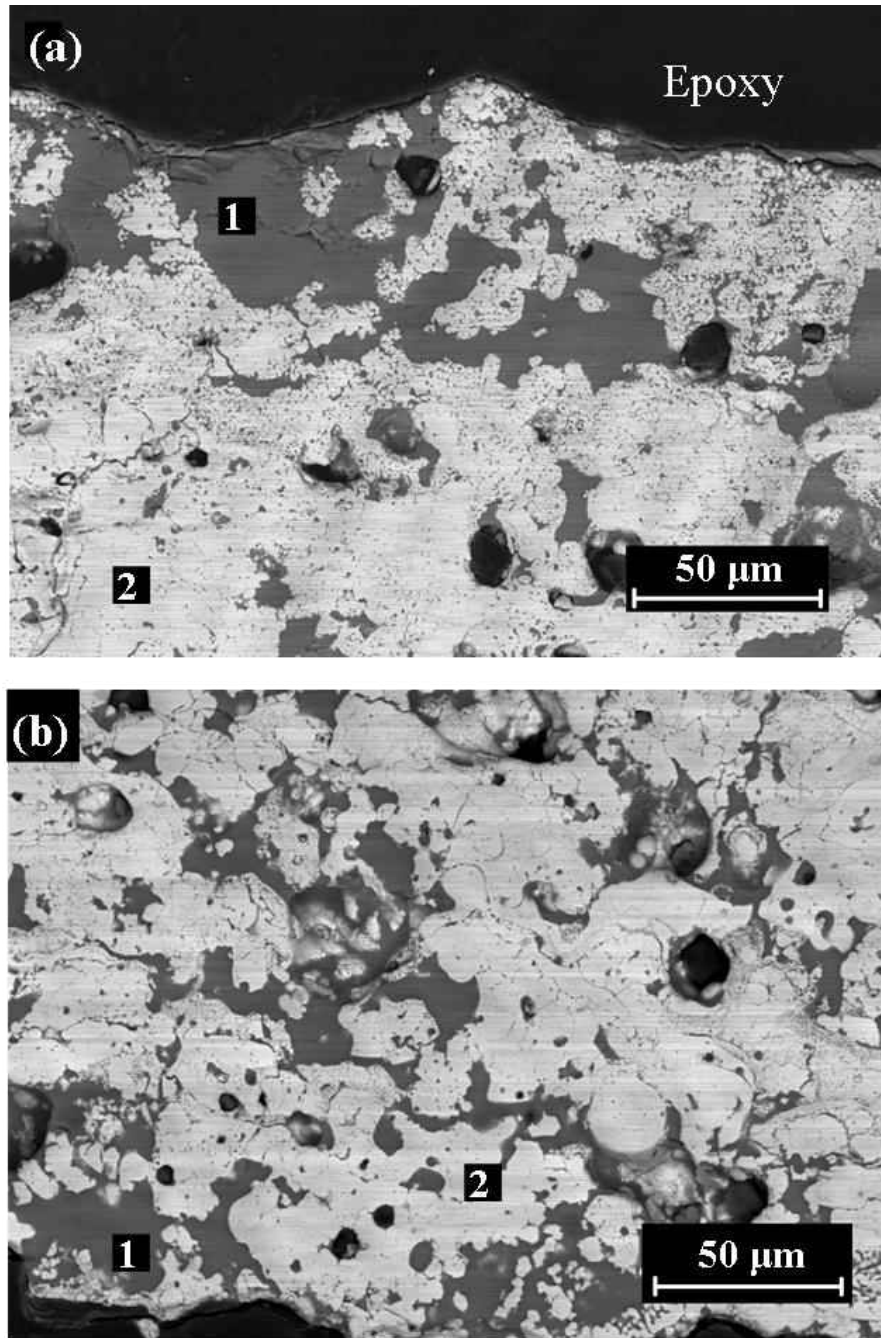


Figure 4.: Cross-sectional backscattered electron micrographs near the (a) top and (b) bottom surfaces of the APS YSZ coating subjected to molten CMAS infiltration at 1250°C for 4 h. Regions 1 and 2 correspond to solidified CMAS and bulk YSZ.

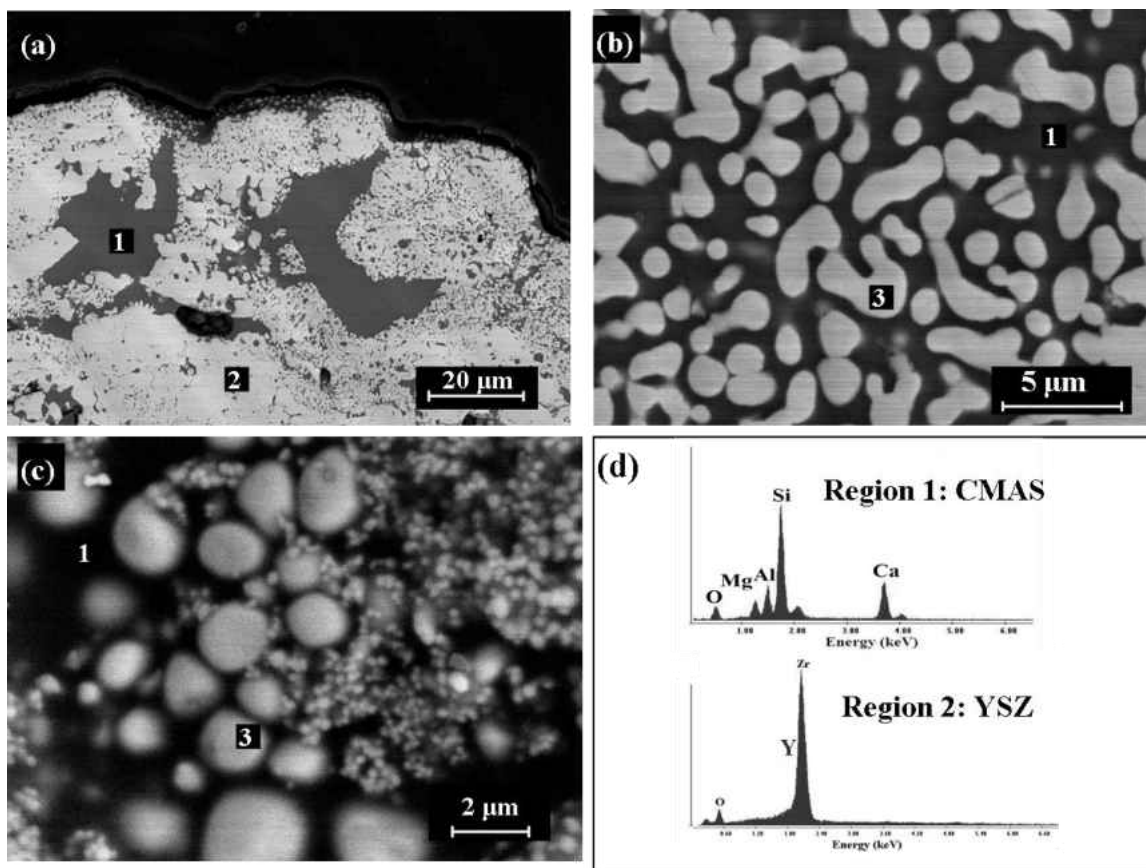


Figure 4.: Backscattered electron micrographs obtained from the YSZ coating infiltrated by molten CMAS at 1300°C for 4 h. (a) and (b) Cross-sections at low and high magnifications respectively. (c) Micrograph of surface morphology showing the CMAS infiltrated coating with coarse and fine reprecipitated ZrO_2 grains from CMAS melt. (d) Characteristic XEDS spectra from solidified CMAS and bulk YSZ. Regions 1, 2 and 3 correspond to solidified CMAS, bulk YSZ and reprecipitated ZrO_2 respectively.

XRD patterns obtained from the CMAS infiltrated APS YSZ (1300°C for 4h) specimens are presented in Fig. 4.22. Similar XRD patterns were obtained for all specimens when CMAS infiltration had occurred. The disruptive phase transformation of metastable tetragonal zirconia (t' - ZrO_2) to monoclinic zirconia ($t' \rightarrow t \rightarrow m+f$) was observed. In addition to the presence of m - ZrO_2 phase on both the top (YSZ surface exposed to CMAS) and bottom surfaces of the YSZ after

CMAS infiltration, phase transformation of t' -ZrO₂ to fluorite cubic (f) ZrO₂ on the bottom surface of the YSZ was also observed from XRD patterns.

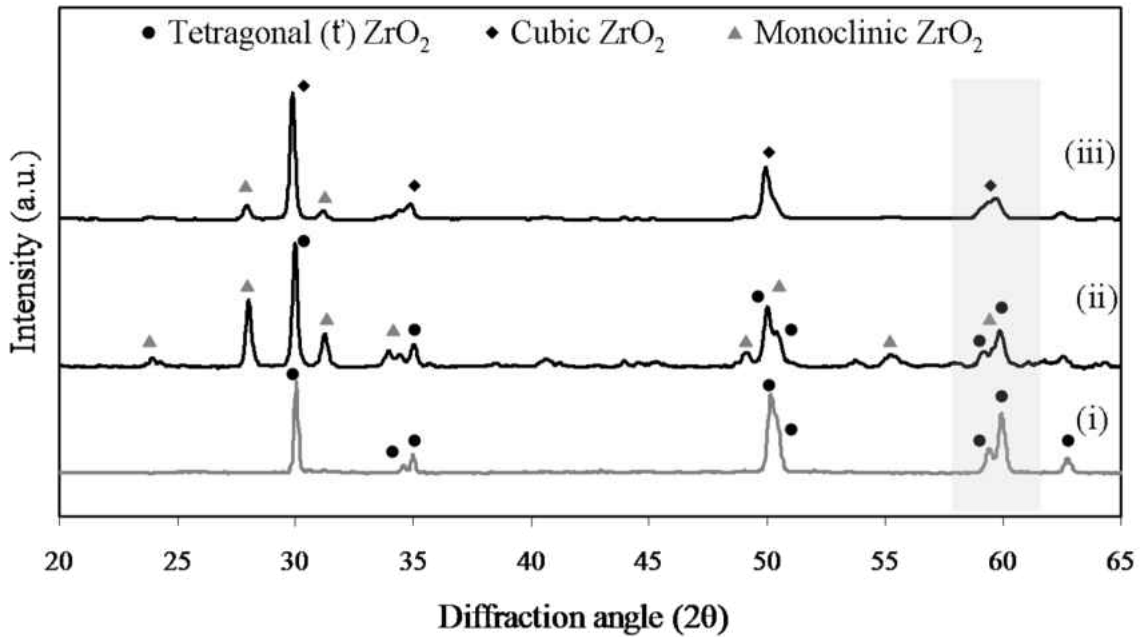


Figure 4.:X-ray diffraction patterns illustrating the phase transformation of YSZ due to CMAS infiltration: (a) Collected patterns from (i) as sprayed YSZ coating – top surface, (ii) Top surface and (iii) bottom surface of the YSZ infiltrated by molten CMAS at 1300°C for 4 h.

It should be noted that a significant phase transformation to monoclinic zirconia phase was only observed on the top surface, where the phase transformation to yttria rich f-ZrO₂ seems to dominate the CMAS interaction mechanisms in the bottom YSZ surface. A magnified view of the XRD patterns collected at a narrow 2θ range of 57° to 62° are presented in Fig. 4.23. Near the bottom surface of the YSZ after CMAS interaction, the two adjacent Bragg reflections from planes (103) and (211) of tetragonal zirconia transition to a single peak that corresponds to the reflection from (311) plane of cubic ZrO₂. It should be noted that even though the top YSZ surface was directly exposed to CMAS melt and suffered the disruptive phase transformation to

m-ZrO₂, presence of t'-ZrO₂ at a significant level is observed from the peak-doublet as seen in Fig. 4.23.

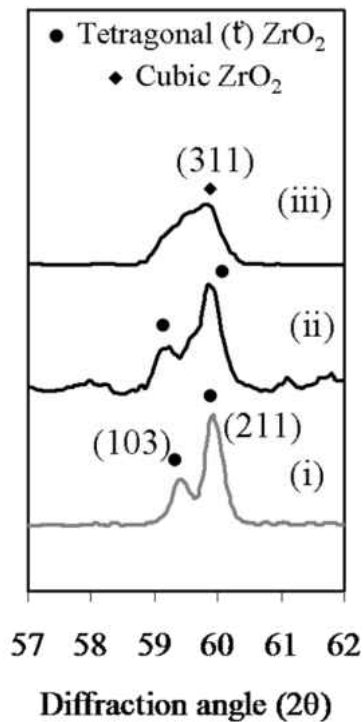


Figure 4.: Magnified representation of the XRD pattern at a narrow 2θ range of 57° to 62° collected from (i) as sprayed YSZ coating – top surface, (ii) Top surface and (iii) bottom surface of the YSZ after infiltration by molten CMAS at 1300°C for 4 h.

In order to examine the CMAS interaction with YSZ in detail, investigations by TEM, STEM and SAED (selected area electron diffraction) were thoroughly carried out on CMAS degraded YSZ sample prepared by FIB-INLO technique from regions of interest. Bright field TEM micrographs obtained from the YSZ specimen subjected to molten CMAS attack at 1350°C for 2 h are presented in Figs. 4.24 & 4.25. Both metastable tetragonal zirconia (t'-ZrO₂) and monoclinic zirconia (m-ZrO₂) were present in the CMAS infiltrated specimens. This is consistent with the XRD results. The electron diffraction patterns obtained from the three primary regions

were indexed as t' -ZrO₂ with a zone axis of [113], m-ZrO₂ with a zone axis of [302] and the completely amorphous CMAS glass. Analysis was also performed by XEDS equipped with both TEM and SEM to confirm the CMAS dissolution of YSZ during high-temperature degradation.

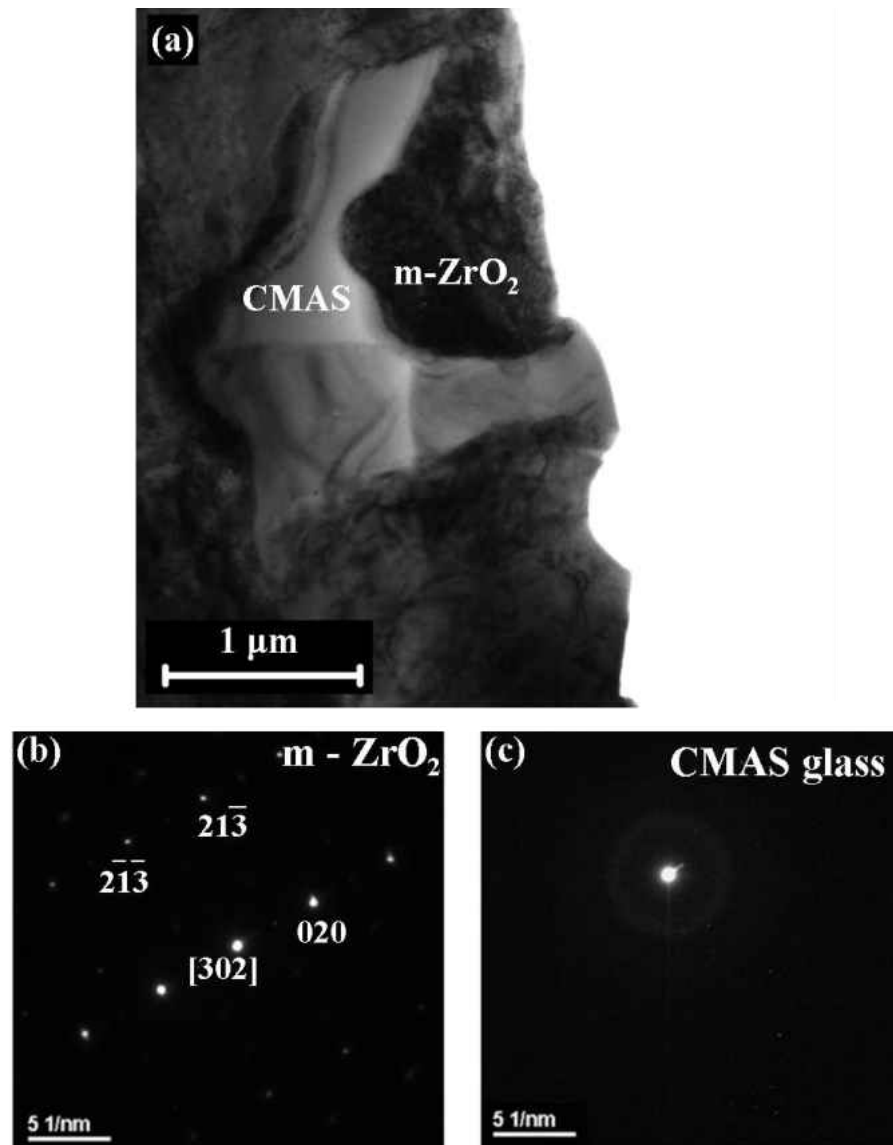


Figure 4.: (a) Bright-field TEM micrograph obtained from the APS YSZ coating subjected to molten CMAS attack at 1350°C for 2 h. The corresponding electron diffraction patterns obtained from the phases present, which are indexed as (b) monoclinic ZrO₂ and (c) amorphous CMAS glass.

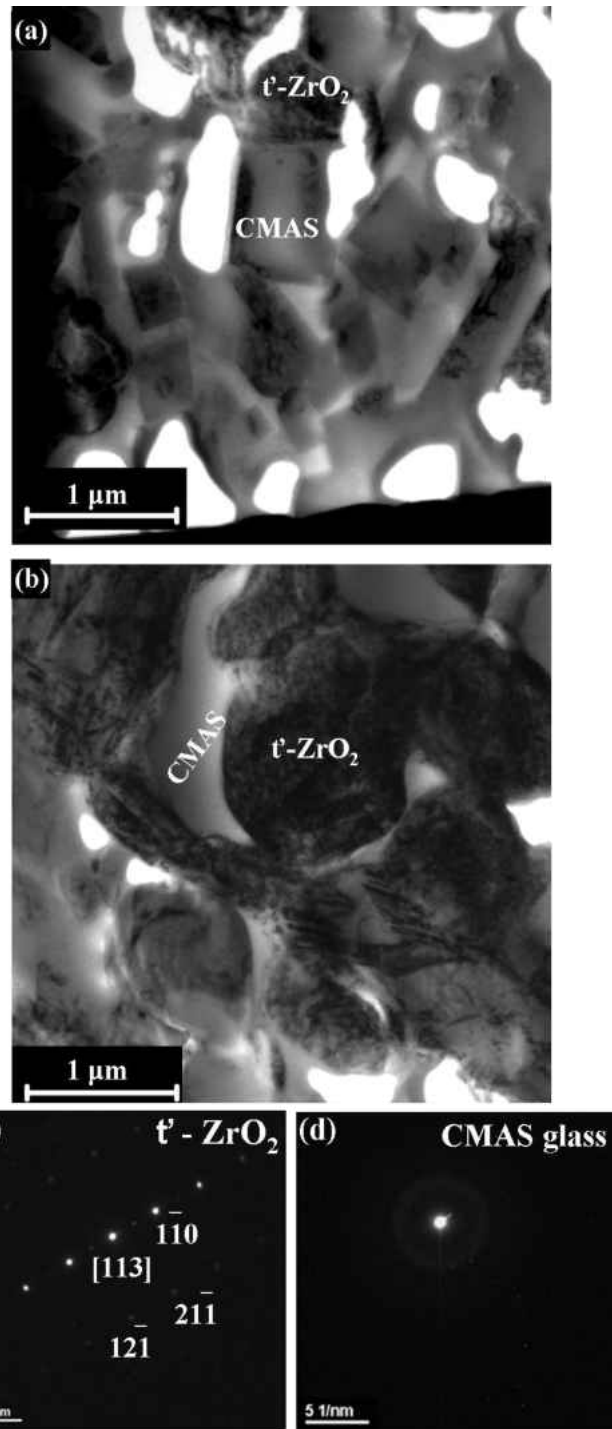


Figure 4.: (a) and (b) Bright-field TEM micrographs obtained from the APS YSZ after exposure to molten CMAS at 1350°C for 2 h showing significant presence of remaining t' -ZrO₂ in unaffected YSZ. (c) and (d) Corresponding electron diffraction patterns from t' -ZrO₂ and amorphous CMAS glass.

4.4. Thermochemical Degradation of APS CoNiCrAlY by Corrosive Molten Deposits

4.4.1. Vanadium Pentoxide (V_2O_5)

In this investigation, the interactions of V_2O_5 melt with pre-oxidized CoNiCrAlY bond coats were examined at 700°C and 900°C for a duration of 2 h. Figure 4.26 presents the XRD pattern obtained from pre-oxidized CoNiCoCrAlY coating subjected to the V_2O_5 melt at 700°C for 2 h, and identifies the reaction product as a substitutional Ni solid solution (fcc) and chromium-aluminum orthovanadate, $(Cr,Al)VO_4$. The presence of unreacted V_2O_5 after testing on the specimen surface was also observed by XRD. Moreover, the presence of unreacted V_2O_5 and appreciable XRD peaks from the γ -Ni solid solution reveals the minimal thermochemical degradation by V_2O_5 at 700°C.

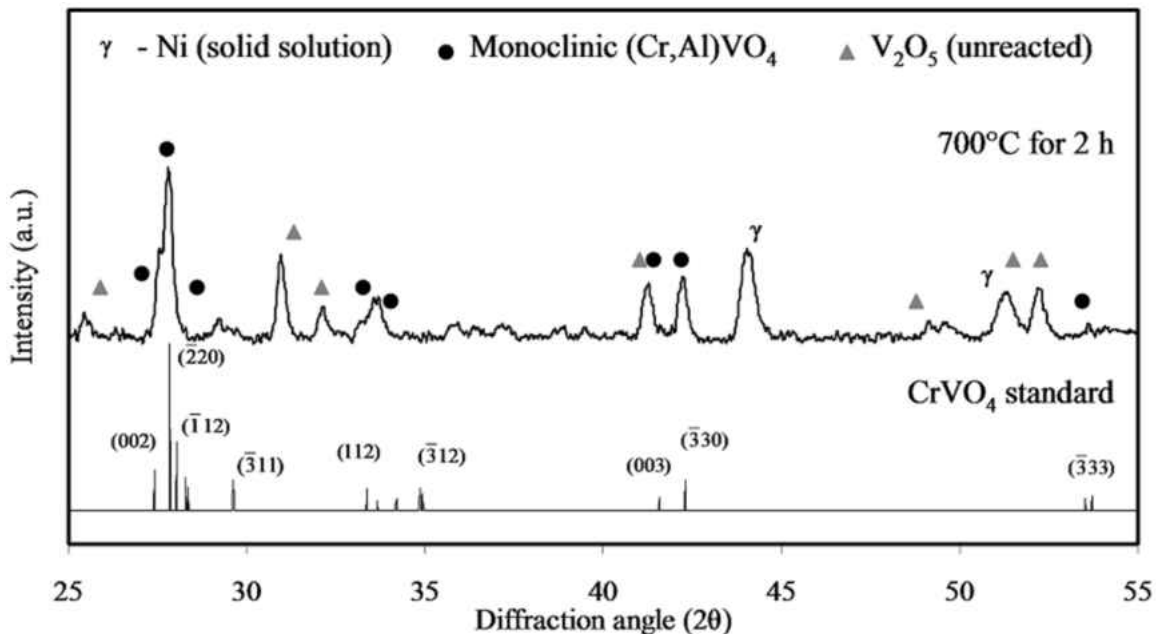


Figure 4.: XRD pattern from V_2O_5 degraded CoNiCrAlY surface revealing monoclinic $(Cr,Al)VO_4$ as the primary phase constituent evolved during thermochemical interaction between APS CoNiCrAlY and molten V_2O_5 after 2 h at 700°C.

The surface morphology and microstructural evolution due to the interactions of the APS CoNiCrAlY and the V₂O₅ melt are illustrated by secondary electron micrographs in Figs. 4.27(a) and (b). Based on the Al/Cr ratio determined by XEDS, (Cr,Al)VO₄ was found in two different morphologies; as thin large platelets of 5 μm in diameter (region 1 – Al rich) and as uniformly fine disc-shaped grains of 1 μm in size (region 2 – Cr rich). The corresponding XEDS spectra obtained from two different shaped grains presented in Figs. 4.27(c) and (d) reveal the qualitative information on elemental composition of the reaction product (Cr,Al)VO₄.

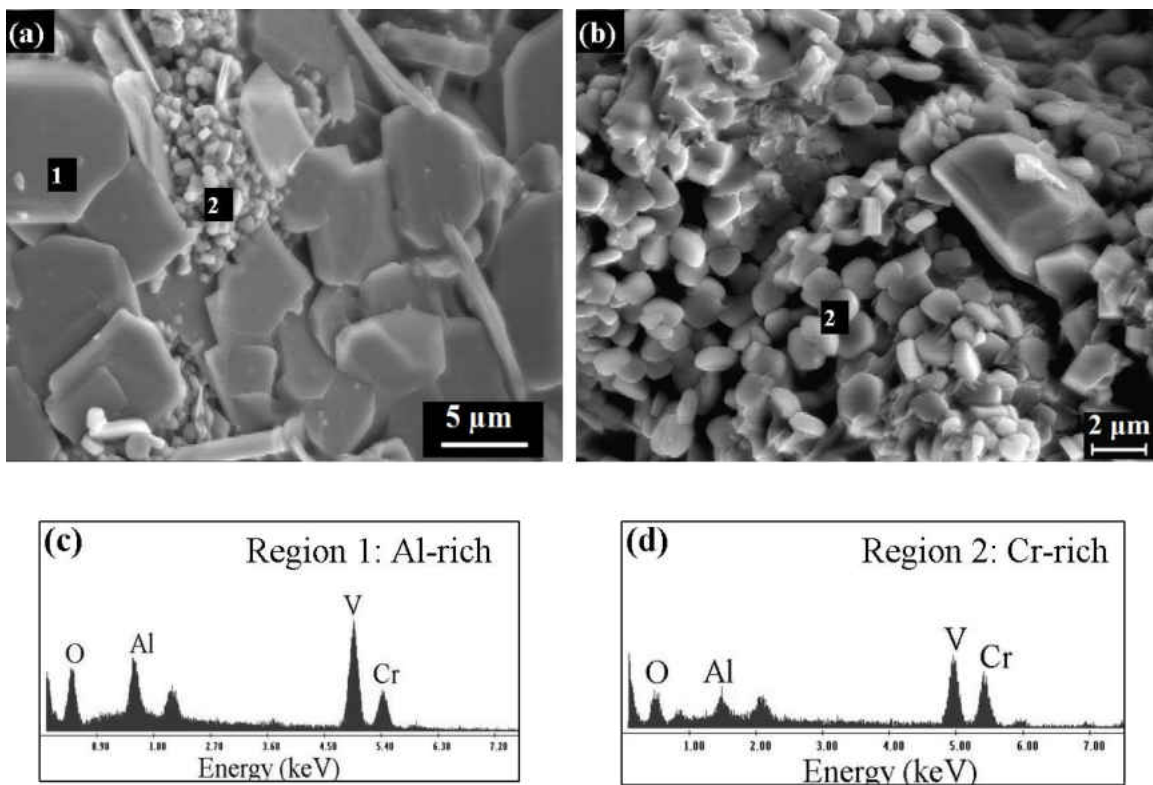


Figure 4.: (a) and (b) Secondary electron micrographs showing the surface morphologies of microstructural evolution during APS CoNiCrAlY – V₂O₅ melt interaction at 700°C for 2 h; (c) and (d) Characteristic XEDS spectra obtained from regions of interest.

The cross-sectional backscattered electron micrograph presented in Fig. 4.28(a) illustrates a minimal interaction between CoNiCrAlY and the V_2O_5 melt; although the infiltration was complete. A significant accumulation of V_2O_5 melt at the bottom surface of the coating has occurred due to the penetration of the melt through the interconnected cracks of the coating. Ingression of the V_2O_5 melt is also clearly evident in Fig. 4.28(b). The presence of solidified V_2O_5 melt along with the internal oxide (alumina) at the inter-splat boundaries of pre-oxidized APS CoNiCrAlY is observed.

Tests performed at 900°C for 2 h showed a completely different interaction of V_2O_5 with CoNiCrAlY. The XRD pattern shown in Fig. 4.29 identifies the reaction products due to the interaction between pre-oxidized CoNiCrAlY and V_2O_5 melt at 900°C. Orthorhombic $(Co,Ni)_3(VO_4)_2$ and cubic $(Ni,Co)(Cr,Al)_2O_4$ were found as the predominant reaction products, and both a vanadate of Co and Ni and a spinel oxide of Co/Ni and Al/Cr were found to be substitutional solid-solution compounds with significant substitutions of Co for Ni and Cr for Al. Morphological changes due to degradation by V_2O_5 at 900°C are also evident in the secondary electron micrographs in Fig. 4.30. Crystals of cobalt-nickel orthovanadate (region 1) varying in sizes up to 15 μm were found to be embedded on the surface in addition to the significant spinel oxide $[(Ni,Co)(Cr,Al)_2O_4]$ formation (region 2).

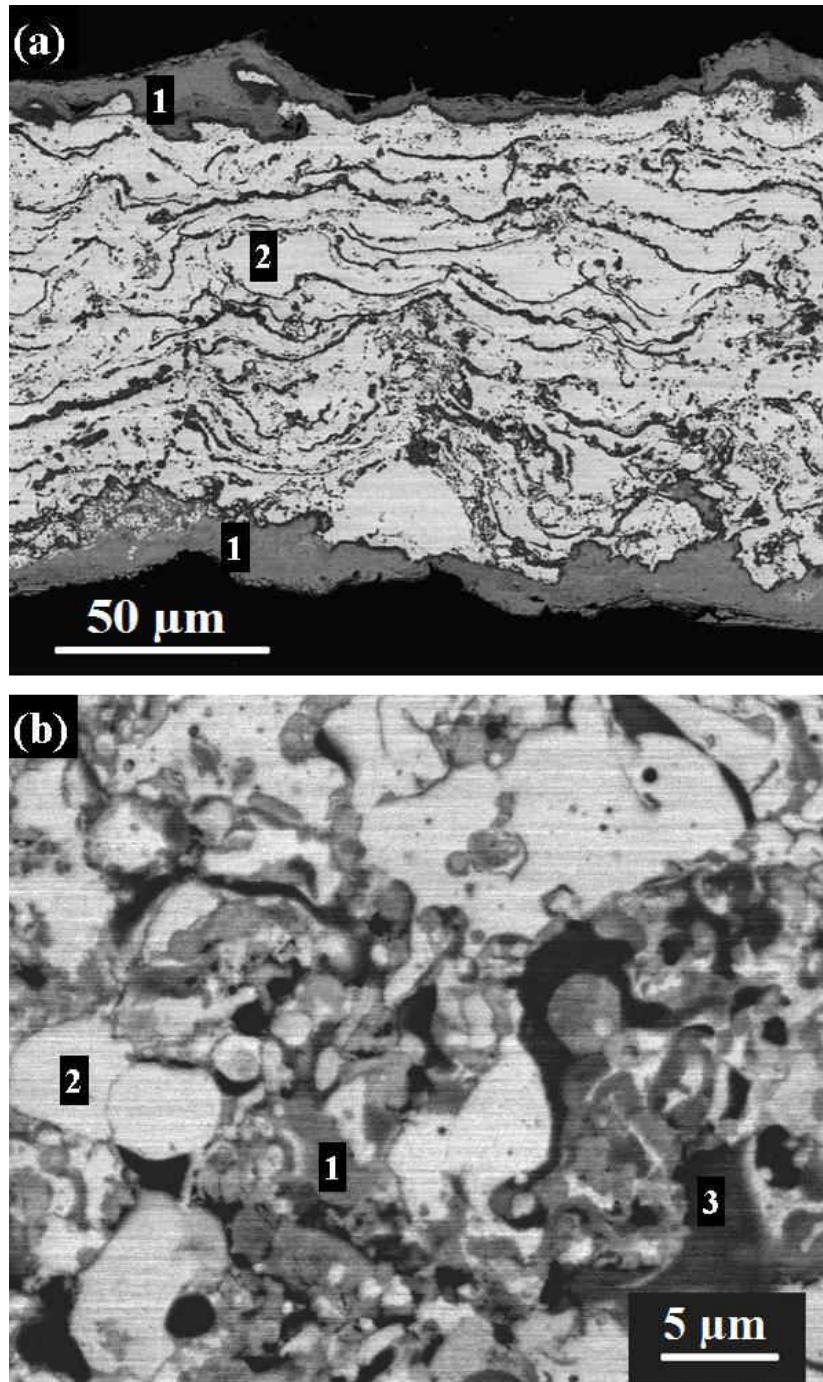


Figure 4.: Cross-sectional backscattered electron micrographs demonstrating the accumulation of V_2O_5 melt at bottom of the coating in (a) and the melt infiltration throughout free-standing APS CoNiCrAlY in (b). Regions 1, 2 and 3 correspond to V_2O_5 melt, bulk CoNiCrAlY coating and internal alumina resulted from pre-oxidation treatment, respectively.

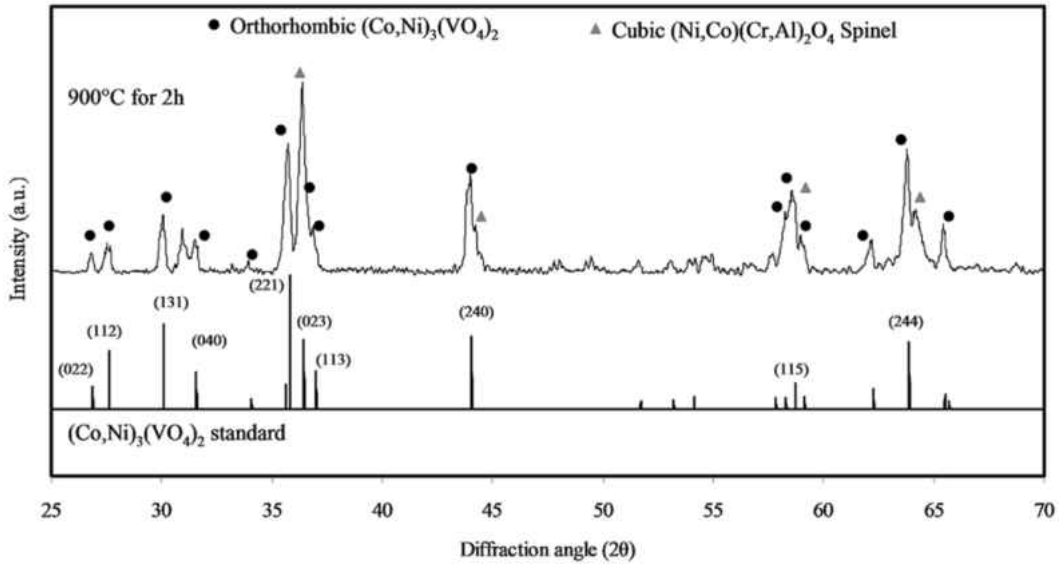


Figure 4.: XRD pattern from the V_2O_5 degraded CoNiCrAlY surface confirming orthorhombic $(Co,Ni)_3(VO_4)_2$ and cubic $(Ni,Co)(Cr,Al)_2O_4$ as the primary phase constituents evolved during thermochemical interaction between APS CoNiCrAlY and molten V_2O_5 after 2 h at $900^\circ C$.

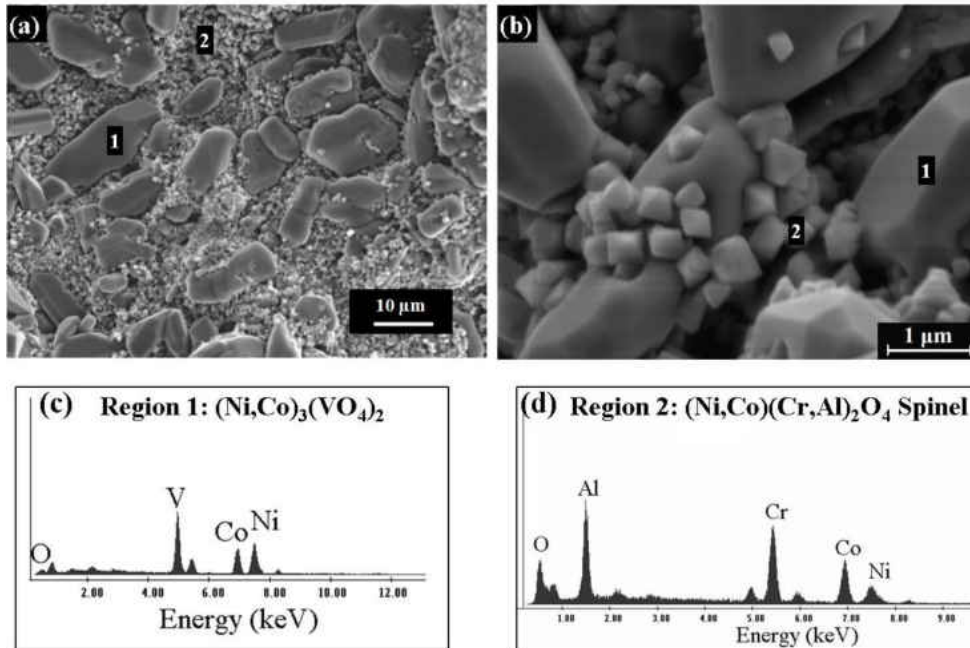


Figure 4.: (a) and (b) Secondary electron micrographs showing the surface morphologies of microstructural evolution during APS CoNiCrAlY – V_2O_5 melt interaction at $900^\circ C$ for 2 h; (c) and (d) Characteristic XEDS spectra obtained from regions of interest.

Unlike the insignificant interaction observed at 700°C, extensive degradation via dissolution of CoNiCrAlY by the V₂O₅ melt was observed at 900°C as shown by the cross-sectional backscattered electron micrograph in Fig. 4.31(a). A thick (>100 μm) scale on top of the unaffected CoNiCrAlY was primarily the constituents dissolved and reacted by V₂O₅ melt. This scale was found to be composed of (Co,Ni)₃(VO₄)₂ and (Ni,Co)(Cr,Al)₂O₄ by XRD results. Presence of YVO₄ was also observed by the respective XEDS spectrum. Corresponding XEDS spectra from regions of interest are presented in Figs. 4.31(b) and (c).

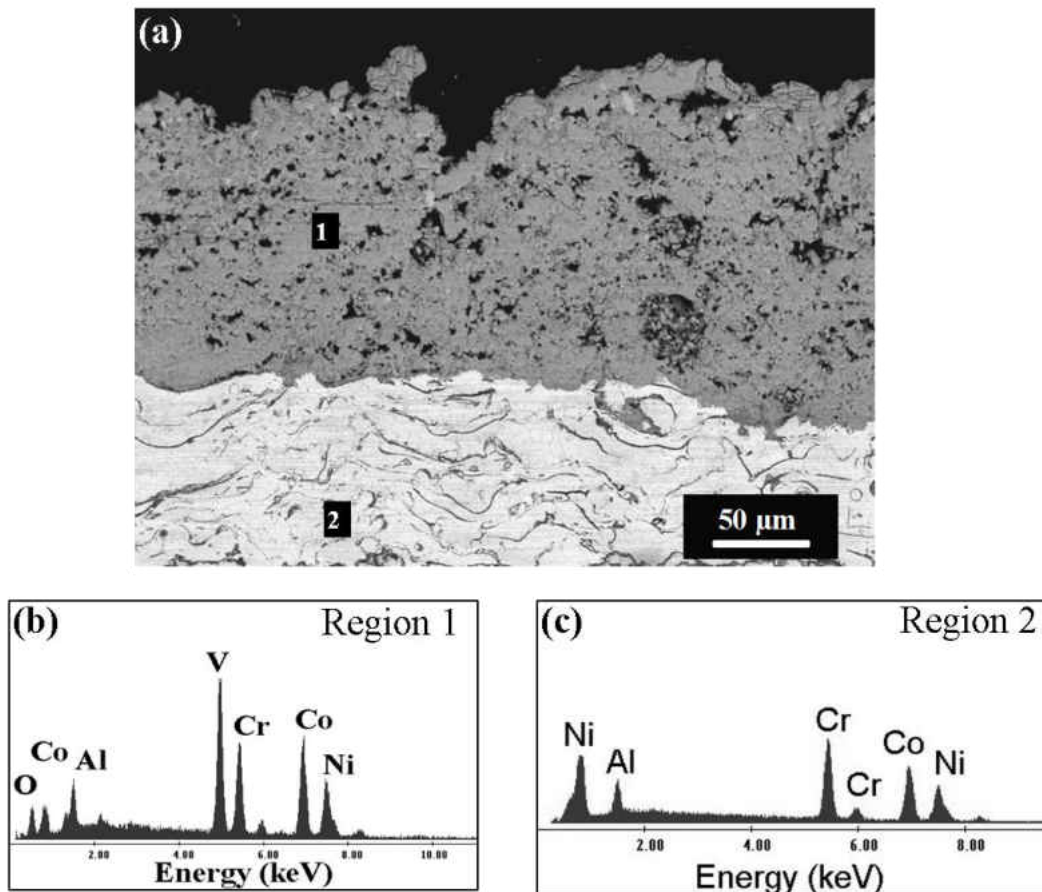


Figure 4.: (a) Cross-sectional backscattered electron micrograph demonstrating the extent of degradation by V₂O₅ melt, where region 1 is the 100 μm-thick scale developed by consumption of free-standing APS CoNiCrAlY; (b) and (c) Characteristic XEDS spectra obtained from regions of interest – region 1: V-rich corroded scale and region 2: unaffected CoNiCrAlY bulk.

4.4.2. Phosphorus Pentoxide (P_2O_5)

In this study, the pre-oxidized CoNiCrAlY coating was exposed to P_2O_5 melt at $350^\circ C$ for 2 h. This low temperature, at which P_2O_5 is in molten state, was chosen to minimize the vaporization of P_2O_5 . A visual observation of the tested CoNiCrAlY specimens clearly indicated a significant degradation by P_2O_5 melt. Figure 4.32 presents the XRD pattern that identifies the formation of two different phosphates, namely monoclinic $(Ni,Co)(PO_3)_2$ and monoclinic $(Cr,Al)(PO_3)_3$. The surface morphology of hot-corrosion tested specimen was examined along with XEDS analysis on reaction products; however a cross-sectional analysis was not possible due to the significant consumption of coating constituents by molten P_2O_5 .

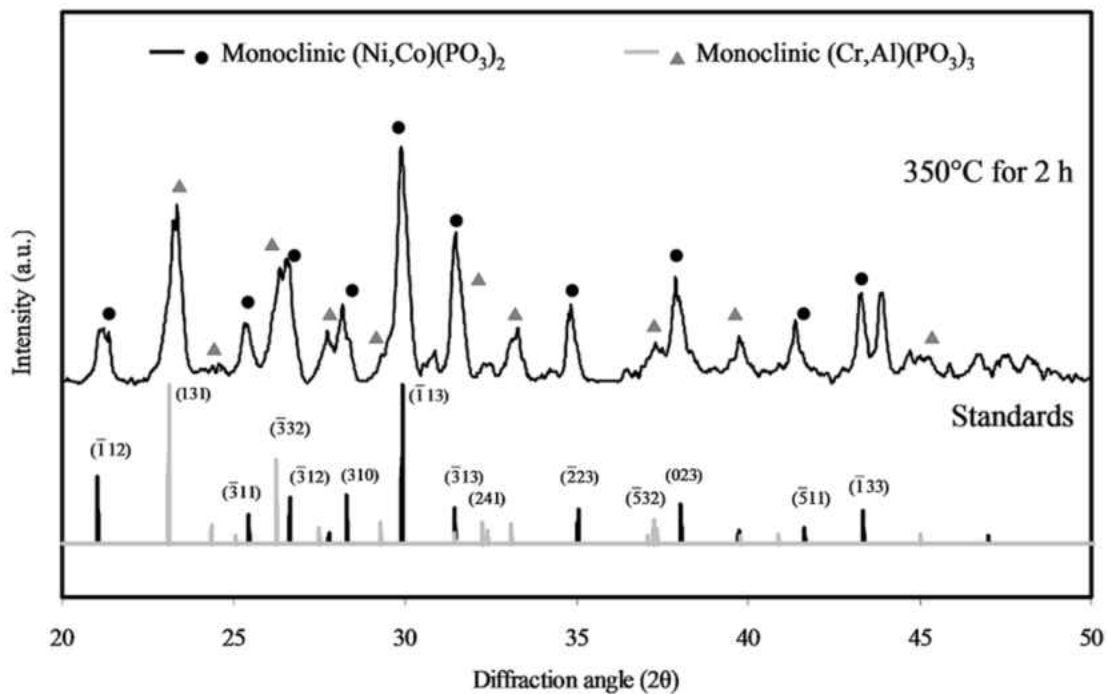


Figure 4.: XRD pattern from P_2O_5 degraded CoNiCrAlY surface revealing the presence of monoclinic $(Ni,Co)(PO_3)_2$ and monoclinic $(Cr,Al)(PO_3)_3$ as the primary phase constituents of interaction between APS CoNiCrAlY and molten P_2O_5 at $350^\circ C$ for 2 h.

Figure 4.33 shows the surface morphology evolved in CoNiCrAlY due to interaction with molten P_2O_5 at $350^\circ C$. The reaction products were found to have different morphologies that are clearly seen in Fig. 4.33(a): rice-shaped particles of cobalt nickel polyphosphate with uniform size of $5\ \mu m$ in length, and large grains of chromium aluminum polyphosphate. XEDS spectra obtained from two different reaction products are presented in Figs. 4.33 (b) and (c), which reveal the substitution of Co for Ni and Cr for Al, and therefore the reactions products were confirmed as substitutional solid-solution phosphates of Ni/Co and Al/Cr.

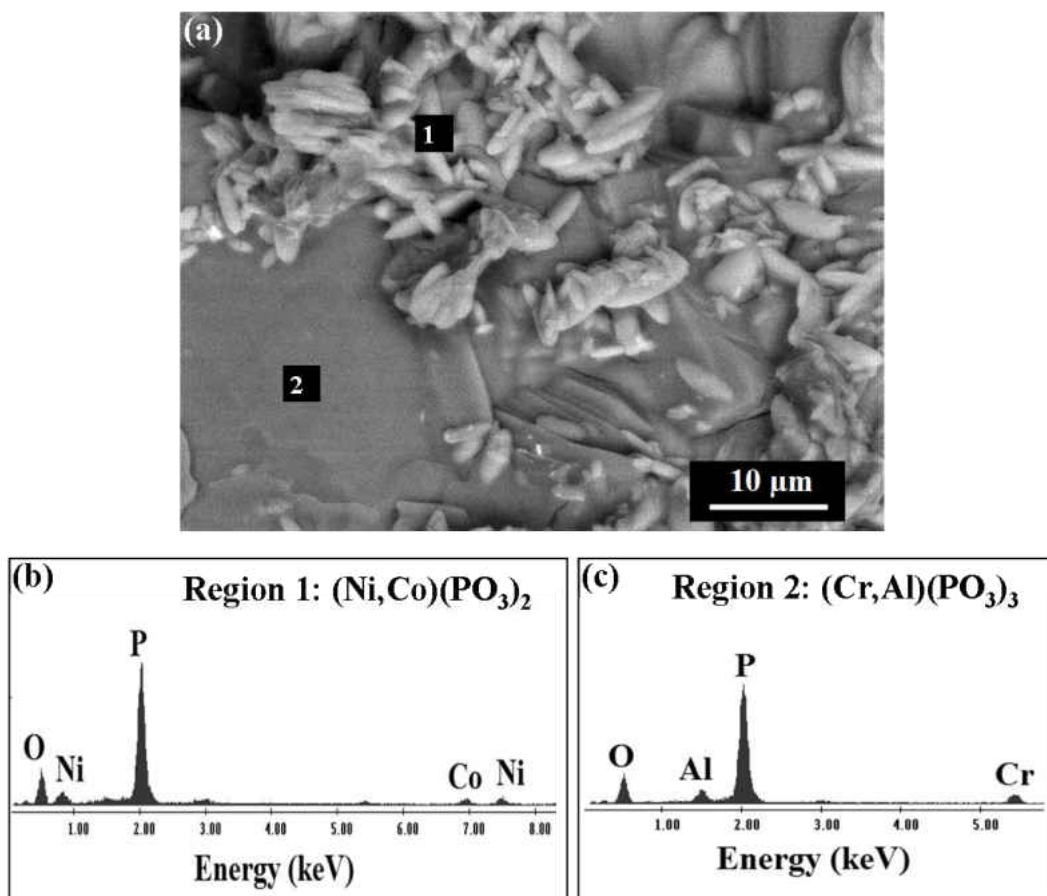


Figure 4.: (a) Backscattered electron micrograph showing the morphological difference of reaction compounds, region 1 – $(Ni,Co)(PO_3)_2$, and region 2 – $(Cr,Al)(PO_3)_3$ after free-standing APS CoNiCrAlY was exposed to P_2O_5 at $350^\circ C$ for 2 h. (b) and (c) Characteristic XEDS spectra obtained from different reaction products.

4.4.3. Sodium Sulfate (Na_2SO_4)

Degradation of free-standing APS CoNiCrAlY coatings both in as-sprayed and pre-oxidized (1100°C, 20 h treatment) condition was tested for hot corrosion resistance against Na_2SO_4 attack. CoNiCrAlY in as-sprayed condition suffered severe degradation due to Na_2SO_4 when tested in an enclosed quartz capsule (in order to maintain a salt film) at 1000°C for 50 h. Secondary electron micrographs of the hot corroded CoNiCrAlY surface shown in Fig. 4.34 highlights the significant formation of chromium sulfide (Cr_2S_3) through widely known sulfidation mechanism [10]. Lateral growth of faceted polynuclear sulfide (Cr_2S_3) can be clearly seen (region 1). XEDS from these large faceted sulfide grains is shown in Fig. 4.34(c). Besides, sulfides of Ni/Co as substitutional solid solution compound, (Ni,Co)S (region 2) was also observed as whiskers at the polynuclear Cr_2S_3 particle interface. Cross-sectional backscattered electron micrographs presented in Fig. 4.35 reveals the severe attack on the coating through accelerated internal oxidation and localized sulfidation. Molten Na_2SO_4 ingress through the inter-splat boundaries of the APS CoNiCrAlY resulted in direct thermochemical interaction. Subsequent increase in the oxygen partial pressure resulting from dissociation of penetrated sulfate melt caused significant internal oxidation (alumina formation at inter-splat boundaries). Fig. 4.35 (b) also reveals the localized internal sulfidation (i.e., formation of Cr_2S_3) within the bulk of the APS CoNiCrAlY. Thus, a direct contact of molten Na_2SO_4 with CoNiCrAlY resulted in extensive consumption of coating constituents through hot corrosion mechanisms.

On the other hand, these MCrAlY coatings having been developed for the purpose of oxidation/hot corrosion resistance, and a continuous thick alumina as surface TGO scale would obviously protect the coating system from molten sulfate attack. Free-standing APS CoNiCrAlY

coating after preoxidation with appreciably thick TGO alumina as surface oxide scale was found to degrade minimally through classical hot corrosion mechanism, when in contact with Na_2SO_4 melt at 1000°C . Cross-sectional backscattered electron micrographs presented in Fig. 4.36 reveal the formation of oxide scales such as $(\text{Al,Cr})_2\text{O}_3$ mixed oxide (region 2) and $(\text{Ni,Co})(\text{Al,Cr})_2\text{O}_4$ spinel (region 3) due to the presence of molten sulfate salt film at the surface (region 1).

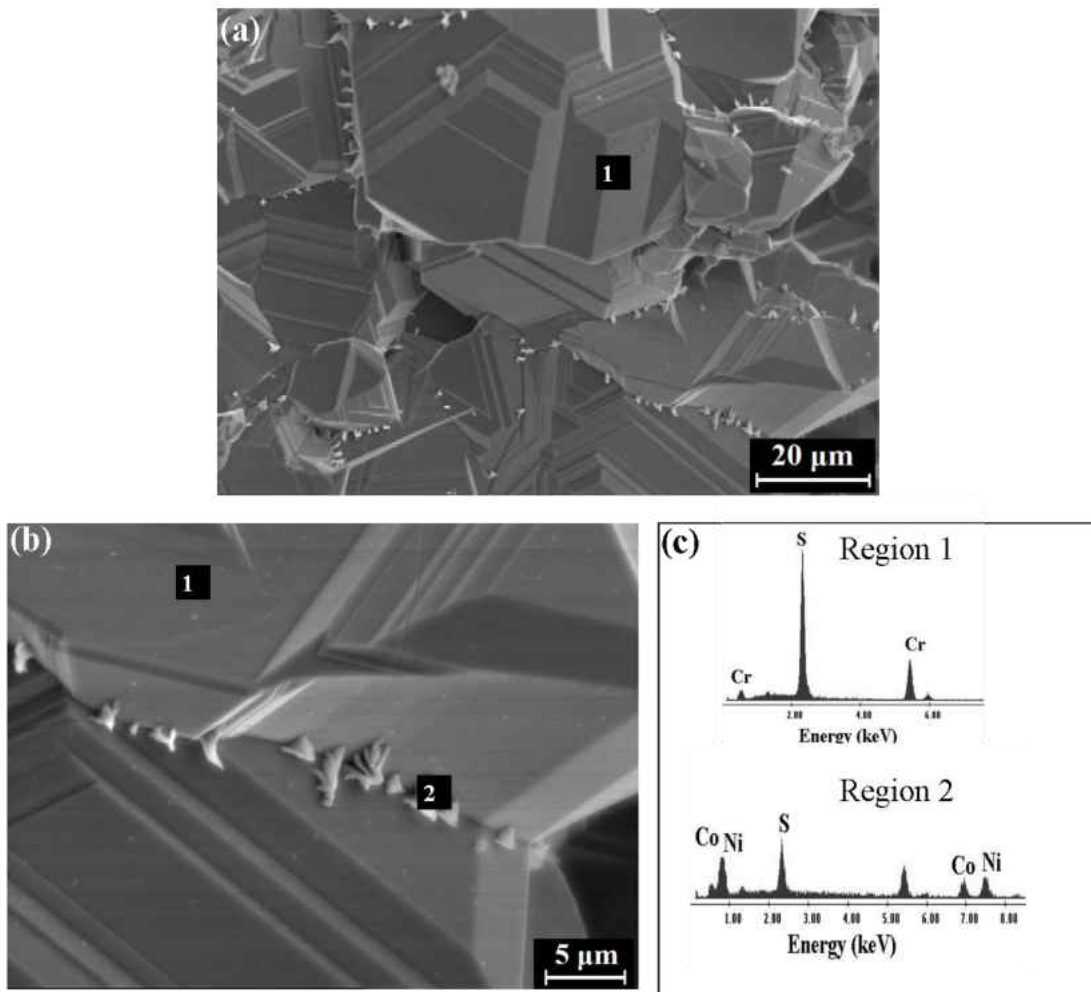


Figure 4.: (a) and (b) Secondary electron micrographs illustrating the surface morphology and phase evolution due to significant degradation by Na_2SO_4 melt of as-sprayed APS CoNiCrAlY at 1000°C for 50 h; (c) XEDS spectra identifying the reaction products as Cr_2S_3 .

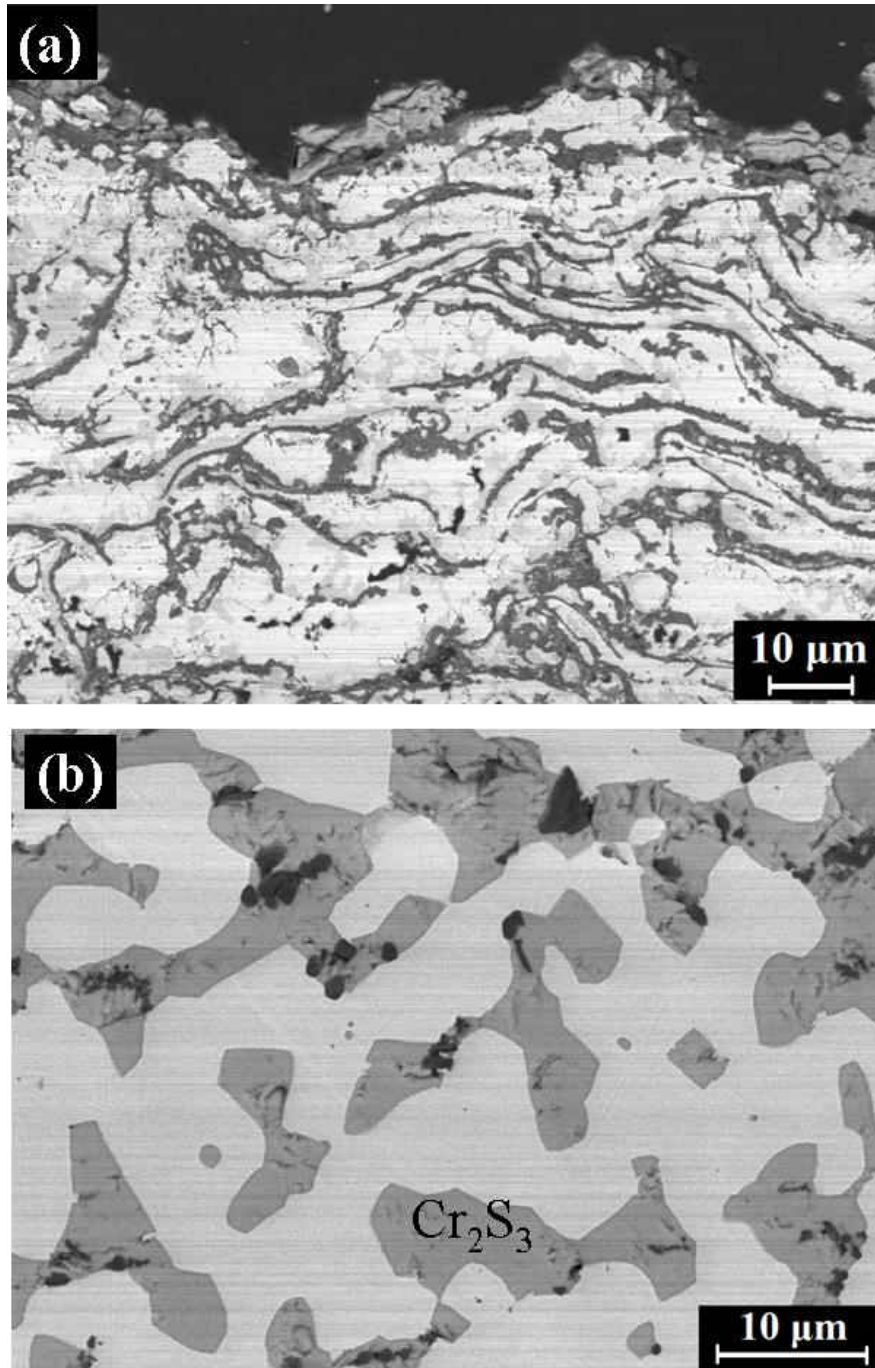


Figure 4.: Cross-sectional backscattered electron micrographs of Na_2SO_4 degraded as-sprayed APS CoNiCrAlY at 1000°C for 50 h: (a) degradation through significant internal oxidation is evident, (b) localized sulfidation resulted in formation of Cr_2S_3 within the bulk of CoNiCrAlY is observed.

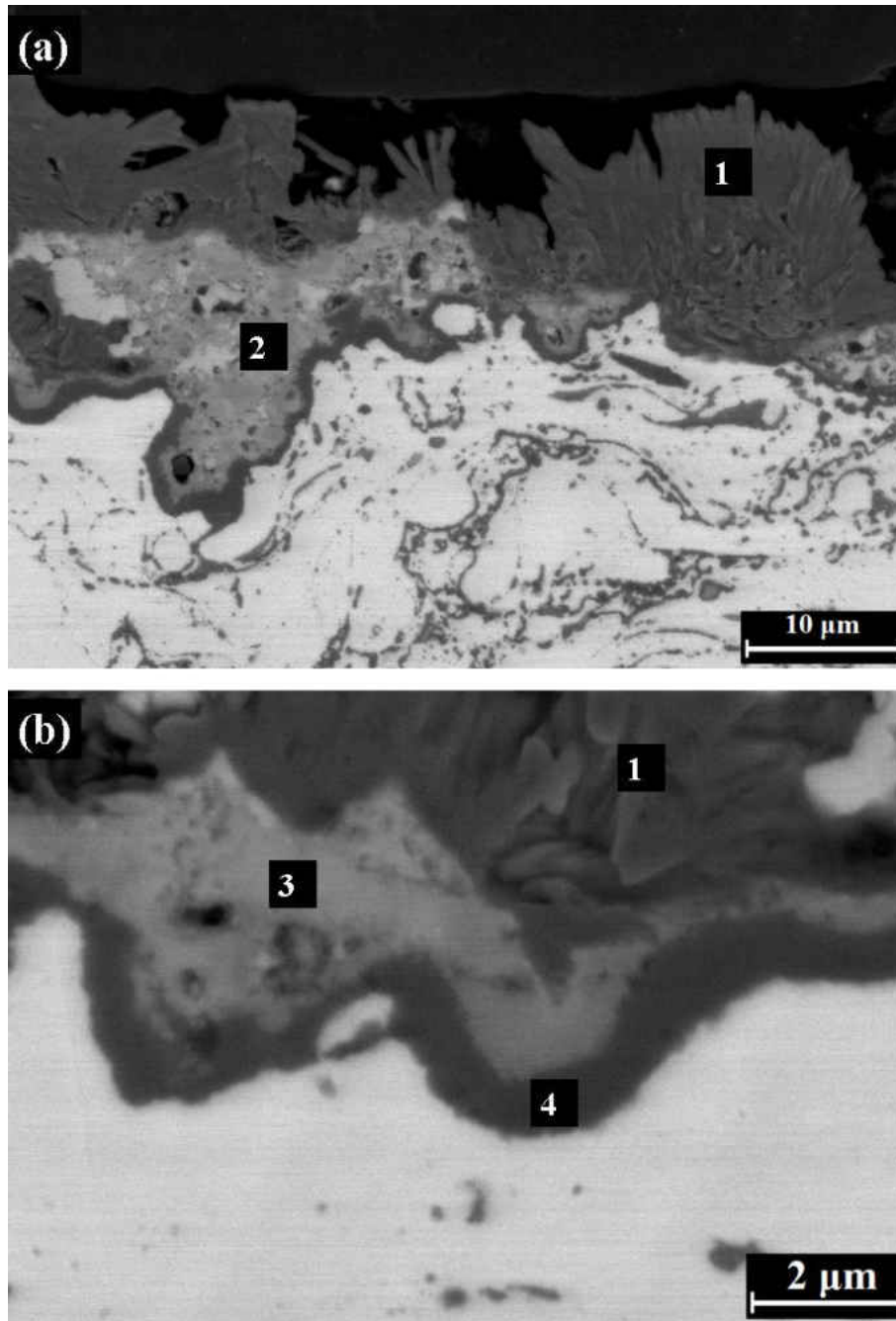


Figure 4.: Cross-sectional backscattered electron micrographs of Na₂SO₄ degraded pre-oxidized APS CoNiCrAlY at 1000°C for 50 h: (a) Presence of Na₂SO₄ deposit (region 1) and mixed oxide scale (Al,Cr)₂O₃ (region 2) are seen; (b) Presence of Na₂SO₄ deposit (region 1), spinel oxide (Ni,Co)(Al,Cr)₂O₄ (region 3) and TGO alumina (region 4) are observed as the surface scale constituents.

4.4.4. Calcium Sulfate (CaSO_4)

Calcium rich deposits, commonly observed in gas turbine operation can be detrimental if deposited as CaSO_4 . APS CoNiCrAlY in pre-oxidized state suffered degradation due to CaSO_4 deposit when subjected to isothermal molten-deposit testing at 1000°C for 50 h. A cross-sectional backscattered electron micrograph highlighting the reaction products that were confirmed through XEDS analysis are presented in Fig. 4.37.

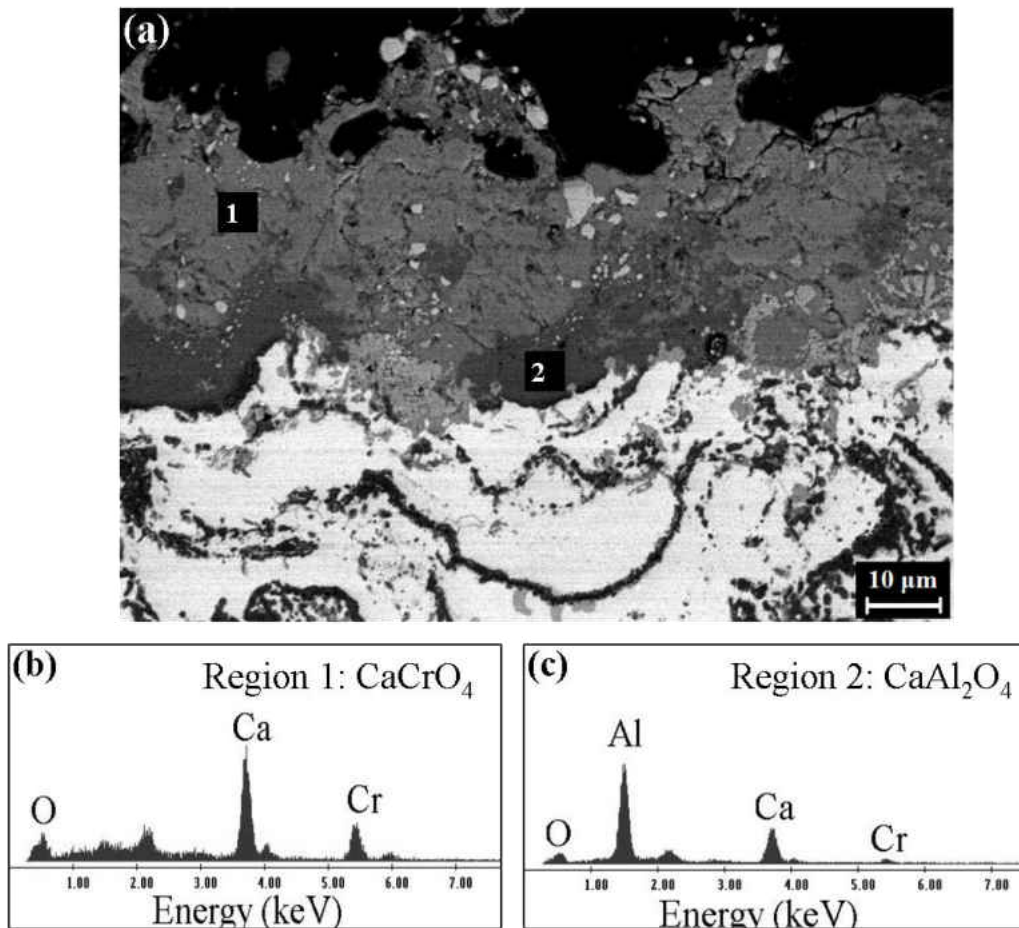


Figure 4.: (a) Cross-sectional backscattered electron micrograph of CaSO_4 degraded CoNiCrAlY (pre-oxidized) at 1000°C for 50 h. (b) and (c) XEDS spectra collected from different reaction products.

CaSO₄ was found to directly interact with oxide constituents of CoNiCrAlY surface resulting in dissolution of protective oxides (Al₂O₃, Cr₂O₃). Formation of calcium chromate (Region 1: CaCrO₄) and calcium aluminum oxide (Region 2: CaAl₂O₄) at the CaSO₄/coating interface was observed. It should be noted that the degradation was limited only to the top 30 μm of CoNiCrAlY. There was no evidence of TGO alumina scale, and this suggests a complete dissolution of protective oxides by CaSO₄.

4.4.5. Sodium Metavanadate (NaVO₃)

In order to investigate the degradation of CoNiCrAlY, both in as-sprayed and pre-oxidized state by molten NaVO₃ deposit, coatings in contact with NaVO₃ were subjected to isothermal testing at 900°C for 5 h. Cross-sectional views of the tested specimen are presented in Figs. 4.38 and 4.39. The as-sprayed CoNiCrAlY was found to undergo a significant degradation through dissolution of coating constituents by NaVO₃ melt. Melt ingress through the APS CoNiCrAlY was also evident as presented in Fig. 4.38(b). XEDS spectrum from constituents of CoNiCrAlY dissolved by V rich melt (region 1) as seen in Fig. 4.38(c) reveals no preferential dissolution. An average 40 μm thick scale was observed at the surface due to a significant thermochemical interaction between free-standing APS CoNiCrAlY and NaVO₃ melt. On the other hand, pre-oxidized coating was found to be relatively resistant to NaVO₃ attack in comparison to V₂O₅ attack as discussed earlier. Backscattered electron micrographs showing the cross-sections of pre-oxidized CoNiCrAlY after exposure to NaVO₃ melt are presented in Fig. 4.39. No direct dissolution of coating constituent was observed. A continuous (Ni,Co)(Al,Cr)₂O₄ spinel (region 1) as the surface oxide scale is seen in Fig. 4.39 (a). It is also observed that the

oxide scale consisting of spinel and TGO alumina is not dense and the local disintegration of oxide scale is evident as seen in Fig. 4.39 (b).

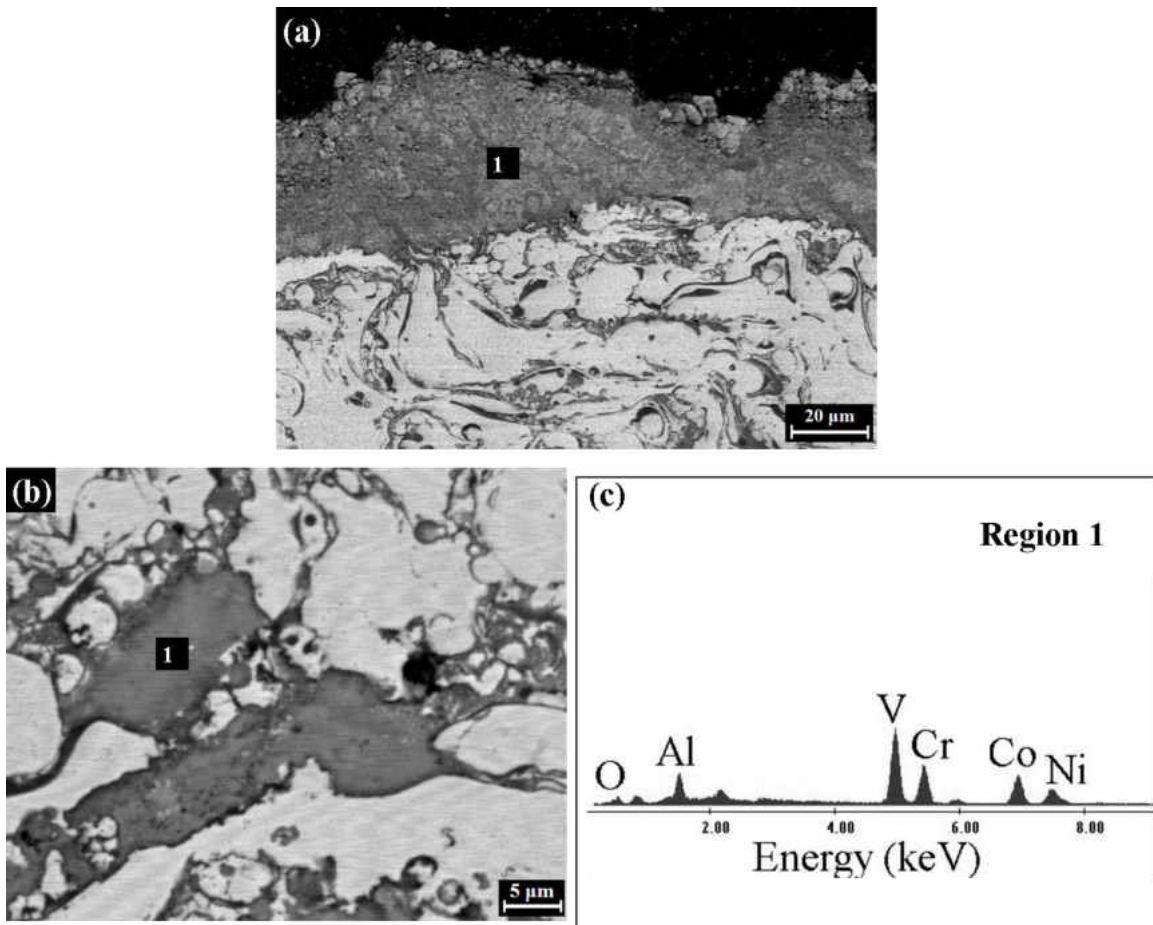


Figure 4.: (a) and (b) Cross-sectional backscattered electron micrographs of CoNiCrAlY (in as-sprayed state) after exposure to NaVO₃ at 900°C for 5 h showing the dissolution of coating constituents by V rich melt, (c) Corresponding XEDS spectrum from region 1.

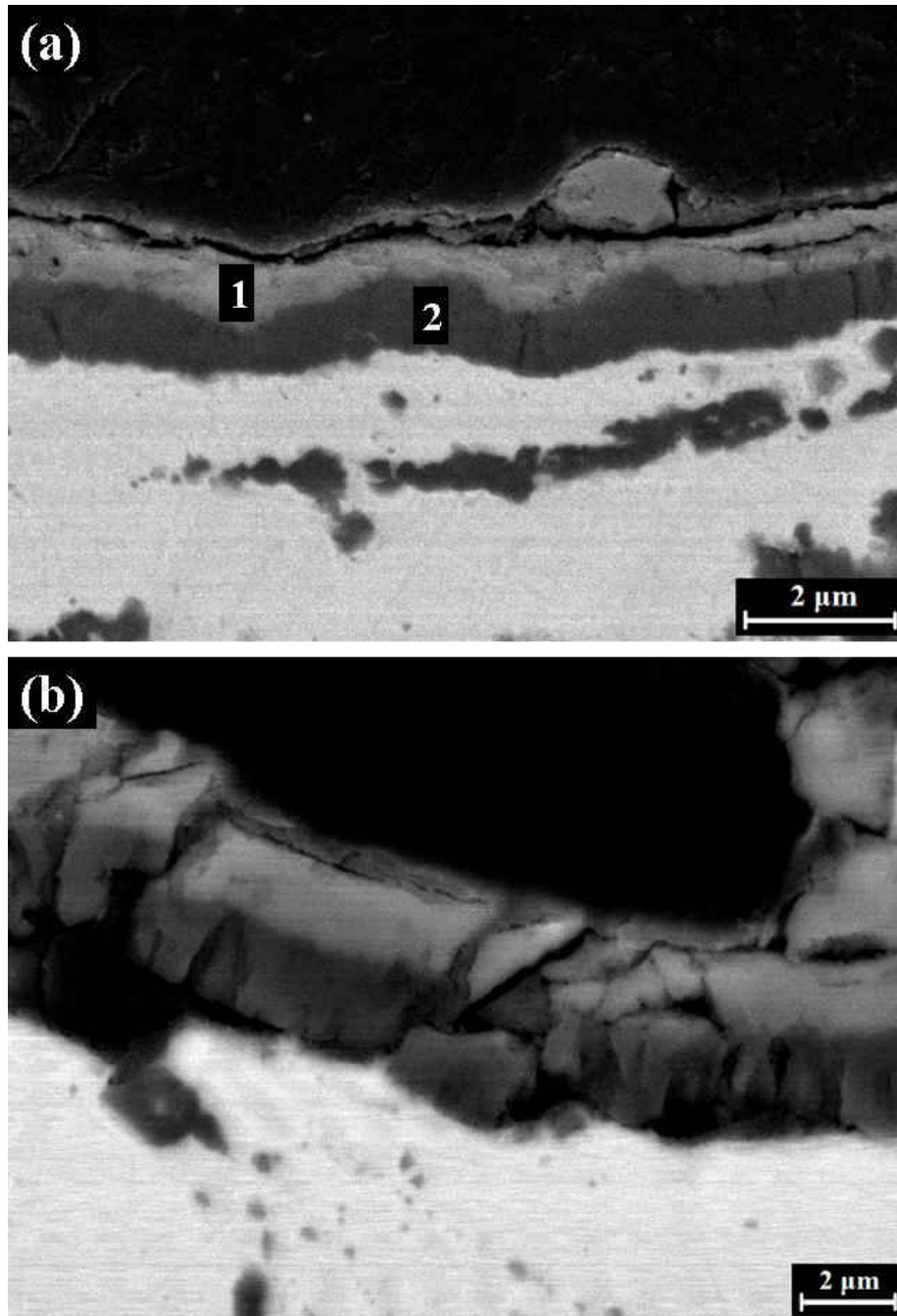


Figure 4.: (a) and (b) Cross-sectional backscattered electron micrographs of CoNiCrAlY (in pre-oxidized state) after exposure to NaVO₃ at 900°C for 5 h showing the modified surface scale (TGO) constituents; region 1: (Ni,Co)(Al,Cr)₂O₄ spinel and region 2: TGO alumina (α Al₂O₃).

4.5. Thermochemical Degradation of APS CoNiCrAlY by Molten CMAS Deposit

Molten CMAS has been found to readily ingress the porous ceramic topcoat of TBCs. Hence, CMAS could also degrade the TGO and bond coat layers of TBCs. Even though it is very unlikely for a metallic coating (ORCs or bond coat of TBCs) to experience such a high surface temperature for CMAS deposits to melt and degrade, it should be taken into consideration that CMAS deposit can melt even at temperatures lower than 1150°C based on the composition [29]. With the increasing TIT, understanding the degradation of alumina forming MCrAlY coatings by CMAS deposits becomes mandatory for the expansive applications of MCrAlY coatings. In this study, pre-oxidized APS CoNiCrAlY coatings were exposed to CMAS and subjected to isothermal heat-treatment at 1250°C for 5 h. CMAS was found to readily consume CoNiCrAlY coating constituents and the TGO scale through thermochemical interaction. Surface morphologies of the APS CoNiCrAlY after testing with CMAS deposit are shown in secondary electron micrographs shown in Fig. 4.40. A CMAS wetted surface is seen with platelet-like crystals (region 1) embedded on the surface that resulted from crystallization of CMAS melt due to a change in its composition attributed to the thermochemical dissolution of TGO alumina. Significant formation of spinel oxide [region 2: $(\text{Ni},\text{Co})(\text{Al},\text{Cr})_2\text{O}_4$] is also evident as seen in Fig. 4.40(b). The corresponding XEDS spectra obtained from compounds evolved with different morphologies are presented in Fig. 4.40 (c). Cross-sectional views of CoNiCrAlY after high-temperature testing with CMAS are presented by backscattered electron micrographs in Fig. 4.41. These demonstrated a significant degradation by CMAS melt. The APS CoNiCrAlY coating was found to be attacked up to 40 μm in thickness. The CMAS-degraded CoNiCrAlY layer was found to be composed of crystallized CMAS (region 1), applied CMAS (region 2) and

spinel oxides. The corresponding XEDS spectra as presented in Fig. 4.41 (c) reveals that the crystallized CMAS had higher Al content in comparison to that of applied CMAS. This is attributed to the extensive dissolution of the TGO alumina.

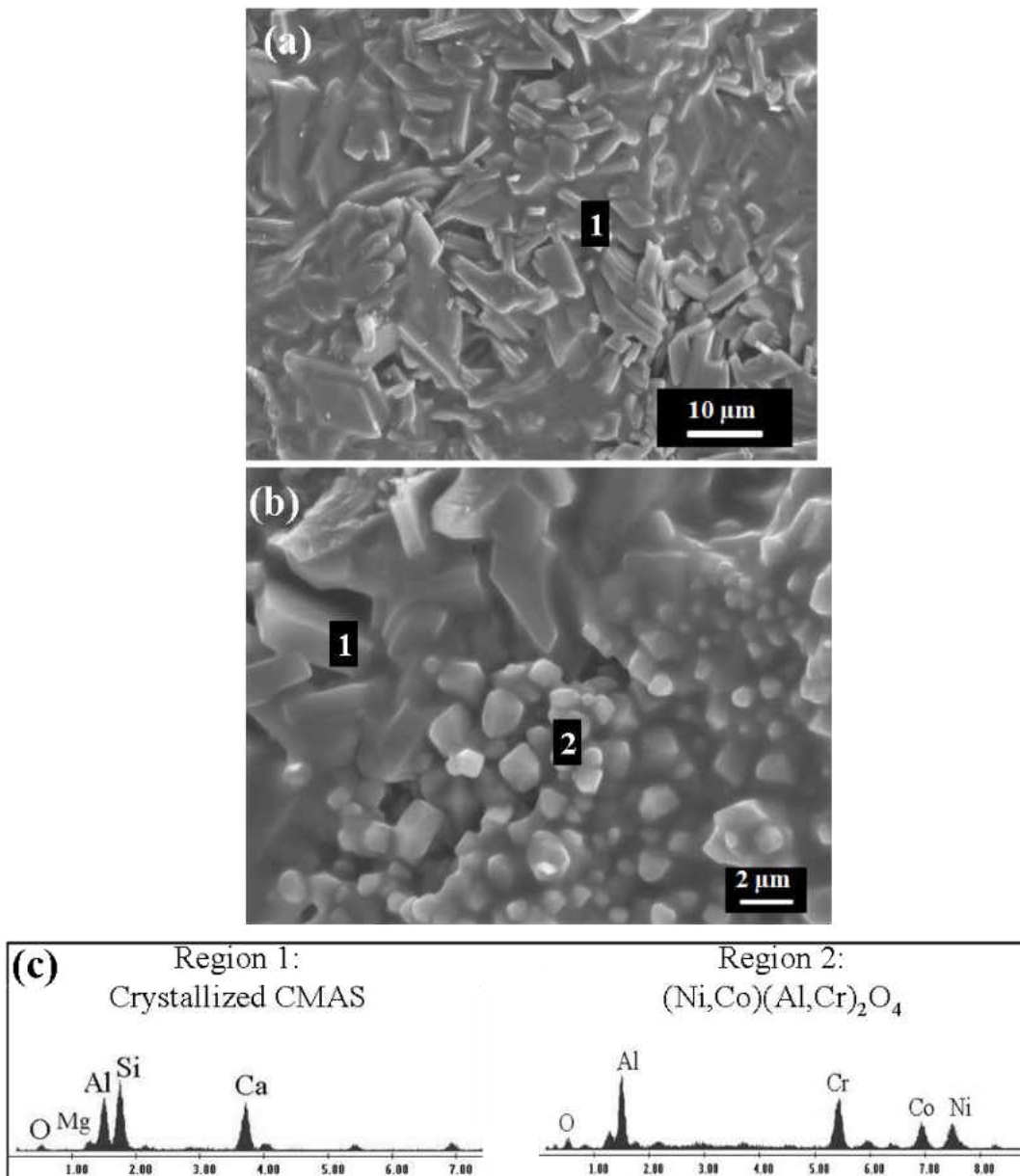


Figure 4.: (a) and (b) Secondary electron micrographs of CoNiCrAlY (pre-oxidized) surface after degraded by CMAS deposit at 1250°C for 5 h showing microstructural evolution due to thermochemical interaction; (c) Respective XEDS spectra from regions of interest.

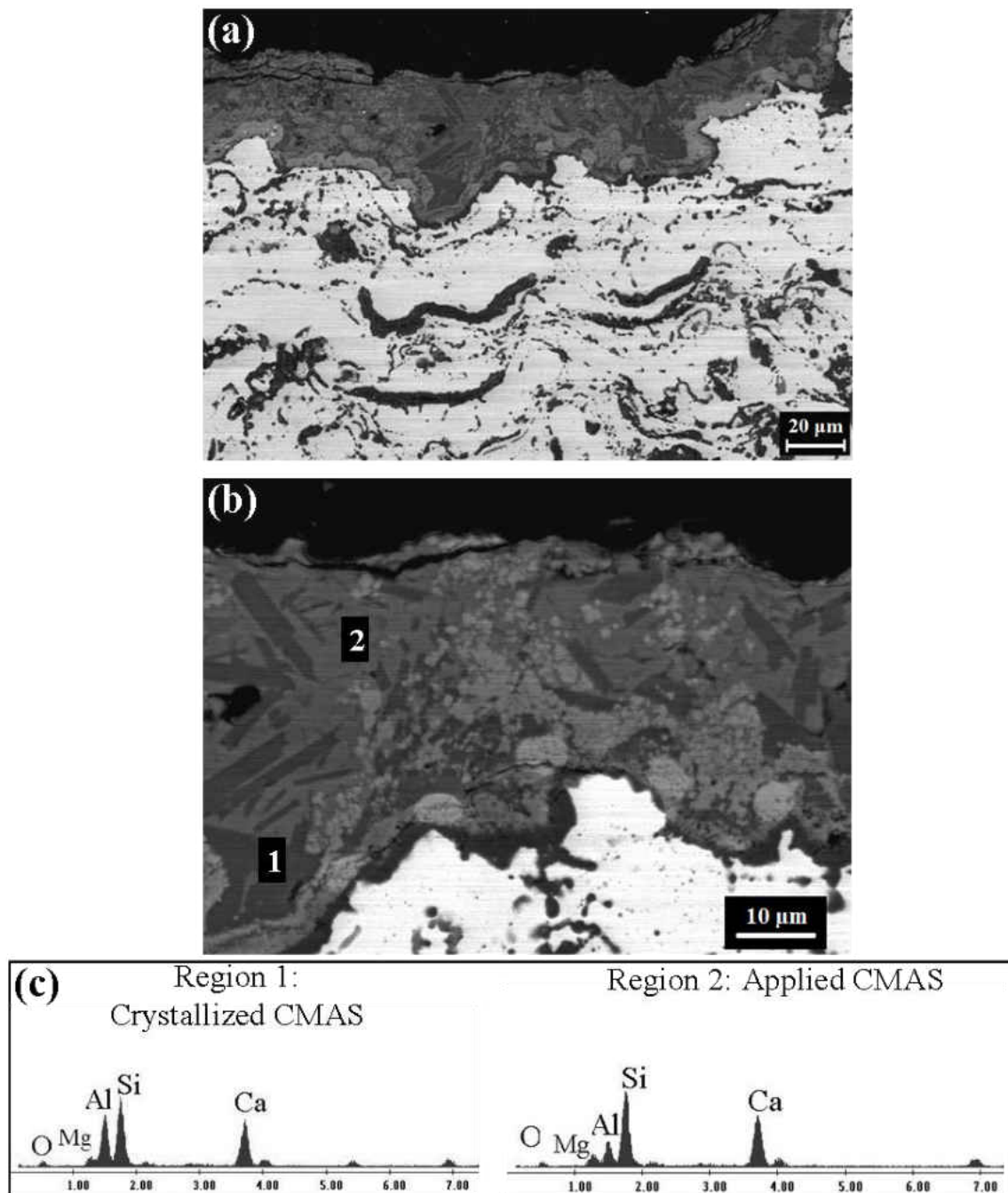


Figure 4.: (a) and (b) Cross-sectional backscattered electron micrographs of CoNiCrAlY (pre-oxidized) after degraded by CMAS deposit at 1250°C for 5 h showing microstructural evolution due to thermochemical interaction; (c) Corresponding XEDS spectra from regions of interest; region 1: crystallized CMAS, region 2: applied CMAS.

4.6. Ceramic Overlay for APS YSZ by EPD

4.6.1. YSZ Overlay

In order to protect APS YSZ TBCs from melt ingress, a ceramic overlay of desired porosity and thickness that can act as a sacrificial oxide overlay and/or impermeable ceramic coating was examined in this study. For YSZ TBCs, an overlay composed of dense YSZ, being the obvious choice, was fabricated. Through a controlled EPD process, which is a particle-by-particle deposition technique followed by a densification step, a YSZ overlay of 25 μm was readily achieved. Protection of thermally sprayed TBCs by a EPD YSZ overlay entails the overlay to be dense in order to suppress the melt ingress. Hence, to achieve a dense crack-free YSZ overlay, the YSZ green compact after deposition followed by drying in ambient conditions, was sintered at two different sintering conditions. Sintering at 1300°C and 1350°C for 4 h was employed to achieve YSZ overlay coatings of desired density.

The phase constituents of the APS YSZ, green YSZ powder compact after deposition through EPD, and the dense YSZ overlay after sintering at 1300°C for 4 h were examined by XRD as presented in Fig. 4.42. The primary phase constituent of the as-sprayed APS YSZ was the metastable tetragonal ZrO_2 phase (t' - ZrO_2), which is the desirable ZrO_2 phase for TBCs. Even though the green powder compact processed by EPD was primarily composed of the equilibrium ZrO_2 phases such as transformable tetragonal (t) and fluorite-cubic (f) phases with traces of monoclinic (m) phase, after controlled sintering step, the YSZ overlay was found to have completely transformed to tetragonal ZrO_2 (t- ZrO_2).

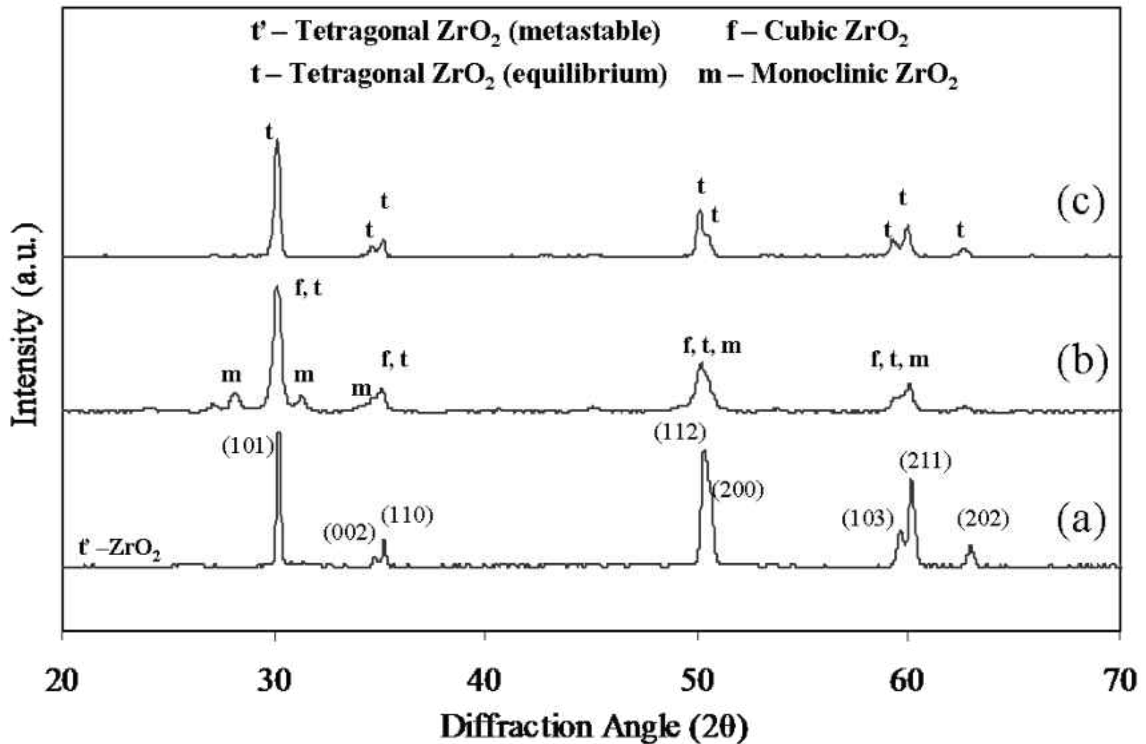


Figure 4.: XRD patterns obtained from (a) Air plasma sprayed (APS) YSZ coating that is primarily composed of metastable tetragonal ZrO₂ phase (t' - ZrO₂), (b) YSZ green compact obtained from EPD consisting of a mixture of ZrO₂ equilibrium phases and (c) YSZ overlay coating after sintering at 1300°C for 4 h primarily composed of t' - ZrO₂.

Secondary electron images obtained from the green YSZ powder compact and sintered YSZ overlay are presented in Figs. 4.43(a) and (b), respectively. A crack-free powder compact obtained from EPD after drying is evident from its surface morphology as shown in Fig. 4.43(a). A typical YSZ surface after sintering at 1300 °C for 4 h is shown by the secondary electron micrograph in Fig. 4.43(b). To compare the surface finish obtained from APS and EPD techniques, a part of APS YSZ was masked during the EPD YSZ overlay process. Interconnected surface cracks and pores, typical to APS processed coating and a crack-free surface obtained

from EPD that would be beneficial in protecting the APS YSZ coating against melt ingression are clearly seen in Fig. 4.44.

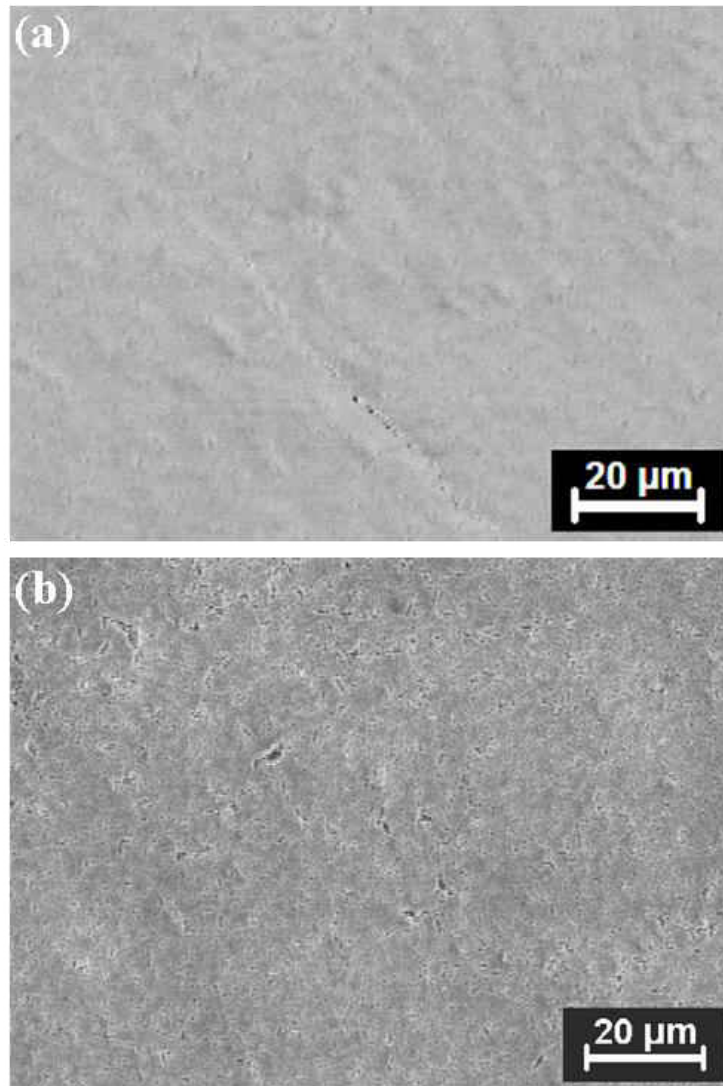


Figure 4.: Secondary electron micrographs illustrating the surface morphology of (a) YSZ green compact after EPD and (b) YSZ overlay coating after sintering at 1300°C for 4 h.

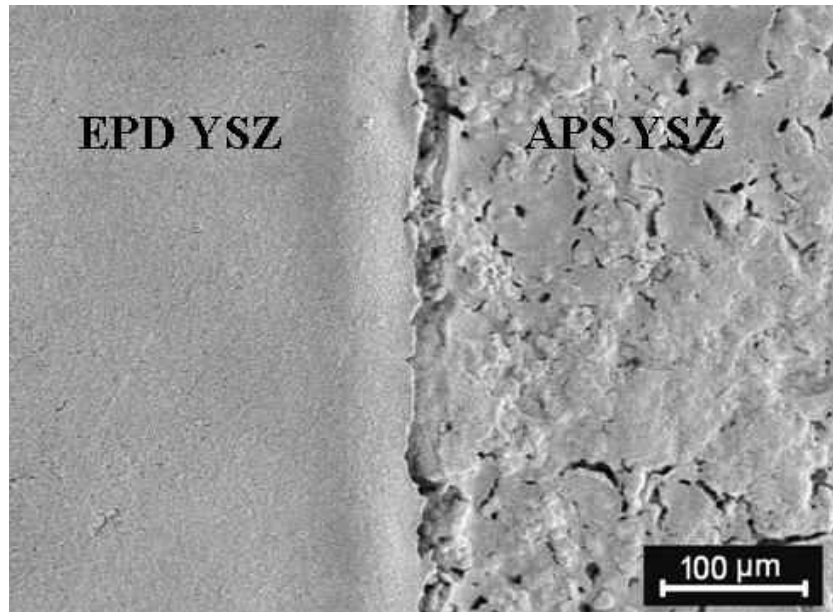


Figure 4.: Secondary electron micrographs demonstrating the crack-free EPD YSZ surface morphology on a APS YSZ specimen with the right half uncoated during EPD.

Cross-sectional secondary electron micrographs obtained from the EPD YSZ overlay, sintered at 1300°C for 4 h, are presented in Fig. 4.45. Interface between the EPD overlay coating and the APS YSZ, presented in Fig. 4.45(a), exhibits a good adhesion of the EPD overlay coating. A magnified view of the bulk of the EPD YSZ overlay coating shown in Fig. 4.45(b) reveals uniformly distributed microvoids that resulted from typical sintering characteristics of YSZ powder compact, which started with sub-micron YSZ particles. Even though the observed microstructural characteristics of YSZ overlay after sintering at 1300°C are promising in providing protection against melt ingress, a denser YSZ overlay with fewer microvoids could be achieved by sintering at higher temperatures. Hence, sintering at 1350°C for 4 h was also employed in this study.

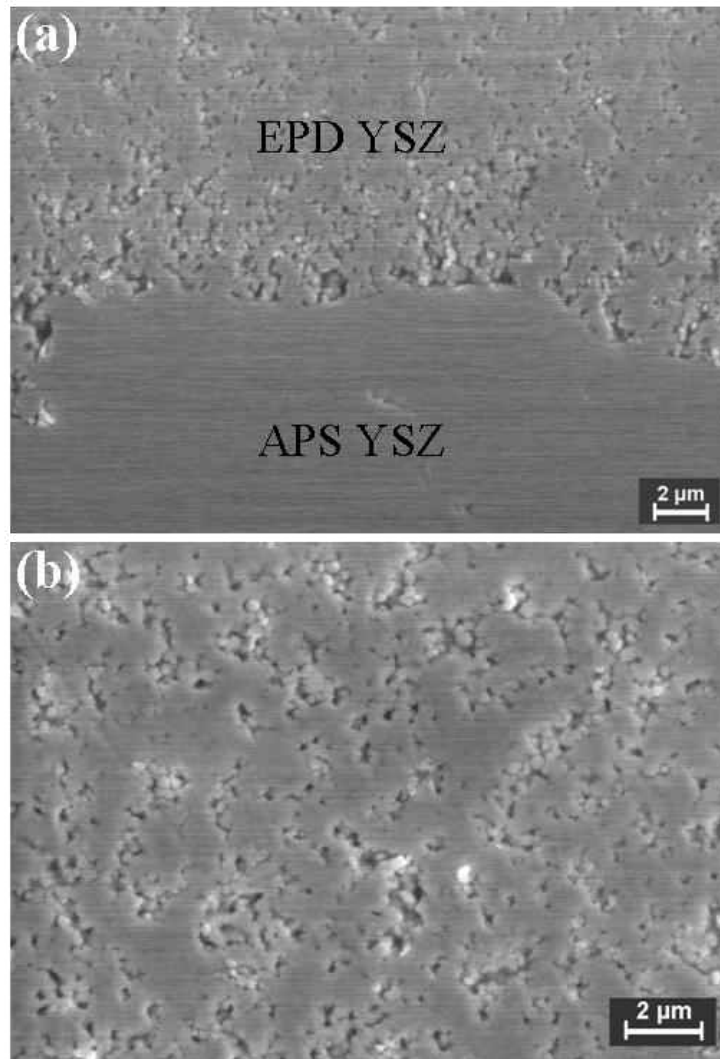


Figure 4.: Cross-sectional secondary electron micrographs showing the typical EPD overlay microstructure: (a) a continuous YSZ overlay coating fabricated by EPD followed by sintering at 1300°C for 4 h and (b) the EPD YSZ / APS YSZ coating interface.

As expected, a higher sintering temperature resulted in a denser microstructure of the EPD YSZ overlay. Figures 4.46(a) and (b) present the secondary electron images obtained from the surfaces of YSZ overlay after sintering at 1300°C and 1350°C for 4 h, respectively. It is clearly seen that YSZ overlay sintered at 1350°C is denser with fewer microvoids. Cross-sectional secondary electron micrographs presented in Figs. 4.47(a) and (b) demonstrate that a

dense and continuous YSZ overlay of 25 μm in thickness was obtained after sintering at 1350°C for 4 h.

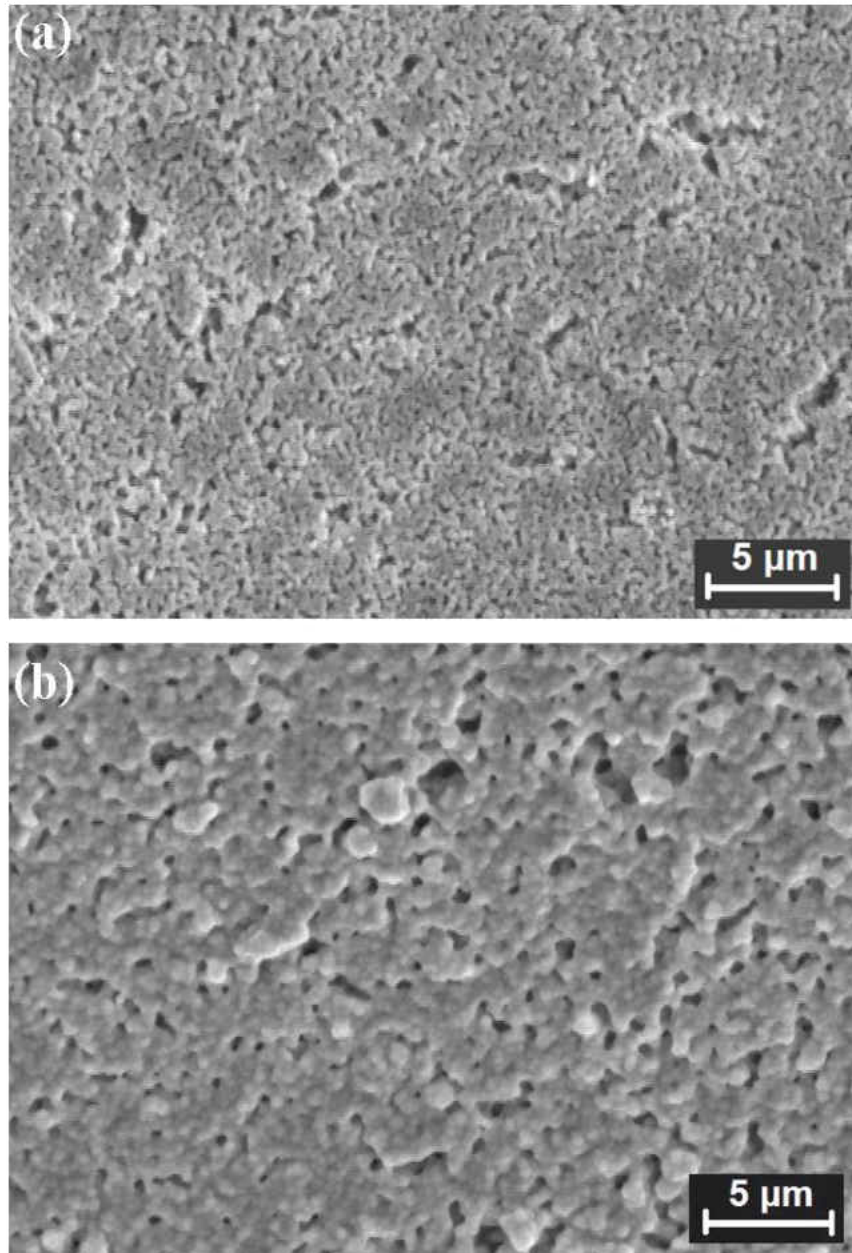


Figure 4.: Secondary electron micrographs revealing the surface morphology of (a) YSZ overlay coating after sintering at 1300 °C for 4 h and (b) YSZ overlay coating after sintering at 1350 °C for 4 h.

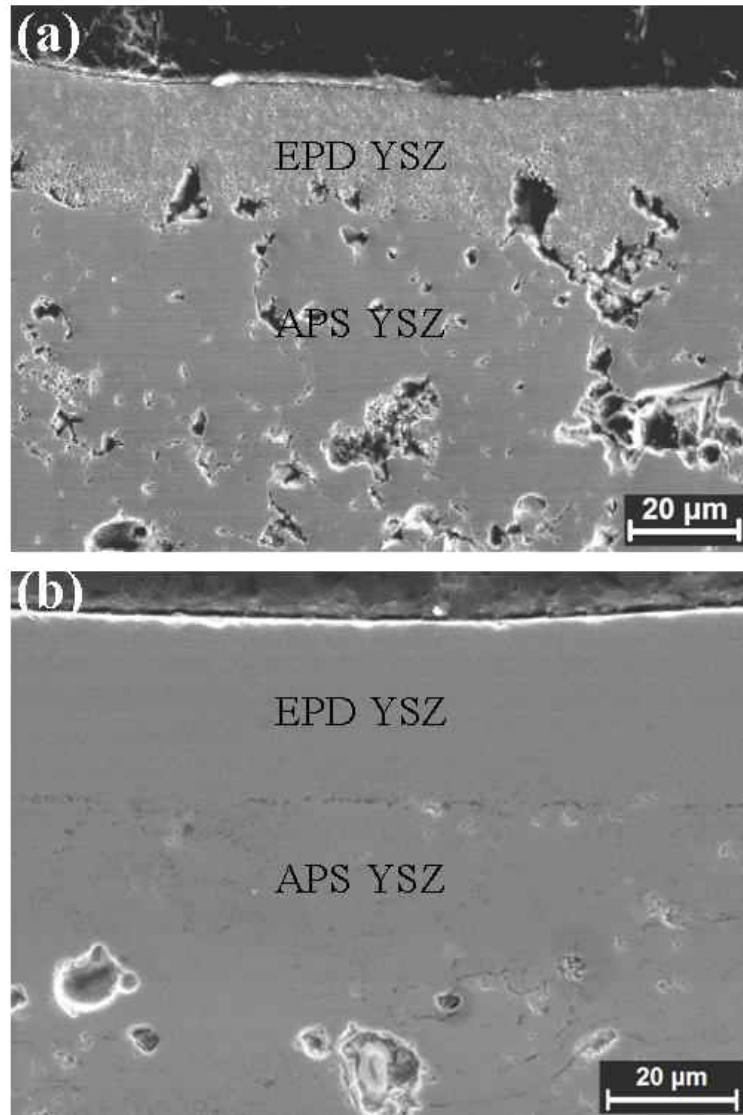


Figure 4.: Cross-sectional secondary electron micrographs of EPD YSZ overlay coatings with varying porosity by different sintering conditions: (a) sintered at 1300°C for 4 h and (b) sintered at 1350°C for 4 h.

APS YSZ with a dense YSZ overlay processed by EPD and sintering at 1350°C for 4 h was subjected to CMAS exposure at 1300°C for 1 h. CMAS, having excellent wettability and low viscosity was found to infiltrate and dissolve even the relatively dense EPD YSZ and thus attacked the APS YSZ. This concludes that even though the melt penetration might have been

reduced, CMAS ingress into APS YSZ was not completely arrested. Figure 4.48 illustrates the presence of solidified CMAS as islands within the APS YSZ. Attack through the ingress of CMAS into the EPD YSZ is also clearly seen in Fig. 4.48(b).

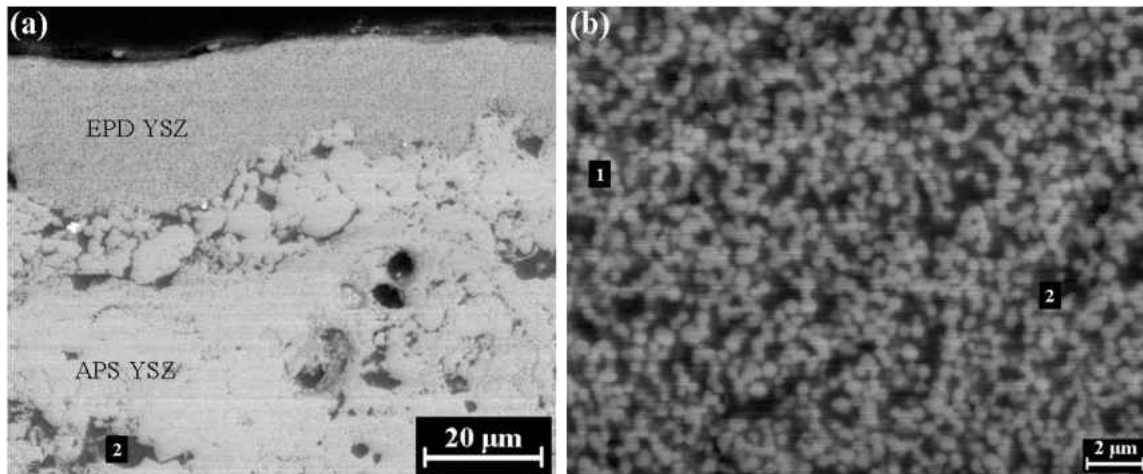


Figure 4.: Cross-sectional backscattered electron micrographs showing the ingress CMAS through EPD YSZ during high-temperature CMAS exposure at 1300°C for 1 h: (a) CMAS infiltrated APS YSZ with EPD YSZ overlay, (b) a magnified view of EPD YSZ overlay after S attack; Region 1: YSZ , Region 2: solidified CMAS.

It should be noted that the YSZ as a dense EPD overly is also susceptible to thermochemical degradation by corrosive melt such as vanadates, sulfates and CMAS. Even though melt penetration rate can be reduced through employing a dense YSZ overlay, a complete protection requires trapping of molten compounds through thermochemical interaction. Overlay coating of desired oxide ceramic that can trap corrosive melt through formation/crystallization of compounds having a higher melting temperature and thus also increase the viscosity of melt would be a promising solution. Thus, in this study, an attempt has been taken to fabricate a desired overlay by EPD to achieve alumina and/or magnesia based coatings in order to trap CMAS and vanadate/sulfate deposits, respectively.

4.6.2. Alumina Overlay

Alumina, a promising candidate to trap CMAS deposits through thermochemical interaction, was employed as a sacrificial overlay ceramic in this study. Crack-free alumina overlay coatings of thickness up to 100 μm were produced with deposition durations ranging up to 15 minutes using the EPD and densification process parameters elaborated in Chapter 3. EPD alumina overlay was achieved through sintering the homogeneous alumina ($\alpha\text{-Al}_2\text{O}_3$) power compact at 1200°C for 10 h. XRD pattern collected from the free-standing APS YSZ modified with EPD alumina overlay is presented in Fig. 4.49. Presence of rhombohedral $\alpha\text{-Al}_2\text{O}_3$ as the primary phase constituent of the EPD overlay on APS YSZ is presented by the XRD results.

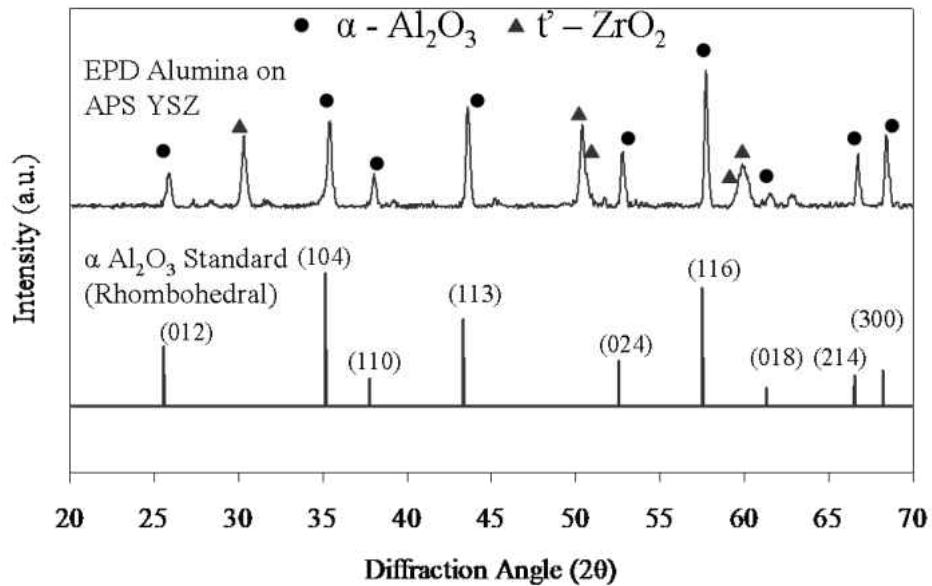


Figure 4.: XRD pattern collected from the surface of EPD alumina overlay on free-standing APS YSZ coating showing rhombohedral $\alpha\text{-Al}_2\text{O}_3$ as the primary phase constituent.

Microstructural homogeneity of the synthesized alumina overlay was also thoroughly examined. Sintered microstructure of alumina overlay is seen in the presented secondary electron micrographs in Fig. 4.50. Initial assessment of the microstructure reveals excellent packing homogeneity associated with a well-dispersed EPD suspension. Such a crack-free overlay with uniform pore distribution is promising for strain-tolerant durable overlay coating applications for TBCs.

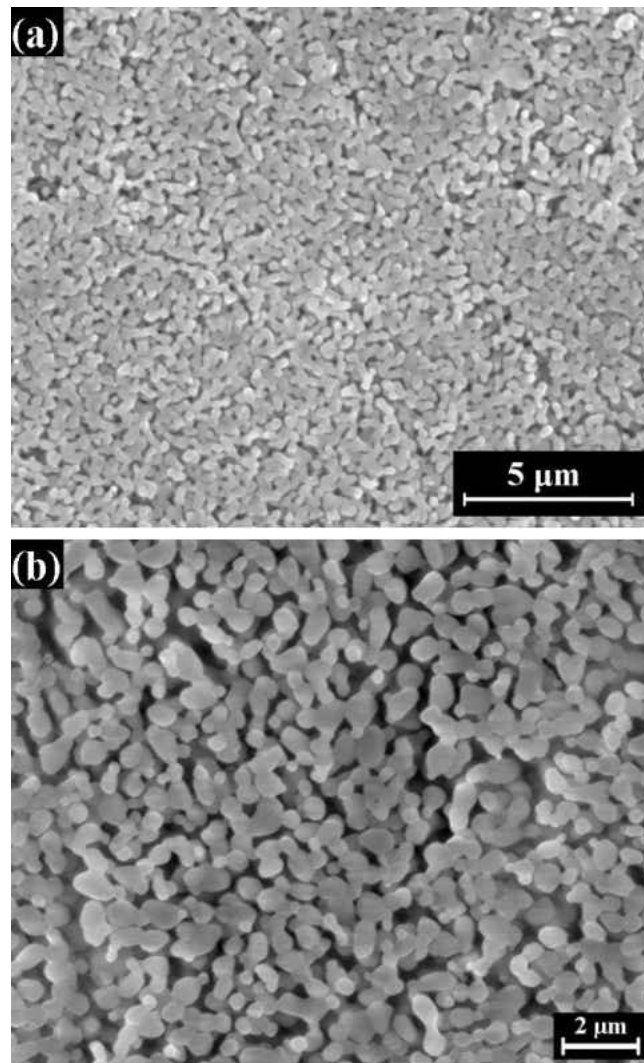


Figure 4.: Secondary electron micrographs of EPD alumina overlay achieved by sintering at 1200°C for 10 h reveal the typical sintered microstructure.

Figure 4.51 presents the cross-sectional microstructures of the EPD alumina overlay of 60 μm thickness (4 minutes of EPD) on the free-standing APS YSZ that was sintered at 1200°C for 10 h. A continuous crack-free adherent EPD overlay is observed in Fig. 4.51(b) with a dense sintered alumina microstructure with a uniform pore distribution.

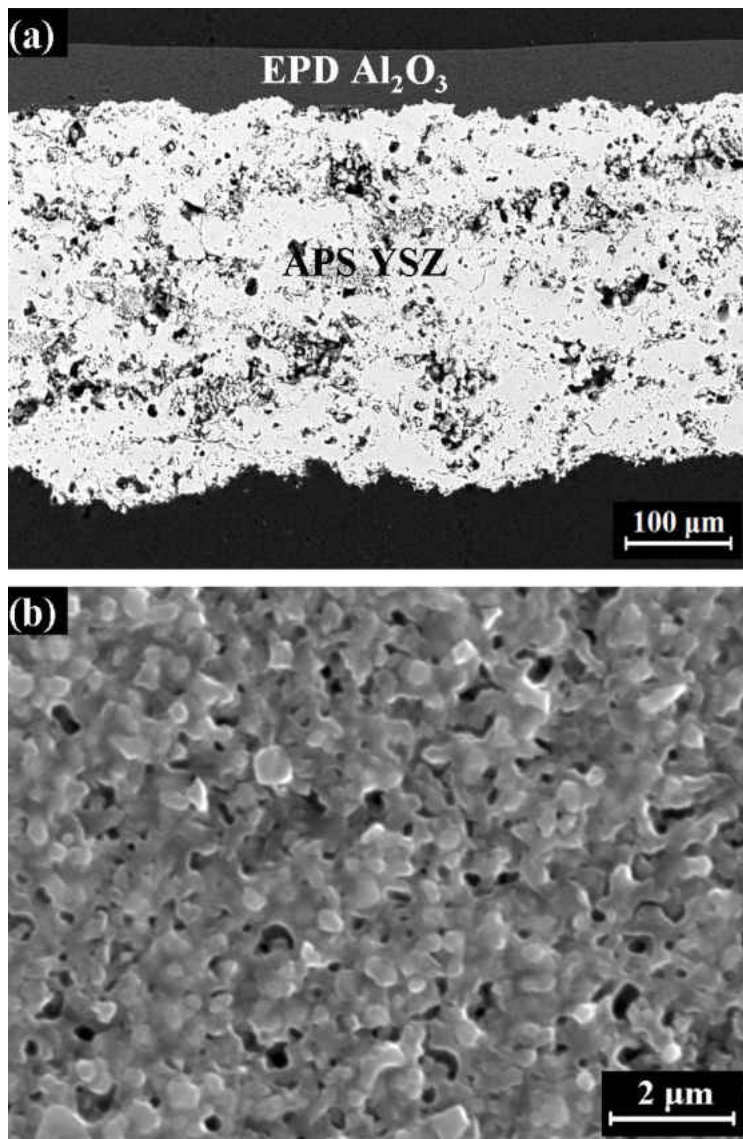


Figure 4.: Cross-sectional micrographs: (a) backscattered electron micrograph showing free-standing YSZ coatings with 60 μm thick alumina overlay achieved by EPD followed by sintering at 1200°C for 10h; (b) secondary electron micrograph showing a magnified view of cross-sectional microstructure of EPD overlay.

Overlay thickness can be readily controlled by the EPD deposition time, while other influencing parameters such as applied voltage, EPD bath solid concentration, bath chemistry can be fixed as constants. A plot of overlay thickness as a function of deposition time during the EPD with all other parameters held constant is presented in Fig. 4.52. An initial linear relationship followed by a non-linear thickness saturation regime is observed. Alumina overlay up to 100 μm thick was readily achieved by EPD with deposition duration of 15 minutes. Cross-sectional secondary electron micrographs shown in Fig. 4.53 illustrate the adherent uniform crack-free alumina overlay of 100 μm thickness deposited on the APS YSZ. Promising interfacial adherence between the EPD alumina and the APS YSZ is also evident from the micrograph shown in Fig. 4.53(b). The free standing YSZ with alumina overlay, when subjected to isothermal testing with CMAS deposit at 1300°C for 1 h demonstrated the promising ability of the EPD overlay in protecting the APS YSZ from the CMAS attack. Secondary electron micrographs shown in Fig. 4.54 demonstrate the microstructural evolution due to crystallization of the CMAS from thermochemical interaction with alumina overlay.

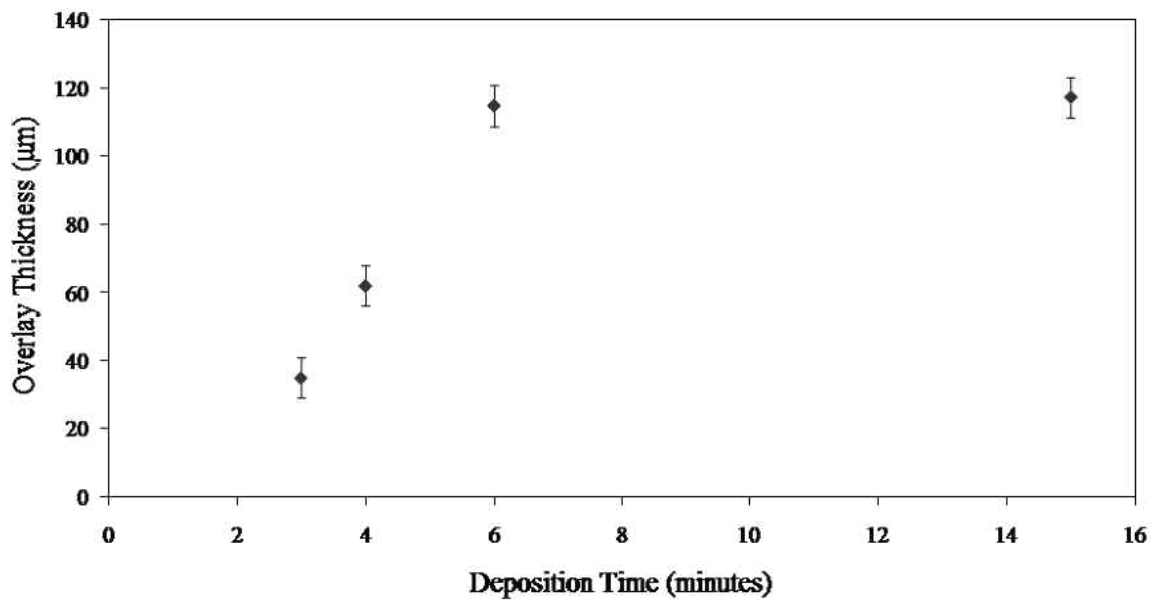


Figure 4.: Plot of sintered alumina overlay thickness vs. deposition time during EPD processing of alumina overlay for APS YSZ.

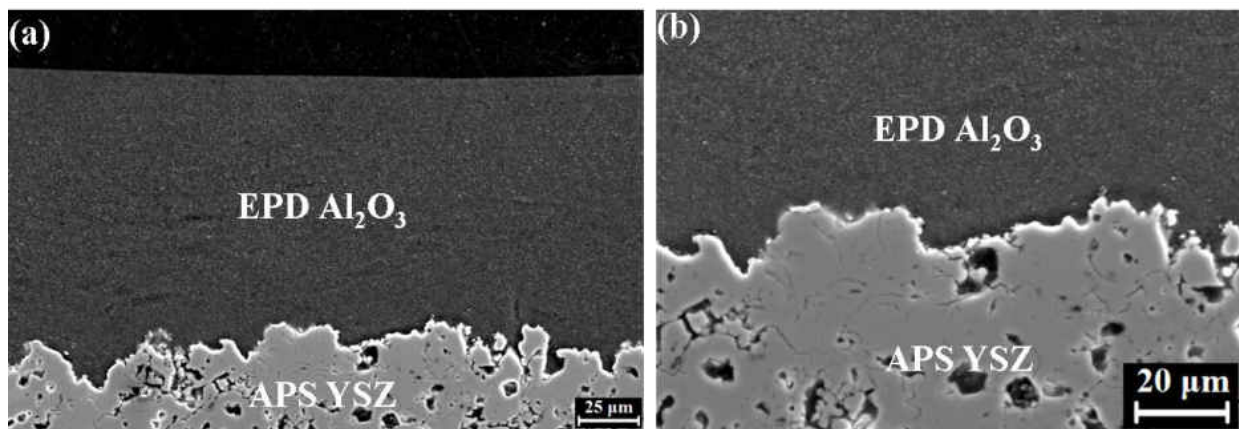


Figure 4.: Cross-sectional secondary electron micrographs showing (a) a 100 μm thick alumina overlay achieved by EPD for 15 minutes followed by sintering at 1200°C for 10 h and (b) APS YSZ/EPD Alumina interface.

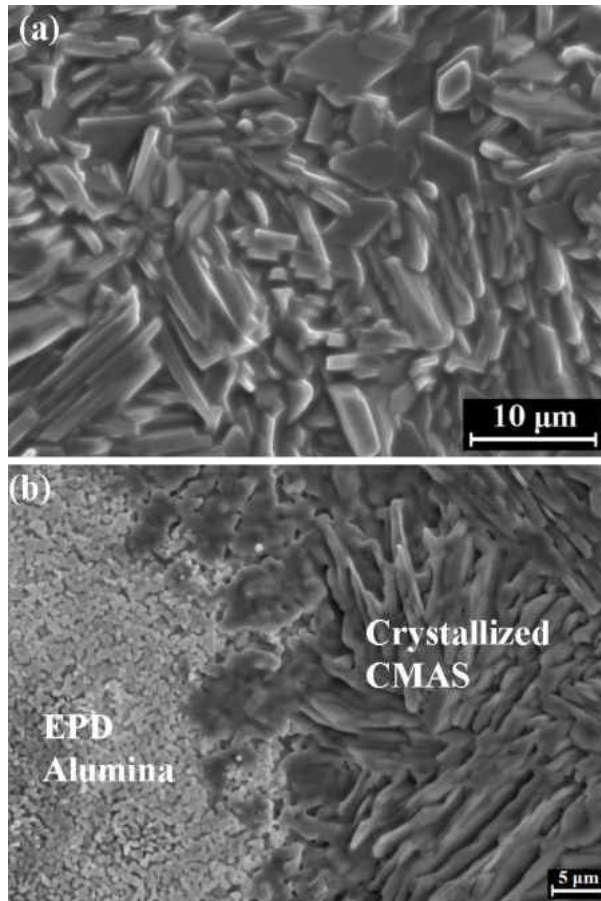


Figure 4.: Secondary electron micrographs showing the surface microstructural evolution due to thermochemical interaction between APS YSZ with alumina overlay and CMAS melt at 1300°C for 1 h: (a) CMAS crystallized as platelets; (b) Alumina overlay arresting the CMAS melt ingress through crystallization.

CMAS was found to crystallize as platelets, which are visible in Fig. 4.54. Platelet-like morphology of crystallized CMAS along with unreacted alumina overlay is also observed in Fig. 4.54(b). Cross-sectional electron micrographs demonstrating the complete arrest of CMAS ingress due to thermochemical interaction with alumina overlay of desired microstructural characteristics are evident in Fig. 4.55.

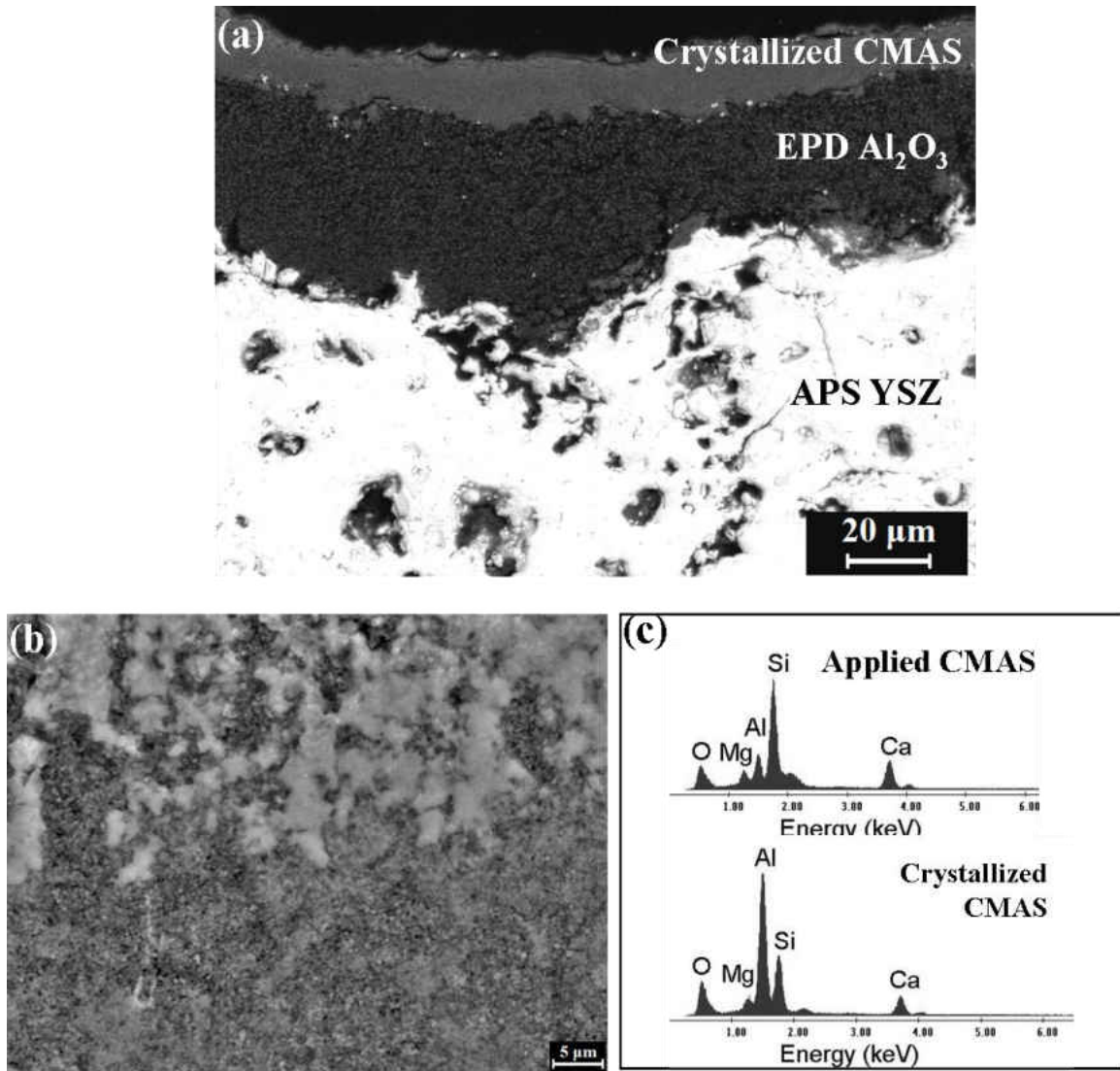


Figure 4.: Cross-sectional backscattered electron micrograph demonstrating the complete arrest of CMAS melt ingress by the crack-free alumina overlay; (b) secondary electron micrograph also reveals the suppression of CMAS melt ingress and (c) Corresponding XEDS spectra revealing the increase of Al content in crystallized CMAS.

CMAS melt was completely arrested within the EPD alumina overlay with a penetration thickness only up to 20 μm. A magnified view illustrating the complete arrest of the CMAS within alumina overlay is also presented in Fig. 4.55(b). The corresponding XEDS spectrum obtained from crystallized CMAS regions presented along with XEDS spectrum of the applied

CMAS in Fig. 4.55 (c) reveals the enrichment of Al content in the CMAS that resulted in CMAS crystallization. XRD pattern obtained from CMAS-attacked surface of the APS YSZ protected with EPD alumina overlay is presented in Fig. 4.56. Primary phase constituents of crystallized CMAS are hexagonal anorthite ($\text{CaAl}_2\text{Si}_2\text{O}_8$) and orthorhombic MgAl_2O_4 spinel.

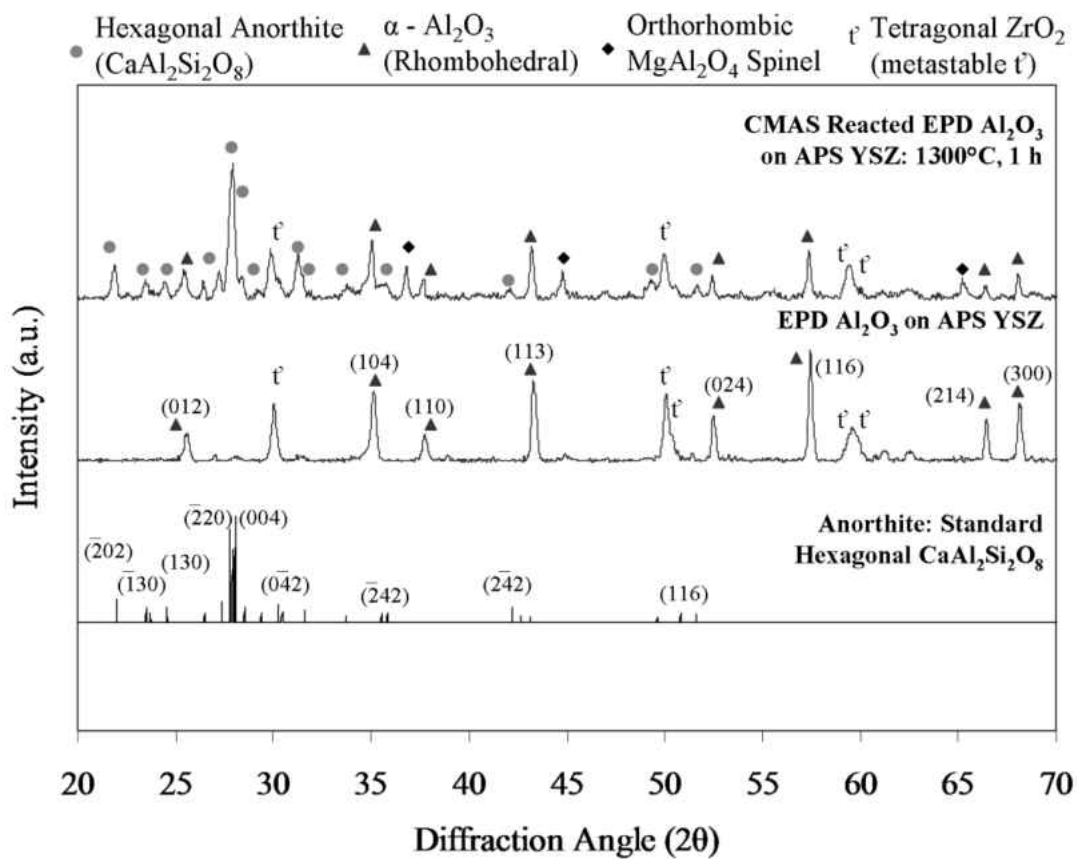


Figure 4.: XRD patterns obtained from as-processed EPD alumina overlay and CMAS interacted EPD alumina after isothermal testing at 1300°C for 1 h. Primary phase constituents corresponding to the complete crystallization of CMAS due to the interaction are hexagonal anorthite ($\text{CaAl}_2\text{Si}_2\text{O}_8$) and orthorhombic MgAl_2O_4 spinel.

A sample from CMAS-interacted EPD alumina overlay was prepared by FIB-INLO for a detailed investigation by TEM. Bright field TEM micrographs along with the corresponding selected area electron diffraction patterns indexed to two different primary phase constituents:

the elongated anorthite crystals ($\text{CaAl}_2\text{Si}_2\text{O}_8$ platelets) and equiaxed MgAl_2O_4 spinel as presented in Figs. 4.57 and 4.58, respectively.

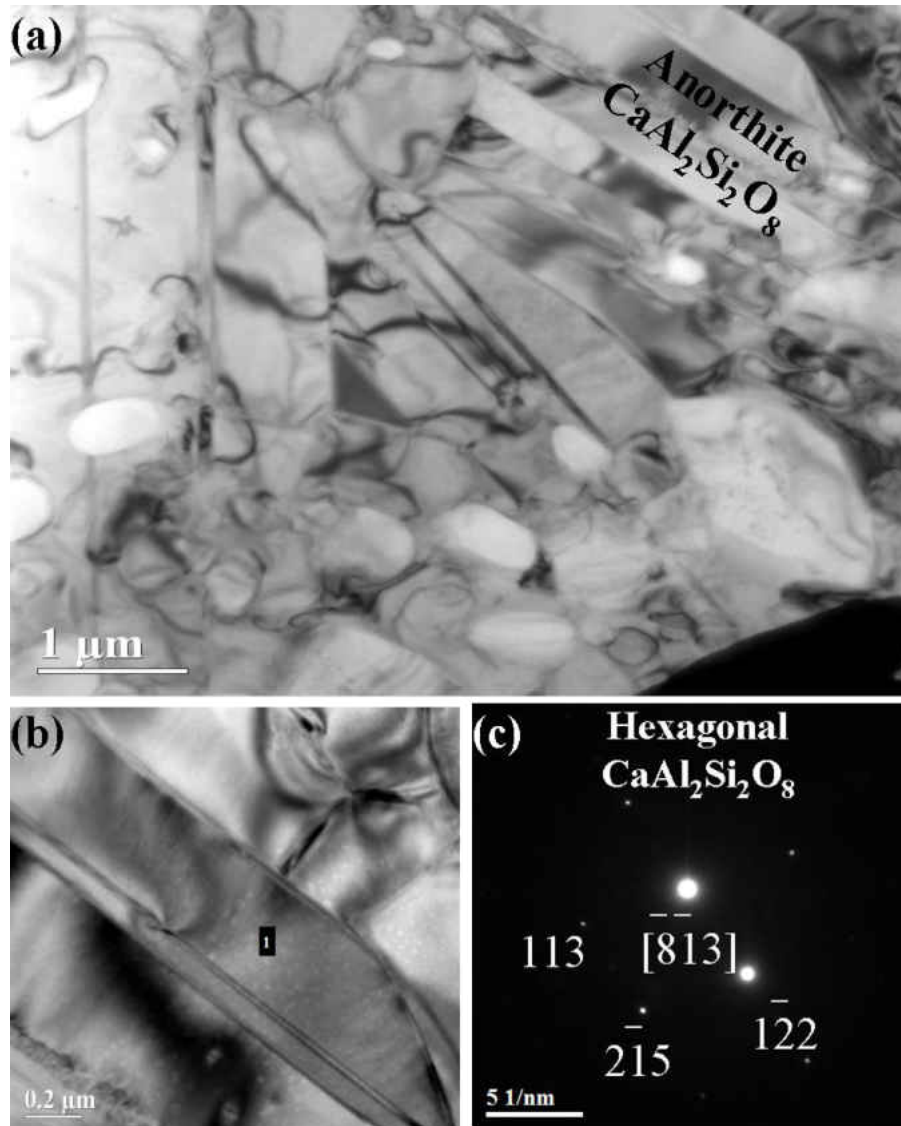


Figure 4.: (a) and (b) Bright field TEM micrographs obtained from crystallized CMAS region resulted from thermochemical interaction with alumina at 1300°C for 1 h highlighting and the presence of anorthite ($\text{CaAl}_2\text{Si}_2\text{O}_8$) platelets and (c) the corresponding selected area electron diffraction pattern obtained from platelet (region 1) indexed to $\text{CaAl}_2\text{Si}_2\text{O}_8$.

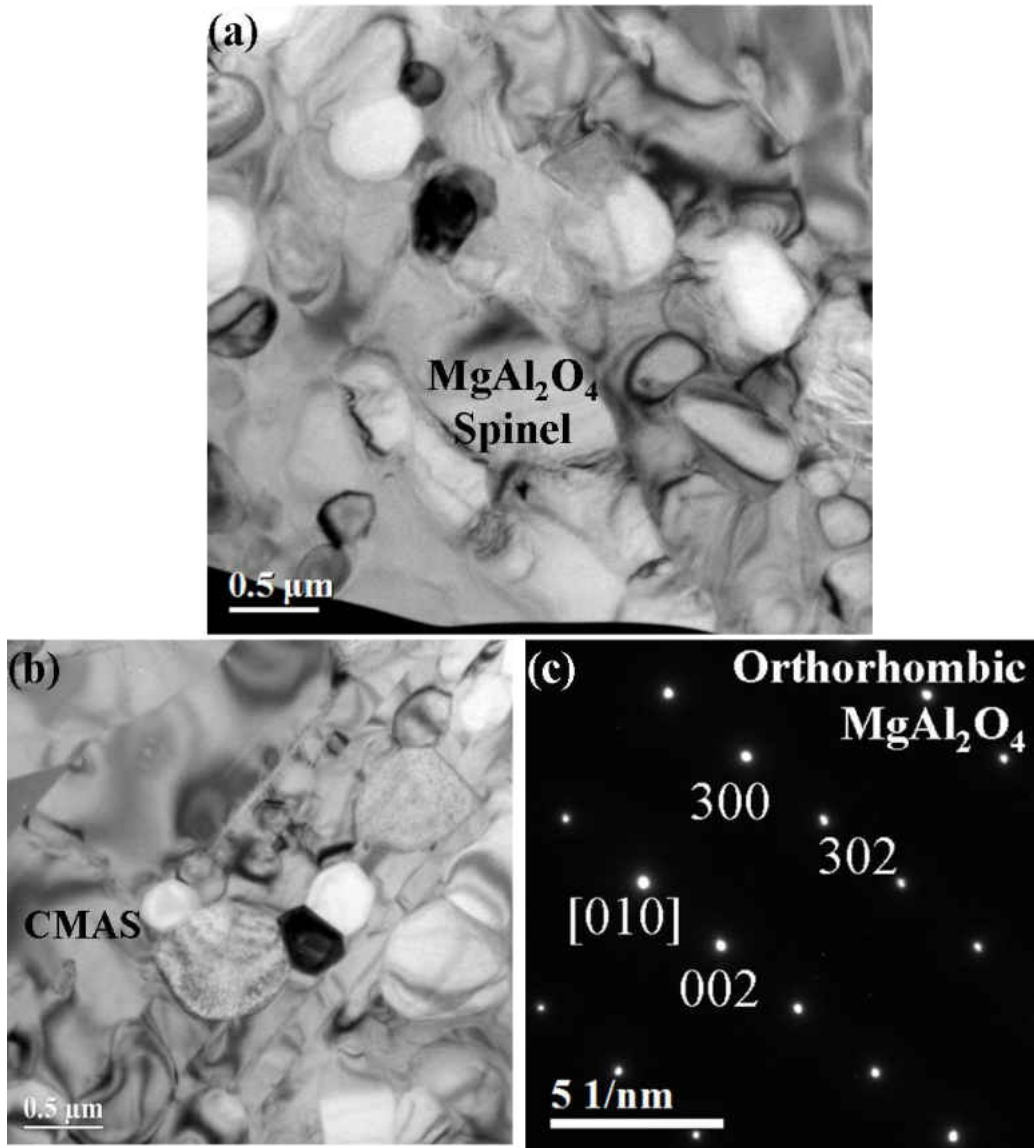


Figure 4.: (a) and (b) Bright field TEM micrographs obtained from crystallized CMAS region resulted from thermochemical interaction with alumina at 1300°C for 1 h highlighting the presence of equiaxed spinel MgAl₂O₄ and (c) the corresponding selected area electron diffraction pattern indexed to orthorhombic MgAl₂O₄.

4.6.3. Magnesia Overlay

Magnesia overlay would be a promising solution to trap corrosive acidic melts such as V_2O_5 and SO_3 (from sulfates). MgO overlay was processed by EPD technique followed by sintering at 1100°C for 10 h. MgO, having a relatively higher CTE in comparison to the YSZ, cannot yield a durable thick dense overlay. However, a thinner MgO overlay (up to $25\ \mu\text{m}$) of relatively higher porosity can be a choice for durable overlay to protect APS TBCs from hot corrosion. Secondary electron micrographs presented in Fig. 4.59 show the uniform, crack-free surface and homogeneous particle compact resulted from the EPD and controlled sintering.

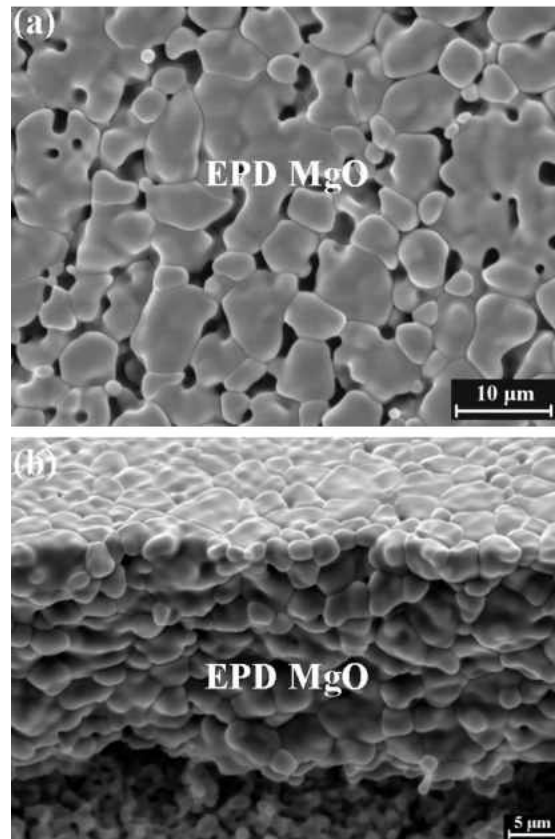


Figure 4.: (a) Secondary electron micrograph of MgO surface achieved by EPD on the APS YSZ followed by sintering at 1100°C for 10 h. (b) Secondary electron micrograph of a fractured MgO cross-section showing the microstructural homogeneity.

A sintered MgO microstructure seen in Fig. 4.59(a) shows the typical surface morphology. A dense sintered cross-sectional microstructure is also evident from the micrograph of fractured MgO overlay on the APS YSZ as presented in Fig. 4.59(b). A cross-sectional backscattered electron micrograph shown in Fig. 4.60 reveals the uniformly continuous 25 μm thick EPD MgO overlay produced after sintering at 1100°C for 10 h. In order to assess the potential of EPD MgO overlay coatings in hot corrosion resistance, APS YSZ with 25 μm thick EPD MgO overlay was subjected to V_2O_5 attack at 900°C for 1 h. Significant changes in the surface morphology of EPD MgO overlay was observed as presented in Fig. 4.61 (a). A cross-sectional view of the EPD MgO overlay on APS YSZ after V_2O_5 testing, presented in Fig. 4.61(b), shows the complete suppression of V_2O_5 melt ingress within the MgO overlay.

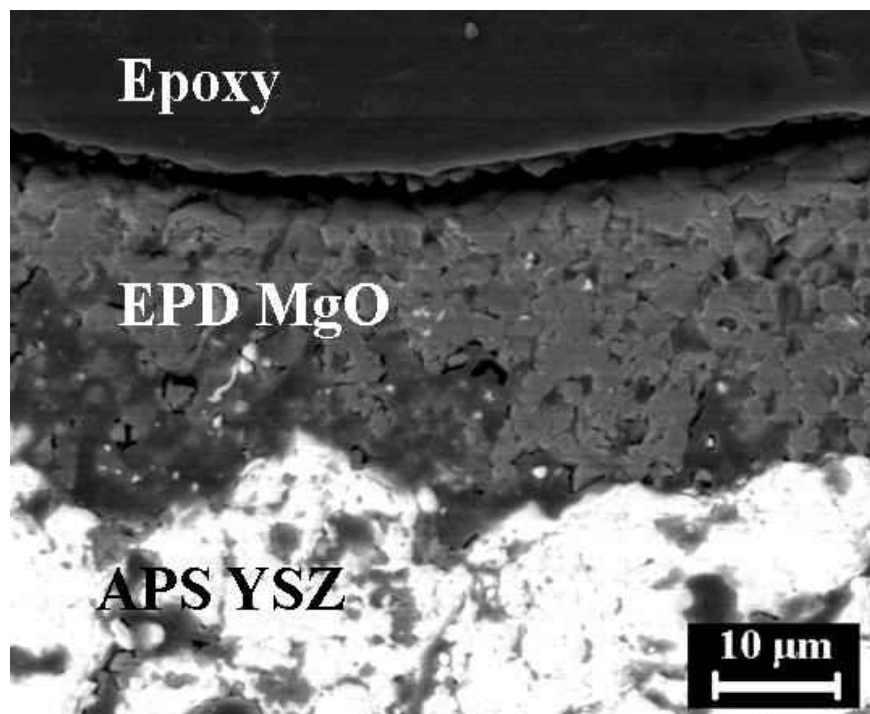


Figure 4.: Cross-sectional backscattered electron micrograph shows the 25 μm thick EPD MgO overlay on a free-standing APS YSZ specimen.

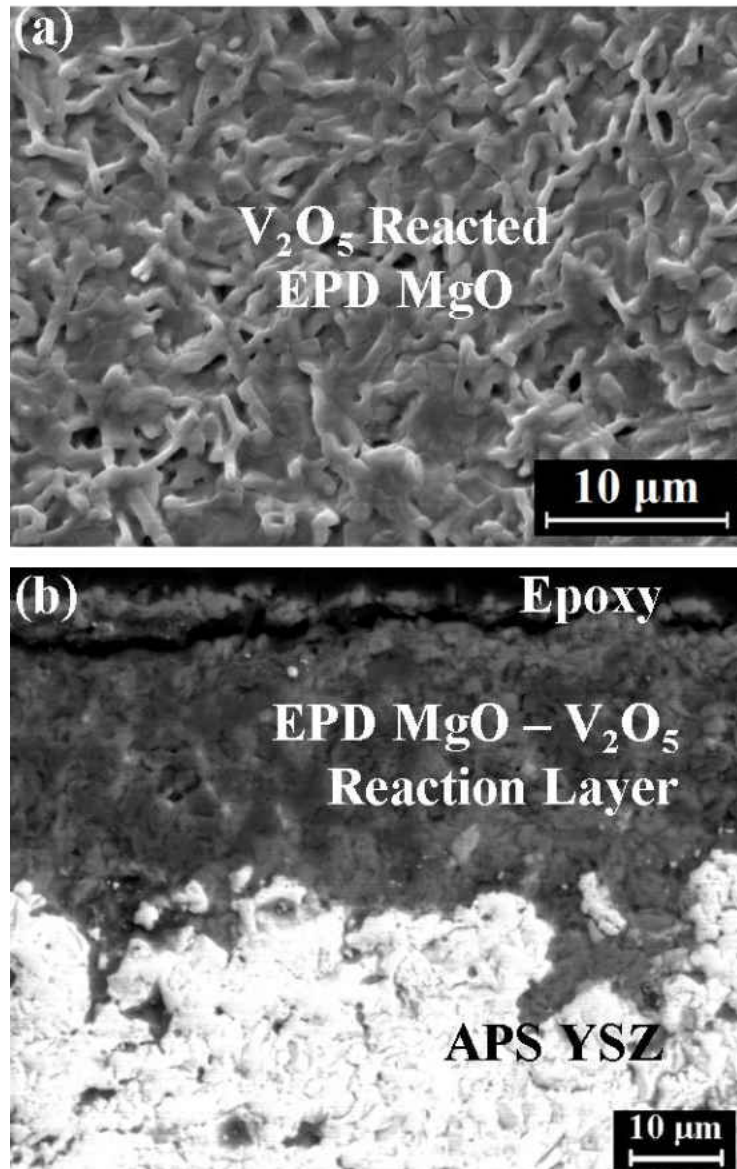


Figure 4.: (a) Secondary electron micrograph shows the surface morphological changes of MgO overlay due to microstructural evolution during interaction with V_2O_5 deposit at 900°C for 1 h, (b) Cross-sectional backscattered electron micrograph highlighting the suppression of V_2O_5 melt ingress and MgO- V_2O_5 interaction layer.

Interaction of MgO with V_2O_5 was found to protect the APS YSZ. The MgO overlay trapped the corrosive melt by readily forming reaction products. The reaction products were identified by XRD analysis, as presented in Fig. 4.62. The primary phase constituents of the

interaction layer were found to be triclinic $\text{Mg}_2\text{V}_2\text{O}_7$ and orthorhombic $\text{Mg}_3\text{V}_2\text{O}_8$. These reaction products possess high melting temperature (T_m : $\text{Mg}_2\text{V}_2\text{O}_7$: 930°C , $\text{Mg}_3\text{V}_2\text{O}_8$: 1070°C) and thus facilitated in arresting V_2O_5 melt ingress.

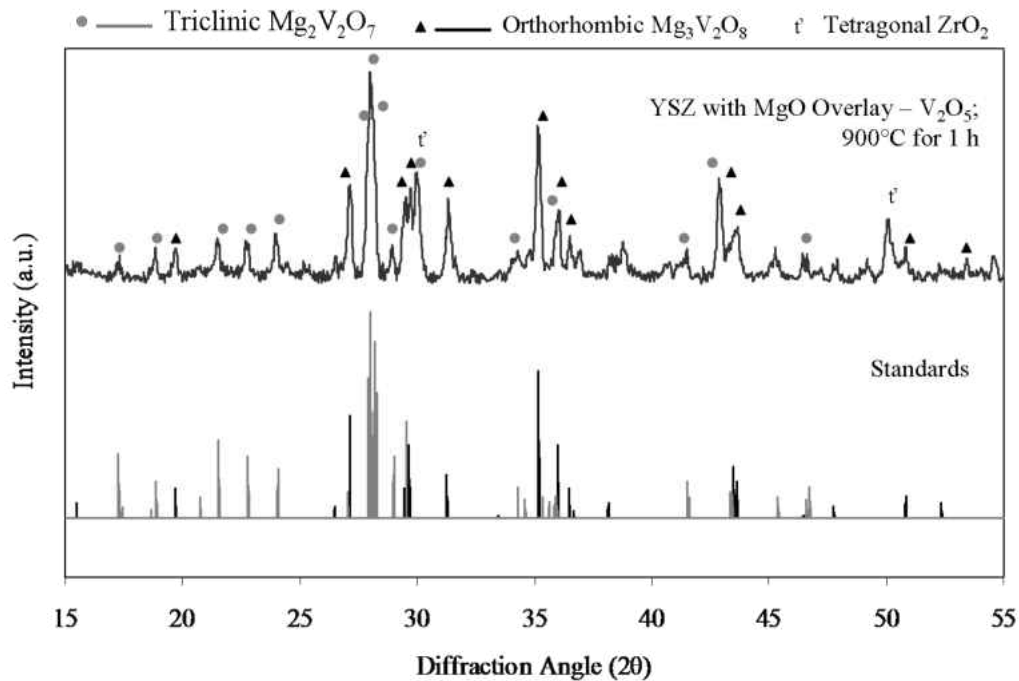


Figure 4.: XRD pattern obtained from V_2O_5 -interacted EPD MgO after isothermal testing at 900°C for 1 h. Primary phase constituents corresponding to the complete arrest of V_2O_5 melt ingress are triclinic $\text{Mg}_2\text{V}_2\text{O}_7$ and orthorhombic $\text{Mg}_3\text{V}_2\text{O}_8$.

4.6.4. Alumina-Magnesia Composite Overlay

In order to develop a overlay for APS TBCs that can provide complete protection against a combination of corrosive molten deposits such as V_2O_5 , Na_2SO_4 and CMAS, fabrication of a composite overlay composed of Al_2O_3 and MgO through codeposition of particles by EPD was also examined in this study. For EPD of Al_2O_3 -MgO overlay, a colloidal dispersion of individual particles of Al_2O_3 and MgO with a weight ratio of 1:1 with the EPD process and sintering

conditions aforementioned in Chapter 3. Free-standing APS YSZ with Al_2O_3 -MgO composite overlay was individually studied in contact with corrosive V_2O_5 melt at $900\text{ }^\circ\text{C}$ and CMAS melt at $1250\text{ }^\circ\text{C}$. Cross-sectional backscattered electron micrographs presented in Fig. 4.63 reveal the continuous, crack-free, adherent nature of the composite overlay. The overlay was found to be composed of Al_2O_3 , MgO and MgAl_2O_4 spinel as seen from respective XEDS spectra presented in Fig. 4.63 (c). Spinel formation occurred during the sintering treatment.

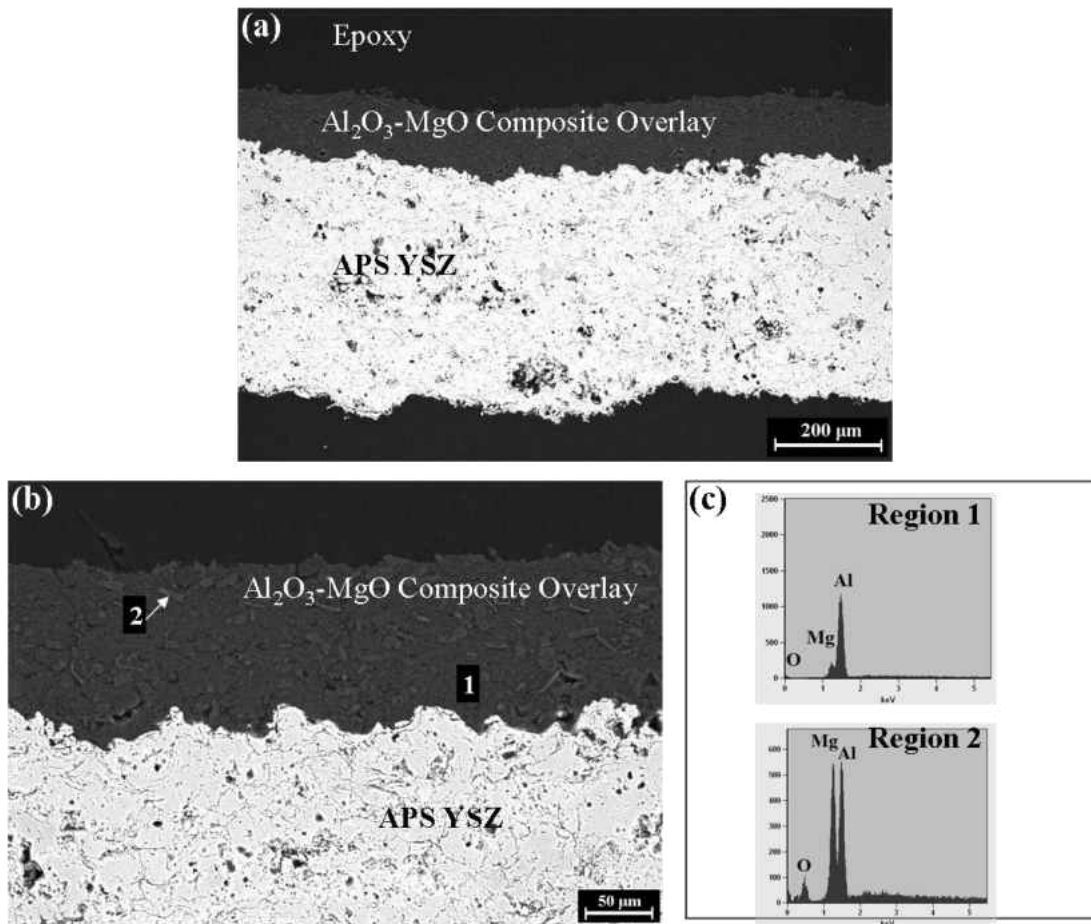


Figure 4.: Cross-sectional backscattered electron micrographs (a and b) illustrate the continuous crack-free characteristics of Al_2O_3 -MgO composite overlay on APS YSZ achieved by electrophoretic codeposition followed by sintering at 1100°C for 5 h; (c) Characteristic XEDS spectra from regions 1 and 2 confirm the phase constituents of overlay as Al_2O_3 -MgO composite and MgAl_2O_4 spinel respectively.

The APS YSZ with the composite overlay was found to be resistant to molten CMAS attack. After a 1 h isothermal exposure of the coating assembly to CMAS deposit at 1250°C, crystallization of CMAS due to thermochemical interaction with Al₂O₃-MgO composite was evident. Figures 4.64 (a) and (b) present the secondary electron micrographs obtained from the surface of the CMAS-interacted specimen that revealed the crystallization of CMAS to equiaxed crystals. The cross-sectional backscattered electron micrographs shown in Figs. 4.64 (c) and (d) demonstrate the complete suppression of CMAS melt ingress limited within the composite overlay, which is attributed to the crystallization of CMAS. The APS YSZ was found to be completely protected from CMAS attack. The crystallized CMAS was found to consist of diopside [Ca(Mg,Al)(Si,Al)₂O₆] and anorthite [CaAl₂Si₂O₈] crystals.

Similarly, after a 1 h isothermal exposure to V₂O₅ deposit at 900°C, magnesium vanadate compound formation due to thermochemical interaction between the corrosive V₂O₅ melt with Al₂O₃-MgO composite was also observed. Figure 4.65 presents the evolution of V-rich reaction products that can be seen from the surface secondary electron micrograph in Fig. 4.65 (a). The cross-sectional backscattered electron micrograph in Fig. 4.65 (c) highlights the arrest of V₂O₅ melt ingress through formation of magnesium vanadates (Mg₂V₂O₇ and Mg₃V₂O₈) that possess higher melting temperatures. However, V₂O₅ being highly acidic corrosive melt, some attack on the underlying YSZ up to 30 μm deep was also observed. An optimum protection can be achieved by employing such a composite overlay with tailored composition (starting EPD bath composition) and microstructure (starting particle size).

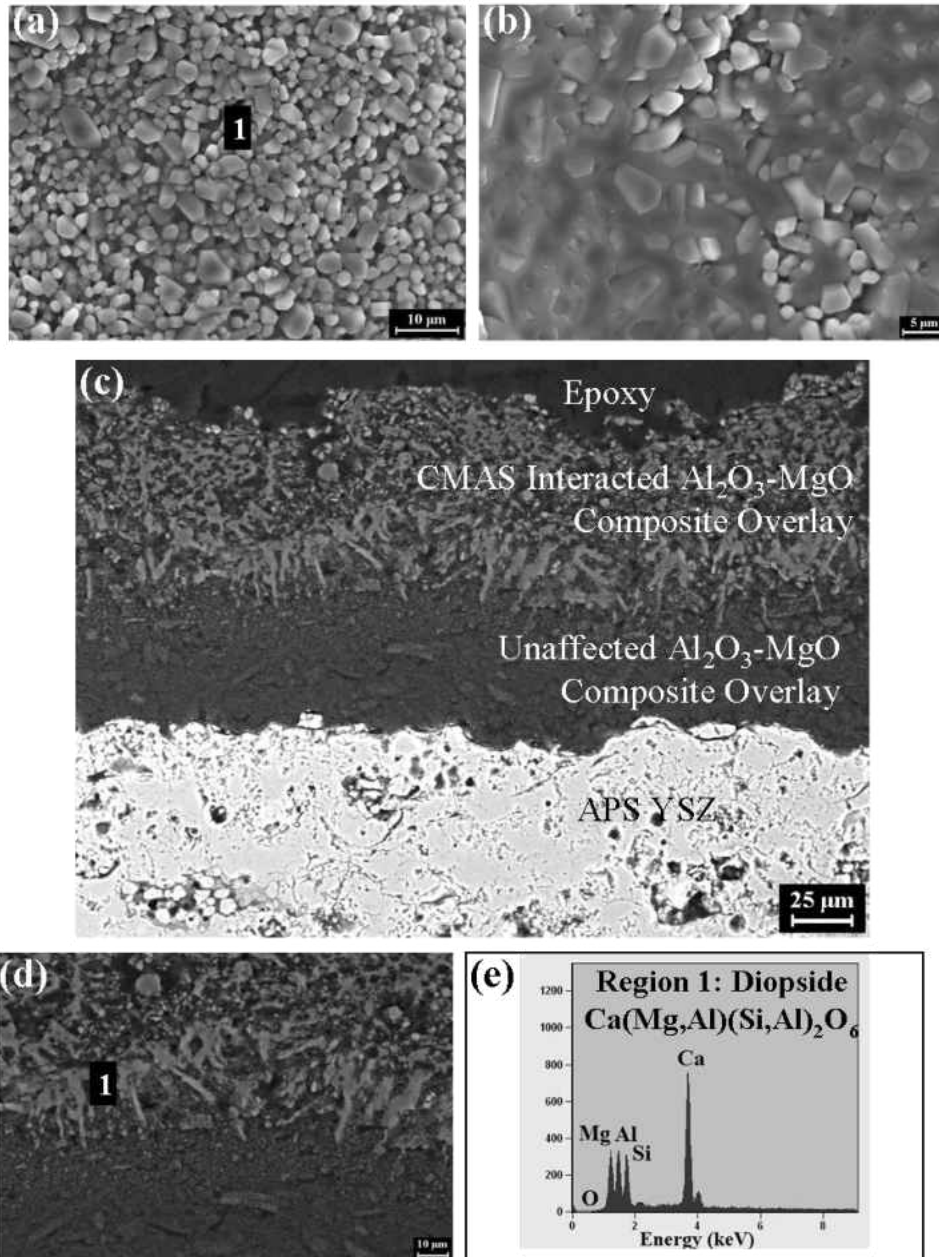


Figure 4.: Microstructural evolution due to thermochemical interaction of CMAS and Al₂O₃-MgO composite overlay (on APS YSZ) at 1250°C for 1 h: (a) and (b) surface secondary electron micrographs illustrating the crystallization of CMAS due to thermochemical interaction with the composite barrier overlay; (c) and (d) cross-sectional backscattered electron micrographs demonstrating the complete suppression of CMAS ingress through crystallization; (e) characteristic XEDS spectrum of region 1 confirm Diopside [Ca(Mg,Al)(Si,Al)₂O₆] as one of the products of crystallized CMAS.

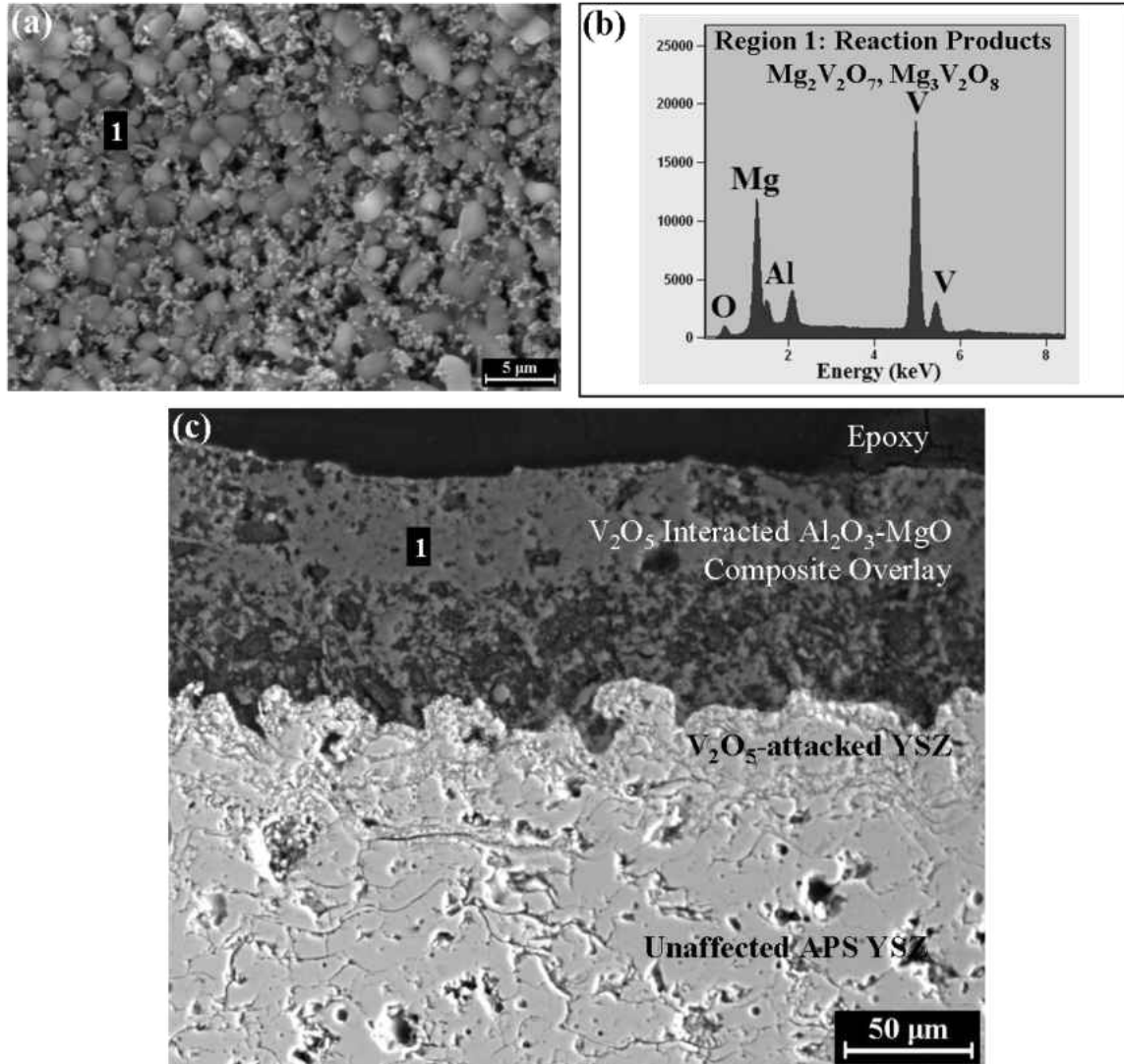


Figure 4.: Microstructural evolution due to thermochemical interaction of V_2O_5 melt and Al_2O_3 - MgO composite overlay (on APS YSZ) at $900^\circ C$ for 1 h: (a) surface secondary electron micrograph showing the evolution of V-rich reaction products due to thermochemical interaction with the composite barrier overlay; (b) characteristic XEDS spectrum of V-rich reaction products [$Mg_2V_2O_7$ and $Mg_3V_2O_8$]; (c) cross-sectional backscattered electron micrograph demonstrating the complete suppression of V_2O_5 ingress through formation of reaction products that have melting temperature.

4.7. Commercial TBCs modified with EPD Overlay

Commercial-production TBCs consisted of APS 8YSZ topcoat and LPPS CoNiCrAlY bond coat on IN738LC superalloy substrate discs (1" in diameter) were modified with a protective Al₂O₃ overlay through the EPD process. The process parameters (EPD and sintering conditions) employed for overlay deposition on these commercial TBCs are the same parameters used for the EPD-Al₂O₃ overlay on free-standing APS YSZ coatings. Using 1-hour thermal cyclic exposure testing at 1100°C without any corrosive deposit, TBCs with and without a 75 μm thick EPD Al₂O₃ overlay were found to possess a similar coating durability. As presented in Fig. 4.66, the average TBC lifetime that is defined as the number of thermal cycles for the failure of the YSZ topcoat (a minimum of 50% area spallation), for TBCs with and without Al₂O₃ overlay, was found to be 191 and 196 cycles, respectively.

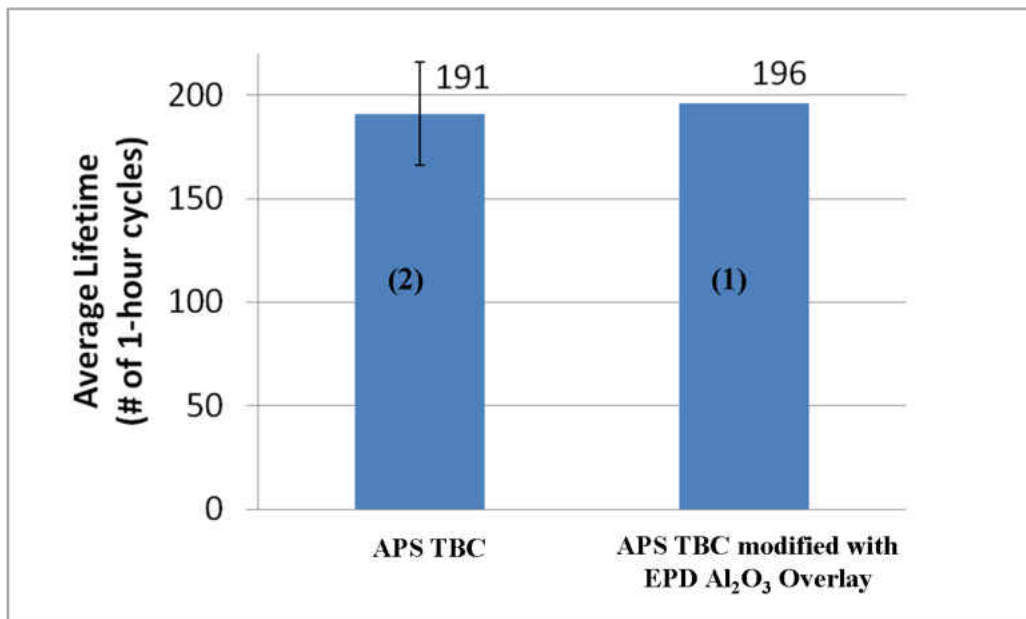


Figure 4.: Plot of average lifetime of TBCs with and without EPD Al₂O₃ overlay assessed through 1-hour thermal cyclic exposure testing at 1100°C under the absence of any corrosive deposit.

Typical APS TBC failure, a complete spallation of the YSZ topcoat, was observed for all commercial TBCs (with and without alumina overlay). Macrographs shown in Fig. 4.67 demonstrate the promising durability of EPD alumina overlay. TBC with alumina overlay that failed through delamination of the YSZ topcoat after 196 “1-hour” thermal cycles revealed the promising structural integrity of EPD overlay. A completely intact Al_2O_3 overlay was found on the spalled YSZ topcoat. Figure 4.67 also shows the failure of TBCs without a protective overlay, which is a typical APS TBC failure through a complete YSZ spallation.

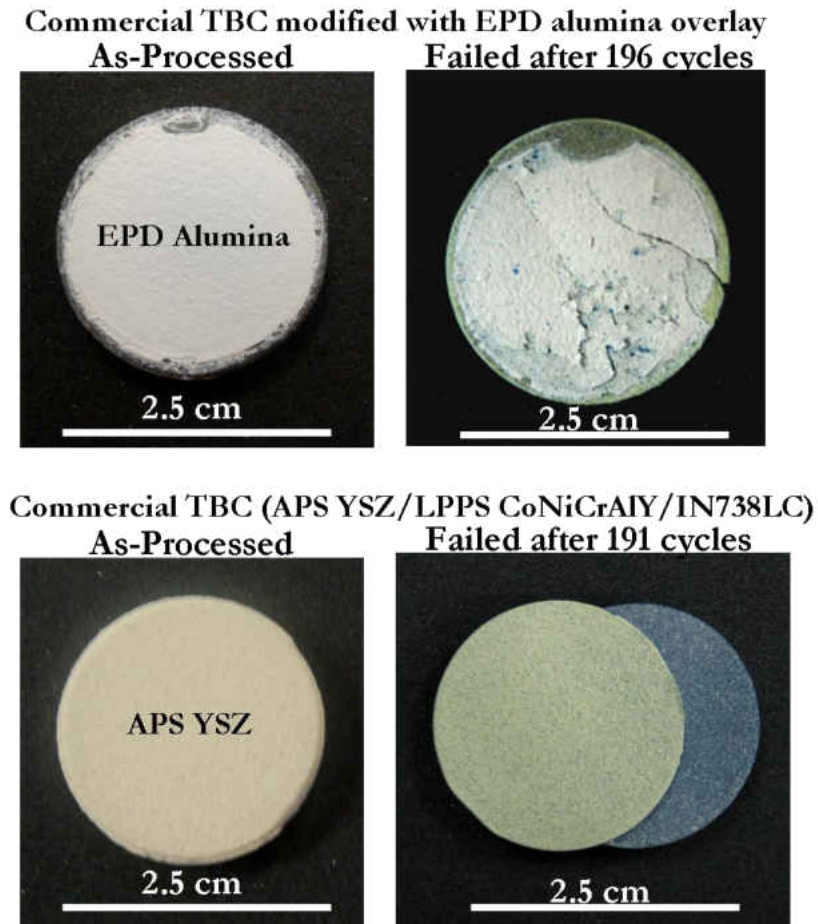


Figure 4.: Macrographs of commercial TBCs with and without EPD Al_2O_3 overlay before and after failure during 1-hour thermal cyclic exposure at 1100°C under the absence of any corrosive deposit.

Cross-sectional backscattered electron micrographs of TBCs without protective overlay after failure are presented in Fig. 4.68. Typical APS TBC failure through a complete delamination of the YSZ, which resulted from the crack initiation within the YSZ topcoat close to the YSZ/TGO interface followed by link-up of these in-plane cracks, is evident. The bond coat was found to be completely β -NiAl-depleted γ phase.

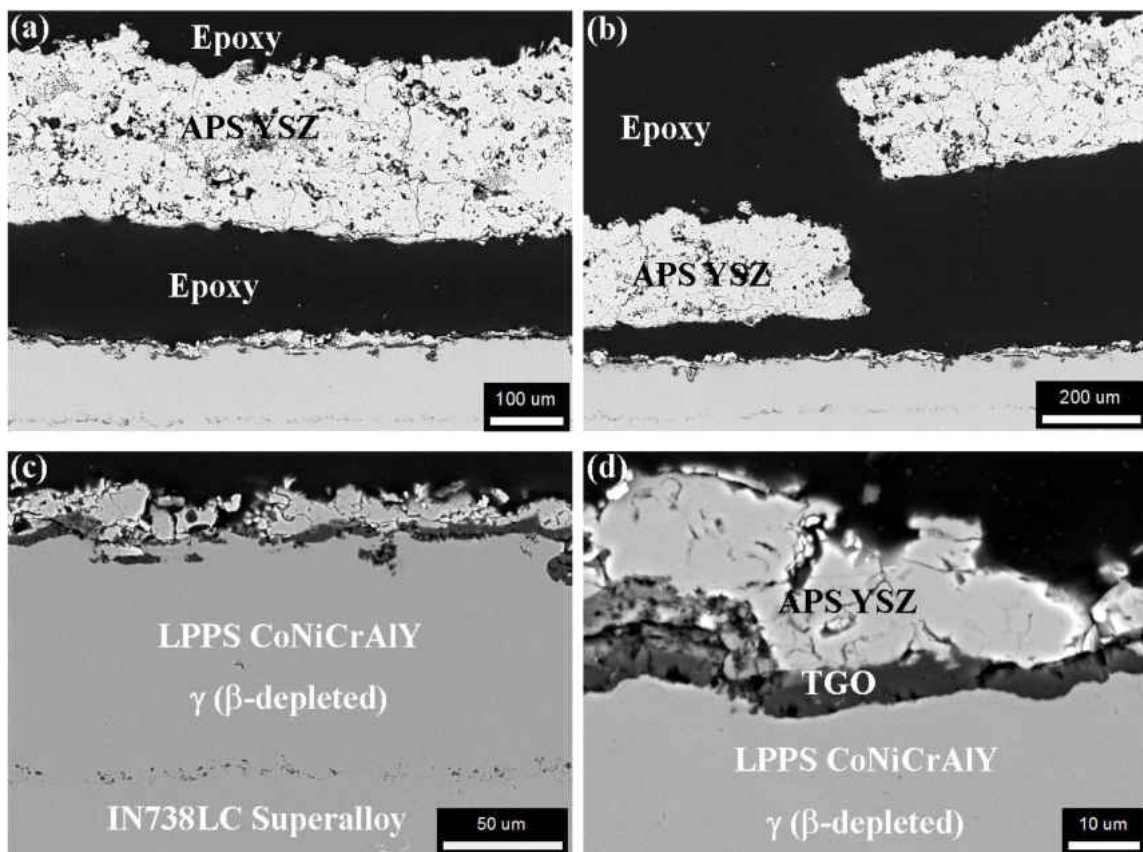


Figure 4.: Cross-sectional backscattered electron micrographs of commercial TBC without EPD Al_2O_3 overlay failed after an average lifetime of 191 “1-hour” cycles at 1100°C .

In the case of TBCs with a $75\ \mu\text{m}$ -thick EPD Al_2O_3 overlay that failed after a lifetime of 196 “1-hour” cycles at 1100°C , the TBC failure was found to be similar: complete delamination of the YSZ topcoat due to link-up of in-plane cracks within the YSZ. The promising durability of

EPD alumina overlay is clearly demonstrated in Fig. 4.69, which highlights the intact EPD alumina overlay even after TBC failure. Even though localized in-plane cracks within the EPD Al_2O_3 overlay are observed, a completely adherent overlay was present throughout the entire cross-section.

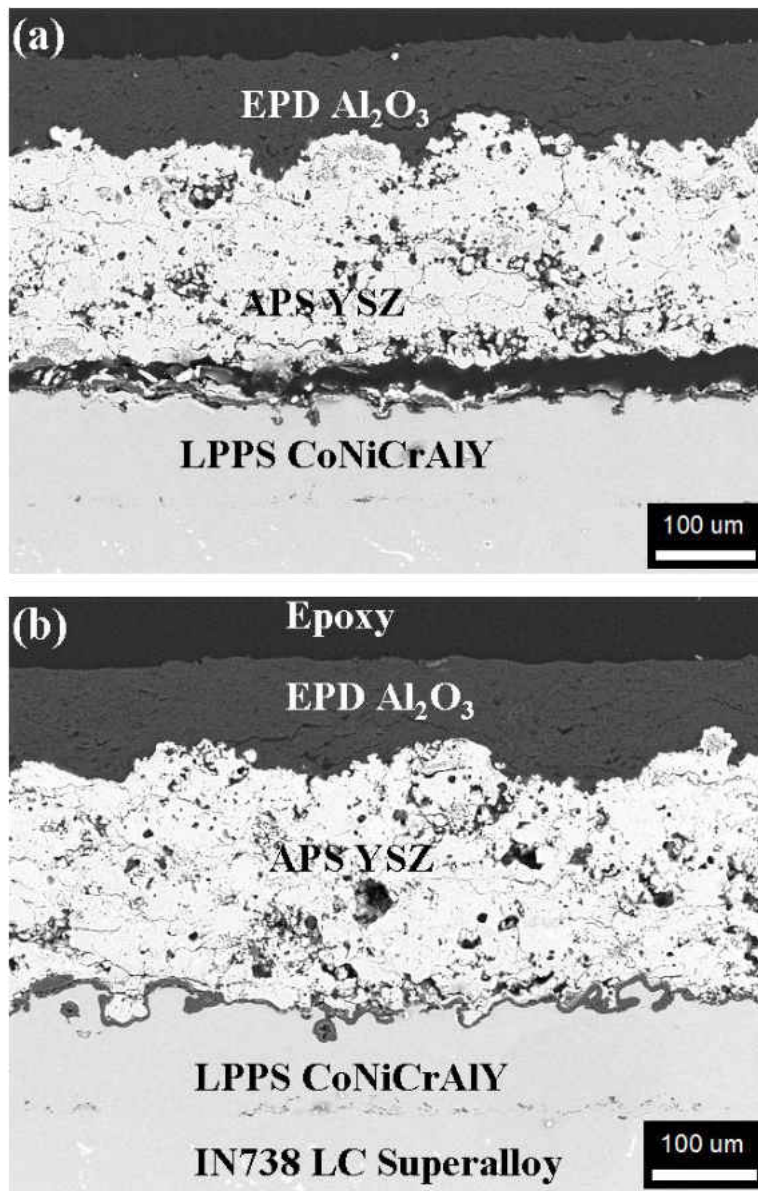


Figure 4.: Cross-sectional backscattered electron micrographs of commercial TBC modified with a 75 μm thick EPD Al_2O_3 overlay failed after a lifetime of 196 “1-hour” cycles at 1100°C.

CHAPTER 5: DISCUSSION

5.1. Degradation of APS YSZ by Molten Deposits due to Fuel Impurities

5.1.1. Degradation of APS YSZ by V₂O₅ Deposit

Below the melting temperature of V₂O₅ (T_m = 690°C), the APS YSZ was found to be chemically inert against any V₂O₅ attack with no evidence of solid-solid interaction. Between 690°C and 747°C, the APS YSZ was found to degrade by molten V₂O₅ through solid-liquid thermochemical interaction. Formation of zirconium pyrovanadate (ZrV₂O₇) as the only reaction product was associated with degradation mechanism. ZrV₂O₇ formation is expected to enrich the YSZ with yttria due to selective reaction of ZrO₂ with V₂O₅. Enrichment of the YSZ with yttria should consequently promote the formation of yttria-rich fluorite-cubic ZrO₂ phase [63]. However, results from this study suggest that ZrV₂O₇ formation was found to be not associated with ZrO₂ phase transformation. The YSZ phase constituent was observed to be the tetragonal ZrO₂ (t'-ZrO₂) phase after V₂O₅ attack at temperatures between 690°C and 747°C within our experimental durations. One of the reasons attributing to this reaction mechanism with no ZrO₂ phase transformation could be the slow reaction kinetics involved in the formation of cubic-ZrV₂O₇ as reported earlier [128]. However, the slow reaction kinetics is not reflected in the results from the cross-sectional microstructural analysis in this study. A significant amount of ZrV₂O₇ formation with the presence of unreacted V₂O₅ melt, as observed in the YSZ exposed to V₂O₅ melt at 720°C even for a short duration of 30 minutes (Fig. 4.5) suggests that the thermochemical interaction is not slow at 720°C. The reaction product ZrV₂O₇ might contain the yttria stabilizer as a solid solution with Y³⁺ substituting Zr⁴⁺ cations. Thus from the observed

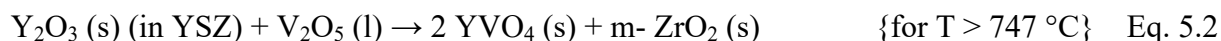
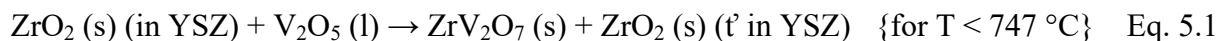
mechanism of ZrV_2O_7 formation with no evidence of ZrO_2 phase transformation, degradation of the YSZ due to molten V_2O_5 attack below 747°C occurred through preferential consumption of ZrO_2 of the YSZ that might have resulted in only a minor enrichment of unreacted YSZ with yttria content.

Experimental results on the YSZ exposed to V_2O_5 melt at temperature above 747°C confirm a completely different degradation mechanism. Reaction of V_2O_5 with yttria stabilizer to form yttrium vanadate (YVO_4) was observed to be the thermochemical interaction at temperature above 747°C . A significant tetragonal- YVO_4 formation led to the disruptive zirconia phase transformation ($t^2 \rightarrow t \rightarrow m+f$) to monoclinic (m) ZrO_2 phase. YVO_4 that occurs as a minimally soluble precipitate is highly stable up to 1810°C , and acts as a low activity sink that would leach the yttria stabilizer from the YSZ [129].

The two different reactions observed could be explained based on the melting behavior of the reaction product, ZrV_2O_7 . According to the studies reported on $\text{ZrO}_2 - \text{V}_2\text{O}_5$ system, the only compound found to exist in the system was zirconium pyrovanadate (ZrV_2O_7) [27]. ZrV_2O_7 melts incongruently at 747°C to ZrO_2 and a liquid mixture with composition of 64% V_2O_5 + 36% ZrO_2 [128, 130]. This incongruent melting gave rise to the different reactions observed in this study, at a temperature of 800°C and 720°C (i.e., above and below the incongruent melting temperature, respectively). At temperatures above 747°C , liquid V_2O_5 resulting from the incongruent melting of ZrV_2O_7 as well as the remaining unreacted V_2O_5 melt directly reacts with Y_2O_3 stabilizer of YSZ to form YVO_4 . XEDS spectra obtained from the solidified V-rich residue in the YSZ after exposure to V_2O_5 melt at 800°C (YVO_4 formation temperature regime) contained a large amount of Zr and V, which may have resulted from the incongruent melting of

ZrV₂O₇. In addition, pure solid ZrO₂ resulting from the incongruent melting of ZrV₂O₇ would be composed of monoclinic ZrO₂ phase.

Reactions 1 and 2 given below represent the solid-liquid thermochemical degradation mechanisms of YSZ by molten V₂O₅ at temperature below and above 747°C, respectively.



Aforementioned, the V₂O₅ in reaction 2 comes from the incongruent melting of ZrV₂O₇ and the initially applied, remaining V₂O₅.

In order to support the argument on YVO₄ formation that is expected to occur above 747°C, various hot corrosion tests were performed at temperatures ranging from 750°C to 900°C for different exposure periods. It was found that the formation of YVO₄ is the predominant reaction mechanism for all temperatures above 747°C leading to the consequent phase transformation.

Although the available literature reports the YVO₄ formation as the only chemical interaction between the YSZ and V₂O₅ [35-40] at high temperatures, this study confirmed the preferential consumption of ZrO₂ of YSZ by V₂O₅ melt form ZrV₂O₇ at lower temperature (T < 747°C).

In this study, an attempt was made to investigate the reaction kinetics associated with the degradation of the YSZ by V₂O₅ melt at temperatures above 747°C through YVO₄ formation and destabilization of the YSZ (t'→t→m+f). Evolution of m-ZrO₂ as a function of exposure time as

discussed in Chapter 4 (Fig. 4.10) was examined. The YSZ samples exposed to V_2O_5 melt at three different temperatures ($T = 750^\circ\text{C}$, 760°C and 770°C) for various duration up to 120 minutes were thoroughly analyzed by XRD. The volume fraction (V_m) of m-ZrO₂ phase transformed due to the aforementioned degradation mechanism (YVO₄ formation) was quantified from XRD spectra based on the relative peak intensities of m ($\bar{1}11$), m (111), t (101) and/or c(111) using the relation proposed by Garvie [131]:

$$V_m = \frac{I(11\bar{1})_m + I(111)_m}{I(11\bar{1})_m + I(111)_m + I(111)_{t,c}} \quad \text{Eq. 5.3}$$

Evolution of m-ZrO₂ after high-temperature isothermal exposure at temperatures above 1450°C and the phase transformation kinetics have been studied by Clarke et al. using the classic Avrami–Johnson–Mehl–Kolmogorov (AJMK) type mechanism-based phenomenological expression [132, 133]. Typical AJMK expression for phase transformation kinetics can be written as:

$$f = 1 - \exp(-k t^n) \quad \text{Eq. 5.4}$$

where, f is the volume fraction, t is the annealing time, n is the Avrami exponent, which is a constant dependent on the phase transformation and crystallization mechanism, and k is the temperature-dependent reaction rate constant that follows Arrhenius-type temperature dependence. Thus, k(T) can be written as:

$$k(T) = k_0 \exp\left(-\frac{Q_A}{RT}\right) \quad \text{Eq. 5.5}$$

where k_0 is the pre-exponential Arrhenius constant, Q_A is the activation energy, R is the universal gas constant and T is the reaction temperature (K).

In order to examine the phase transformation kinetics associated with the evolution of monoclinic ZrO₂ that resulted from YVO₄ reaction product formation, volume fraction of m-ZrO₂ evolved (f_m) was normalized (f_m/f_m (max)) using the value obtained at infinite long time (f_m (t=∞)). For a specific isothermal reaction temperature, the normalized volume fraction of m-ZrO₂ (f_m(t)) calculated using the XRD results from the YSZ exposed to various durations were plotted against time as presented in Fig. 5.1. AJMK expression for mechanisms involving an incubation period (τ) can be written as:

$$f_m = 1 - \exp(-k(t-\tau)^n) \quad \text{Eq. 5.6}$$

Such an incubation period was observed in YSZ-V₂O₅ degradation reaction mechanism at 750°C and 760°C. At a relatively higher temperature of 770°C, the incubation period was negligible. For phase transformation kinetics following AJMK type expression (Eq. 5.6), it has been a common practice to plot $\ln \ln (1/(1-f))$ vs. $\ln (t-\tau)$, which should follow a linear relation. Thus the Avrami exponent (n) and temperature-dependent rate constant (k) can be deduced. Such plots gave the values of n and k for all three temperatures, which were used to fit the data plotted in Fig. 5.1. The AJMK type expression was fitted as shown in Fig. 5.1. The constants and the incubation period for the degradation associated with V₂O₅ attack on the YSZ at three different temperatures are also listed in Table 5.1.

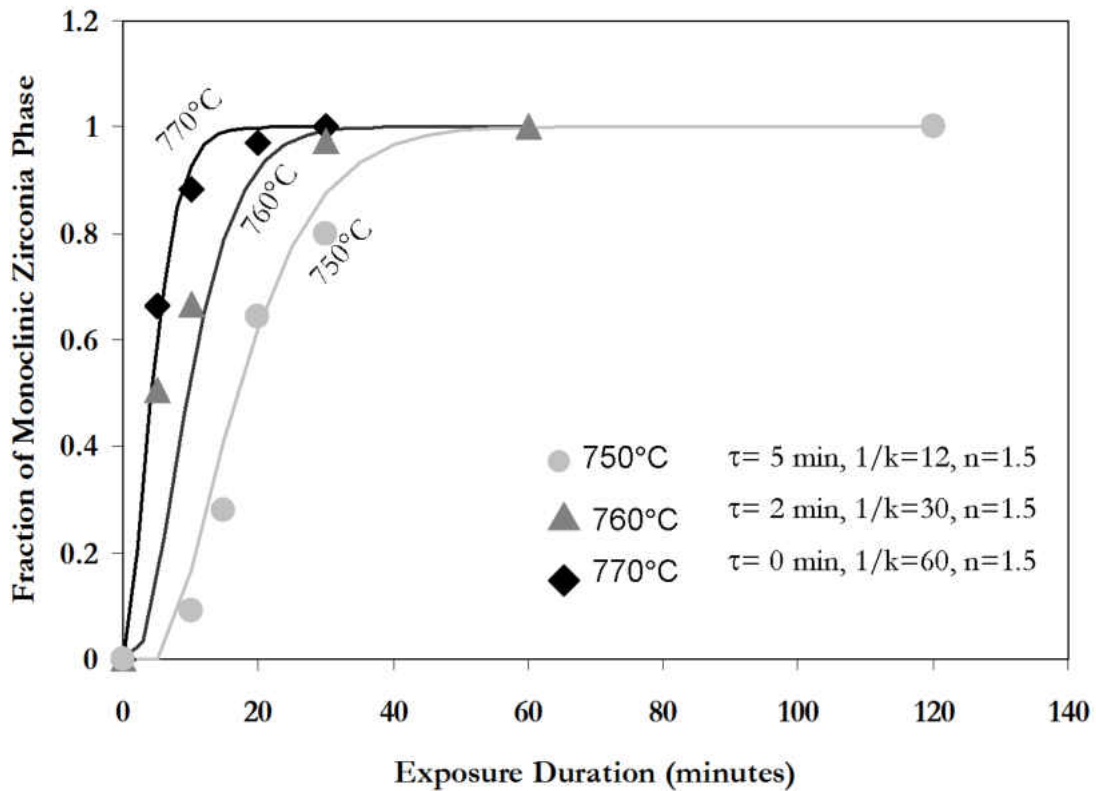


Figure 5.: Plot of volume fraction of monoclinic zirconia phase (f_m) vs. exposure duration (t) associated with V_2O_5 attack of YSZ at three different temperatures and the corresponding AJMK expression-fit.

Table 5.: The constants and the incubation period for the degradation mechanism associated with V_2O_5 attack of YSZ at three different temperatures.

Exposure Temperature (°C)	Incubation Period τ (minutes)	1/k	k (Temperature-dependent rate constant)	Avrami Exponent n
750°C	0	12	0.83333	1.5
760°C	2	30	0.33333	1.5
770°C	5	60	0.16666	1.5

Values of temperature-dependent rate constant (k) determined at three different temperatures were employed to derive the Arrhenius-type phenomenological expression using the plot $\ln(k)$ vs. $1/T$ as shown in Fig. 5.2. This plot yields the activation energy (QA) for the degradation reaction (m-ZrO₂ evolution due to YVO₄ formation), which was calculated to be 713 kJ/mol. It is worth mentioning that even though, similar attempts have been taken to derive the thermodynamic information associated with m-ZrO₂ phase evolution due to ZrO₂ destabilization during high-temperature aging at $T > 1400^\circ\text{C}$ [132, 133], there is no existing report on such thermodynamic information related to hot corrosion attack of the YSZ based ceramics. The reported activation energy values for $t' \rightarrow t \rightarrow m+f$ phase transformation are close to 100 kJ/mol [60], a value similar to the activation energy for oxygen vacancy diffusion. A high activation energy estimated from this study, could be attributed to the YSZ dissolution mechanism that results in phase transformation during molten deposit interaction. Phase transformation mechanisms associated with molten deposit interaction is not yet clearly understood [134]. YSZ-V₂O₅ interaction has been understood as a general YSZ dissolution mechanism followed by preferential YVO₄ formation and reprecipitation to yttria-poor m-ZrO₂ phase. This has been demonstrated by the change in microstructure of YSZ after interaction with V₂O₅ melt, where typical lamellar microstructure was absent. The temperature-dependent rate constant (k) is also plotted against T as shown in Fig. 5.3. This clearly reveals the Arrhenius-type dependence along with an expression:

$$k(T) = 4.35 \times 10^{34} \exp\left(-\frac{713524}{RT}\right) \quad \text{Eq. 5.7.}$$

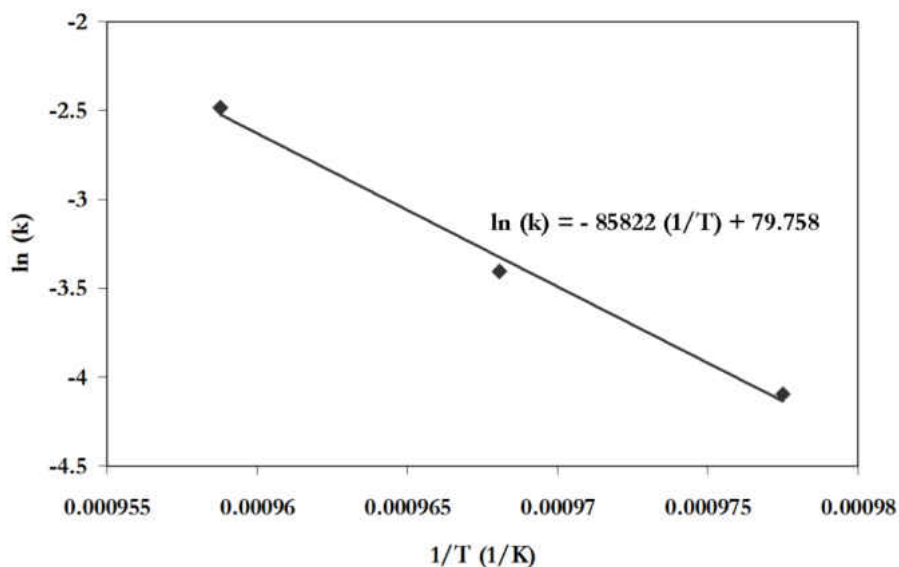


Figure 5.: Plot of $\ln(k)$ vs $1/T$ shows the Arrhenius type temperature dependence of the rate constant (k).

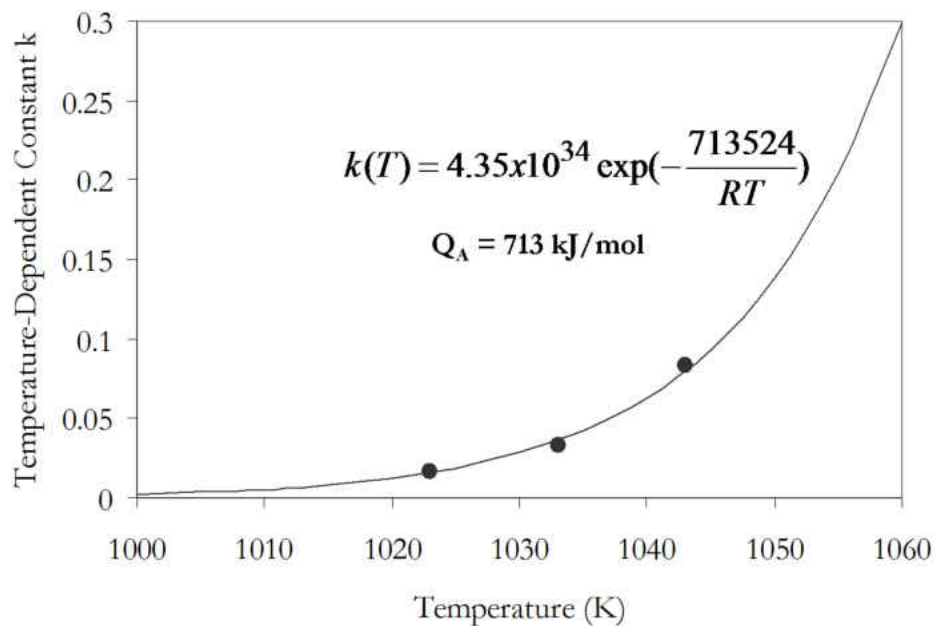
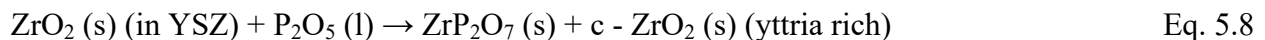


Figure 5.: Plot of temperature-dependent k vs. temperature (T) and the derived Arrhenius relation.

The Avrami exponent (n) typically yields an information about the phase transformation and nucleation and growth mechanisms. A value of n less than 2 is usually expected for phase transformation mechanism with a decreasing nucleation rate, when the growth mechanism is diffusion controlled [135]. In this case, an Avrami exponent of 1.5 was estimated for all three temperatures, where the phase transformation mechanism was controlled by the thermochemical reaction between the solid YSZ and V₂O₅ melt. It should be noted that the YSZ destabilization observed in this V₂O₅ attack is solely due to the preferential depletion of yttria stabilizer due to YVO₄ formation. Such a low value of n can be expected when the polymorphic phase transformation mechanism is reaction-controlled.

5.1.2. Degradation of APS YSZ by P₂O₅ Deposit

During rapid heating, P₂O₅ melts at 340°C and sublimes at 360°C. However, P₂O₅ could undergo phase transition to other polymorphs during gradual heating [136] and sublimes at a relatively lower temperature of 200°C. Although phosphorus was expected to behave similar to vanadium in degrading the YSZ, the only reaction mechanism observed between YSZ and P₂O₅ was the formation of zirconium pyrophosphate (ZrP₂O₇). This reaction enriches the YSZ with yttria content and thus zirconia existed as yttria rich zirconia phase (fluorite-cubic). Thus the YSZ – P₂O₅ interaction can be expressed by:



Similar results were observed for temperature as low as 200°C due to the thermal instability of P₂O₅ as discussed above. Samples tested in molten P₂O₅ at elevated temperatures of

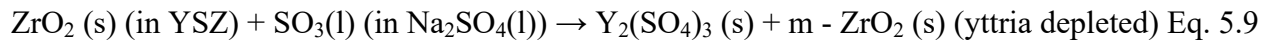
1200°C also showed similar reaction product due to the fact that ZrP_2O_7 is stable up to 1500°C [137]. P_2O_5 melts, infiltrates the YSZ, and reacts with ZrO_2 of the YSZ before it sublimates even in testing conditions with a rapid heating rate to the desired high testing temperature.

Chemical interaction of P_2O_5 with the YSZ has not been understood. Jones [12] had reported a speculative argument on the degradation of the YSZ by P_2O_5 . Formation of ZrP_2O_7 can be expected to be the dominant degradation mechanism. It was also speculated that Y_2O_3 stabilizer could directly react with P_2O_5 to form YPO_4 similar to the widely known YVO_4 formation in YSZ- V_2O_5 interaction [12]. However, this study concludes that there is no reaction involving Y_2O_3 stabilizer, and the only degradation reaction between the YSZ and P_2O_5 was found to be the formation of ZrP_2O_7 with a subsequent phase transformation of t' - ZrO_2 to yttria rich fluorite cubic (f) phase.

5.1.3. Degradation of YSZ by molten Na_2SO_4

ZrO_2 itself has been well-known to be chemically inert against molten Na_2SO_4 attack. ZrO_2 based ceramics have been employed as an inert electrode material for high-temperature hot corrosion studies in corrosive sulfate medium (Na_2SO_4 - K_2SO_4) [138]. However, YSZ could still undergo hot corrosion attack through preferential depletion of Y_2O_3 stabilizer by highly acidic SO_3 of Na_2SO_4 melt. Even though a destabilization reaction mechanism resulting in $\text{Y}_2(\text{SO}_4)_3$ formation, which is similar to the YVO_4 formation as discussed earlier, has been speculated, no microstructural observation exist in literature. This study revealed the limited degradation on YSZ by Na_2SO_4 melt resulting in the evolution of m- ZrO_2 phase. For a duration of 100 h at 1000°C exposure temperature, at an accelerated hot corrosion test (50 mg/cm^2) in an

encapsulated testing holder, only a minor evolution of m-ZrO₂ at a content less than 0.05 volume fraction was observed as presented in Chapter 4.2.3. It should be noted that presence of Na₂SO₄ with SO₃ (g) at a relatively high partial pressure could destabilize the YSZ by reacting with Y₂O₃ stabilizer to form Y₂(SO₄)₃ [28]. The acidic dissolution of yttria stabilizer by SO₃ melt of Na₂SO₄, which is expected to be the only thermochemical degradation mechanism between the YSZ and Na₂SO₄, can be written as:



5.1.4. Degradation of YSZ by Molten Na₂SO₄ + V₂O₅ mixture (50 – 50 mol. %)

Na₂SO₄ itself was found to have negligible thermochemical interaction with the YSZ at elevated temperature. The dissociation reaction of Na₂SO₄ at elevated temperature is given by:

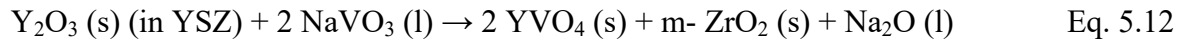


In the presence of V₂O₅, this Na₂O in liquid state tends to form vanadates of sodium such as sodium metavanadate (NaVO₃) as seen in the equilibrium phase diagram presented in Fig. 3.4 [127]. Formation of NaVO₃ (T_m = 610°C) can be written as:



The degradation of the YSZ by molten Na₂SO₄ in the presence of V₂O₅ as investigated in this study using a 50-50 wt.% Na₂SO₄-V₂O₅ mixture demonstrated a significant degradation of the YSZ through destabilization that is attributed to the yttria depletion similar to that of YSZ–V₂O₅ interaction (at temperature above 747°C). However, YVO₄ formation and YSZ destabilization (t'→t→m+f) was found to occur at temperature as low as 700°C when sodium vanadates form due to the presence of both V₂O₅ and Na₂SO₄. This was observed to be the only

degradation mechanism of the YSZ due to thermochemical interaction with Na₂SO₄-V₂O₅ mixture (or NaVO₃). Equation 5.12 given below represents the degradation mechanism of the YSZ by NaVO₃, which is consistent with the findings reported earlier [43, 47].



5.2. Degradation of APS YSZ by Molten CMAS Deposits

CMAS being a critical threat to the turbine materials system in aero-propulsion applications, all previous studies only focused in examining the degradation of EBPVD YSZ by CMAS melt. Even though the thermochemical interaction between the YSZ and CMAS would remain the same irrespective of the microstructure, APS YSZ with high relative density can be expected to be more-resistant to CMAS attack. In this study, it was revealed that the CMAS, being low-viscous and having a better wetting property, readily infiltrated the APS YSZ through the interconnected cracks and pores at exposure temperatures starting at 1250°C. Cross-sectional microstructural analysis revealed a similar microstructure for all the YSZ samples that suffered CMAS attack at temperatures above 1250°C. This suggests that the degradation mechanism remains the same at all exposure temperatures, once the CMAS deposit melts at $T > 1250^\circ\text{C}$. The accumulation of CMAS melt in the interconnected pores and cracks of the YSZ coatings resulted in a gradual dissolution of the YSZ in CMAS melt followed by reprecipitation of ZrO₂ grains during solidification with a different microstructure and composition based on the local melt chemistry. XRD as well as selected area electron diffraction patterns obtained from the CMAS infiltrated APS YSZ (1300°C for 4h) specimens revealed the disruptive phase transformation of metastable tetragonal zirconia (*t'*-ZrO₂) to monoclinic + cubic zirconia (*t'* → *t*+*f* → *m*+*f*). XRD

results also revealed that the YSZ surface exposed to CMAS had greater volume fraction of m-ZrO₂ phase. The other surface of the free-standing YSZ to which, the CMAS melt reached through infiltration through the YSZ thickness, was found to possess a significant amount of yttria-rich cubic ZrO₂ phase. This discrepancy in phase transformation to Y₂O₃-poor monoclinic ZrO₂ and Y₂O₃-rich cubic ZrO₂ phases is attributed to the variation in local content of the Y₂O₃ stabilizer from the original YSZ solid solution during reprecipitation. This argument is in agreement with the earlier reported literature [30]. The Y₂O₃-rich cubic ZrO₂ phase at the bottom surface is due to the enrichment of Y₂O₃ in the CMAS melt during its infiltration through the 300 μm-thick YSZ.

The available literature on the degradation of EB-PVD YSZ by CMAS melt reported similar thermochemical interactions. The dissolution of YSZ by CMAS melt followed by reprecipitation of ZrO₂ grains with a globular microstructure has been observed [30]. Similarly, in this study, the surface and cross-sectional microstructural observations reveal the spherical morphology of the reprecipitated ZrO₂ grains. Site-specific samples from the YSZ specimen exposed to CMAS melt at 1350°C, was prepared by FIB-INLO for a thorough investigation by TEM. Selected area electron diffraction confirmed these reprecipitated grains to be monoclinic ZrO₂ phase. XEDS analysis performed using TEM as well as SEM further revealed the presence of Y and Zr in the solidified CMAS melt. Few local regions of the CMAS residue was found to have a significantly higher Y:Zr (8:1) content (atomic ratio) compared to the desired ratio of 1:12 in the bulk YSZ of the 7-8 YSZ coatings. Few localized spots were identified to be extremely richer in Y content. Thus the mechanism of YSZ dissolution by CMAS followed by reprecipitation of ZrO₂ with a composition based on the local melt chemistry that resulted in the

evolution of yttria-poor m-ZrO₂ as well as yttria-rich f-ZrO₂ phases is determined to be the high-temperature thermochemical degradation mechanism between the APS YSZ and CMAS melt.

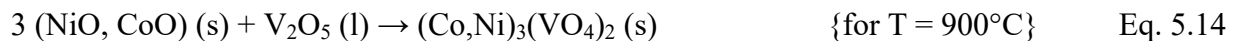
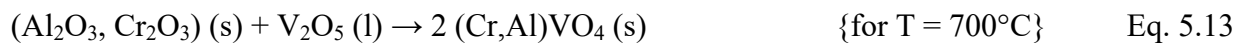
5.3. Degradation of APS CoNiCrAlY by Molten Deposits from Fuel Impurities

5.3.1. Degradation of APS CoNiCrAlY by V₂O₅ Deposit

Free standing APS CoNiCrAlY coatings exposed to V₂O₅ melt exhibited two different degradation mechanisms at temperatures of 900°C and 700°C. V₂O₅ is a strong acidic oxide, and acidic dissolution of protective oxide scale in oxidation/hot corrosion resistant materials had been studied earlier [102, 139]. In general, trivalent protective oxides such as Cr₂O₃ and Al₂O₃ would behave as basic oxides in the presence of a strong acidic medium, and would readily be dissolved in an acidic medium such as V₂O₅ melt. The reaction product due to the dissolution of trivalent oxides (M₂O₃, M = Al or Cr) by V₂O₅ melt could be represented as MVO₄ (M = Al or Cr). In this investigation, at 700°C, V₂O₅ melt was found to react with such trivalent protective oxide to form substitutional-solid solution type chromium-aluminum orthovanadate (Cr,Al)VO₄. The shape of this reaction product crystallized out on the surface was dependent on the Al/Cr ratio in (Cr,Al)VO₄. Al-rich product was found to be thin large platelets and Cr-rich vanadate product was found to be uniformly fine disc-shaped. At elevated temperatures, these metal orthovanadates (T_m: AlVO₄ = 695°C, CrVO₄ = 810°C) melt, which promote further reaction with coating constituents [102]. At 700°C, the infiltration rate was dominant compared to the dissolution rate for V₂O₅ melt. Accumulation of V₂O₅ melt was clearly visible at the bottom

surface of free standing coating, which subsequently can interact with the underlying superalloy substrate in a typical TBC system.

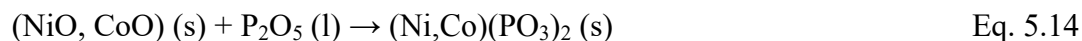
Instability of the metal orthovanadates above 810°C implies that there will be a different interaction between CoNiCrAlY and V₂O₅ melt at 900°C. Interaction of V₂O₅ melt at 900°C for 2 h revealed the extensive consumption of CoNiCrAlY constituents through the formation of nickel-cobalt orthovanadate, (Ni,Co)₃(VO₄)₂, a substitutional solid solution orthovanadate product. The metal orthovanadates of Ni and/or Co are stable up to 1300°C [102]. Additional interaction at 900°C observed was the extensive formation of spinel oxides. Dissolution rate of coating by V₂O₅ melt was greater than the infiltration rate, and no residual V₂O₅ melt was observed. The V₂O₅ melt extensively consumed the CoNiCrAlY by forming a reaction scale 100 μm in thickness at 900°C after 2 h. This region was found to have reaction products such as cobalt-nickel orthovanadate (Co,Ni)₃(VO₄)₂, yttrium vanadate (YVO₄) and spinel, (Ni,Co)(Al,Cr)₂O₄. This reaction scale could also have resulted from the formation and subsequent melting of other unstable metal orthovanadates such as AlVO₄ and CrVO₄. Thus the V₂O₅ - CoNiCrAlY interaction could be explained by the following reactions:



These degradation reactions were observed to consume CoNiCrAlY that was preoxidized in order to have an appreciably thick TGO (α - Al₂O₃) scale as protective oxide scale. Thus a significant degradation of CoNiCrAlY by acidic V₂O₅ attack can be generalized by using the equations 5.13 and 5.14, irrespective of the oxidized microstructure of CoNiCrAlY.

5.3.2. Degradation of APS CoNiCrAlY by P₂O₅ Deposit

Formation of two different phosphates was observed as a result of the interaction between pre-oxidized APS CoNiCrAlY and P₂O₅ melt with a significant consumption of CoNiCrAlY. P₂O₅ melt had been classified as strongly acidic oxide and hot-corrosion is typically controlled by Lewis acid-base oxide reactions, where oxides of acidic and basic nature interact readily [12]. Both NiO and CoO are basic oxides, where as Al₂O₃ and Cr₂O₃ are classified as amphoteric oxides, which would act as basic oxides in a strongly acidic medium and vice-versa. Thus P₂O₅ was found to readily react with oxides of Ni, Co, Al and Cr to form phosphate reaction products such as (Ni,Co)(PO₃)₂ and (Cr,Al)(PO₃)₃. These phosphates could be classified as divalent-cation polyphosphates (M^{II}(PO₃)₂, where M = Ni and/or Co) and trivalent-cation polyphosphates (M^{III}(PO₃)₃, where M = Al and/or Cr). The divalent-cation polyphosphates are usually stable up to the melting point, where as trivalent-cation polyphosphates such as (Al,Cr)(PO₃)₃ decomposes to monophosphates [(Al,Cr)PO₄] above 1000°C [138]. The P₂O₅ - CoNiCrAlY interaction could be expressed by the following reactions:

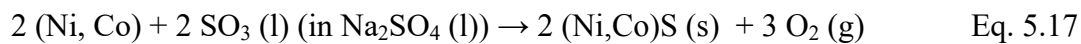
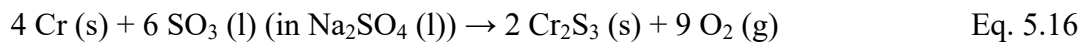


These reactions resulted in the extensive consumption of CoNiCrAlY by P₂O₅ melt.

5.3.3. Degradation of APS CoNiCrAlY by Na₂SO₄ Deposit

Hot corrosion resistance of MCrAlY coatings against fused Na₂SO₄ salt film attack is expected to be superior because of the high Cr content and the excellent chromia forming ability. However, MCrAlY coatings that were primarily developed as an oxidation resistant overlay coating or bond coat in TBCs were designed to form alumina in order to provide excellent oxidation resistance. In this study, exposure of APS CoNiCrAlY specimens both in as-sprayed and preoxidized state was thoroughly examined to investigate the degradation mechanisms by Na₂SO₄ salt film. Test temperature from 900°C to 1000°C was above the melting point of Na₂SO₄ (T_m = 880°C) in order to investigate the Type I hot corrosion mechanisms.

The APS CoNiCrAlY in as-sprayed condition suffered severe attack by molten Na₂SO₄. A significant formation of sulfide reaction products such as chromium sulfide (Cr₂S₃) and substitutional solid solution type nickel-cobalt sulfide, (Ni,Co)S were observed from the surface and cross-sectional microstructural analysis. Direct contact of metallic CoNiCrAlY with corrosive Na₂SO₄ molten film resulted in consumption of coating constituents through sulfide formation. Besides, the APS CoNiCrAlY in as-sprayed condition was found to be susceptible to molten salt film infiltration. Accumulation of corrosive molten salt in the intersplat boundaries was found to degrade the coating extensively by sulfide formation via:

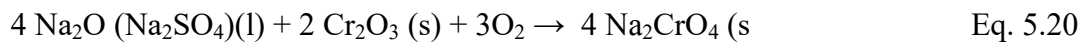
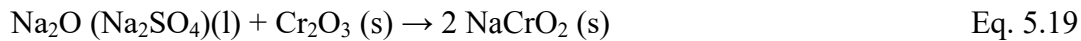


The sulfide formation reactions are associated with oxygen evolution. These reactions occurring at the intersplat boundaries of APS CoNiCrAlY subsequently results in an increase in local p_{O_2} , which leads to a significant internal oxidation. Thus the observed mechanism of accelerated internal alumina formation associated with the sulfide formation (Cr_2S_3 and (Ni,Co)S) during the high-temperature exposure of as-sprayed CoNiCrAlY to corrosive molten Na_2SO_4 resulted in a significant consumption of the APS CoNiCrAlY coating constituents.

Even though MCrAlY-type coatings are expected to be superior in hot corrosion resistance than typical superalloys, preoxidized CoNiCrAlY was found to degrade against molten sulfate attack. Porous $(Al,Cr)_2O_3$ mixed oxide as one of the surface oxide scale constituents, a characteristic of classical hot corrosion mechanism [10], was evident from the investigation of preoxidized CoNiCrAlY exposure to Na_2SO_4 melt. Sulfate salt can dissolve the protective oxide scale through acidic and basic fluxing hot corrosion mechanisms. The relative solubilities of protective oxide scale (e.g., Al_2O_3 , Cr_2O_3 , SiO_2) in Na_2SO_4 melt have been well-documented as discussed in Chapter 2. Although alumina and chromia exhibit minimum solubilities in Na_2SO_4 melt at similar salt basicities ($a_{(Na_2O)}$), chromia scales are typically preferred over alumina for hot corrosion protection [7]. Basic fluxing of alumina ($NaAlO_2$ formation) typically results in a shift in basicity ($a_{(Na_2O)}$) of Na_2SO_4 melt, where increased solubility of alumina occurs. This accelerates the hot corrosion attack and the reprecipitation of porous alumina as a outer surface scale due to supersaturation of alumina in Na_2SO_4 melt and results in non-protective alumina scale formation as a porous surface scale. Thus, a progressive inward attack of metallic specimen by Na_2SO_4 melt could occur until the ingress is completely arrested. On the other hand, Cr, existing in two different valence states (+3 and +6), basic fluxing of Cr_2O_3 protective oxide scale

can result in the formation of two different sodium chromate products (NaCrO_2 , Na_2CrO_4) [7, 10]. Solubility of Cr_2O_3 is higher in Na_2CrO_4 (external scale) and relatively lower in NaCrO_2 (internal scale) and thus helps arrest the progressive hot corrosion attack without reprecipitating as a porous oxide [7].

Experimental results from exposure of preoxidized CoNiCrAlY to Na_2SO_4 melt at 1000°C confirmed the presence of porous $(\text{Cr,Al})_2\text{O}_3$ as one of the surface oxide scale constituents. This result suggests that the basic fluxing of protective alumina scale occurred followed by the enrichment of chromia as the surface oxide scale constituent. Subsequently the precipitation of porous $(\text{Cr,Al})_2\text{O}_3$ can occur. Moreover, due to the high alumina forming ability of CoNiCrAlY, the thick protective alumina itself protected the underlying coating constituent from type I Na_2SO_4 hot corrosion attack. The reactions that describe the basic fluxing mechanism are:

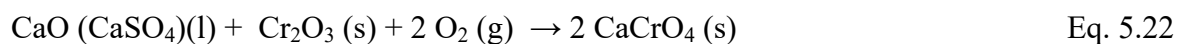
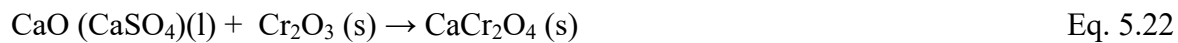
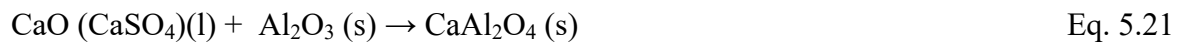


Potassium sulfate, K_2SO_4 is also widely considered as one of the major corrosive species that can degrade the turbine components. In most cases, K_2SO_4 had been documented to degrade the high temperature materials system very similar to Na_2SO_4 . Thus, K_2SO_4 was not considered in this study. However, CaSO_4 , due to an increase in Ca content in alternative fuels and the CaO

rich ash after combustion, was examined as a part of this study as discussed in the following sub-section.

5.3.4. Degradation of APS CoNiCrAlY by CaSO₄ Deposit

CaSO₄ is another threat that can deposit on to hot section turbine components during the use of alternative fuels rich in Ca content. Experimental results from preoxidized CoNiCrAlY exposed to CaSO₄ melt at 1000°C demonstrate the predominant degradation to be the basic fluxing hot corrosion. Both protective oxides, Al₂O₃ and Cr₂O₃ were found to be dissolved by CaSO₄ primarily through basic fluxing resulting in the formation of CaAl₂O₄ and CaCrO₄. A 30 μm thick scale was found to be composed of two different reaction products, CaAl₂O₄ and CaCrO₄. Thus, the preoxidized CoNiCrAlY was found to be more susceptible to hot corrosion by CaSO₄ than Na₂SO₄. Appreciably thick reaction scale without the protective TGO suggests that the solubility of Al₂O₃ in CaSO₄ shifted the melt basicity that might further increase the solubility of alumina. Thus progressive basic fluxing might have occurred. Presence of porous NiO and Cr₂O₃ was also observed in the 30 μm-thick scale. The primary reactions involved in these basic fluxing mechanisms can be described by:



5.3.5. Degradation of APS CoNiCrAlY by NaVO₃ Deposit

In order to understand the degradation by Na₂SO₄+V₂O₅ mixture, the APS CoNiCrAlY specimens, both in as-sprayed and preoxidized condition were exposed to sodium metavanadate, NaVO₃ deposit at 900°C. NaVO₃ is less acidic in nature compared to V₂O₅, and suggests that the degradation will not be as severe as observed during exposure to V₂O₅ melt. The as-sprayed CoNiCrAlY specimen suffered significant degradation by NaVO₃ melt. A 40 μm-thick melt-interacted zone was observed on the CoNiCrAlY surface after an exposure of 5 h. A significant dissolution of oxides of Al, Cr, Co and Ni by NaVO₃ melt was evident. The melt-interacted zone primarily consisted of V-rich solidified residue and spinel oxide [(Ni,Co)(Cr,Al)₂O₄]. Infiltration of V-rich melt through the interconnected splat boundaries of as-sprayed CoNiCrAlY was also evident. This is similar to V₂O₅ attack. According to Lewis acid-base type hot corrosion mechanism, acidic melt such as NaVO₃ typically dissolves oxides of Al and Cr (Al₂O₃, Cr₂O₃), which are amphoteric in nature, that could behave as basic oxides in a strong acidic medium. Basic oxides of Ni and Co (NiO, CoO), can readily be dissolved in a strong acidic medium. The extent of dissolution is dependent on the solubility limit of the corrosive melt. The as-sprayed CoNiCrAlY was also found to show evidence of NiO on the surface after NaVO₃ exposure. Moreover, presence of spinel oxide as the primary constituents of the melt-interacted zone suggests the reprecipitation of oxides as NiO and (Ni,Co)(Cr,Al)₂O₄ spinel due to supersaturation in dissolved oxide content. The preoxidized CoNiCrAlY specimen exhibited superior resistance against NaVO₃ attack, unlike the extensive degradation observed during V₂O₅ exposure. The oxide scale was found to consist of two layers, with the outer scale being the continuous spinel oxide and the inner scale of α-Al₂O₃. The oxide scale, however, was found to be locally

disintegrated. A direct contact of metallic CoNiCrAlY with the corrosive melt can readily result in accelerated oxidation forming oxides of Al, Cr, Ni and Co, where these oxides dissolve at different dissolution kinetics at various extents based on solubility limits. However, protective oxides such as Al_2O_3 and Cr_2O_3 are less likely to be dissolved by a weak acidic melt such as NaVO_3 . No evidence of basic fluxing was observed.

5.4. Degradation of APS CoNiCrAlY by Molten CMAS Deposits

The CMAS can melt at temperature starting 1150°C depending on the composition. MCrAlY type coatings are typically not expected to experience temperatures above 1000°C . Thus the CMAS attack of MCrAlY coatings never received any attention. However, use of low-quality alternative fuels such as bio-mass derived fuel and coal/petcoke fuel blend that can have high ash content, could potentially generate deposits similar to CMAS composition. In this study, the degradation of preoxidized CoNiCrAlY by CMAS melt at 1250°C was examined. Extensive dissolution of the TGO ($\alpha\text{-Al}_2\text{O}_3$) by CMAS melt associated with significant spinel formation was found. Thin platelets were found to be embedded in the CMAS-interacted zone after thermochemical interaction with preoxidized CoNiCrAlY. It has been reported that an increase in Al content in CMAS would result in crystallization of CMAS glass to Anorthite platelets ($\text{CaAl}_2\text{Si}_2\text{O}_8$) [50]. Thus the dissolution of TGO by CMAS melt subsequently resulted in crystallization of CMAS to Anorthite platelets. In addition to CMAS crystallization, an accelerated oxidation of CoNiCrAlY in the presence of CMAS melt resulted in a significant spinel oxide formation $[(\text{Ni},\text{Co})(\text{Cr},\text{Al})_2\text{O}_4]$. After a CMAS exposure at 1250°C for 5 h, a $40\ \mu\text{m}$ thick CMAS-interacted zone was observed on the preoxidized CoNiCrAlY. It is expected that

the degradation would progress until the CMAS melt is completely crystallized to Anorthite. From this understanding of CMAS attack on CoNiCrAlY, where the phenomenon of CMAS arrest through crystallization Anorthite by an increase in the Al content of CMAS, employing an alumina based sacrificial overlay for TBCs was attempted towards finding a promising mitigation approach to protect TBCs from CMAS attack. The various mitigation approaches investigated as a part of this doctoral study will be discussed in the following sections.

5.5. Protection of YSZ TBCs against Molten Deposit Attack by Electrophoretically Deposited Overlay

5.5.1. Rationale behind Selecting EPD as an Overlay Deposition Process for APS TBCs

Employing a protective environmental barrier overlay, in order to protect TBCs against molten deposit-induced hot corrosion attack, gained a greater attention in recent years [44, 104, 105]. The overlay can be either an impermeable sealant-type coating or a sacrificial overlay that can trap the corrosive deposits through thermochemical interactions. Use of an impermeable overlay can greatly reduce the melt ingress into the porous YSZ topcoat of TBCs. On the other hand, a sacrificial overlay can completely arrest the melt ingress by limiting the attack within the overlay thickness. For the YSZ topcoat of TBCs that are generally processed by APS or EBPVD, sacrificial oxide-type overlay coatings can also be deposited by APS or EB-PVD. However, both of these techniques only produce coatings with significant volume defects such as interconnected pores, cracks and intercolumnar gaps. A dense crack-free sacrificial coating with uniformly distributed closed pores at a desired porosity, which possesses adequate adhesion

strength, can be a durable protective barrier overlay for TBCs. On the other hand, sealant-type impermeable overlay can be processed by various techniques such as sputtering, PVD, CVD, which can also yield a dense overlay coating. However, in order to achieve a thicker overlay (10 μm - 25 μm), these techniques might not be cost-effective and yield a durable overlay for TBC applications, where a long term exposure to aggressive combustion environment (e.g., cyclic high temperature) is essential.

A dense protective barrier overlay of desired chemistry can act as

- (i) a sacrificial overlay by trapping corrosive deposits via chemical interaction and
- (ii) a semi-impermeable overlay with desired microstructure that can greatly reduce the rate of melt ingress.

Such a protective overlay of uniform thickness, desired porosity with uniformly distributed closed pores, can be readily achieved by electrophoretic deposition (EPD). EPD is a highly cost-effective, versatile coating processing technique, where particle by particle uniform deposition at a significantly high deposition rate can be easily achieved. However, in order to obtain an overlay of desired porosity with superior adhesion strength, EPD requires a subsequent densification step. Densification through a controlled sintering step with optimized sintering conditions can yield a uniform, crack-free overlay composed of desired chemistry with controlled thickness and porosity.

The starting surface roughness of the YSZ TBCs is also a critical characteristic that dictates the durability of overlay processed by EPD. During sintering that follows EPD, the deposited film can experience detrimental stresses. If the overlay film is sufficiently thin, the stress distribution normal to the plane of the film surface can be considered uniform. The

interfacial adhesion between the EPD overlay and the APS YSZ must be sufficiently high to support the force balance. For a fixed interfacial strength, a critical film thickness can be found above which the interface can no longer support the tensile stress, resulting in interface failure. Moreover, failure by cracking can also be initiated within the film itself by the growth of preexisting flaws. These flaws can easily form during drying. Thus, there are many critical parameters that can affect the durability of sintered overlay. In general, the desired thick overlay coating with good structural integrity at the interface and within the overlay itself can be achieved through a careful drying prior to sintering: achieving a homogenous green structure; a high packing density; superior interfacial adhesion and low sintering rates at low sintered densities. EPD is the best cost-effective and scale-up ready coating processing technique that can produce a durable ceramic overlay with these critical characteristics.

5.5.2. Rationale behind Selecting the EPD Process Parameters for Overlay Deposition

As explained in Chapter 2, EPD is primarily a two-step particle-deposition process; electrophoresis, where charged particles are typically drifted under the influence of an electric field, is followed by deposition - the coagulation of particles to a dense compact mass. Parameters that determine the characteristics of EPD process are (i) those related to the suspension and (ii) those related to the deposition process itself [114]. It is mandatory to prepare a stable colloidal suspension in order to obtain a crack-free homogeneous deposit. Desired characteristics for a stable suspension are low viscosity, high dielectric constant, and low conductivity. For EPD of ceramics, organic solvent based suspension is typically used compared to aqueous suspensions because of the low conductivity, higher density and good chemical

stability. Among the widely available organic solvents, acetone has the lowest viscosity ($\eta = 0.3087$ cP), which is one of the desired properties for a stable suspension with desired solid loading. However, its dielectric constant of 20.7 is relatively low compared to that of other organic solvents [114]. This would limit the charge density on particles in a suspension due to its poor dissociation ability. Thus a mixture of acetone and ethanol was employed in this study, where ethanol has a higher dielectric constant of 24.55 but a higher viscosity of 1.0885 cP [114]. Iodine was used as an additive in order to generate high proton density through chemical reactions. Every molecule of acetone would react with iodine to yield two protons; where as each molecule of ethanol would yield one proton during reaction with iodine according to the respective chemical reactions:



Thus a mixture of acetone and ethanol in a volume ratio of 1:1 was selected with an optimized iodine concentration of 0.4 g/l based on earlier study [119]. This organic solvent mixture with the I_2 at specific concentration yielded a stable colloidal suspension after sufficient ultrasonication and constant hydrodynamic agitation to some extent. An applied voltage of 20 – 30 V/cm was previously reported to produce a homogeneous oxide powder compact depending on the volume ratio of acetone to ethanol [119]. Thus an applied voltage of 25 - 30 V/cm that was employed in this study produced a thick and uniform deposit of the YSZ, Al_2O_3 and MgO powders for deposition durations up to 10 minutes. After EPD, during drying, acetone having a

high vapor pressure of 24,664 Pa (at 20 °C) tends to evaporate rapidly causing cracking due to capillary effect, whereas the presence of ethanol having lower vapor pressure (5866 Pa at 20 °C), helps avoid cracking because of relatively slower drying.

The EPD only provides a deposit of stable powder compact. Producing an adherent coating with desired properties entails the use of a densification step after EPD. Thus in this study, the deposited overlay coatings were subjected to a controlled sintering step (controlled ramp rates, specific temperatures, and specific durations) depending on the sinterability of the overlay material.

5.5.3. YSZ Overlay for APS YSZ TBCs by EPD

The YSZ overlay processed by EPD with the optimized parameters after careful drying and sintering at 1300°C and 1350°C for 4 h, was found to be crack-free and homogeneous. At a relatively higher sintering temperature of 1350°C for 4 h, a dense YSZ overlay coating was produced as presented in Figs. 4.46 and 4.47. The dense continuous overlay coating fabricated with promising adhesion strength would act as a sealant to the APS YSZ coatings to protect against melt ingress. However, due to the fact that the YSZ is highly susceptible to hot corrosion and CMAS-dissolution attack, employing an environmental barrier overlay of the YSZ would not effectively mitigate the corrosive melt attack. In spite of the significantly reduced melt ingress rate, a better protection against melt-induced attack requires a trapping of the corrosive melt. The experimental results of this study also demonstrated the susceptibility of the YSZ overlay to CMAS attack. Employing an overlay composed of another material for the APS YSZ would be more challenging, since additional issues associated with the thermal expansion mismatch and the sintering resistance must be addressed. Thus, in addition to the desired

capability to trap corrosive species through thermochemical interactions, choice of overlay material must consider other properties such as least thermal expansion mismatch with the YSZ, sinterability, erosion resistance and fracture toughness.

5.5.4. Alumina Overlay for APS YSZ TBCs by EPD

Mitigation of the CMAS Attack by EPD Alumina Overlay

Alumina as an overlay ceramic for the APS YSZ TBCs can effectively protect TBCs from CMAS attack. During thermochemical interaction with alumina, due to a shift in CMAS glass composition by Al enrichment, CMAS melt can crystallize and its ingress can be arrested [50]. The highly stable and durable alumina/YSZ interface is also well-known from the YSZ/TGO interfacial characteristics. Therefore, alumina can be a highly durable material for use with the YSZ during high temperature cyclic exposure. Experimental results of this investigation on producing alumina overlay by EPD followed by controlled sintering step, demonstrated the ability to produce a durable, crack-free, uniformly thick, homogeneous alumina overlay with controlled thickness and porosity. Alumina green compact with superior packing homogeneity and high packing density processed by EPD also potentially lowered the temperature and time required for sintering. In this study, a relative density of ~95% was achieved for the EPD alumina overlay after sintering at 1200°C for 10 h. Starting powder size can be also minimized to accelerate the densification step. It is worth mentioning that use of smaller (e.g., nano) powders and innovative sintering techniques can help reduce the temperature and time of sintering, and minimize any degradation of TBCs and underlying metallic components during post-EPD processing.

The APS YSZ with dense alumina overlay was found to be a promising CMAS-attack-resistant coating system. During the CMAS exposure, due to the absence of interconnected pores/cracks in dense alumina overlay, a direct thermochemical interaction via dissolution of alumina by CMAS melt was found to dominate over the mechanism of CMAS melt infiltration. Crystallization of CMAS to anorthite (T_m : 1553°C) and $MgAl_2O_4$ spinel (T_m : 2135°C) during thermochemical interactions with alumina completely arrested the CMAS melt ingress. Based on the available equilibrium CaO-SiO₂-Al₂O₃ ternary phase diagram, presented in Fig. 5.4, typical CMAS glass composition without considering the Mg content falls in pseudo-wollastonite field, whose glass composition is difficult to crystallize [50]. Enrichment of Al content in CMAS shifted this “difficult-to-crystallize” pseudo-wollastonite glass composition to a “crystallizable” Al-rich glass composition that falls in the anorthite field. Thus the dissolution of α -Al₂O₃ by CMAS resulted in crystallization of CMAS to anorthite platelets (CaAl₂Si₂O₈). Concurrently, a localized enrichment of Mg content promoted the formation of $MgAl_2O_4$ spinel. Formation of these compounds with high melting temperature would be beneficial in further protection from both thermodynamic stability and kinetics aspects.

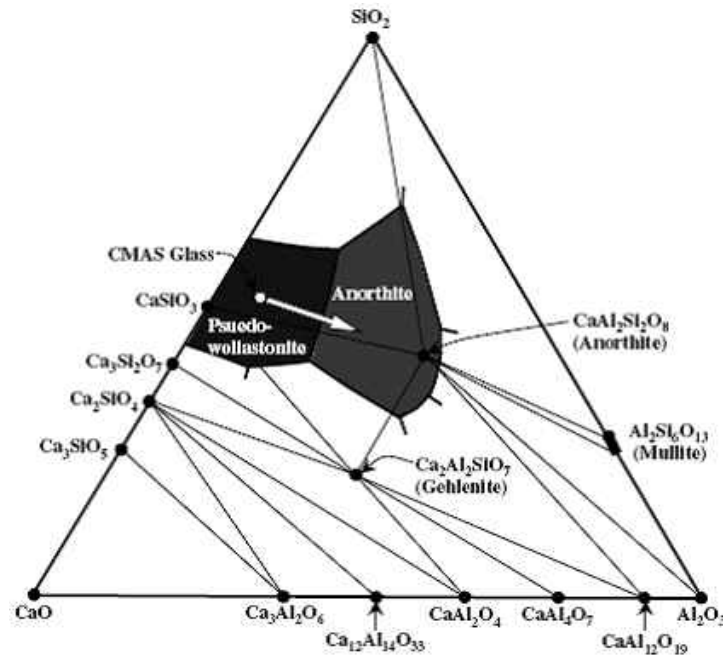


Figure 5.: Equilibrium CaO-SiO₂-Al₂O₃ ternary isotherm at 1200°C [50].

Kinetics of Electrophoretic Deposition of Alumina

As a part of this investigation, a phenomenological expression that models the kinetics of electrophoretic deposition and the effect of the influencing parameters was derived. Figure 5.5 presents the thickness of the EPD overlay as a function of time. This EPD overlay deposition kinetics can be understood by the following discussion.

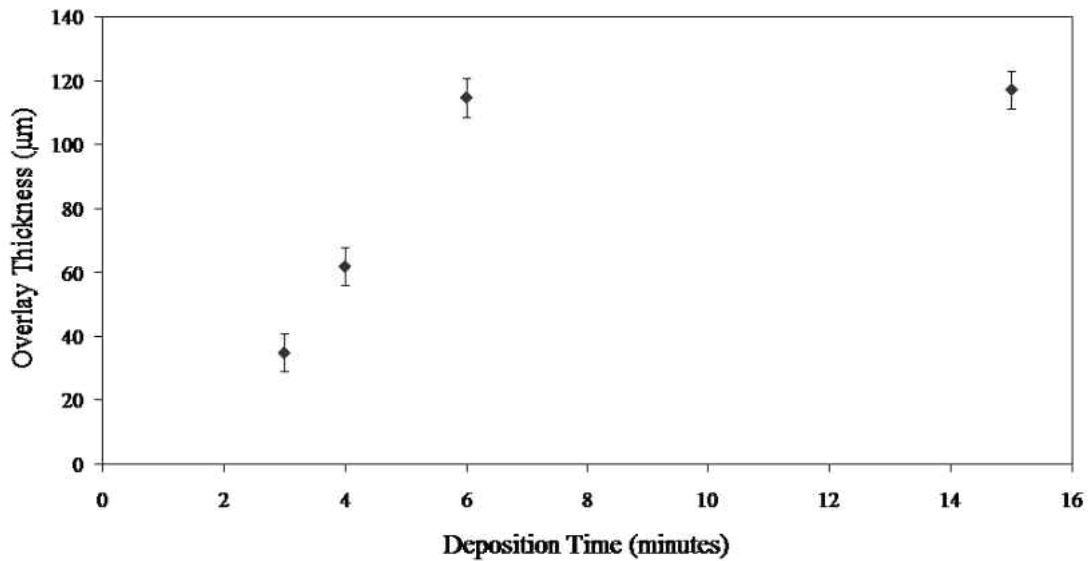


Figure 5.: Plot of alumina overlay thickness as a function of deposition duration during EPD.

The first model for EPD kinetics was proposed by Hamaker in 1940 [140] and is expressed by Eq. 5.25. This model can be applied for electrophoretic cells with planar geometry and relates the deposited mass per unit area, m (g), with slurry properties such as suspension solid concentration, C_s (g/cc), and electrophoretic mobility, μ ($\text{cm}^2\text{s}^{-1}\text{V}^{-1}$). The physical and electrical conditions imposed on the system such as electric field per unit distance, E (V cm^{-1}), deposition area, A (cm^2), and deposition time, t (s) are also taken into account as:

$$m(t) = \int_{t_1}^{t_2} C_s \mu E A dt \quad \text{Eq. 5.25}$$

A simple linear relation expressed by Eq. 5.26 between deposit thickness and time can be derived for cases, when all the influencing parameters (C_s , μ , E , A) are kept constant:

$$m(t) = C_s \mu E A t \quad \text{Eq. 5.26}$$

In this investigation and in general, the solid concentration is typically not kept constant throughout the EPD process. With a selected starting solid concentration of EPD suspension, the process typically proceeds with a continuously decreasing solid concentration due to deposition. Thus, the expression relating the deposited mass and time with decreasing concentration can be written as:

$$m(t) = m_0(1 - e^{-kt}) \quad \text{Eq. 5.26}$$

where m_0 is the total solid content in the colloidal suspension that can be deposited after an infinite EPD duration, assuming a 100% deposition efficiency, and k is the rate constant. Eq. 5.26 can also be rewritten in order to express the variation of overlay thickness (δ) variation as a function of time as:

$$\delta(t) = \delta_{\max}(1 - e^{-kt}) \quad \text{Eq. 5.27}$$

where the maximum thickness that could be theoretically achieved (δ_{\max}) and the rate constant (k) can be expressed as:

$$\delta_{\max} = \frac{m_0}{A\rho(1 - P)} \quad \text{Eq. 5.28}$$

$$k = f \mu E \quad \text{Eq. 5.29}$$

where, ρ is the theoretical density of the deposit material (alumina), P is the porosity of the deposit film, f is the efficiency factor considering the fact that not all the particles drifted to the work piece (cathode) take part in deposition, μ is the electrophoretic mobility, E is the potential difference per unit distance between the electrodes (inert anode and the work piece cathode).

Equation 5.27, however, can only be used for a process employing a constant current. In this study, a constant-voltage route was taken, in which case, the potential difference between the electrodes during the process of cathodic deposition is dependent on the surface resistance of the electrodes. Based on ohm's law, as an electrically insulating ceramic film thickens, the voltage difference between the electrodes decreases linearly with the growth of ceramic film due to a decrease in current density. With an appreciably thick ceramic film on cathode, the potential difference reaches a very low value (~ 0 V/cm) and further deposition becomes impossible. Thus, to express the behavior that could attribute to the voltage-dependent thickness variation as observed in this study, Eq. 5.27 can be rewritten as:

$$\delta(t) = \delta_{\max} \left\{ 1 - e^{-\left[\frac{k_1}{k_2(t)} \right] t} \right\} \quad \text{Eq. 5.30}$$

where, k_1 is the modified rate constant independent of film growth $\delta(t)$ and $k_2(t)$ is the constant directly proportional to $\delta(t)$. Eq. 5.30 can be solved to derive a phenomenological expression that describes the relationship between film thickness $\delta(t)$ and deposition duration (t), where $\delta(t)$ is in μm and t is in minutes.

$$\left[1 - \frac{\delta(t)}{\delta_{\max}} \right]^{k_2(t)} = e^{-k_1 t} \quad \text{Eq. 5.31}$$

Using Eq. 5.31, the experimental data on overlay deposition kinetics ($\delta(t)$ vs. t) from this study, were fitted in order to obtain an expression with estimated modified rate constant, k_1 . The modified rate constant is dependent on various characteristics of the EPD system such as electrophoretic mobility of the charges particles (μ), applied voltage (E), deposition efficiency

factor (f), area of the deposition surface (A) and the electrical resistivity of the deposit material. Plot shown in Fig. 5.6 presents the best fitted curve and the experimental data (markers) of this study with the rate constant estimated to be 3.7961 min^{-1} . A phenomenological description relating the time-dependent deposit thickness, $\delta(t)$ in μm and the deposition duration, t in minutes can be expressed as:

$$\left[1 - \frac{\delta(t)}{\delta_{\max}}\right]^{k_2(t)} = e^{-3.8t} \quad \text{Eq. 5.32}$$

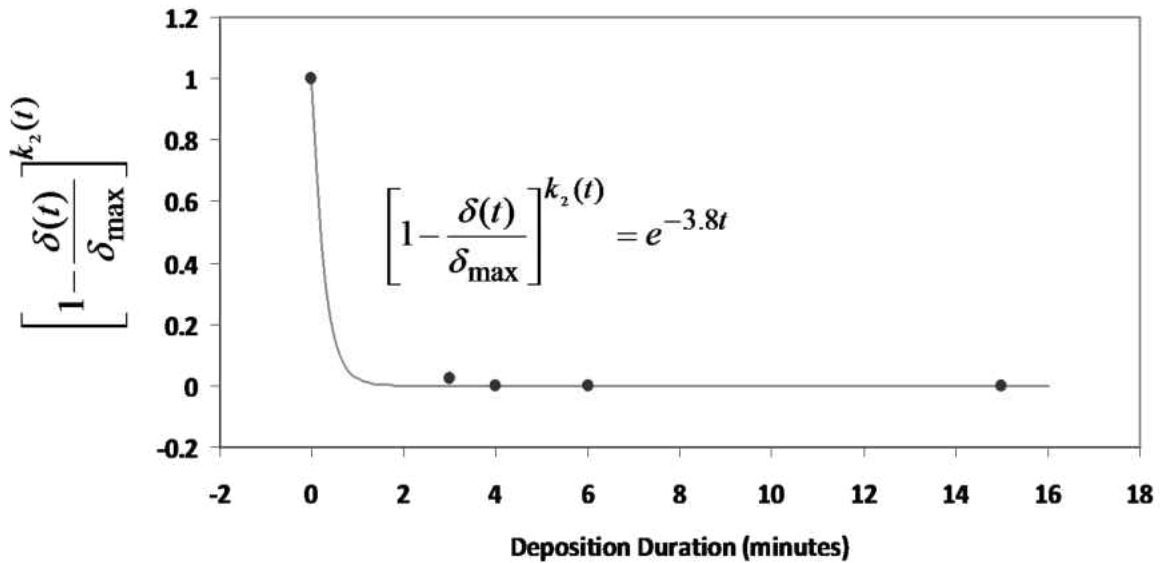


Figure 5.: Plot used to derive the phenomenological expression that explains the film growth kinetics.

In order to explain the EPD kinetics, a schematic growth plot, $\delta(t)$ vs. time is presented in Fig. 5.7.

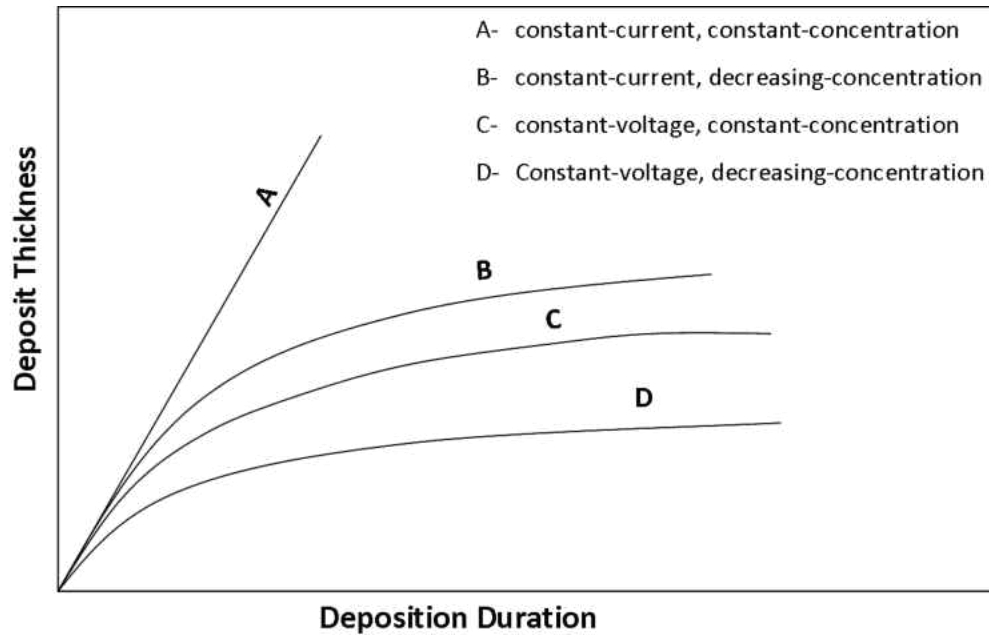


Figure 5.: A schematic plot showing the overlay thickness variation as a function of deposition duration during EPD with various controlling parameters (voltage, suspension concentration).

A linear growth during EPD as illustrated by curve A in Fig. 5.7 is typically expected for constant-current and constant-suspension concentration. For such a process, the voltage difference can be kept constant due to the constant current density flow. Moreover, the constant-suspension concentration (C_s) can be maintained by gradually increasing the solid content to the colloidal EPD bath during the process. Such a process will typically follow Eq. 5.26. Curve B in Fig. 5.7 illustrates a typical behavior described by Eq. 5.27, where an increase in thickness only depends on the varying suspension concentration. For a EPD process with constant-voltage and constant-suspension concentration as shown by curve C in Fig. 5.7, a gradual decrease in the voltage difference between the electrodes would result in a parabolic growth that can be explained based on Ohm's and Faraday's law. For EPD process with constant-voltage and decreasing-suspension concentration, an initial linear increase followed by saturation is typically

observed as described by curve D in Fig. 5.7. This is attributed to the changes in both suspension concentration and the voltage difference between the electrodes. It is clear that the EPD process can be tailored to obtain the desired deposition rate. However, a rapid deposition could result in poor particle packing homogeneity.

5.5.5. MgO Overlay for APS YSZ TBCs by EPD

Similar to the CMAS-mitigation mechanism observed by employing a dense alumina overlay against CMAS melt attack, a dense MgO overlay produced by EPD demonstrated a promising protection against corrosive V_2O_5 melt ingress. The 25 μm thick MgO overlay was found to be effective in suppressing V_2O_5 melt ingress. Reactions to form magnesium vanadates ($Mg_3V_2O_8$ and $Mg_2V_2O_7$) that have higher melting temperature than the V_2O_5 melt would be beneficial to mitigate the V_2O_5 and similar acidic oxide attack on TBCs by increasing the melting temperature and viscosity of such molten deposits. The MgO overlay can also be envisioned for hot corrosion resistance against molten sulfate attack on TBCs. Formation of $MgSO_4$ could be the attributing mechanism, which traps the corrosive sulfate deposits (Na_2SO_4 , K_2SO_4 and $CaSO_4$). $MgSO_4$ has a higher melting temperature ($T_m = 1124^\circ\text{C}$) than any of the corrosive sulfate deposits that could degrade the gas turbine materials by the classic hot corrosion mechanisms.

5.5.6. Al_2O_3 -MgO composite Overlay by Electrophoretic Codepositon for APS YSZ TBCs

In order to achieve an universal overlay that can protect TBCs from all types of melt-induced corrosion attack, a composite composed of alumina and magnesia was also investigated

as part of this study. Electrophoretic codeposition was found to readily yield such a composite overlay by employing a starting colloidal suspension having alumina and magnesia powders of similar particle size at a specific starting concentration (50-50 wt.%). The Al_2O_3 -MgO overlay produced by codeposition, followed by a sintering step was found to provide an overall protection against both molten CMAS and V_2O_5 hot corrosion attack. Besides the presence of Al_2O_3 , MgO in the composite overlay was also found to facilitate the crystallization of CMAS melt through formation of diopside $[\text{Ca}(\text{Mg},\text{Al})(\text{Si},\text{Al})_2\text{O}_6]$. Mechanism of CMAS crystallization through formation of anorthite $[\text{CaAl}_2\text{Si}_2\text{O}_8]$, similar to the mitigation mechanism observed with pure alumina overlay was also observed. The CMAS melt ingress was found to be effectively arrested within the composite overlay. V_2O_5 attack was also significantly suppressed by the Al_2O_3 -MgO composite overlay. Alumina is not effective in trapping V-rich corrosive deposits such as V_2O_5 due to the fact that the common reaction product aluminum vanadate, AlVO_4 melts at 695°C . Thus the composite overlay is not as effective as the pure MgO overlay. However, a presence of MgO in the composite overlay that had a dense microstructure was found to arrest V_2O_5 melt ingress through formation of $\text{Mg}_2\text{V}_2\text{O}_7$ and $\text{Mg}_3\text{V}_2\text{O}_8$. Formation of MgAl_2O_4 spinel during high-temperature sintering of the Al_2O_3 -MgO composite overlay for densification was found to be inert in terms of trapping the corrosive deposits through thermochemical interactions.

5.6. Promising Durability of EPD Overlay-Modified Commercial TBCs

With due consideration for real-engine applications, alumina overlay processed with optimized EPD parameters was deposited on a commercial-production TBCs that consisted of APS 8YSZ topcoat, LPPS CoNiCrAlY bond coat on a IN738LC superalloy substrate. Furnace cyclic tests at 1100°C with a 1-hour dwell time for each cycle demonstrated the promising durability of a crack-free uniform 75 μm-thick alumina overlay. The promising structural integrity of the YSZ based commercial APS TBCs modified with alumina overlay, which was examined by cross-sectional microstructural analysis after TBC failure with a coating lifetime of 196 cycles. The YSZ/Al₂O₃ overlay interface remained intact. The interfacial adhesion could be attributed to the initial YSZ surface roughness (as-sprayed) as well as the ability to fabricate a durable ceramic overlay with uniform pore distribution by EPD. The acceptable thermal expansion mismatch between the YSZ and alumina; CTE of YSZ is $10.5 \times 10^{-6} / ^\circ\text{C}$ and that of alumina is $7 \times 10^{-6} / ^\circ\text{C}$, yields the durable overlay. However, TBCs modified with alumina overlay showed evidence of crack population due to the generation of significant in-plane tensile stress within the 75 μm-thick alumina alumina overlay. In real-engine application, where a lower concentration of corrosive deposits is expected, a thinner overlay (20 μm - 30 μm thick) can be effective in protection with reliable durability.

CHAPTER 6: CONCLUSION

Free-standing APS 8YSZ and APS CoNiCrAlY (i.e., as-sprayed and preoxidized) specimens with thickness of 300 μm have been subjected to isothermal furnace testing in the presence of various corrosive impurities that could typically deposit on turbine airfoils during service in an aggressive combustion environment. Deposits such as V_2O_5 , P_2O_5 , Na_2SO_4 , CaSO_4 , NaVO_3 and a $\text{Na}_2\text{SO}_4+\text{V}_2\text{O}_5$ mixture (50-50 mol.%) that can be formed as a combustion by-product during the use of high-impurity alternative fuels have been thoroughly examined in this study. In addition, air-borne sand ingestion has been a critical threat in recent years, where sand with a specific composition of CaO , MgO , Al_2O_3 and SiO_2 (commonly referred to as CMAS sand) can adhere and deposit on the hot-section turbine components. Degradation of TBCs and ORCs by CMAS sand, in the molten state, was also thoroughly investigated. After identifying the individual degradation mechanisms of APS TBCs and ORCs by these corrosive deposits, attempts to mitigate the corrosive-melt induced attack on high temperature protective coatings have also been explored. Employing a dense overlay coating for the APS YSZ, which can act as a semi-impermeable and a sacrificial layer in order to protect the porous TBCs was demonstrated to be a promising mitigation approach in this study. EPD followed by a controlled sintering step was found to yield a ceramic overlay of desired thickness, chemistry and porosity. The noble microstructural characteristics of these ceramic overlays processed by EPD, are uniform thickness, homogeneity, uniformly distributed closed-pore distribution, and excellent YSZ/overlay adhesion. These features enable the use of crack-free dense overlays as prime-reliant environmental barrier overlay systems for TBCs.

Various individual degradation mechanisms of the APS YSZ due to attack by corrosive molten deposits are summarized as follows:

- ✓ Two different reaction mechanisms were observed from the YSZ–V₂O₅ interaction depending on the temperature. Formation of ZrV₂O₇ was observed to be the predominant reaction below 747°C. Above 747°C, V₂O₅ melt degrades the YSZ by reacting with the yttria stabilizer to form YVO₄. This leads to a disruptive zirconia phase transformation to monoclinic phase. These two different reaction mechanisms were explained by the incongruent melting behavior of ZrV₂O₇ at 747°C.
- ✓ Studies on molten Na₂SO₄ showed that the molten sodium sulfate is chemically inert for YSZ with evidence of minor thermochemical degradation, although its infiltration into the interlamellar gaps and pores of the YSZ and crystallization while cooling would result in thermo-mechanical damage.
- ✓ At elevated temperatures, Na₂O in molten state, dissociated from Na₂SO₄, tends to form vanadates of sodium such as sodium metavanadate, NaVO₃, in the presence of V₂O₅. Degradation behavior of the YSZ by the sodium vanadates from Na₂SO₄+V₂O₅ mixture was studied at 700°C. The YVO₄ formed without any evidence of ZrV₂O₇ formation, similar to that for the YSZ-V₂O₅ interaction above 747°C. Presence of Na₂SO₄ enhances the high temperature degradation of the YSZ by V₂O₅.
- ✓ Degradation studies of the YSZ by P₂O₅ revealed that the only observed reaction between ZrO₂ and P₂O₅ was the formation of ZrP₂O₇, which enriched the yttria content in the YSZ leading to the phase transformation to fluorite-cubic phase.

- ✓ Molten CMAS attack degraded APS YSZ through a general dissolution of YSZ rather than a preferential depletion of Y_2O_3 or ZrO_2 in the YSZ. CMAS was found to melt and readily infiltrate the free-standing APS YSZ coatings within a short time. All YSZ samples were observed to be completely infiltrated by molten CMAS starting at 1250°C for all time durations investigated in this study (2 to 4 h). Infiltrated microstructures and phase transformations were found to be independent of exposure temperature, once the CMAS melt penetrates into the porous YSZ coating through the cracks and interlamellar gaps. A significant amount of Y_2O_3 depleted monoclinic ZrO_2 phase evolved from CMAS melt after dissolution of the t' - ZrO_2 was observed. The reprecipitated ZrO_2 grains have a spherical morphology in general. TEM results were consistent with XRD analysis. Both monoclinic and metastable tetragonal ZrO_2 phases were identified. Presence of yttria-rich cubic ZrO_2 phase was also present. CMAS melt readily dissolved the YSZ, then reprecipitated ZrO_2 with a composition based on local melt chemistry that deviates in Y_2O_3 stabilizer content from the original YSZ coating.

Individual degradation mechanisms of CoNiCrAlY due to corrosive molten deposits are summarized as follows:

- ✓ Different degradation mechanisms were observed from the V_2O_5 melt interaction with CoNiCrAlY at 700°C and 900°C. At 700°C, formation of chromium-aluminum orthovanadate, $(Cr,Al)VO_4$ was found. However, the infiltration rate was found to be greater than the dissolution rate resulting in a significant accumulation of V_2O_5 melt at the bottom surface of free-standing CoNiCrAlY. At 900°C, an extensive dissolution of CoNiCrAlY by V_2O_5 melt

produced reaction products of nickel-cobalt orthovanadate, $(\text{Ni,Co})_3(\text{VO}_4)_2$. In addition, degradation at 900°C resulted in an extensive formation of spinel oxide, $(\text{Ni,Co})(\text{Al,Cr})_2\text{O}_4$.

- ✓ Examination of P_2O_5 melt interaction with CoNiCrAlY at 350°C for 2 h revealed the formation of two different polyphosphates, namely $(\text{Ni,Co})(\text{PO}_3)_2$ and $(\text{Cr,Al})(\text{PO}_3)_3$ via a significant consumption of CoNiCrAlY.
- ✓ As-sprayed CoNiCrAlY was found to be susceptible to classic Type I hot corrosion attack during exposure to Na_2SO_4 melt at 1000°C . A significant formation of chromium sulfide (Cr_2S_3) and accelerated internal oxidation at the intersplat boundaries of the APS CoNiCrAlY was observed. Preoxidized CoNiCrAlY showed a better resistance against molten Na_2SO_4 attack, however, formation of porous $(\text{Cr,Al})_2\text{O}_3$ and $(\text{Ni,Co})(\text{Al,Cr})_2\text{O}_4$, in addition to the $\alpha\text{-Al}_2\text{O}_3$ as the TGO scale constituent could not be avoided.
- ✓ Molten CaSO_4 was found to consume the CoNiCrAlY constituents through basic fluxing mechanism leading to the formation of CaCrO_4 and CaAl_2O_4 . Thus protective oxide formation was hindered in the presence of CaSO_4 deposit.
- ✓ NaVO_3 attacked the APS CoNiCrAlY, only in its as-sprayed condition, unlike the more acidic V_2O_5 deposit. The CoNiCrAlY after a preoxidation treatment was found to be more resistant against NaVO_3 attack with a minor modification in the oxide scale formation.
- ✓ Extensive dissolution of the TGO, $\alpha\text{-Al}_2\text{O}_3$, of the CoNiCrAlY coatings by CMAS melt and significant spinel oxide formation were identified as the degradation mechanisms of the APS CoNiCrAlY coatings..

After a detailed investigation on the degradation of the YSZ and CoNiCrAlY by various corrosive deposits, it was obvious that the melt ingression into these coating systems should be inhibited in order to mitigate the melt induced-deposit attack. Experimental results from this study demonstrated that a dense, crack-free, sacrificial oxide overlay can effectively perform as an environmental barrier overlay for the APS TBCs. A protective overlay of uniform thickness and uniformly distributed closed pores can be readily achieved by electrophoretic deposition (EPD). Experimental results from this study demonstrated that EPD α -Al₂O₃ environmental barrier overlay can be a durable overlay that can effectively protect TBCs from CMAS attack. Dense crack-free alumina overlay coatings for TBCs were successfully fabricated by EPD followed by sintering at a relatively low temperature of 1200°C for 10 h. Attributed mechanisms of protection include the suppression of CMAS melt infiltration due to the novel microstructural characteristics and thermochemical interaction of α -Al₂O₃ overlay with CMAS melt that enriches the Al content in the CMAS melt. A shift in the CMAS glass composition to a crystallizable Al-rich glass composition promoted the formation of anorthite (CaAl₂Si₂O₈) platelets and MgAl₂O₄ spinel. The EPD kinetics was also analyzed using a time-dependent thickness variation profile and a phenomenological expression that describes the deposition kinetics.

The EPD MgO overlay was found to provide effective protection against V₂O₅ corrosive melt through thermochemical interactions that yield magnesium vanadates such as Mg₂V₂O₇ and Mg₃V₂O₈, which have higher melting temperature. Even though the dense YSZ overlay with desired microstructure was envisioned as a promising overlay due to its excellent TBC/overlay interfacial adhesion strength, the YSZ without any beneficial thermochemical interaction failed to effectively protect the underlying TBC system against melt-induced degradation. As an

attempt to fabricate an overlay that can effectively protect TBCs from corrosive deposits due to low-quality alternative fuel usage and air-ingestion of CMAS sand, codeposition of alumina and magnesia through EPD was performed, which yielded a Al_2O_3 -MgO composite overlay. This composite overlay was found to be promising in protecting the APS YSZ based TBCs from various melt-induced attacks through various thermochemical interactions.

Thermal cyclic testing of TBCs on bond-coated superalloy substrate, modified with EPD alumina overlay of 75 μm in thickness, further demonstrated the promising application of EPD alumina overlay. A dense EPD overlay composed of appropriate chemistry would be beneficial to effectively mitigate molten deposit attack on TBCs by reducing the viscosity of the melt and forming crystalline reaction products with high melting point via thermochemical interactions. EPD is a versatile cost-effective technique that can be tailored to further develop a highly-durable overlay of desired chemistry and microstructure for protection of TBCs and gas turbine components from any high temperature corrosion attack, typically dictated by the aggressiveness of the alternative-fuel combustion environment.

APPENDIX A:
FUTURE DIRECTIONS

From this doctoral study, it is obvious that achieving a clear understanding of thermochemical degradation of high temperature protective coatings due to molten deposit attack is mandatory for expansive applications of TBCs and ORCs. This dissertation demonstrated that these prime-reliant porous ceramic coating systems can be effectively protected against corrosive melt-induced attack by employing thermochemical interaction-type trapping mechanisms in order to capture various corrosive compounds. The study also demonstrated the promising ability of the EPD technique to process sacrificial-type overlay ceramic coatings with desired microstructural characteristics. Based on the findings from this study, the following research directions could lead to various technological developments to improve the advanced turbine materials system.

1. A durability study with a thermal gradient across the individual layers of the discussed multilayer TBC system in order to assess the potential of sacrificial/impermeable overlay for use in real-engine operating conditions.
2. Thorough investigation on degradation of alternate TBC topcoat materials, e.g., a single zirconate ($\text{Gd}_2\text{Zr}_2\text{O}_7$, $\text{La}_2\text{Zr}_2\text{O}_7$, $\text{Nd}_2\text{Zr}_2\text{O}_7$) layer, double ceramic layer (DCL) by various corrosive molten deposits.
3. Assessment of a Gd_2O_3 -based environmental barrier overlay processed by EPD as a protective overlay for APS TBCs against CMAS attack as well as vanadate-sulfate-type hot corrosion attack. Very few oxide materials that are reliable as an overlay material for

YSZ can also trap a wide variety of corrosive deposits through thermochemical interactions. Gd_2O_3 seems to be a promising material for such applications.

4. Refinement of the EPD overlay processing technique in order to achieve overlay of desired characteristics through modifying the EPD and densification process parameters (e.g., starting particle size, favorable sintering conditions).
5. Assessment of EPD as a topcoat processing technique for TBC applications, especially for achieving alternate ceramic topcoat with tailored microstructure, where a rapid quench microstructure is not mandatory.

APPENDIX B:
**LIST OF PUBLICATIONS AND PRESENTATIONS FROM THIS
DISSERTATION**

Peer-Reviewed Journal Publications:

1. Prabhakar Mohan, Biao Yuan, Travis Patterson, Vimal Desai, and Yongho Sohn, "Degradation of yttria-stabilized zirconia thermal barrier coatings by vanadium pentoxide, phosphorus pentoxide, and sodium sulfate", *Journal of American Ceramic Society*, 90 [11] (2007) 3601-3607.
2. Prabhakar Mohan, Biao Yuan, Travis Patterson, Vimal Desai and Yongho Sohn, "Degradation of yttria-stabilized zirconia thermal barrier coatings by molten CMAS (CaO-MgO-Al₂O₃-SiO₂) deposits", *Materials Science Forum Vols. 595-598* (2008) pp 207-212.
3. Prabhakar Mohan, Travis Patterson, Vimal Desai and Yongho Sohn, "Degradation of APS CoNiCrAlY bond coats in thermal barrier coatings by vanadium and phosphorus pentoxides", *Surface and Coatings Technology*, 203 (2008) 427-431.
4. Prabhakar Mohan, Bo Yao, Travis Patterson and Yongho Sohn, "Electrophoretically deposited alumina as protective overlay for thermal barrier coatings against CMAS degradation", *Surface & Coatings Technology* 204 (2009) 797-801.
5. Prabhakar Mohan, Travis Patterson, Bo Yao and Yongho Sohn, "Degradation of thermal barrier coatings by fuel impurities and CMAS: Thermochemical Interactions and Mitigation approaches", *Journal of Thermal Spray Technology*, 19 [1-2] (2010) 156-167.

Conference Proceedings:

1. Prabhakar Mohan, Travis Patterson and Yongho Sohn, "Degradation of thermal barrier coatings by molten CMAS (CaO-MgO-Al₂O₃-SiO₂) deposits, AIAA 2009-1433, Proceedings of 47th AIAA Aerospace Sciences Meeting, Jan 2009, Orlando, FL.
2. Prabhakar Mohan, Travis Patterson and Yongho Sohn, "Electrophoretic deposition of environmental barrier overlay coating for yttria-stabilized zirconia thermal barrier coatings", GT2009-59839, Proceedings of ASME TurboExpo 2009, June 2009, Orlando, FL.
3. Yongho Sohn, Prabhakar Mohan, Patrick Schelling and Duc Nguyen, "Degradation of thermal barrier coatings by fuel impurities and CMAS", Proceedings of International Thermal Spray Conference and Exposition (ITSC 2009), May 2009, Las Vegas, NV.

Conference Presentations:

1. “Degradation mechanisms of YSZ topcoat in TBCs by V_2O_5 , P_2O_5 and Na_2SO_4 ” – Oral presentation made at TMS 2007 annual meeting and exhibition, Feb 25 – Mar 1, 2007, Orlando, FL, USA.
2. “Degradation of YSZ topcoat by V_2O_5 and P_2O_5 ” – Poster presentation made at 34th International Conference on Metallurgical Coatings and Thin Films (ICMCTF 2007), Apr 23-27, 2007, San Diego, CA, USA.
3. “Degradation of YSZ TBCs by V_2O_5 and P_2O_5 ” – Poster presentation made at 3rd ASM Annual student poster competition, ASM Central Florida chapter, Apr 2007, Orlando, FL, USA.
4. “Degradation mechanisms of YSZ TBCs by V_2O_5 , P_2O_5 and Na_2SO_4 ” – Oral presentation made at Graduate Research Forum 2007, Apr 3, 2007, UCF, Orlando, FL, USA.
5. “Microstructural analysis of CMAS induced degradation in YSZ TBCs” – Oral presentation made at 32nd International Conference on Advanced Ceramics and Composites (ICACC), Jan 27 – Feb 1, 2008, Daytona Beach, FL, USA.
6. “Microstructural analysis of thermal barrier coatings and Ni-base superalloys after syngas exposure” – Oral presentation made at 32nd International Conference on Advanced Ceramics and Composites (ICACC), Jan 27 – Feb 1, 2008, Daytona Beach, FL, USA.
7. “Degradation of APS CoNiCrAlY bond coats in TBCs by vanadium, phosphorus and sodium compounds” – Oral presentation made at 35th International Conference on Metallurgical Coatings and Thin Films (ICMCTF 2008), Apr 28 - May 2, 2008, San Diego, CA, USA.
8. “Degradation of YSZ TBCs by molten CMAS deposits” – Oral presentation (Invited) made at 7th International symposium on High-Temperature Corrosion and Protection of Materials (HTCPM), May 18-23, 2008, Les Embiez, France.
9. “Sulfate-induced high temperature degradation of APS TBCs” – Presented at 33rd International Conference on Advanced Ceramics and Composites (ICACC), Jan 18-23, 2009, Daytona Beach, FL, USA.
10. “Degradation of YSZ TBCs by molten CMAS deposits” – Presented at 47th American Institute of Aeronautics and Astronautics (AIAA): Aerospace Sciences Meeting, Jan 5-8, 2009, Orlando, FL, USA.

11. “Electrophoretically Deposited Alumina as Protective Overlay for Thermal Barrier Coatings Against CMAS Degradation” – Presented at the International Conference on Metallurgical Coatings and Thin Films (ICMCTF 2009), April 27 - May 1, 2009, San Diego, CA, USA.
12. “Degradation of thermal barrier coatings by fuel impurities and CMAS” – Presented at the International Thermal Spray Conference and Exposition (ITSC 2009), May 4-7, 2009, Las Vegas, NV, USA.
13. “Electrophoretic deposition of environmental barrier overlay coatings for yttria stabilized zirconia thermal barrier coatings”- Presented at the ASME Turbo Expo: Power for Land, Sea and Air, June 8-12, 2009, Orlando, FL, USA.
14. “Environmental barrier overlay for thermal barrier coatings by electrophoretic deposition” – Poster presented at the at 34th International Conference on Advanced Ceramics and Composites (ICACC), Jan 25-29, 2010, Daytona Beach, FL, USA.
15. “Durability assessment of electrophoretically deposited environmental barrier overlay for air plasma sprayed thermal barrier coating” – Oral presentation at the International Conference on Metallurgical Coatings and Thin Films (ICMCTF 2010), April 26 - 30, 2010, San Diego, CA, USA.

LIST OF REFERENCES

1. R.A. Rapp, "Hot corrosion of materials", *Pure & Appl. Chem.*, 62 [1] (1990) 113-122.
2. J. Stringer, "High temperature corrosion issues in energy-related systems", *Materials Research*, 7 [1] (2004) 1-9.
3. V. Desai, "Materials for high-temperature protection", *Journal of Metals*, 58 [1] (2006) 15.
4. G.Y. Lai, "High temperature corrosion of engineering alloys", ASM International, Materials Park, OH, USA, 1990.
5. G.J. Santoro, "Hot corrosion of four superalloys: HA-188, S-57, IN-617, and TD-NiCrAl", *Oxidation of metals*, 13 [5] (1979) 405-435.
6. P. Kofstad and G. Akesson, "Sulfate-induced high temperature corrosion of nickel", *Oxidation of metals*, 14 [4] (1980) 301-323.
7. R.A. Rapp, "Chemistry and electrochemistry of hot corrosion of metals", *Materials Science and Engineering*, 87 (1987) 319-327.
8. R.A. Rapp, "Hot corrosion of materials: a fluxing mechanism?", *Corrosion Science*, 44 (2002) 209-221.
9. R.C. Reed, "The Superalloys: Fundamentals and Applications", Cambridge University Press, Cambridge, UK, 2006.
10. S. Bose, "High Temperature Coatings", Butterworth-Heinemann Publishers (Elsevier Inc.), Jordan Hill, Oxford, UK, 2007.
11. R.A. Miller, "Oxidation-based model for thermal barrier coating life", *J. Am. Ceram. Soc.*, 67 [8] 517-521 (1984).
12. R.L. Jones, "Thermal barrier coatings", in *Metallurgical and ceramic protective coatings*, Ed. Stern, K. H., Chapman & Hall, (London), 1996, pp. 194-235.
13. R.A. Miller, "Current status of thermal barrier coatings – an overview", *Surf. Coat. Technol.*, 30 [1] (1987) 1-11.
14. J. Stringer, "Coatings in the electricity supply industry: past, present, and opportunities for the future", *Surf. Coat. Technol.*, 108–109 (1998) 1-9.

15. N. P. Padture, M. Gell, and E. H. Jordan, "Thermal barrier coatings for gas-turbine engine applications", *Science*, 296 (2002) 280-284.
16. A.G. Evans, D.R. Mumm, J.W. Hutchinson, G.H. Meier, and F.S. Pettit, "Mechanisms controlling the durability of thermal barrier coatings", *Prog. Mater. Sci.*, 46 (2001) 505-553.
17. A.G. Evans, M.Y. He, and J.W. Hutchinson, "Mechanism based scaling laws for the durability of thermal barrier coatings", *Prog. Mater. Sci.*, 46 (2001) 249.
18. M.J. Stiger, N.M. Yanar, M.G. Topping, F.S. Pettit, and G.H. Meier, "Thermal barrier coatings for the 21st century", *Z. Metallk.*, 90 (1999) 1069-1078.
19. J. Liu, J.W. Byeon, and Y.H. Sohn, "Effects of phase constituents/microstructure of thermally grown oxide on the failure of EB-PVD thermal barrier coating with NiCoCrAlY bond coat", *Surf. Coat. Technol.*, 200 (2006) 5869-5876.
20. B.W. Kempshall, Y.H. Sohn, S.K. Jha, S. Laxman, R.R. Vanfleet, and J. Kimmel, "A microstructural observation of near-failure thermal barrier coating: a study by photostimulated luminescence spectroscopy and transmission electron microscopy", *Thin Solid Films.*, 466 (2004) 128-136.
21. W. Brandl, H.J. Gradke, D. Toma and J. Kruger, "The oxidation behavior of sprayed MCrAlY coatings", *Surf. Coat. Technol.* 86-87 (1996) 41-47.
22. N.J. Simms, P.J. Kilgallon, C. Roach, and J.E. Oakey, "Development of oxides at TBC - bond coat interfaces in burner rig exposure", *Mater. High Temp.* 20 (2003) 519-526.
23. J.Y. Kwon, J.H. Lee, Y.G. Jung, and U. Paik, "Effect of bond coat nature and thickness on mechanical characteristic and contact damage of zirconia-based thermal barrier coatings", *Surf. Coat. Technol.* 201 (2006) 3483-3490.
24. T. Patterson, A. Leon, B. Jayaraj, J. Liu, and Y.H. Sohn, "Thermal cyclic lifetime and oxidation behavior of air plasma sprayed CoNiCrAlY bond coats for thermal barrier coatings", *Surface and Coatings Technology*, 203 [5-7] (2008) 437-441.
25. F.J. Belzunce, V. Higuera and S. Poveda, "High temperature oxidation of HFPD thermal sprayed MCrAlY Coatings", *Materials Science and Engineering A297* (2001) 162-167.
26. Scrivani, U. Bardi, L. Carrafiello, A. Lavacchi, and F. Niccolai, "A comparative study of high velocity oxygen fuel, vacuum plasma spray, and axial plasma spray for the deposition of CoNiCrAlY bond coat alloy", *J. Therm. Spray Technol.* 12 (4) (2003) 504-507.

27. D. Toma, W. Brandl and U. Koster, "Studies on the transient stage of oxidation of VPS and HVOF sprayed MCrAlY coatings", *Surface and Coatings Technology* 120–121 (1999) 8–15.
28. R. L. Jones, "Some aspects of the hot corrosion of thermal barrier coatings", *J. Therm. Spray Technol.*, 6 [1] (1997) 77-84.
29. M. P. Borom, C. A. Johnson, and L. A. Peluso, "Role of environmental deposits and operating surface temperature in spallation of air plasma sprayed thermal barrier coatings", *Surf. Coat. Technol.*, 86–87 (1996) 116-126.
30. S. Kramer, J. Yang, and C.G. Levi, "Thermochemical interaction of thermal barrier coatings with molten CaO-MgO-SiO₂-Al₂O₃ (CMAS) deposits", *Journal of American Ceramic Society*, 89 [10] (2006) 3167-3175.
31. B. A. Nagaraj, and D. J. Wortman, "Burner rig evaluation of ceramic coatings with vanadium-contaminated fuels", *Trans. ASME: J. Eng. Gas Turbines Power*, 112 (1990) 536-542.
32. R. J. Bratton, S. K. Lau, and S. Y. Lee, "Evaluation of present-day thermal barrier coatings for industrial/utility applications", *Thin Solid Films*, 73 [2] (1980) 429-437.
33. P. E. Hodge, R. A. Miller, and M. A. Gedwill, "Evaluation of the hot corrosion behavior of thermal barrier coatings", *Thin Solid Films*, 73 [2] (1980) 447-453.
34. C. Leyens, I. G. Wright, and B. A. Pint, "Hot Corrosion of an EB-PVD Thermal Barrier Coating System at 950°C", *Oxid. Met.* 54 [5-6] (2000) 401-424.
35. B. R. Marple, J. Voyer, C. Moreau, and D. R. Nagy, "Corrosion of thermal barrier coatings by vanadium and sulfur compounds", *Mater. High Temp.*, 17 [3] (2000) 397-412.
36. R. L. Jones, C. E. Williams, and S. R. Jones, "Reaction of Vanadium compounds with ceramic oxides", *J. Electrochem. Soc.*, 133 [1] (1986) 227-230.
37. D. W. Sustitzky, W. Hertl, and C. B. Carter, "Destabilization of Zirconia Thermal Barriers in the Presence of V₂O₅", *J. Am. Ceram. Soc.*, 71 [11] (1988) 992-1004.
38. W. Hertl, "Vanadia reactions with yttria stabilized zirconia", *J. Appl. Phys.*, 63 [11] (1988) 5514-5520.
39. J.C. Hamilton and A.S. Nagelberg, "In-situ raman spectroscopic study of yttria-stabilized zirconia attack by molten sodium vanadate", *J. Am. Ceram. Soc.*, 67 [10] (1984) 686-690.

40. S. A. Muqtader, R. K. Sidhu, E. Nagabhushan, K. Muzaffaruddin, and S. G. Samdani, "Destabilization behaviour of ceria-stabilized tetragonal zirconia polycrystals by sodium sulfate and vanadium oxide melts", *J. Mater. Sci. Lett.*, 12 [11] (1993) 831-833.
41. C. Mercer, S. Faulhaber, A.G. Evans, and R. Darolia, "A delamination mechanism for thermal barrier coatings subject to calcium–magnesium–alumino-silicate (CMAS) infiltration", *Acta Materialia*, 53 [4] (2005) 1029-1039.
42. S. Bose, T.E. Strangman, in *Materials and practices to improve resistance to fuel derived environmental damage in land and sea- based turbines*. Edited by D. Olson, G. Edwards, P. Bollinger, A. Lasseigne, and G. Atkins, EPRI, Palo Alto, CA and Colorado School of Mines, Golden, CO, Oct. 2003.
43. C. Batista, A. Portinha, R. M. Ribeiro, V. Teixeira, and C. R. Oliveira, "Evaluation of laser-glazed plasma-sprayed thermal barrier coatings under high temperature exposure to molten salts", *Surf. Coat. Technol.*, 200[24] (2006) 6783-6791.
44. Z. Chen, N.Q. Wu, J. Singh, and S.X. Mao, "Effect of Al₂O₃ overlay on hot-corrosion behavior of yttria-stabilized zirconia coating in molten sulfate-vanadate salt", *Thin Solid Films* 443 (2003) 46-52.
45. C. Ramachandra, K.N. Lee, and S.N. Tewari, "Durability of TBCs with a surface environmental barrier layer under thermal cycling in air and in molten salt", *Surf. Coat. Technol.*, 172 (2003) 150-157.
46. S. Raghavan, and M. J. Mayo, "The hot corrosion resistance of 20 mol% YTaO₄ stabilized tetragonal zirconia and 14 mol% Ta₂O₅ stabilized orthorhombic zirconia for thermal barrier coating applications", *Surf. Coat. Technol.*, 160 (2002) 187-196.
47. S. Y. Park, J. H. Kim, M. C. Kim, H. S. Song, and C. G. Park, "Microscopic observation of degradation behavior in yttria and ceria stabilized zirconia thermal barrier coatings under hot corrosion", *Surf. Coat. Technol.*, 190 (2005) 357-365.
48. R. L. Jones, R. F. Reidy, and D. Mess, "Scandia, yttria-stabilized zirconia for thermal barrier coatings", *Surf. Coat. Technol.*, 82 (1996) 70-76.
49. R. Vassen, X. Cao, F. Tietz, D. Basu, and D. Stover, "Zirconates as new materials for thermal barrier coatings", *J. Am. Ceram. Soc.*, 83[8] (2000) 2023–2028.
50. Aygun, A.L. Vasiliev, N.P. Padture, and X. Ma, "Novel thermal barrier coatings that are resistant to high-temperature attack by glassy deposits", *Acta Mater.*, 55 (2007) 6734.

51. S. Kramer, J. Yang, and C.G. Levi, "Infiltration-inhibiting reaction of gadolinium zirconate thermal barrier coatings with CMAS melts", *J. Am. Ceram. Soc.*, 91 [2] (2008) 576–583.
52. D.R. Clarke and C.G. Levi, "Materials design for the next generation thermal barrier coatings", *Annu. Rev. Mater. Res.*, 33, (2003) 383–417.
53. P. Mohan, B. Yuan, T. Patterson, V.H. Desai, Y.H. Sohn, Degradation of yttria-stabilized ZrO₂ thermal barrier coatings by vanadium pentoxide, phosphorous pentoxide, and sodium sulfate, *J. Am. Ceram. Soc.*, 90 [11] (2007) 3601-3607.
54. P. Mohan, B. Yuan, T. Patterson, V.H. Desai, Y.H. Sohn, Degradation of yttria-stabilized zirconia thermal barrier coatings by molten CMAS (CaO-MgO-Al₂O₃-SiO₂) deposits, *Materials Science Forum*, 595-598 (2008) 207-212.
55. P. Mohan, T. Patterson, V.H. Desai, and Y.H. Sohn, Degradation of Free-Standing Air Plasma Sprayed CoNiCrAlY Coatings by Vanadium and Phosphorus Pentoxides, *Surf. Coat. Technol.*, 203 (2008) 427-431.
56. P. Mohan, B. Yao, T. Patterson and Y.H. Sohn, "Electrophoretically deposited alumina as protective overlay for thermal barrier coatings against CMAS degradation", *Surface & Coatings Technology*, 204 (2009) 797–801.
57. P. Mohan, T. Patterson, B. Yao and Y.H. Sohn, "Degradation of thermal barrier coatings by fuel impurities and CMAS: Thermochemical Interactions and Mitigation approaches", *Journal of Thermal Spray Technology*, 19 [1-2] (2010) 156-167.
58. P. Mohan, T. Patterson and Y.H. Sohn, "Electrophoretic deposition of environmental barrier overlay coating for yttria-stabilized zirconia thermal barrier coatings", GT2009-59839, Proceedings of ASME TurboExpo 2009, June 2009, Orlando, FL.
59. R. C. Garvie, R. H. J. Hannink, and R. T. Pascoe, "Ceramic Steel", *Nature*, 258 (1975) 703–704.
60. J. Chevalier, L. Gremillard, A. Virkar and D.R. Clarke, "The tetragonal-monoclinic transformation in zirconia: lessons learned and future trends", *J. Am. Ceram. Soc.*, 92 [9] (2009) 1901–1920.
61. V. Virkar and R. L. K. Matsumoto, "Ferroelastic Domain Switching as a Toughening Mechanism in Tetragonal Zirconia", *J. Am. Ceram. Soc.*, 69 [10] (1986) C224–226.
62. R. C. Garvie, "Stabilization of the Tetragonal Structure in Zirconia Microcrystals", *J. Phys. Chem.*, 82 [2] (1978) 218–224.

63. D. Yong, J. Zhanpeng, and P. Huang, "Thermodynamic assessment of the ZrO_2 - $YO_{1.5}$ system," *J. Am. Ceram. Soc.*, 74 [7] (1991) 1569-1577.
64. P. Duwez, F. H. Brown, and F. Odell, "The Zirconia–Yttria System", *J. Electrochem. Soc.*, 98 [9] (1951) 356–362.
65. H. G. Scott, "Phase Relationships in the Zirconia–Yttria System," *J. Mater.Sci.*, 10, 1527–35 (1975).
66. R. Stevens, "An Introduction to Zirconia," Magnesium Elektron Ltd., Twickenham, UK, 1983, pp,7.
67. A.N. Khan and J. Lu, "Behavior of air plasma sprayed thermal barrier coatings, subject to intense thermal cycling", *Surface and Coatings Technology*, 166 (2003) 37-43
68. S. Stecura, "Optimization of the NiCrAl-Y/ZrO₂-Y₂O₃ thermal barrier system" NASA Tech. Memo. 86905, NASA, Cleveland OH.
69. T. Patterson, "Effects of internal oxidation on thermo-mechanical properties of atmospheric plasma sprayed CoNiCrAlY coatings", M.S. Thesis, University of Central Florida, 2008.
70. T.E. Strangman, "Thermal barrier coatings for turbine airfoils", *Thin Solid Films*, 127, (1985) 93-105.
71. F.C. Toriz, A.B. Thakker and S.K. Gupta, "Flight service evaluation of thermal barrier coatings by physical vapor deposition at 5200 H", *Surface and Coatings Technology*, 39-40 (1989) 161-172.
72. B. Franke, "Nondestructive evaluation of thermal barrier coatings with thermal wave imaging and photostimulated luminescence spectroscopy", M.S. Thesis, University of Central Florida, 2005.
73. V. K. Tolpygo, D. R. Clarke and K. S. Murphy, "Oxidation-induced failure of EB-PVD thermal barrier coatings", *Surface and Coatings Technology*, 146-147 (2001) 124-131.
74. V. K. Tolpygo and D. R. Clarke "Morphological evolution of thermal barrier coatings induced by cyclic oxidation", *Surface and Coatings Technology*, 163-164 (2003) 81-86.
75. M. Madhwal, E.H. Jordan and M. Gell, "Failure mechanisms of dense vertically-cracked thermal barrier coatings", *Materials Science and Engineering A* 384 (2004) 151–161.

76. Hongbo Guo, Seiji Kuroda, and Hideyuki Murakami, "Microstructures and Properties of Plasma-Sprayed Segmented Thermal Barrier Coatings", *J. Am. Ceram. Soc.*, 89 [4] (2006) 1432–1439.
77. S.D. Graham, M.F. DeSoi, M.L. Smith, M.W. Wallace and R.L. Ling, "Dense vertically cracked thermal barrier coating process to facilitate post-coat surface finishing", United States Patent: No. US 6,432,487 B1.
78. V.K. Tolpygo, D.R. Clarke, K.S. Murphy, "Oxidation-induced failure of EB-PVD thermal barrier coatings", *Surface and Coatings Technology* 146–147 (2001) 124–131.
79. K.W. Schlichting, N.P. Padture, E.H. Jordan and M. Gell, "Failure modes in plasma-sprayed thermal barrier coatings", *Materials Science and Engineering A342* (2003) 120–130.
80. Rabiei and A.G. Evans, "Failure mechanisms associated with the thermally grown oxide in plasma-sprayed thermal barrier coatings", *Acta mater.* 48 (2000) 3963–3976.
81. T. Strangman, D. Raybould, A. Jameel and W. Baker, "Damage mechanisms, life prediction, and development of EB-PVD thermal barrier coatings for turbine airfoils", *Surface & Coatings Technology* 202 (2007) 658–664.
82. Trunova, T. Beck, R. Herzog, R.W. Steinbrech and L. Singheiser, "Damage mechanisms and lifetime behavior of plasma sprayed thermal barrier coating systems for gas turbines—Part I: Experiments", *Surface & Coatings Technology* 202 (2008) 5027–5032.
83. T. Beck, R. Herzog, O. Trunova, M. Offermann, R.W. Steinbrech and L. Singheiser, "Damage mechanisms and lifetime behavior of plasma-sprayed thermal barrier coating systems for gas turbines — Part II: Modeling", *Surface & Coatings Technology* 202 (2008) 5901–5908.
84. J. Liu, "Mechanisms of lifetime improvement in thermal barrier coatings with Hf and/or Y modification of CMSX-4 superalloy substrates", Ph.D. Dissertation, University of Central Florida, 2007.
85. J.L. Smialek, D.T. Jayne, J.C. Schaeffer, and W.H. Murphy, "Effects of hydrogen annealing, sulfur segregation and diffusion on the cyclic oxidation resistance of superalloys: a review", *Thin Solid Films*, Vol. 253 [1-2] (1994) 285-291.
86. T.B. Massalski, J.L. Murray, L.H. Bennett, edited by H.Baker, *Binary Alloy Phase Diagrams*, 1st ed., ASM International, Metals Park, OH, 1986.
87. J. R. Nicholls, N. J. Simms, W. Y. Chan, and H. E. Evans, "Smart overlay coatings — concept and practice", *Surface and Coatings Technology* 149 [2-3] (2002) 236-244.

88. I.G. Wright and B.A. Pint, "Some effects of interactions among minor element additions on the high-temperature oxidation behavior of Ni-base alumina-forming alloys", First International Conference on Industrial Gas Turbine Technologies CAME-GT Brussels, 10-11 July 2003.
89. S. Laxman, B. Franke, B.W. Kempshall, Y.H. Sohn, L.A. Giannuzzi and K.S. Murphy, "Phase transformations of thermally grown oxide on (Ni,Pt)Al bondcoat during electron beam physical vapor deposition and subsequent oxidation", *Surface and Coatings Technology* 177 –178 (2004) 121–130
90. W.R. Chen, X. Wu, D. Dudzinski and P.C. Patnaik, "Modification of oxide layer in plasma-sprayed thermal barrier coatings", *Surface & Coatings Technology* 200 (2006) 5863–5868.
91. D. M. Lipkin and D. R. Clarke, "Measurement of the stress in oxide scales formed by oxidation of aluminum-containing alloys", *Oxid. Met.*, 45 (1996) 267-280.
92. K. W. Schlichting, K. Vaidyanathan, Y. H. Sohn, E. H. Jordan, M. Gell and N. P. Padture, "Application of Cr³⁺ photoluminescence piezo-spectroscopy to plasma-sprayed thermal barrier coatings for residual stress measurement', *Mater. Sci. Eng. A*, 291 (2000) 68-77.
93. S. M. Meier, D. M. Nissley, K. D. Sheffler, T. A. Cruse, *J. Eng. Gas Turbines Powers*, 112 (1990) 521.
94. E. Schumann, C. Sarioglu, J. R. Blachere, F. S. Pettit, G. H. Meier, "High temperature stress measurement during oxidation of NiAl", *Oxid. Met.*, 53 (2000) 259.
95. V.K. Tolpygo and D.R. Clarke, "On the rumpling mechanism in nickel-aluminide coatings Part I: an experimental assessment", *Acta Materialia* 52 (2004) 5115–5127.
96. V.K. Tolpygo and D.R. Clarke, "On the rumpling mechanism in nickel-aluminide coatings Part II: characterization of surface undulations and bond coat swelling", *Acta Materialia* 52 (2004) 5129–5141.
97. V.K. Tolpygo and D.R. Clarke, "Surface rumpling of a (Ni,Pt)Al bond coat induced by cyclic oxidation", *Acta Mater.* 48 (2000) 3283-3293.
98. M. Matsumoto, T. Kato, K. Hayakawa, N. Yamaguchi, S. Kitaoka and H. Matsubara, "The effect of pre-oxidation atmosphere on the durability of EB-PVD thermal barrier coatings with CoNiCrAlY bond coats", *Surface & Coatings Technology* 202 (2008) 2743–2748.

99. U. Schulz, K. Fritscher, C. Leyens, and M. Peters, "Influence of processing on microstructure and performance of electron beam physical vapor deposition (EB-PVD) thermal barrier coatings", *Trans. ASME: Journal of Engineering for Gas Turbines and Power*, 124 (2002) 229-234.
100. T.J. Nijdam, and W.G. Sloof, "Combined pre-annealing and pre-oxidation treatment for the processing of thermal barrier coatings on NiCoCrAlY bond coatings", *Surface & Coatings Technology* 201 (2006) 3894–3900.
101. M. Matsumoto, K. Wada, N. Yamaguchi, T. Kato, and H. Matsubara, "Effects of substrate rotation speed during deposition on the thermal cycle life of thermal barrier coatings fabricated by electron beam physical vapor deposition" *Surface & Coatings Technology* 202 (2008) 3507–3512.
102. E. Rocca, P. Steinmetz, and M. Moliere, "Revisiting the inhibition of vanadium-induced hot corrosion in gas turbines", *Transactions of the ASME*, 125 (2003) 664-669.
103. C. Mercer, S. Faulhaber, A.G. Evans, and R. Darolia, "A delamination mechanism for thermal barrier coatings subject to calcium–magnesium–alumino-silicate (CMAS) infiltration", *Acta Materialia*, 53 [4] (2005) 1029-1039.
104. W.C. Hasz, M.P. Borom, and C.A. Johnson, "Protection of thermal barrier coating with an impermeable barrier coating", U.S. Patent No. 5871820 (1999).
105. W.C. Hasz, C.A. Johnson and M.P. Borom, "Protection of thermal barrier coatings by a sacrificial surface coating", U.S. Patent No. 5660885 (1997).
106. Zaplatynsky, "Performance of laser-glazed zirconia thermal barrier coatings in cyclic oxidation and corrosion burner rig test", *Thin Solid Films* 95 (1982) 275-284.
107. S. Ahmaniemi, P. Vuoristo and T. Mantyla, "Improved sealing treatments of thick thermal barrier coatings", *Surface and Coatings Technology*, 151-152 (2002) 412-417.
108. D.R. Clarke and S.R. Phillpot, "Thermal barrier coating materials", *Materials Today*, June 2005, 22-29.
109. B.R. Marple, J. Voyer, M. Thibodeau, D.R. Nagy and R. Vassen, "Hot corrosion of lanthanum zirconate and partially stabilized zirconia thermal barrier coatings", *Transactions of the ASME: Journal of Engineering for Gas Turbines and Power*, 128 (2006) 144-152.
110. W. Ma, S. Gong, H. Li and H. Xu, "Novel thermal barrier coatings based on La₂Ce₂O₇/8YSZ double-ceramic-layer systems deposited by electron beam physical vapor deposition", *Surface & Coatings Technology*, 202 (2008) 2704–2708.

111. Z. Xu, L. He, R. Mu, X. Zhong, Y. Zhang, J. Zhang and X. Cao, "Double-ceramic-layer thermal barrier coatings of La₂Zr₂O₇/YSZ deposited by electron beam-physical vapor deposition", *Journal of Alloys and Compounds*, 473 (2009) 509–515.
112. B.A. Nagaraj, J.L. Williams and J.F. Ackerman, "Thermal barrier coating resistant to deposits and coating method therefor", US Patent No. 6627323 B2 (2003).
113. Van der Biest, and L.J. Vandeperre, "Electrophoretic deposition of materials," *Annual Review in Materials Science*, 29 (1999) 327-352.
114. L. Besra, and M. Liu, "A review on fundamentals and applications of electrophoretic deposition (EPD)," *Progress in Materials Science*, 52 (2007) 1–61.
115. P. Sarkar, and P.S. Nicholson, "Electrophoretic deposition (EPD): Mechanisms, kinetics, and applications to ceramics," *J. Am. Ceram. Soc.*, 79[8] (1996) 987-2002.
116. Van der Biest, E. Joos, J. Vleugels and B. Baufeld "Electrophoretic deposition of zirconia layers for thermal barrier coatings", *J. Mater. Sci.*, 41 (2006) 8086–8092.
117. Z. Xu, G. Rajaram, J. Sankar and D. Pai, "Electrophoretic deposition of YSZ electrolyte coatings for solid oxide fuel cells", *Surface & Coatings Technology*, 201 (2006) 4484–4488.
118. L. Besra, C. Compson, and M. Liu, "Electrophoretic deposition on non-conducting substrates: The case of YSZ film on NiO–YSZ composite substrates for solid oxide fuel cell application", *Journal of Power Sources*, 173 (2007) 130–136.
119. S.T. Aruna, and K.S. Rajam, "A study on the electrophoretic deposition of 8YSZ coating using mixture of acetone and ethanol solvents", *Materials Chemistry and Physics*, 111 (2008) 131–136.
120. P. Sarkar, X. Huang and P.S. Nicholson, "Zirconia/alumina functionally graded composites by electrophoretic deposition techniques", *J. Am. Ceram. Soc.*, 76 [4] (1993) 1055-1056.
121. B. Ferrari and R. Moreno, "EPD kinetics: a review", *Journal of the European Ceramic Society* 30 (2010) 1069–1078.
122. R. Fischer, E. Fischer, D. De Portu and E. Roncari, "Preparation of ceramic micro-laminate by electrophoresis in aqueous system", *J. Mater. Sci. Lett.*, 14 [1] (1995) 25–27.

123. T. Mathews, N. Rabu, J.R. Sellar and B.C. Muddle, "Fabrication of $\text{La}_{1-x}\text{Sr}_x\text{Ga}_{1-y}\text{Mg}_y\text{O}_{3-(x+y)/2}$ thin films by electrophoretic deposition and its conductivity measurement", *Solid State Ionics*, 128 (2000) 111–115.
124. P. Ducheyne, S. Radin, M. Heughebaert and J.C. Heughebaert, "Calcium phosphate ceramic coatings on porous titanium: effect of structure and composition on electrophoretic deposition, vacuum sintering and in vitro dissolution", *Biomaterials*, 11[4] (1990) 244–254.
125. Zhitomirsky and A. Petric, "Electrolytic and electrophoretic deposition of CeO_2 films", *Materials Letters*, 40 (1999) 263.
126. K. Yamashita, M. Nagai and T. Umegaki, "Fabrication of green films of single and multi-component ceramic composites by electrophoretic deposition technique", *J. Mater. Sci.* 32 (1997) 6661–6664.
127. R.S. Roth, T. Negas, and L.P. Cook, *Phase diagrams for ceramists*, Vol. IV, Fig. 5127, The American Ceramic Society, Columbus, OH, pp.89 (1981).
128. R.C. Buchanan and G.W. Wolter, "Properties of Hot-Pressed Zirconium Pyrovanadate Ceramics", *J. Electrochem. Soc.*, 130 [9] (1983) 1905-1910.
129. R.L. Jones, "Thermogravimetric Study of the 800°C Reaction of Zirconia Stabilizing Oxides with $\text{SO}_3\text{-NaVO}_3$ ", *J. Electrochem. Soc.*, 139 [10] (1992) 2794-2799.
130. Burdese and M.L. Borlera, "The system $\text{ZrO}_2\text{-V}_2\text{O}_5$," *Ann. Chim. (Rome)*, 50, (1960) 1570-1572.
131. R.C. Garvie and P.S. Nicholson, "Phase analysis in zirconia systems", *J. Am. Ceram. Soc.*, 55 [6] (1972) 303-305.
132. V. Luggi and D.R. Clarke, "High temperature aging of YSZ coatings and subsequent transformation at low temperature", *Surface and Coatings Technology* 200 (2005) 1287 – 1291.
133. V. Luggi and D.R. Clarke, "Transformation of electron-beam physical vapor-deposited 8 wt.% yttria-stabilized zirconia thermal barrier coatings", *J. Am. Ceram. Soc.*, 88 [9] (2005) 2552-2558.
134. Z. Chen, J. Mabon, J.G. Wen and R. Trice, "Degradation of plasma-sprayed yttria-stabilized zirconia coatings via ingress of vanadium oxide", *Journal of the European Ceramic Society*, 29 [9] (2009) 1647-1656.

135. J. Malek, "The applicability of Johnson-Mehl-Avrami model in the thermal analysis of the crystallization kinetics of glasses", *Thermochimica Acta* 267 (1995) 61-73.
136. M.T. Averbuch-Pouchot and A. Durif, "Phosphorus Oxides", pp 11-18 in *Topics in phosphate chemistry*, World Scientific, Singapore, 1996.
137. J. Alamo and R. Roy, "Revision of crystalline phases in the system $ZrO_2-P_2O_5$," *J. Am. Ceram. Soc.*, 67 [5] c80-c82 (1984).
138. H.-J. Rätzer-Scheibe, "Electrochemical corrosion studies of uncoated and coated Ni-base superalloys in molten sulphate", *Molten Salt Forum*, Vol. 7 (2003) 295-310.
139. M. Seiersten, H.J. Rätzer-Scheibe, and P. Kofstad, "Sodium vanadate induced corrosion of MCrAlY coatings", *Materials and Corrosion*, 38 (1987) 532-540.
140. H.C. Hamaker, "Formation of a deposit by electrophoresis", *Trans. Faraday Soc.*, 35 (1940) 279-287.